



TECHNISCHE UNIVERSITÄT MÜNCHEN
TUM School of Engineering and Design

Hybrid Life Support Systems

Daniel Markus Kaschubek, M.Sc.

Vollständiger Abdruck der von der TUM School of Engineering and Design der Technischen Universität München zur Erlangung des akademischen Grades eines

Doktors der Ingenieurwissenschaften

genehmigten Dissertation.

Vorsitzender: Prof. Dr.-Ing. Markus Ryll

Prüfer der Dissertation: 1.) Prof. Prof. h.c. Dr. rer.nat. Dr. h.c. Ulrich Walter
2.) Prof. James Nabity, Ph.D.

Die Dissertation wurde am 07.07.2021 bei der Technischen Universität München eingereicht und durch die TUM School of Engineering and Design am 01.11.2021 angenommen.

This page intentionally left blank.



Acknowledgments

More than 150 years ago, Justus von Liebig postulated the "Law of the Minimum," which Adolf Mayer extended to include the influence of all growth factors. It states: "The yield depends on the nutrients present in the minimum" (Justus von Liebig, 1855) or "The yield depends on the production factor present in the minimum" (Adolf Mayer, 1869). This extended minimum law is still valid today, as six years of "plant research" have shown me. Whether in the biosphere Earth or in deep space, the development of a seed into a plant is only as good as its environmental conditions allow it to be. Many people close to me have contributed to the growth of this "plant" in all these years and thus brought it to maturity. I thank all these people from the bottom of my heart.

A decisive role in plant growth are the soil and the climate. In the case of my dissertation, these are Professor Ulrich Walter and the Department of Astronautics. I would like to thank Professor Walter not only for welcoming me into the "LRT" family and for the good atmosphere at the chair, which has always encouraged innovative and independent work, but especially for his advice and support, with which he has always helped and guided me through this work.

The soil pH is a major growth factor in plants, as is water pH in algae. My thanks to Professor James Nabity for the constructive collaboration with CU Boulder. The scientific interactions with Professor Nabity and his graduate students have often provided me with new perspectives and approaches, thus advancing my work.

I would also like to thank Dr. Claas Olthoff, who has often steered the wild growth of this "plant" back into an orderly direction and strengthened it by desprouting and staking out the shoots. As a mentor and friend, he has contributed significantly to the yield of the plant with his critical questions and our professional discussions.

Without water, a plant inevitably wilts, and this "plant" is no exception. The exchange and collaboration with my LRT colleagues have always been an important source of fresh ideas for me. With Laura, Matthias and Christian I could not only discuss simulations and lunar landing sites, they were also always willing to proofread my work and helped me with their constructive comments and valuable suggestions. I could always rely on Martin's help around IT and learning new programming techniques. Thank you all for the time we spent together at LRT.

To Mike Ewert and Molly Anderson, I thank you for the time we spent together at Johnson Space Center and the many technical discussions we had afterwards. When I had questions about NASA systems or documents, they were always there to help and advise me. They are the nutrients that this "plant" needs for healthy growth.

The CO₂ of this "plant" is provided by Professor Markus Czupalla through the development of V-HAB and Jonas Schnaitmann through the improvement of its programming fundamentals. This forms the basis of my work and enables photosynthesis for this "plant". I thank you for this sound basis. I also thank Professor Markus Czupalla for the many technical discussions on life support systems.

Many students have also contributed to various shoots and branches of this work, whether by developing models or conducting experiments. My thanks to all those I had the privilege to accompany on their journey, and who have accompanied me on my own.

In many a storm that arose over this "plant", my friends have stood by me helpfully and protectively. Thank you for taking my mind off things from time to time, so I could devote myself to my work again with even greater zeal.

My parents sowed the seed and protected the seedling from which this work has now grown. They have always supported and encouraged me and my curiosity and made it possible for me to study, and especially to stay at the Johnson Space Center during my master's thesis. For all this I am very grateful to you.

I am especially grateful to my wife Susanne for her tireless aid and for everything you did for me during this time. Through her support, she gave me the energy to finish this work. "What sunshine is to flowers, smiling faces are to men." (Joseph Addison, 1672 - 1719). For this "plant" Susanne is the sunlight.

Thank You.

This page intentionally left blank.



Danksagung

Bereits vor über 150 Jahren postulierte Justus von Liebig das „Gesetz vom Minimum“, das Adolf Mayer auf den Einfluss aller Wachstumsfaktoren erweiterte. Es besagt: „Der Ertrag ist abhängig von dem im Minimum vorhandenen Nährstoffen“ (Justus von Liebig, 1855) bzw. „Der Ertrag ist abhängig von demjenigen Produktionsfaktor, der im Minimum vorhanden ist“ (Adolf Mayer, 1869). Dieses erweiterte Minimumgesetz gilt auch heute noch, wie mir sechs Jahre „Pflanzenforschung“ gezeigt haben. Ob in der Biosphäre Erde oder im tiefen Weltraum, die Entwicklung eines Samenkorns zu einer Pflanze ist nur so gut, wie seine Umgebungsbedingungen es zu lassen. Zum Wachstum dieser „Pflanze“ haben in all den Jahren viele mir nahestehende Menschen beigetragen und sie so erst zur Reife gebracht. Bei all diesen Menschen bedanke ich mich von Herzen.

Eine entscheidende Rolle beim Pflanzenwachstum spielen der Nährboden und das Klima. Im Falle meiner Dissertation sind dies Professor Ulrich Walter und der Lehrstuhl für Raumfahrttechnik. Professor Walter danke ich nicht nur für die Aufnahmen in die Familie „LRT“ und für die gute Atmosphäre am Lehrstuhl, die innovatives und selbstständiges Arbeiten immer gefördert hat, sondern insbesondere auch für seinen Rat und seine Unterstützung, mit denen er mir immer zur Seite stand und mich durch diese Arbeit geleitet hat.

Der pH-Wert des Bodens ist bei Pflanzen, wie auch der pH-Wert des Wassers bei Algen, ein wesentlicher Wachstumsfaktor. Bei Professor James Nabyt bedanke ich mich für die konstruktive Zusammenarbeit mit der CU Boulder. Der wissenschaftliche Austausch mit Professor Nabyt und seinen Doktoranden hat mir oft neue Perspektiven und Herangehensweisen aufgezeigt und meine Arbeit so vorangebracht.

Mein Dank gilt auch Dr. Claas Olthoff, der den Wildwuchs dieser „Pflanze“ oft wieder in eine geordnete Richtung gelenkt und sie durch Entspitzen und Ausgeizen der Triebe gestärkt hat. Als Mentor und Freund hat er mit seinen kritischen Fragen und unseren fachlichen Diskussionen maßgeblich zum Ertrag der Pflanze beigetragen.

Ohne Wasser welkt eine Pflanze unweigerlich und diese „Pflanze“ ist hier keine Ausnahme. Der Austausch und die Zusammenarbeit mit meinen Kolleg*Innen des LRT ist mir stets eine wichtige Quelle frischer Ideen gewesen. Mit Laura, Matthias und Christian konnte ich nicht nur über Simulationen und Mondlandestellen diskutieren, sie waren auch stets bereit meine Arbeiten Korrektur zu lesen und haben mich mit ihren konstruktiven Anmerkungen und wertvollen Anregungen weitergebracht. Auf Martins Hilfe rund um IT und das Erlernen neuer Programmieretechniken konnte ich mich immer verlassen. Ich danke euch allen herzlich für die gemeinsame Zeit am LRT.

Bei Mike Ewert und Molly Anderson bedanke ich mich für die gemeinsame Zeit am Johnson Space Center und die vielen fachlichen Diskussionen, die wir auch danach noch geführt haben. Bei Fragen zu Systemen oder Dokumenten der NASA standen sie mir stets mit Rat und Tat zur Seite. Sie sind die Nährstoffe, die diese „Pflanze“ für ein gesundes Wachstum braucht.

Das CO₂ dieser „Pflanze“ liefern Professor Markus Czupalla durch die Entwicklung von V-HAB und Jonas Schnaitmann durch die Verbesserung von dessen programmiertechnischen Grundlagen. Dies bildet die Grundlage meiner Arbeit und ermöglicht dieser „Pflanze“ erst die Photosynthese. Für diese fundierte Basis danke ich ihnen. Professor Markus Czupalla danke ich außerdem für die vielen fachlichen Diskussionen zu Lebenserhaltungssystemen.

Nicht zuletzt haben auch viele Studierende an verschiedenen Trieben und Verzweigungen dieser Arbeit mitgewirkt, sei es durch die Entwicklung von Modellen oder der Durchführung von Versuchen. Allen, die ich auf ihrer Reise begleiten durfte und die auch mich begleitet haben, gilt mein Dank.

Bei so manchem Sturm, der über dieser „Pflanze“ aufgezogen ist, standen meine Freunde mir hilfsbereit und schützend zur Seite. Danke, dass ihr mich ab und an auf andere Gedanken gebracht habt, so dass ich mich anschließend mit noch größerem Eifer wieder der Arbeit widmen konnte.

Meine Eltern haben den Samen gesät und den Keimling geschützt, aus dem nun diese Arbeit entstanden ist. Sie haben mich und meine Wissbegierde immer unterstützt und gefördert und mir das Studium, und insbesondere auch den

Aufenthalt am Johnson Space Center während meiner Masterarbeit, ermöglicht. Für all das bin ich ihnen sehr dankbar.

Besonders dankbar bin ich meiner Frau Susanne für ihren unermüdlichen Beistand und alles, was sie für mich in dieser Zeit getan hat. Durch ihren Rückhalt hat sie mir die Energie gegeben, diese Arbeit fertigzustellen. „Was der Sonnenschein für die Blumen ist, das sind lachende Gesichter für die Menschen.“ (Joseph Addison, 1672 – 1719). Für diese „Pflanze“ ist Susanne das Sonnenlicht.

Vielen Dank.



Abstract

For the current international goal of expanding into the solar system, environmental control and life support systems (ECLSS) are required for humans to survive the hostile environments of deep space. To support this goal, more biological subsystems are integrated into ECLSS for long duration missions to produce food and close the carbon loop. These subsystems include algae, microbes and higher plants which can complement the current physical/chemical (PC) systems to create hybrid ECLSS. In this thesis a simulation tool for hybrid ECLSS that can perform dynamic, holistic, system-level simulations is developed.

As a first step the required plant growth area for a human is minimized with an optimization algorithm which has the nutritional demands as boundary conditions. Through this approach the area is reduced to 57 m² compared to the previously assumed 164 m². Then, the implementation of biological systems is analyzed with an equivalent system mass (ESM) trade-off which includes spare parts. Plant growth chambers outperform the current ISS ECLSS after 15.6 years but only if the nutrient cycle can be closed.

Therefore, closing the nutrient cycle of a biological ECLSS is a primary requirement for the further development of such systems. To achieve this, dynamic analysis is required to correctly size the required buffers and control logics. However, the current analysis tools neglect or oversimplify the biological processes, e.g. the nutrient uptake of plants or the urea and feces production of the human. Therefore, the lack of an analysis tool for these aspects is considered a key gap currently preventing the development of biological ECLSS.

To close this gap, this thesis improves the tool Virtual Habitat to include the previously neglected aspects. For this purpose, first principles models of the required PC systems are developed. Nutrient dynamics are added to the plant model and the human model now includes the protein metabolism. These are necessary to depict the primary nutrient cycle of nitrogen in the ECLSS. A biological waste recycling system closes the nutrient cycle, which is modelled with enzymatic kinetics.

Three different mission scenarios with varying biological components are analyzed to study the interaction between the systems. The first scenario studies the addition of plants into the ISS ECLSS. The results show the impact on the water imbalance between the Russian and US segment, which changes by up to 10.8 kg. In addition, the reduction of produced water by the Sabatier reactor was analyzed and deemed negligible. The second mission scenario is a Moon base at the lunar south pole and includes lighting conditions and a regenerative fuel cell system for energy storage. Here the addition of a small plant growth chamber and a larger photo bio reactor were analyzed, as well the potential usage of a Sabatier reactor to create methane and oxygen as rocket fuel. The production of fuel is feasible with a potential production of 6.73 kg/d from a crew of six. The photo bioreactor only improves the system if it is sized to process the urine of the crew and supplies part of the diet. However, the potential improvements are counteracted by a reduced fuel production of 5.26 kg/d. The third mission scenario analyses a permanent Mars base with full food provision from plants. To accommodate the large plant growth areas an upscaled version of the ISS condensing heat exchanger and an adjusted control logic were derived to maintain temperature and humidity values within the desired area. The nutrient dynamics of the system were also analyzed and overall showed the difficulty in maintaining a balance for all involved substances due to the different time frames for each process. The tool can calculate the nitrogen nutrient cycle for all involved subsystems and can support the sizing of nutrient buffers. For the considered case about 33.3 kg of nitrate are required as buffer. The tool also supports the addition of further nutrients to the cycling analysis.

This page intentionally left blank.



Zusammenfassung

Ein aktuelles internationale Ziel, ist die Expansion in das Sonnensystem. Hierzu werden Umweltkontroll- und Lebenserhaltungssysteme (ECLSS) benötigt, um Menschen in den feindlichen Umgebungen des tiefen Weltraums am Leben zu halten. Die Integration von mehr biologischen Subsystem in ECLSS für lange Zeiträume ermöglicht die Produktion von Essen und damit das Schließen des Kohlenstoffkreislaufs. Diese Subsysteme umfassen Algen, Mikroben und höhere Pflanzen und können die derzeitigen physikalisch-chemischen (PC) Systeme zu hybriden ECLSS ergänzen. In dieser Arbeit wird eine Simulationsumgebung für hybride ECLSS entwickelt die dynamische, holistische Analysen auf Systemebene erlaubt.

In einem ersten Schritt wird mit einem Optimierungsalgorithmus die benötigte Pflanzenwachstumsfläche für einen Menschen unter Berücksichtigung der benötigten Nährstoffe minimiert. Durch diesen Ansatz kann die Fläche auf 57 m² gegenüber den bisher angenommenen 164 m² reduziert werden. Die Implementierung von biologischen Systemen wird anschließend mit einem Equivalent System Mass (ESM) Trade-off analysiert, der auch Ersatzteile einschließt. Es zeigt sich, dass Pflanzenwachstums-kammern das aktuelle ISS ECLSS nach 15,6 Jahren übertreffen, sofern der Nährstoffkreislauf geschlossen werden kann.

Die Schließung des Nährstoffkreislaufs ist daher für biologische ECLSS eine primäre Anforderung an die weitere Entwicklung solcher Systeme. Um dies zu erreichen, ist eine dynamische Analyse erforderlich, die die erforderlichen Puffer und Steuerungslogiken richtig dimensioniert. Die derzeitigen Analysewerkzeuge vernachlässigen oder vereinfachen jedoch die biologischen Prozesse, wie z. B. die Nährstoffaufnahme von Pflanzen oder die Harnstoff- und Fäkalienproduktion des Menschen. Daher wird das Fehlen eines Analysewerkzeugs für diese Aspekte als eine zentrale Problematik angesehen, die die Entwicklung von biologischen ECLSS derzeit verhindert.

Um diese Lücke zu schließen, wird in dieser Arbeit das Tool Virtual Habitat um die bisher vernachlässigten Aspekte erweitert. Zu diesem Zweck werden Modelle der benötigten PC-Systeme auf Basis physikalischer Grundlagen entwickelt. Das Pflanzenmodell wird um die Nährstoffdynamik erweitert und das Menschmodell umfasst nun auch den Proteinstoffwechsel. Dadurch wird der primären Nährstoffkreislauf von Stickstoff im ECLSS dargestellt. Ein biologisches Abfall-Recycling-System, das mit enzymatischer Kinetik modelliert wird, schließt den Nährstoffkreislauf.

Es werden drei verschiedene Missionsszenarien mit unterschiedlichen biologischen Komponenten analysiert, um die Wechselwirkung zwischen den Systemen zu untersuchen. Das erste Szenario untersucht die Ergänzung von Pflanzen in das ISS ECLSS. Die Ergebnisse zeigen die Auswirkungen auf das Wasserungleichgewicht zwischen dem russischen und dem amerikanischen Segment, welches sich um bis zu 10,8 kg ändert. Darüber hinaus wurde die Auswirkung auf die Wasserproduktion des Sabatier-Reaktor analysiert und als vernachlässigbar eingestuft. Das zweite Missionsszenario ist eine Mondbasis am Mondsüdpol. Es geht auf die Lichtverhältnisse ein und beinhaltet ein regeneratives Brennstoffzellensystem zur Energiespeicherung. Hier wurde die Zunahme einer kleinen Pflanzenkammer und eines größeren Photobioreaktors analysiert, sowie die mögliche Nutzung eines Sabatierreaktors zur Erzeugung von Methan und Sauerstoff als Raketentreibstoff betrachtet. Es zeigt sich, dass die Herstellung von Treibstoff umsetzbar ist und bei einer sechsköpfigen Besatzung eine potentielle Produktion von 6,73 kg/d Methan und Sauerstoff erzielt werden kann. Der Photobioreaktor trägt nur zu einer Verbesserung des Systems bei, wenn er so dimensioniert ist, dass er den Urin der Besatzung verarbeitet und einen Teil der Nahrung liefert. Allerdings wird auf diese Weise die Treibstoffproduktion auf 5,26 kg/d gesenkt, was die möglichen Verbesserungen schmälert. Das dritte Missionsszenario analysiert eine permanente Marsbasis mit vollständiger Nahrungsversorgung aus Pflanzen. Um die großen Pflanzenanbauflächen unterzubringen, wird eine hochskalierte Version des ISS-Kondensationswärmetauschers und eine angepasste Steuerungslogik abgeleitet, um Temperatur- und Feuchtigkeitswerte im gewünschten Bereich zu halten. Die Nährstoffdynamik des Systems wird ebenfalls analysiert und zeigt insgesamt die Schwierigkeit, aufgrund der unterschiedlichen Zeitskalen der Prozesse, ein Gleichgewicht für alle beteiligten Stoffe aufrechtzuerhalten. Außerdem kann das Tool den Stickstoff-Nährstoffkreislauf für alle beteiligten Subsysteme berechnen und die Dimensionierung von Nährstoffpuffern unterstützen. Im betrachteten Fall werden etwa 33.3 kg Nitrat als Puffer benötigt. Das Framework unterstützt auch das Hinzufügen weiterer Nährstoffe zur Kreislaufanalyse.

This page intentionally left blank.



Contents

Acknowledgments.....	III
Danksagung.....	V
Abstract.....	VII
Zusammenfassung.....	IX
Contents.....	XI
Symbols.....	XV
Abbreviations & Acronyms.....	XVII
1 Introduction.....	1
1.1 Motivation.....	1
1.2 Scope.....	2
1.2.1 Definitions.....	2
1.2.2 Mission Types.....	2
1.3 Approach.....	4
2 Background: Life Support Systems.....	6
2.1 Physical/Chemical Systems.....	6
2.1.1 Air Revitalization.....	6
2.1.2 Water Reprocessing.....	8
2.1.3 Waste Management.....	8
2.2 Biological Systems.....	9
2.2.1 Plant Growth Chambers.....	9
2.2.2 Algae Reactors.....	9
2.2.3 Urine and Biological Waste Processing.....	10
2.3 Closed Ecological Life Support Systems.....	11
2.3.1 MELiSSA.....	11
2.3.2 Small Closed Ecosystem.....	12
2.3.3 Closed Ecology Experiment Facilities.....	12
2.3.4 Lunar Palace.....	14
2.3.5 Discussion.....	14
3 State of the Art.....	15
3.1 Life Support Simulation Tools.....	15
3.1.1 BioSim.....	15
3.1.2 HabNet.....	16
3.1.3 Resource Tracking Module.....	16
3.1.4 SICLE.....	16
3.1.5 ELISSA.....	16
3.1.6 EcoSimPro.....	16
3.1.7 V-HAB 1.0.....	16

3.2	Physical/Chemical Life Support Component Models	17
3.2.1	Water Processing Assembly.....	17
3.2.2	Carbon Dioxide Removal Assembly.....	17
3.2.3	Sabatier Reactor	17
3.2.4	Condensing Heat Exchanger	17
3.3	Biological Life Support Component Models	18
3.3.1	Models for Higher Plants	18
3.3.2	Biological Waste Processor Models.....	19
3.3.3	Algae Reactor Models.....	19
3.4	Human Models.....	20
3.4.1	HumMod.....	20
3.4.2	V-HAB Human model	20
4	Gap Analysis.....	21
4.1	Gap Identification	21
4.1.1	System-Level Gaps	22
4.1.2	Subsystem-Level Gaps.....	23
4.1.3	Summary of Research Gaps.....	25
4.2	Tool Selection	26
4.3	Objectives	26
4.3.1	Research Questions	27
4.3.2	Model Requirements	27
5	Methodology.....	28
5.1	Life Support Trade Off Tool.....	28
5.1.1	Adjustments to Previous Versions	28
5.1.2	Mars Base ECLSS Trade-Off Analysis.....	40
5.1.3	Summary	50
5.2	Virtual Habitat	51
5.2.1	Basic Structure	51
5.2.2	Infrastructure.....	53
5.2.3	Domains	54
5.2.4	Solvers	56
5.2.5	Generalized pH-Model.....	59
5.2.6	User Interface.....	61
5.3	Physical/Chemical Life Support Models	63
5.3.1	Selection of Subsystems	63
5.3.2	CDRA	63
5.3.3	SCRA.....	67
5.3.4	CCAA	69
5.3.5	WPA	71



5.3.6	UPA.....	75
5.3.7	BPA.....	76
5.3.8	Electrolyzer.....	78
5.3.9	Ilmenite Hydrogen Reduction Reactor.....	83
5.4	Biological Life Support Subsystem Models.....	89
5.4.1	Plant Model.....	89
5.4.2	Algae.....	98
5.4.3	CROP.....	102
5.5	Human Model.....	107
5.5.1	Respiration and Cardiovascular Layer.....	108
5.5.2	Metabolism Layer.....	108
5.5.3	Water Balance Layer.....	112
5.5.4	Digestion Layer.....	112
5.5.5	Thermal Layer.....	113
5.5.6	Overview of new V-HAB Human Model.....	114
5.5.7	Human Model Validation.....	115
6	Mission Scenario Case Studies.....	117
6.1	Limitations.....	117
6.2	Parallelization of Simulations.....	117
6.3	Mission Scenario One: ISS.....	118
6.3.1	Model Structure.....	118
6.3.2	Results.....	120
6.3.3	Discussion.....	126
6.4	Mission Scenario Two: Moon Base.....	128
6.4.1	Model Structure.....	129
6.4.2	Results.....	133
6.4.3	Discussion.....	139
6.5	Mission Scenario Three: Permanent Mars Base.....	141
6.5.1	Model Structure.....	141
6.5.2	Results.....	145
6.5.3	Discussion.....	158
7	Discussion.....	160
7.1	Summary.....	160
7.2	Conclusion.....	162
7.3	Future Work.....	164
7.3.1	Subsystem Models.....	164
7.3.2	Hybrid Life Support Analyses.....	165
7.3.3	V-HAB.....	165
8	References.....	167

Appendix A	Figures and Tables	179
A.1	List of Figures	179
A.2	List of Tables	183
Appendix B	Overview of Carbon Dioxide Reprocessing Reactions	185
B.1	Sabatier Reactor	185
B.2	Vertical Bosch Reactor	185
B.3	Solid Oxide Electrolysis	185
Appendix C	Overview of Available System Level ECLSS Models	186
Appendix D	Human Model Derivation – Metabolism Layer	187
D.1	Citric Acid Cycle	187
D.2	Glycolysis	188
D.3	Protein.....	189
D.4	Fatty Acids.....	190



Symbols

α_j^i	separation factor between j and i	b	boundary vector of upper limits for optimization
α_A	anode charge transfer coefficient	b_{eq}	vector containing the target values for optimization
α_C	cathode charge transfer coefficient	$e(t)$	error of time t for control logics
$\alpha_{transport}$	mass transport charge transfer coefficient	C_i	concentration of substance i
β_{CO_2}	correction factor for CO_2	$C_{i,0}$	initial concentration of substance i
$\beta_{leakage}$	correction factor for leakage	$C_{i,e}$	effluent/outlet concentration of substance i
δ	membrane thickness	C_{min}	minimum concentration
ε	emissivity	$C_{T,i}$	total concentration of substance i
ϵ	void fraction	$C_{cap,i}$	thermal capacity of phase i
ζ_{growth}	momentary growth inhibition factor	C_{eq}	cooling equivalency factor
ζ_{global}	global growth inhibition factor	c_i	concentration of substance i
$\Lambda_{score,i}$	MCA score for alternative i	$c_{initial PO_4}$	sum of the initial concentrations of all substances that contain a PO_4 group
λ_{ij}	performance of alternative i for criterion j	$c_{i,j}$	concentration of nutrient i in plant j
λ	membrane water content	$c_{p,i}$	specific heat capacity of substance i
ξ_{kin}	kinetic overpotential correction factor	F	Faraday constant
$\xi_{transport,T}$	mass transport temperature correction factor	$H_{Reactor}$	height of reactor
$\xi_{transport,p}$	mass transport pressure correction factor	I	electric current
ρ_i	density of substance i	i	current density
σ	Stefan-Boltzmann constant	$i_{inflection}$	inflection current density
$\sigma_{elec.}$	electric conductivity	i_{max}	maximum current density
Ψ_b	average sphericity of bubbles	J_{max}	maximum molar influx
\mathbf{A}	generic matrix	$\mathbf{K}_{exter}^{A,B,C,D}$	matrix representing the external chemical reactions of the processing steps A,B,C and D
$A_{membrane}$	membrane area	$\mathbf{K}_{inter}^{A,B,C}$	matrix representing the enzymatic inhibition model for reaction A,B,C
$A_{Reactor}$	reactor surface area	$K_{differential}$	differential parameter for control logic
$A_{SolarCells}$	solar cell area	K_i	dissociation constant for substance i
$a_{i,j}$	entry of matrix \mathbf{A} from row i and column j		

$K_{integral}$	integral parameter for control logic	$r_{reactor}$	reactor radius
K_m	Michaelis-Menten Parameter	S	scaling factor
k_m	linear driving force linearization factor	T_i	temperature of i
		t	time
$K_{proportional}$	proportional parameter for control logic	t_A	time of canopy closure
l_{lower}	lower limits for vector x	t_{EBCT}	empty bed contact time
l_{upper}	upper limits for vector x	t_{eq}	crew time equivalency factor
M_i	molar mass for substance i	t_M	time of crop maturity
$\Delta m_{O_2,pot.}$	oxygen mass consumption potential	$t_{preheat}$	preheat time
m_i	mass of substance i	t_Q	time of onset of canopy senescence
\dot{m}_i	mass flow of substance or branch i	t_w	residence time of water
n_{cells}	number of cells	U_Ω	ohmic overpotential
Δp_i	pressure difference in branch i	U_{cell}	cell voltage
P_i	pressure of phase i	$U_{kin.}$	kinetic overpotential
P_{el}	electric power	$U_{kin.,cor.}$	corrected kinetic overpotential
P_{Heater}	electrical heater power	U_{O_2}	oxygen utilization
P_{shadow}	required electric power during shadow	U_{OC}	open circuit voltage
		U_{rev}^0	reversible cell voltage
P_{eq}	power equivalency factor	$U_{transport}$	mass transport overpotential
p_i	partial pressure of substance i	$U_{transport,cor.}$	corrected mass transport overpotential
$p_{flow,i}$	pressure of flow phase i	$u(t)$	change in control parameter
\dot{Q}_j	heat flow of branch j	\dot{V}	volumetric flowrate
\dot{Q}_{Loss}	loss heat flow	$\dot{V}_{O_2,max}$	maximum aerobic volumetric oxygen consumption of a human
q	current loading of e.g. CO ₂	V	volume
q^*	equilibrium loading of e.g. CO ₂	V_{eq}	volume equivalency factor
q_T	total loading over all substances	$\nu^{A,B,C,D}$	chemical reaction rates of processing steps A,B,C and D
R	universal gas constant	v_b	average velocity of bubble
$R_{c,j}$	conductive/convective thermal resistance of branch j	ν_{tot}	total chemical reaction rates
$R_{r,j}$	radiative thermal resistance of branch j	w_j	weight for criterion j
r_b	average bubble radius	x	vector to be optimized, in this case plant growth areas
$r_{C/D}$	charge to discharge ratio	z_k	charge number
r_{O_2}	rate of oxidation		



Abbreviations & Acronyms

ACLS	Advanced Closed Loop System	CROP	Combined Regenerative Organic Food Production
ADP	Adenosine Di-Phosphate ($C_{10}H_{12}N_5O_{10}P_2^{3-}$)	DA	Distillation Assembly
AMP	Adenosine Mono-Phosphate ($C_{10}H_{12}N_5O_7P_1^{4-}$)	DLR	German Aerospace Center
ARFTA	Advanced Recycle Filter Tank Assembly	EBCT	Empty Bed Contact Time
ARS	Air Revitalization System	ECLSS	Environmental Control and Life Support System
ArtEMISS	Arthrospira sp. gene Expression and mathematical Modelling on cultures grown in the International Space Station	ELISSA	Environment for Life-Support Systems Simulation and Analysis
ATP	Adenosine Tri-Phosphate ($C_{10}H_{12}N_5O_{13}P_3^{4-}$)	ELS	Exploration Life Support
BPA	Brine Processing Assembly	ESA	European Space Agency
BR	Bosch Reactor	ESM	Equivalent System Mass
BVAD	Baseline Values and Assumptions Document (Anderson et al. 2018)	EVA	Extra Vehicular Activity
CAMRAS	Carbon-dioxide And Moisture Removal Amine Swing-bed	FAD	Flavin Adenine Dinucleotide
CCAA	Common Cabin Air Assembly	FGB	Functional Cargo Block
CDRA	Carbon Dioxide Removal Assembly	F2F	Flow to Flow processor
CEEF	Closed Ecology Experiment Facilities	GUI	Graphical User Interface
CELSS	Closed Ecological Life Support Systems	IMV	Intra-Modular-Ventilation
CFD	Computational Fluid Dynamics	ISPR	International Standard Payload Rack
cfm	Cubic Feet per Minute	ISRU	In-Situ Resource Utilization
CHX	Condensing Heat Exchanger	ISS	International Space Station
CM	Crew Member	JEM	Japanese Experiment Module
CoMANDR	Counter-diffusion Membrane Aerated Nitrifying Denitrifying Reactor	LDF	Linear Driving Force
		LED	Light Emitting Diode
		LiSTOT	Life Support Trade Off Tool
		LP	Lunar Palace
		LSR	Life Support Rack
		LSS	Life Support System
		MBR	Membrane Bio-Reactor
		MCA	Multi Criteria Analysis
		MCL	Model Confidence Level
		MEC	Modified Energy Cascade

MELiSSA	Micro-Ecological Life Support System Alternative	SCRA	Sabatier Carbon Reduction Assembly
NADH	Nicotinamide Adenine Dinucleotide Hydride	SICLE	SIimulator for Closed Life and Ecology
NASA	National Aeronautics and Space Administration	SM	Service Module
OGA	Oxygen Generation Assembly	SOE	Solide Oxide Electrolysis
PAR	Photosynthetic Active Radiation	TCCV	Temperature Control and Check Valve
PBR	Photo Bio Reactor	TEWL	Trans-Epidermal Water Loss
PC	physical/chemical	TRL	Technological Readiness Level
PEM	Proton Exchange Membrane	UPA	Urine Processing Assembly
PGC	Plant Growth Chamber	VBA	Visual Basic for Applications
PID	Proportional–Integral–Derivative	VBOS	Vertical Bosch
PMM	Permanent Multipurpose Module	V-HAB	Virtual Habitat
P2P	Phase to Phase processor	VRA	Volatiles Removal Assembly
RFCS	Regenerative Fuel Cell System	WPA	Water Processing Assembly
SCE	Small Closed Ecosystem	WSS	Water Storage System
		WSTA	Wastewater Storage Tank Assembly

1 Introduction

1.1 Motivation

For the current international goal of expanding into the solar system (International Space Exploration Coordination Group 2018), environmental control and life support systems (ECLSS) are required to support humans in the hostile environments of deep space. The development of ECLSS requires consideration of dynamic effects within the system as purely steady state considerations would not provide the necessary insights (Babcock et al. 1984: 263; Jones 2003: 1; Czupalla 2011). Traditionally, two aspects of ECLSS design are considered to require dynamic analysis: the correct sizing of buffers and the definition of suitable control logics (Jones 2003: 1). In addition to these two aspects, current research suggests that deep space exploration requires even better understanding of possible failure modes and better capabilities of the systems to detect and diagnose failure states and automatically enter a safe operation mode. Quick resupply and error analysis from Earth, as used for the ISS, is not feasible for deep space missions. (Eshima and Nability 2020; Rines et al. 2019; Alemany et al. 2019: 10)

If the goal is not only a short visit but a permanent stay, physical/chemical (PC) Life Support Systems (LSS) are not considered sufficient for the resupply of a habitat (Harper et al. 2016: 40). However, for biological LSS the sizing of buffers is even more challenging since the ecosystem on Earth relies on the large buffers available within it (Rummel and Volk 1987: 59). Due to mass limitations, it is not feasible to use such large buffers in biological LSS, which therefore require better control of the system to maintain the desired conditions. In addition, biological systems must interface with PC components creating a hybrid LSS. To ensure that all subsystems function together further system-level analysis of the interactions between the involved subsystems is required before hybrid LSS can be developed (Anderson et al. 2017a). Such a system analysis involves different time scales, from seconds for the PC systems to months for the biological systems, which makes a dynamic analysis of hybrid LSS challenging. Furthermore, it is not sufficient to use simplified averaged or fitted models for the analysis. Instead validated models that accurately predict the behavior of the involved subsystems are required (Anderson et al. 2017a). Current analysis efforts are either focused on detailed subsystem models (Coker and Knox 2016a; Hokanson 2004) or simplify aspects. For example, by using steady state value for the human or neglecting nutrient cycling (Detrell and Ewald 2019; Czupalla 2011: 336). They are suitable to size the required buffers for the primary required substances like water and oxygen. However, they do not allow analysis of stability conditions with regard to plant nutrition, as neither the dynamics nor the substances themselves are modelled. Figure 1.1-1 provides a simplified overview of a hybrid LSS and shows the primary involved mass flows. Aside from PC and biological systems, the crew is also considered part of the hybrid LSS because it directly interacts with the system and the biological part of the system could not function without the crew. The next chapter provides an overview of the scope of this thesis regarding the capability gaps described here for system-level ECLSS analysis. Chapter 4 discusses the gap analysis in detail for all aspects of the thesis.

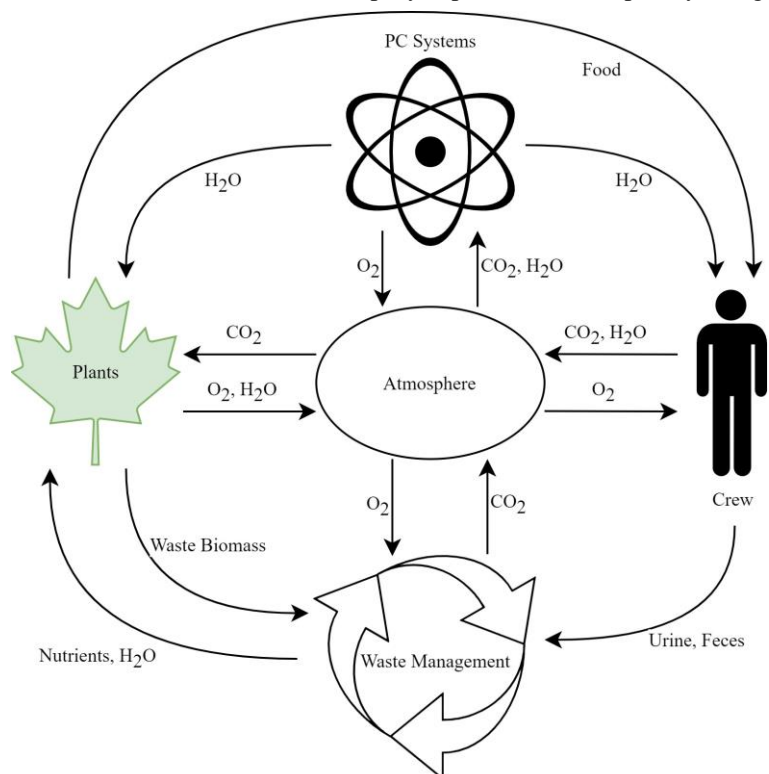


Figure 1.1-1 Simplified representation of a hybrid LSS.

1.2 Scope

Based on the motivation described in the previous chapter the objective of this thesis can be summarized as follows:

To develop a simulation tool for hybrid life support systems that can perform dynamic, holistic, system-level simulations and predict the dynamic exchange rates of energy and mass between the subsystems.

To better specify this objective, the different terms and their intended meaning are defined in detail in the following chapter. Then, three mission scenarios are derived to prove the applicability of the proposed tool to the described problems for developing hybrid LSS. Chapter 4 provides a detailed description of the objective clearly separating it from the state of the art discussed in chapter 3.

1.2.1 Definitions

1.2.1.1 Dynamic Simulation

The term “dynamic” in this case refers to both time dependent variations of parameters, like gas exchange of plants over their growth cycle, as well as variations due to changes in environmental conditions. For example, a change in the atmosphere humidity affects the transpiration rate of both plants and humans in the system.

1.2.1.2 System-Level Simulation

The term “system-level” refers to the objective of modelling the complete system, not individual subsystems. While this requires detailed subsystem models, the objective is not to go beyond state of the art for the subsystem models but rather to combine sophisticated subsystem models into a system-level simulation.

1.2.1.3 Holistic Simulation

The term “holistic” is used to emphasize the necessity to model all relevant parts of the system for an analysis in a dynamic context. Other analysis tools use steady state average values, for example for the humans in the system, and model only some parts of the system dynamically (Detrell and Belz 2017). While models are always an abstraction of reality, if the objective is to model dynamic system-level behavior, such an approach is insufficient as all elements of the system contribute to the overall dynamic behavior.

1.2.2 Mission Types

To show the applicability of the developed tool, three mission scenarios are defined in chapter 1.2.2 and analyzed in chapter 6 using the developed tool. The mission scenarios are selected based on a varying degree of biological component implementation and the current exploration goals of the Global Exploration Roadmap (International Space Exploration Coordination Group 2018).

The first mission scenario is the International Space Station (ISS), which has a PC ECLSS with relatively short stays of 180 days per crew and a quick resupply option from earth. The second mission scenario will be a potential future lunar base, which will cover longer (about one year) but non-permanent stays. For this scenario smaller biological LSS options but also In-Situ Resource Utilization (ISRU) is considered for the ECLSS. The third mission scenario is a permanent Mars base with food production covered entirely by plants. This scenario can therefore be considered the full-scale hybrid ECLSS case. In the following subchapter the three mission scenarios are discussed in more detail. Specific research questions for each scenario will be discussed in chapter 4.3.1.

1.2.2.1 Mission Scenario One: International Space Station

The first considered mission scenario is the International Space Station (ISS), since it is currently the most sophisticated ECLSS in existence. The ECLSS does not utilize biological components but some of the scientific payloads are examples for small scale biological subsystems, specifically the Veggie salad growth experiment (Massa et al., eds. 2016) and the Photobioreactor (Detrell et al. 2020). The ISS ECLSS has a large variety of physical/chemical subsystems to achieve high loop closure as shown in Figure 1.2-1. For this thesis, the ISS without biological components is considered a reference case for a current sophisticated ECLSS. It is therefore used as a baseline in many cases and

analyses to compare potential future ECLSS to the ISS ECLSS. In addition, the implementation of biological components into an existing PC ECLSS is studied using this mission scenario.

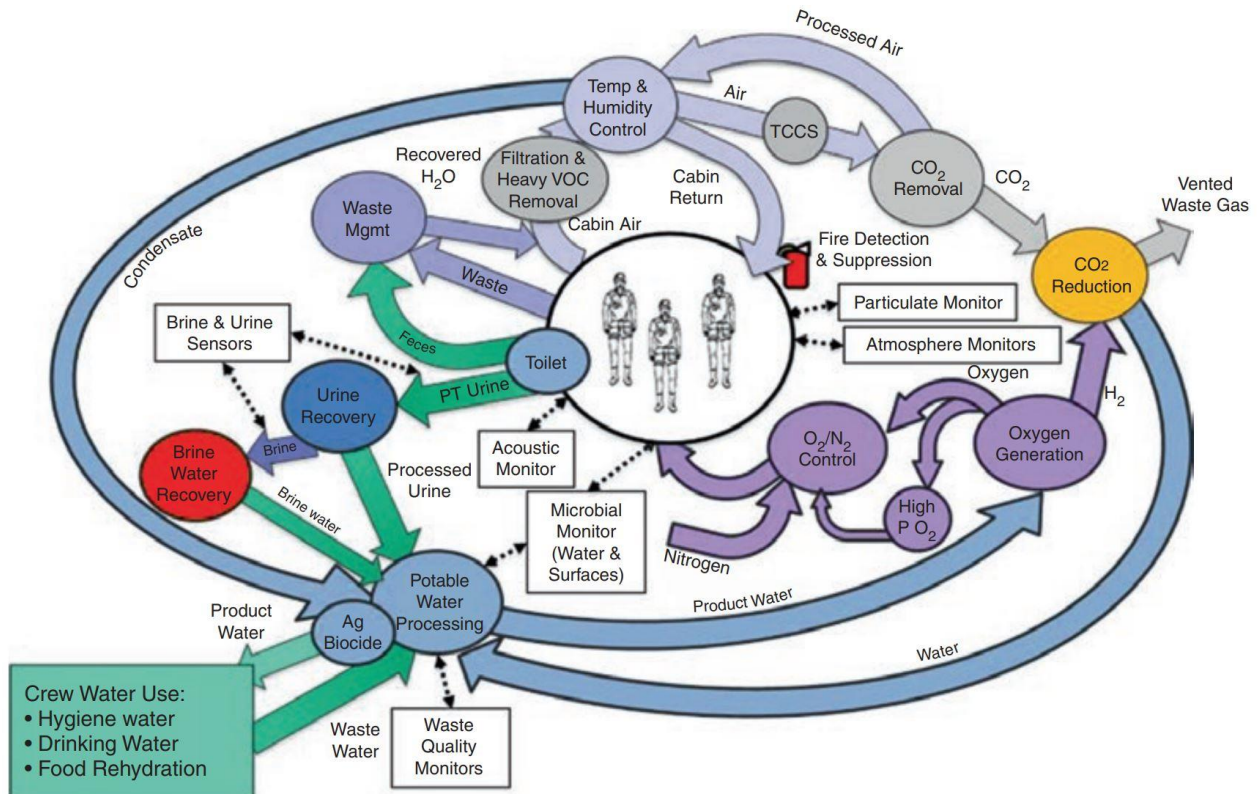


Figure 1.2-1 Mission Scenario One: The life support system of the International Space Station (Seedhouse 2020: 82).

1.2.2.2 Mission Scenario Two: South Pole Moon Base

The second mission scenario is a Moon base at the south pole for long duration (about one year) but not permanent stays. This coincides with the Moon Village proposed by the European Space Agency (ESA) and is the next near-term goal for a surface base. The location has special conditions regarding the thermal and lighting environment, which provide additional challenges to the ECLSS and the energy management of the base. Biological components are considered as a potential addition for this mission scenario and the system with and without biological components is analyzed to showcase the differences and identify potential implementation issues. As this mission scenario considers a surface system, ISRU is possible and considered as an alternative to additional loop-closure. Figure 1.2-2 provides an overview of the system considered for this mission scenario. Note that EVAs are not part of this analysis.

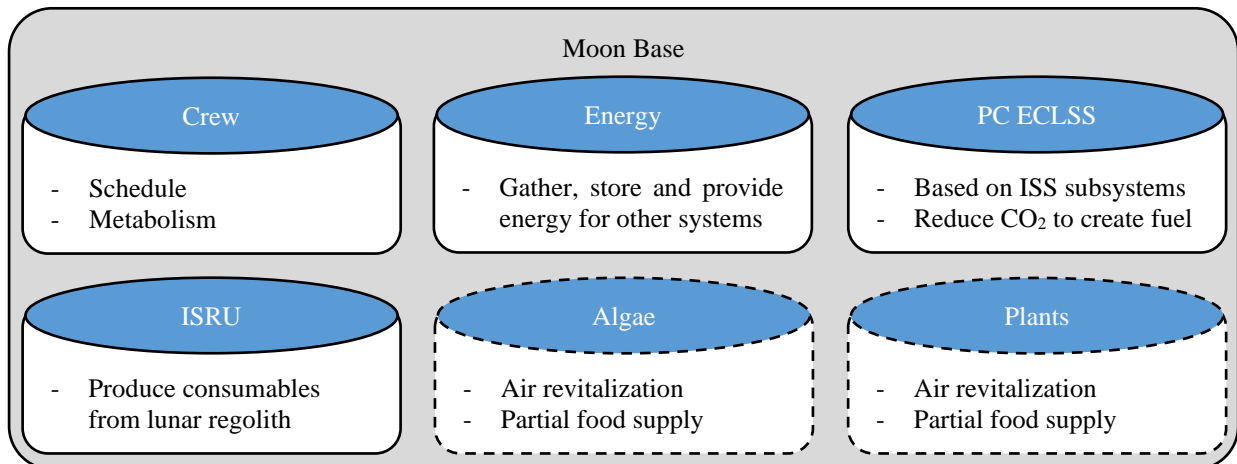


Figure 1.2-2 Mission Scenario Two: south pole Moon base system overview. Dashed systems are optional.

1.2.2.3 Mission Scenario Three: Permanent Martian Base

The third mission scenario shall emphasize the biological subsystems for loop closure in a proposed permanent Martian base. That many biological components for such a LSS are necessary is a valid assumption according to (Harper et al. 2016: 40). Furthermore, such a system coincides with the long-term exploration goals and can be considered the hybrid LSS mission scenario with maximal usage of biological components and the highest loop-closure. While the overall mission duration for this scenario is a permanently crewed outpost on Mars, the crew could potentially change after a few years. Figure 1.2-3 provides an overview of the system considered for this mission scenario.

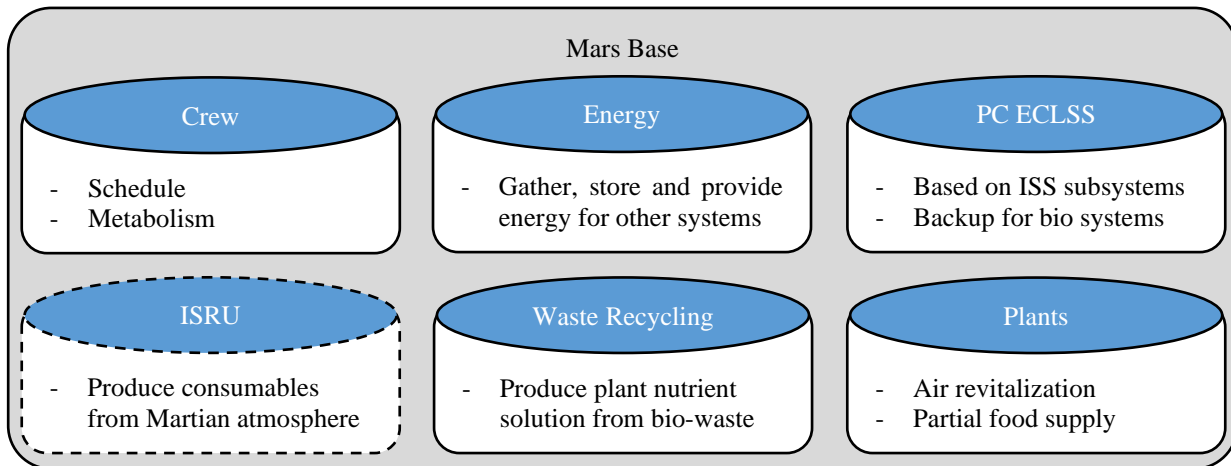


Figure 1.2-3 Mission Scenario Three: Permanent Martian base system overview. Dashed systems are optional.

1.3 Approach

Chapter 2 provides an overview of the current ECLSS state of the art and discusses available subsystems for the different required functions. In chapter 3 the state of the art for ECLSS modelling is analyzed and discussed. By combining the results of these two chapters, a research gap is identified in chapter 4. The identified gap describes the limitations of current simulation tools that lack capabilities or lack models for required subsystems in the necessary level of detail. Therefore, the identified gaps are separated into system-level and subsystem-level gaps. System-level gaps refer to missing capabilities in the current ECLSS modelling tools while subsystem-level gaps refer to missing capabilities in the currently available subsystem models. As final output of these three chapters, the objective of the thesis is specified and the tool for following further studies is selected.

In chapter 5 the methodology for the proposed research is discussed in detail. The chapter is separated into the primary areas where further work on the existing methodologies was necessary. Chapter 5.1 discusses trade-offs for ECLSS and the corresponding derivation of optimal ECLSS for different mission durations. It also covers preliminary analysis of biological LSS and how they must be operated to be viable alternatives or additions to PC LSS. This includes an optimization of growth areas for plants and its composition while considering the required nutrition. Chapter 5.2 discusses work related to the general framework for the proposed simulation tool and for general aspects of the calculation that impact more than one subsystem. Chapter 5.3 covers PC LSS subsystem models and their final implementation, while chapter 5.4 covers this for biological LSS subsystems. In chapter 5.5 the human model is discussed and compared to the most sophisticated currently available human model identified in chapter 3.4. In chapter 6 the three proposed mission scenarios are analyzed and the defined research questions for each mission scenario are discussed. Finally in chapter 7 the overall performed work is summarized and discussed. A conclusion is drawn including whether the intended objective of the thesis was achieved and potential future work and areas for improvement are discussed.

Figure 1.3-1 provides a graphical overview of the dissertation structure.

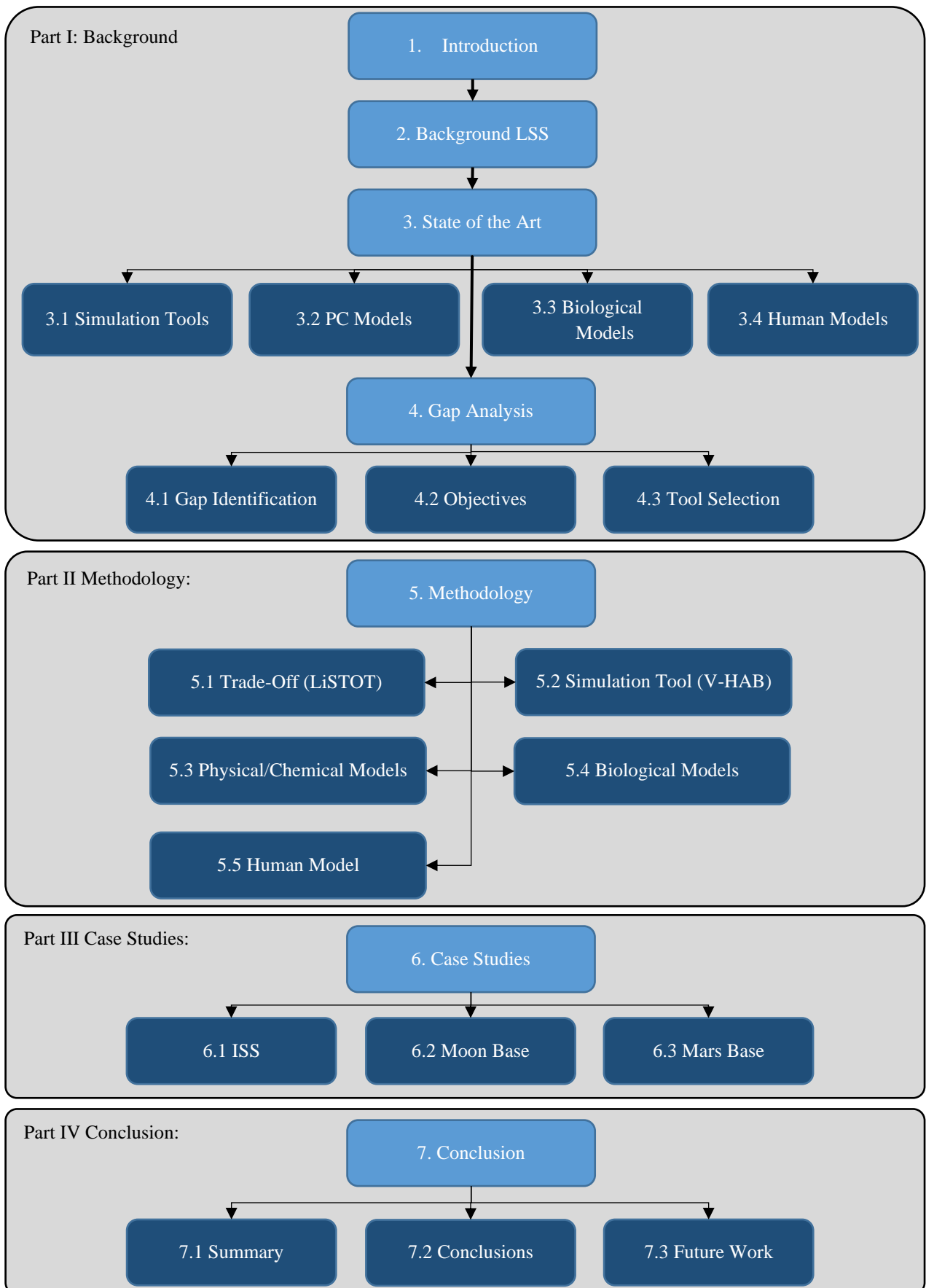


Figure 1.3-1 Dissertation overview.

2 Background: Life Support Systems

Since models are only representations of reality it is necessary to first introduce and discuss the current state of the technologies that shall be modelled in this thesis. The LSS in question can be separated into two categories: physical/chemical (PC) LSS and biological LSS. While PC LSS use a combination of physical and chemical processes to provide the necessary life support functions, biological systems employ plants and microorganisms to achieve a symbiotic relationship with the human.

For the state of the art analysis, this thesis will consider PC systems that are at least at a Technology Readiness Level (TRL) of 5, which corresponds to a functional verification of critical components in a relevant environment (DIN ISO 16290 2016). This selection was made because for less mature systems the available information is insufficient for detailed modelling. For biological systems lower TRL are considered since no mature systems exist at the desired sizes to support humans in an ECLSS. However, for biological systems models for the plants/algae etc. exist even if the system itself is at a low TRL. Therefore, a lower TRL is feasible for the detailed analysis of biological systems.

It is necessary to provide an overview of both PC and biological systems to identify possible interactions between systems and possible areas of optimization. This chapter does not select technologies, it only provides an overview of sufficiently mature technologies currently available. It also does not serve as an introduction into the topic of LSS, since current and up to date references for this topic already exist. Readers who are unfamiliar with the topic LSS in general should refer to the cited literature for the required basic understanding. For example, (Seedhouse 2020) provides a current overview of this topic.

2.1 Physical/Chemical Systems

The current state of the art for a fully integrated physical/chemical system is the LSS of the International Space Station (ISS). It covers the functions of air revitalization and water processing with at least partial loop closure while waste management and food supply are based on resupply from Earth. PC systems are inherently unable to supply food or close the carbon loop and will therefore always remain partially open loop systems. While the Russian life support subsystems of the ISS also have a high enough TRL, the available information on these systems is limited. For this reason, these systems are not considered here.

2.1.1 Air Revitalization

The Air Revitalization System (ARS) of the ISS uses an electrolyzer (the Oxygen Generation Assembly or OGA) to produce oxygen and hydrogen from stored water. For CO₂ removal, the Carbon Dioxide Removal Assembly (CDRA) is used. The CO₂ from CDRA is then combined with the H₂ from OGA in a Sabatier reactor (SCRA) to generate water, thus recovering about 50% of the O₂ from the CO₂ (Seedhouse 2020: 82). Although due to inefficiencies and lean operating conditions the actual recovery rate is closer to 42% (Crusan and Gatens 2017). See also Figure 1.2-1.

For air revitalization two other systems are currently in a mature development state. One is the Carbon-dioxide And Moisture Removal Amine Swing-bed (CAMRAS) developed by Hamilton Sundstrand for the National Aeronautics and Space Administration (NASA) (Swickrath et al. 2011), which will be used on the Orion Spacecraft. The other is the Advanced Closed Loop System (ACLS) or now Life Support Rack (LSR) developed by Airbus for ESA. ACLS is installed as payload on the ISS and expected to finish final checkout (Witt et al. 2020). Both use thermal amine for CO₂ removal and ACLS additionally contains a Sabatier reactor and an electrolyzer to cover all functions that the ISS ARS currently performs. NASA is also working on three new CO₂ removal technologies, of which the Thermal Amine Scrubber is currently on the ISS and therefore the most major system. The other two systems are expected to fly in the coming years (Shaw et al. 2020). However, as the goal for the current Thermal Amine Scrubber demo is to reach TRL 5 (Ranz et al. 2019), none of these systems reaches the previously defined TRL of 5 and therefore they are not further considered in this analysis.



2.1.1.1 Carbon Dioxide Removal

The considered candidate systems for CO₂ removal with a sufficient TRL are shown in Table 2.1-1.

Table 2.1-1: Carbon dioxide removal candidate technologies.

System	TRL	CO ₂ Removal Capacity	Closed Loop Capable	Source
CDRA	9	5.2 kg/d at 259 Pa CO ₂	Yes	(Coker and Knox 2016a)
CAMRAS	9	5.1 kg/d at 150 Pa CO ₂	No	(Button and Sweterlitsch 2013)
ACLS	8	3.0 kg/d at 373 Pa CO ₂	Yes	(Witt et al. 2020)

The ACLS is considered to be TRL 8 since the final checkout is not yet finished. As can be seen from comparing the CO₂ removal capacities, ACLS is designed for a crew of 3, while CAMRAS and CDRA are designed for larger crews. The current target for the CO₂ partial pressure is to remain below 266 Pa (Shull and Schneider 2016), which is also the reason for the partial pressures at which the removal capacity of CDRA and CAMRAS are reported. The ACLS data comes from on orbit data of the ISS, which is therefore higher. ACLS was also designed for the slightly higher partial pressure because the new lower target was only introduced recently. CAMRAS is currently not suitable for closed loop operations, as the outlet stream is a mixture of water and CO₂, which are both vented into space. Therefore, the system currently loses not only CO₂ but also water. To use the outlet stream of CAMRAS for CO₂ reprocessing technologies, the water would have to be removed first and a compressor for the pressure swing would be required.

2.1.1.2 Oxygen Generation

The current state of the art for PC oxygen generation is the electrolysis of water. On the ISS by the American (OGA), Russian (Elektron) and European (ACLS) systems utilize this. Table 2.1-2 provides an overview of these systems.

Table 2.1-2: Oxygen generation candidate technologies.

System	TRL	O ₂ Generation Capacity	Cell Voltage / V	Source
OGA	9	9.2 kg/d at 10 ⁵ Pa	1.65	(Schaezler and Cook 2015; Takada et al. 2019)
Elektron	9	2.6 kg/d		(Schaezler and Cook 2015; Takada et al. 2019)
ACLS	8	2.5 kg/d at 10 ⁶ Pa	1.64	(Witt et al. 2020; Bockstahler et al. 2015)

The cell voltage is an indicator for the electrical efficiency of the electrolysis, which is 89.1 % for the ACLS (Bockstahler et al. 2015) and has a similar value for the OGA based on the cell voltage. The operating pressure and cell voltage for Elektron could not be identified.

2.1.1.3 Carbon Dioxide Reprocessing

A recent analysis compares the different carbon dioxide reprocessing technologies that are currently under development at NASA using an equivalent system mass (ESM) and multi criteria approach (Abney et al. 2020). Most of the considered technologies are below TRL 4, with only two candidates reaching TRLs above 5: the Sabatier Carbon Reprocessing Assembly (SCRA) and the Vertical Bosch (VBOS). The ACLS also includes a carbon dioxide reprocessing assembly based on the Sabatier process and is therefore also considered here. In addition, CO₂ electrolysis with Solid Oxide Electrolysis (SOE) is considered. Table 2.1-3 provides an overview of the candidate technologies.

Table 2.1-3: Carbon dioxide reprocessing candidate technologies. A human equivalent corresponds to the metabolic outputs of a human as defined by (Anderson et al. 2018: 63).

System	TRL	Human Equivalents	Oxygen Recovery / %	Source
SCRA	9	8	~54	(Abney et al. 2020)
VBOS	5.4	8	~100	(Abney et al. 2020)
ACLS	8	3	~50	(Witt et al. 2020)
SOE	5	~1	~100	(McKellar et al. 2010)

Aside from the parameters used in the trade-off study of (Abney et al. 2020), no information on the VBOS could be found during literature review. The Series Bosch Reactor, for which more reporting exists (Greenwood et al. 2018) is only at TRL 3.5. Note that an overview of the chemical reactions for the discussed systems is provided in Appendix B.

2.1.1.4 Temperature and Humidity Control

There are currently two systems that can perform temperature and humidity control. The current state of the art is represented by the Common Cabin Air Assembly (CCAA) on the ISS, which uses a condensing heat exchanger (CHX) to remove humidity. Similar systems using the same principle exist, for example the CHX in the Columbus module. But since the basic operating principle is identical to the CCAA, these systems are not considered individually. New types of CHX that are more reliable are currently under development at NASA (Hansen et al. 2017). Additionally, CAMRAS can be used for humidity control as it not only absorbs CO₂ but also water. For temperature control, a non-condensing heat exchanger would be required, since CAMRAS cannot perform this task.

2.1.1.5 Trace Contaminant Control System

The state of the art for trace contaminant control, which is used on the ISS, is acid-impregnated granular activated carbon (Perry 2017). These charcoal beds are not regenerable, which is the reason why a regenerable version is in development for space suits. The regenerable version uses carbonized 3D printed polymers that can be regenerated at room temperature using vacuum. (Wójtowicz et al. 2019)

2.1.2 Water Reprocessing

The ISS uses the Water Processing Assembly (WPA), Urine Processing Assembly (UPA) and Brine Processing Assembly (BPA) for water reprocessing. The WPA uses particulate filters together with ion exchange beds for filtration and a catalytic reactor that oxidizes organics, which can then be filtered by the ion exchange beds. The UPA uses distillation to recover water from urine (Carter et al. 2017b) producing brine as residue. The BPA recovers water from this brine with ionomer-membrane distillation to reach 98% total water recovery (Kelsey et al. 2018).

For the Lunar Palace facility in China, a urine processing technique was developed to increase the loop closure of biological systems. The urine is first hydrolyzed and then the water and ammonia gas mixture is cooled and collected by using reduced pressure distillation in alkaline conditions (Deng et al. 2016).

2.1.3 Waste Management

For long duration visits to other planets waste management becomes a relevant factor as planetary protection agreements prohibit dumping trash on the surface. However, the PC technologies available for this are all at a TRL lower than 5 as they are currently in the laboratory test stage (TRL 4) and therefore are not considered in detail in this thesis. For completeness, a short overview of the potential systems is provided in this chapter.

Currently NASA is developing a Heat Melt Compactor system that uses heat and pressure to sterilize waste, make it storable and recover a portion of the water content from it (Anderson et al. 2017b). The alternative approach for waste management is the production of gas from trash through various processes. An overview of the potential trash to gas technologies is discussed in (Anthony and Hintze 2014) and summarized in Table 2.1-4. The waste stream assumed by (Anthony and Hintze 2014) is from (Ewert and Broyan 2013) and includes feces, brine and other biological waste. (Anthony and Hintze 2014) also assume that the crew CO₂ is processed into methane by the trash-to-gas technologies. Therefore, the produced methane and oxygen values from the paper cannot be considered applicable to a hybrid LSS where the CO₂ is consumed by plants or algae. The processing of biological waste is also not suitable to hybrid LSS because this results in a high mass requirement for the nutrient supply of biological systems like plant growth chambers. A potential PC technology which allows nutrient recovery is used in a CELSS discussed in chapter 2.3.2. Chapter 5.1.2.5 will discuss the requirement of nutrient recycling in detail.

Table 2.1-4: Overview of PC waste management technologies based on (Anthony and Hintze 2014; Anderson et al. 2017b).

System	TRL	Carbon Recovery / %
Heat Melt Compactor	4	0
Catalytic Wet Air Oxidation	4	56.2
Incineration	4	100
Ozone Oxidation	4	56.5
Pyrolysis	4	38.8
Steam Reforming	4	100



2.2 Biological Systems

In bioregenerative LSS plants or algae produce food and oxygen for the humans while removing CO₂ and reprocessing water. Since direct watering of plants with urine proved to be infeasible (Zolotukhin et al. 2005a) additional biological water treatment systems are used to process urine. Furthermore, in order to close the carbon loop, the processing of biological waste is necessary for systems that want to achieve high loop closures (Wheeler 2003). This chapter is separated into overviews of the individual technologies required for a bioregenerative LSS and an overview of current integrated biological LSS research.

2.2.1 Plant Growth Chambers

Plant growth chambers (PGC) are currently the only technology in development that could close the carbon loop in LSS completely by providing food for the crew. However, the systems currently available provide either a small growth area or are Earth-based demonstrators, which therefore have a lower TRL.

Table 2.2-1: Plant growth chamber candidate technologies.

System	TRL	Growth Area / m ²	Gravity	Source
Advanced Plant Habitat	9	0.2	No	(Monje et al. 2020)
Veggie	9	0.11	No	(Ehrlich et al. 2017)
Mars Lunar Greenhouse	4	44.0	Yes	(Furfaro et al. 2017)
MarsOASIS	4	0.37	Yes	(Darnell et al. 2015)
EDEN ISS	4	12.5	Yes	(Zabel et al. 2020)

The two systems with the largest growth area are the Mars Lunar Greenhouse from the University of Arizona and the EDEN ISS greenhouse. The Mars Lunar Greenhouse is a ground test facility containing four cylinders that can be inflated and extended in space for a Mars or lunar base. It is sized to achieve 100% air revitalization for the intended crew of four astronauts. Each greenhouse has a canopy area of 11 m² and a volume of 21 m³ and uses a hydroponic plant growth system. The greenhouse uses high power sodium lamps instead of light emitting diodes (LED). (Furfaro et al. 2017)

The EDEN ISS project is an international effort to design a future bioregenerative LSS. During the project tests with two twenty-foot shipping containers, which were modified into a greenhouse with a growth area of 12.5 m², were performed in Antarctica during a 12-month space analogue mission. The system uses a combination of aeroponic and nutrient-film-techniques to supply the plants with nutrients and water. (Zabel et al. 2017; Boscheri et al. 2017; Zabel et al. 2020)

A review of PGC systems that have flown to space can be found in (Zabel et al. 2016). But as these do not represent the state of the art they will not be further discussed here.

2.2.2 Algae Reactors

Compared to higher plants, algae reactors have faster reaction times. Thus, they are easier to integrate into LSS. However, in comparison to higher plants they can at most provide ~35 % of the diet (Belz et al. 2014). In addition to air revitalization and partial food supply, algae reactors can also be used for nitrification of urine and produce potable water (Tao et al. 2020). An overview of current algae reactors is provided in Table 2.2-2.

Table 2.2-2: Algae reactor candidate technologies.

System	TRL	Algae Volume / l	Source
PBR	8.5	0.65	(Helisch et al. 2020)
ArtEMISS	9	0.06	(Poughon et al. 2020)
Aquacells	5	1.45	(Häder 2019)
Omegahab	5	1.35	(Häder 2019)
Algae Reactor	3	140	(Ruck et al. 2019)

One high TRL algae reactor is the Photo Bio Reactor (PBR), which was installed on the ISS in 2018. Originally the reactor should receive CO₂ from ACLS, but as ACLS had not finished commissioning a separate CO₂ supply was used instead. The reactor uses *Chlorella vulgaris*, which an astronaut can harvest with a syringe assembly to gather test data. The PBR operation on the ISS had to be aborted because of a sudden lack of power that caused the PBR to stop working. Therefore, the TRL for this technology is set to 8.5. (Detrell et al. 2020; Helisch et al. 2020)

The other flight proven algae reactor ArtEMISS (*Arthrospira* sp. gene Expression and mathematical Modelling on cultures grown in the International Space Station) has only one tenth of the volume and did not allow harvesting of algae during the operation, but aside from this it used similar approaches as the PBR. (Poughon et al. 2020)

All current flight hardware algae reactors are quite small. For this reason, a theoretical design for a minimal size algae reactor for a crew of five humans (Ruck et al. 2019) was included in the table to provide a relation between the current small scale systems and an optimistic theoretical full scale system. But the minimum required size for an algae reactor for life support depends on many factors and varies greatly. A literature survey reported oxygen production rates for terrestrial algae reactor in the range of 2.1 g/(l d) to 53.1 g/(l d) (Niederwieser and Klaus 2018). The oxygen production for PBR was reported to be 0.0051 mol/d (Helisch et al. 2020: 103). With a volume of 0.65 l for the reactor. This results in an oxygen production of only 0.25 g/(l d), which is much lower than the smallest reported oxygen production rates for terrestrial reactors. This is attributed to the oxygen transfer through the membrane, which is inhibited and limits the photosynthetic quotient to 0.31 on average (Helisch et al. 2020: 103). The other ISS experiment ArtEMISS reported oxygen production rates between 0.054 g/(l d) and 0.27 g/(l d) (Poughon et al. 2020: 62) and therefore also shows much lower oxygen productivity compared to the review data. Considering the oxygen consumption of a human of 0.816 kg/d (Anderson et al. 2018: 50) and the values for the space algae reactors a volume of more than 3.2 m³ would be necessary to support one human, which is significantly more than the theoretical optimized 0.028 m³ per human from (Ruck et al. 2019).

2.2.3 Urine and Biological Waste Processing

In biological waste and water recycling the focus is not only on recovering the water from waste streams within the system but also to recover the nutrients. In addition, PC systems often have significant resupply masses and use potentially harmful substances. (Pickett et al. 2020: 65)

Biological waste treatment usually is performed by microbes that are in contact with the waste-water stream and metabolize the contaminants into more useful substances. The microbes are present as a biofilm on a carrier medium, which varies depending on the system. For the Combined Regenerative Food Production (CROP) system this carrier medium is volcanic stone. The Counter-diffusion Membrane Aerated Nitrifying Denitrifying Reactor (CoMANDR) and the Membrane Bio-Reactor (MBR) both use membranes as carrier medium for the biofilm.

A comparison of biological waste water recycling technologies and PC waste water technologies can be found in (Pickett et al. 2020). Table 2.2-3 provides an overview of the current biological waste recycling technologies. It should be noted that the CROP system is only operated for urine recycling in the reported tests while the other two systems treat all waste-water streams. This explains the large difference in water output between these systems. Another important distinction is that CROP is intended to produce water and nutrient supply for higher plants, while the other two systems are intended for potable water production.

Table 2.2-3: Biological waste recycling candidate technologies.

System	TRL	Water Output / l/d	Batch Mode	PC Post Treatment	Potable Output	Source
CoMANDR	4	15.1	No	Yes	Yes	(Christenson et al. 2020)
CROP	4-5	0.4 *	Yes	No	No	(Bornemann et al. 2018)
MBR	4	53.12	No	Yes	Yes	(Li et al. 2018b)

*Estimated based on the reported 4 g urea conversion per day, assuming 16 g urea are produced in 1.6 l of water based on (Anderson et al. 2018: 50)

2.3 Closed Ecological Life Support Systems

Aside from the individual subsystems there are projects striving to create Closed Ecological Life Support Systems (CELSS), which are integrated systems to achieve high loop closure. Table 2.3-1 provides an overview of such systems for which work is currently ongoing.

Table 2.3-1: Closed Ecological Life Support Systems (CELSS) demonstrators.

System	TRL	Crew Size	Plant Area / m ²	Source
MELiSSA	3	0.05*	-	(Walker and Granjou 2017; Alemany et al. 2019)
SCE	3-4	0.08	1.8	(Tikhomirov et al. 2018; Trifonov et al. 2016)
CEEF	4	2	150	(Tako et al. 2017; Tako et al. 2010)
Lunar Palace	4	4	120	(Dong et al. 2017; Fu et al. 2021)

*Estimated based on the reported oxygen consumption of rats used as dummy crew compared to human oxygen consumption from (Anderson et al. 2018: 50)

2.3.1 MELiSSA

The European project Micro-Ecological Life Support System Alternative (MELiSSA) started development in 1988 and uses the approach to characterize all required processes in detail, which is also the reason why it is not finished even after more than 30 years of development (MELiSSA Foundation PS 2021). The current development state provides life support for rats with a PBR for air revitalization resulting in a small scale demonstrator (Alemany et al. 2019). The final concept of MELiSSA suggests the use of multiple compartments to achieve high loop closure. Figure 2.3-1 provides an overview of the planned final configuration of MELiSSA.



Figure 2.3-1 A schematic representation of the MELiSSA loop, with the five compartments and their relations highlighted (Volponi and Lasseur 2020).

The plants for the higher plant compartment are not finalized. At least no publication providing information on this could be identified. The PBR uses *Spirulina* as algae while the other compartments of C1 to C3 also use specific microorganisms. Overall, the goal for MELiSSA is to achieve loop closure for all major substances including trace elements like sulfur and other elements. (Volponi and Lasseur 2020)

The very long development duration of MELiSSA and the current small scale of the demonstrators shows the significant difficulty in achieving a CELSS. Since only parts of the planned system are currently operated together, the TRL for this system was set to 3.

2.3.2 Small Closed Ecosystem

The Small Closed Ecosystem (SCE) is intended as a precursor of a future full-scale CELSS. For this system a physical/chemical wet oxidation reactor that can process urine, feces and plant waste is used instead of biological solutions for waste treatment. Figure 2.3-2 provides an overview of the SCE. (Tikhomirov et al. 2018)

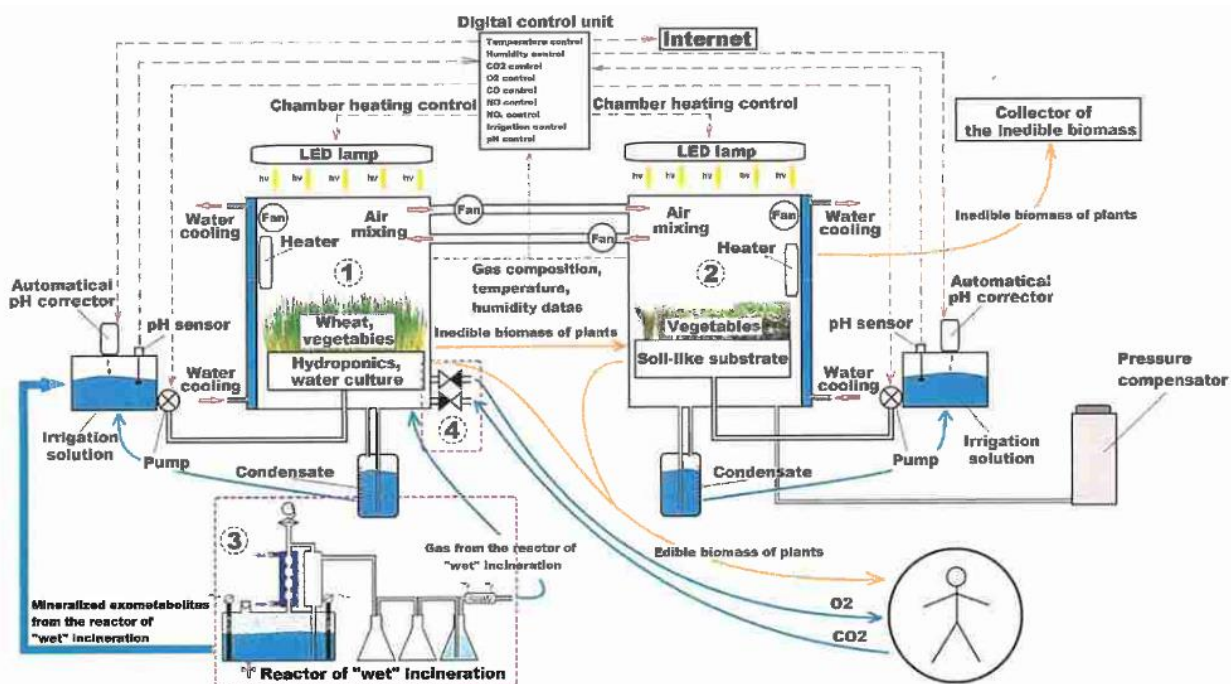


Figure 2.3-2 Flow chart of the SCE when a human is connected to the system (Tikhomirov et al. 2018).

The plants grown in SCE consist of saltwort, chufa, radish, lettuce and primarily wheat (Tikhomirov et al. 2011). Due to the small scale the plant composition of SCE is not yet optimized to provide the complete diet for a human. A future CELSS based on SCE is planned but no further information on it was found during the literature survey. Note that the SCE already exists as test setup while the full scale CELSS based on it is just a concept. Since the actual composition of the planned full scale CELSS is unknown, the TRL for this system can be considered somewhere between 3 and 4.

2.3.3 Closed Ecology Experiment Facilities

The Closed Ecology Experiment Facilities (CEEF) uses a plant growth area of 150 m² and had a crew of two humans and two goats (Tako et al. 2017). (Masuda et al. 2005) discuss the specific cultivation area of the individual plants as well as harvest conditions and the produced average fresh weight per day in CEEF. The cultivation area of CEEF was not sufficient to support the crew and instead 254.85 m² were calculated as the required area per crew member (Masuda et al. 2005: 95). The most significant difference to the previously discussed CELSS is the high integration with PC components as shown in Figure 2.3-3. In addition, the concept does not allow loop closure with regard to minerals, as waste biomass is incinerated, and the ash is not reutilized in the system.

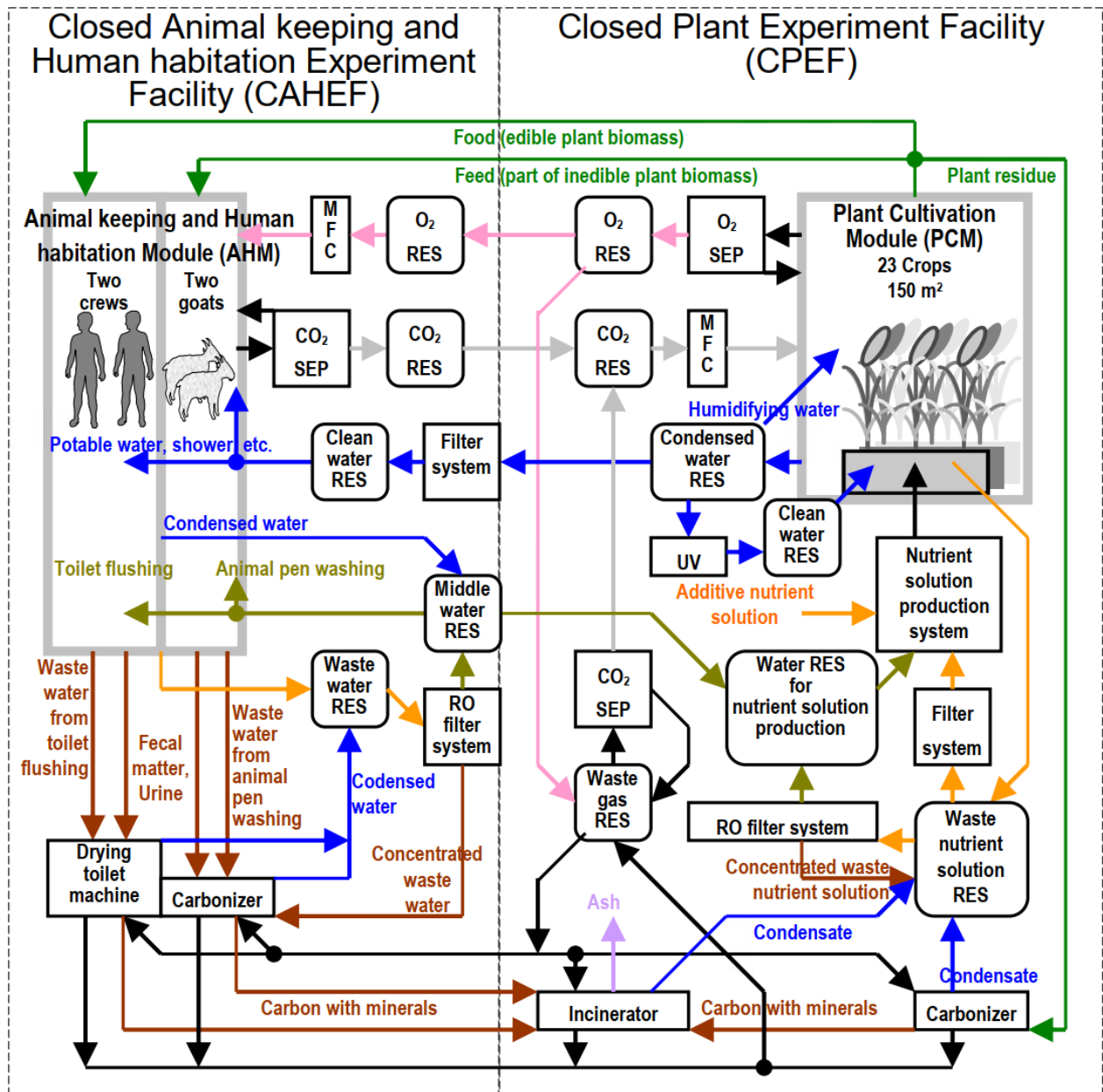


Figure 2.3-3 Material flows in CEEF (Tako et al. 2017).

2.3.4 Lunar Palace

In the Lunar Palace (LP) CELSS initially a total plant growth area of 67 m² together with yellow mealworms was used to provide 78% of the required food for the crew (Fu et al. 2019: 697). In more recent efforts, the plant growth area was increased to 120 m² and a study with four crew members was performed for 365 days (Fu et al. 2021: 6). For water treatment, a combination of PC and biological systems is used to recover waste water and its nitrogen content (Fu et al. 2016). During the LP tests the CO₂ level increased for a crew of three male crewmembers but was adequate for a crew of one male and two female crewmembers (Fu et al. 2016: 934). Figure 2.3-4 provides an overview of the material cycle for the LP CELSS.

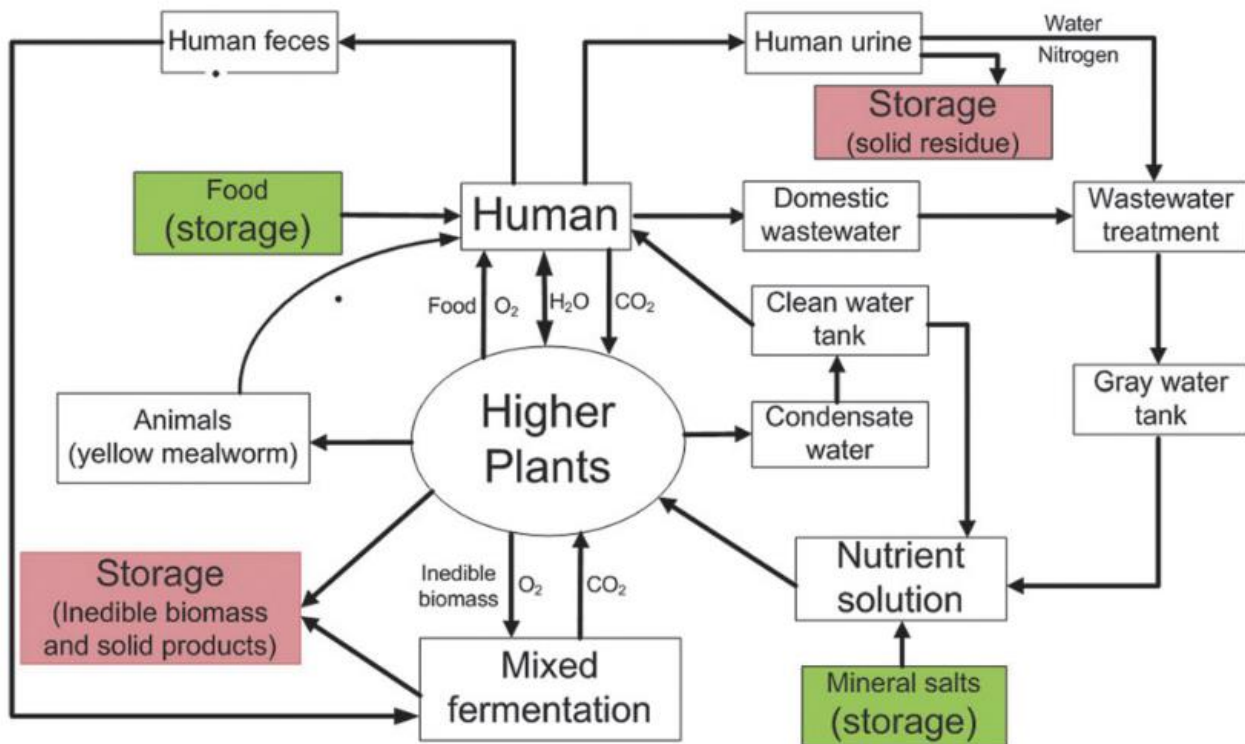


Figure 2.3-4 Material cycling in the Lunar Palace experiment (Dong et al. 2017).

2.3.5 Discussion

Of the discussed CELSS MELiSSA is the one that utilizes biological components the most. Actually, in the publication no specific PC is mentioned but likely at least the humidity control must be performed by a CHX or a similar PC technology. The other CELSS discussed are all examples of hybrid LSS with varying combinations of PC and biological components. Notably, the CEEF utilizes dedicated CO₂ and O₂ removal technologies to first remove these substances from the atmosphere and then supply them as needed. Other facilities use a constant air exchange between the crew cabin and the plant growth chamber to supply the oxygen produced by plants to the crew and the CO₂ of the crew to the plants. Another significant difference is the utilization of animal proteins. MELiSSA does not use any animal proteins source, as the efficiency of protein creation is considered an order of magnitude smaller than for plants (Volponi and Lasseur 2020). On the other hand, LP utilizes yellow mealworms to process inedible plant biomass and provide protein. Although it is stated that the suitability of the menu for international crews must be further evaluated (Fu et al. 2019: 701).

A commonality between the different CELSS is the combination of biological and PC subsystems to achieve the various ECLSS functions. However, none of the currently available systems achieves element cycling for all major substances and most do not even close the carbon loop in their current development state.



3 State of the Art

For this thesis, the relevant state of the art covers the various currently existing modelling tools for LSS. While the first subchapter covers complete life support simulation tools, in many cases research focuses on individual models for plants, humans or individual components. To provide a comprehensive review of the state of the art these models are discussed in the subsequent three chapters.

To be able to compare the available models, the model confidence level (MCL) metric proposed by (Czupalla et al. 2009) will be used, which defines levels of model confidence from 1 to 9 based on a similar metric as the TRL. Notable distinctions in this metric are summarized below, a complete overview of the criteria is provided in Table 1 of (Czupalla et al. 2009).

- MCL 4: time dependent tabulated values from observations are used to model the system.
- MCL 5: governing equations are used to model the subsystem.
- MCL 6: all subsystem models share an environment, and influence and react to that environment.
- MCL 7: some of the subsystem models are correlated using test data.
- MCL 8: all subsystem models are correlated and able to model realistic interconnected system behavior.
- MCL 9: subsystem models are sophisticated enough to predict previously not reported system responses.

3.1 Life Support Simulation Tools

Table 3.1-1 provides an overview of the existing simulation tools for LSS. Detailed explanations for the assigned MCL are provided in the following subchapters covering the individual simulation tools in more detail.

Table 3.1-1: Available life support simulation tools.

Simulation Tool	MCL	Open Source	Source
BioSim	7	Yes	(Kortenkamp and Bell 2003)
HabNet	7	No	(Do et al. 2015)
RTM	4	No	(Chambliss et al. 2016)
SICLE	3	No	(Eshima et al. 2020)
ELISSA	3	No	(Detrell and Ewald 2019)
EcoSimPro	3	No	(EcoSimPro 2018)
V-HAB 1.0	6	No	(Czupalla 2011)

3.1.1 BioSim

A publicly available simulation tool for ECLSS is the BioSim tool from NASA (available at <https://github.com/scottbell/biosim/tree/master>). It can simulate the overall LSS and includes crop and human models. According to (Kortenkamp and Bell 2003) the human model of BioSim is based on (Goudarzi and Ting 1999) and includes dynamic calculations for the respiration and nutritional energy consumption of the crew but the waste production is based on averaged values, which are transformed into percentages. The crop model is based on an earlier version of the baseline values and assumptions document (BVAD), which is no longer available. In the current BVAD (Anderson et al. 2018) however crops are based on the modified energy cascade (MEC) model. This means the limitations discussed in chapter 3.3.1.1 for the MEC model apply to BioSim as well. The waste-water recovery model is based on simple percentages that assume a specific percentage of the waste-water to be recovered. Therefore, BioSim does provide a common environment for simulation and the used models can be assumed to be correlated to NASA data, although no specific source for this assumption was found. For this reason, BioSim is given a MCL of 7, as the condition for MCL 8, that all sub-models are adjusted to simulate the real combined system behavior, is not reached with the simplified waste-water recovery and human models.

3.1.2 HabNet

HabNet is a tool developed by the Massachusetts Institute of Technology to model manned spaceflight missions on a mission architecture level (Do et al. 2015). For habitation system simulations HabNet uses BioSim (Do et al. 2015) and the same limitations as for BioSim from the previous subchapter apply. Therefore, HabNet also receives an MCL of 7. It should be noted, that HabNet focuses on the overall space mission architecture and not the ECLSS. For this reason, it is not considered as a separate tool in this thesis, as it uses BioSim for the relevant calculations.

3.1.3 Resource Tracking Module

The resource tracking module is a LSS simulation tool from NASA that is focused on the water inside a LSS. It uses a high simulation level to enable fast simulations and easy integration into other simulation tools and therefore uses performance data for the modeled system instead of first principles. (Chambliss et al. 2015) It therefore reaches a MCL of 4, as it is based on performance data.

3.1.4 SICLE

The SIMulator for Closed Life and Ecology (SICLE) is a LSS simulation tool that is intended for future hardware in the loop simulations and therefore real time operations (Moriyama et al. 2015). The SICLE methodology described in (Eshima et al. 2020) uses performance values for the subsystems that can be adjusted between 0% and 100%. The MCL for SICLE is therefore also 3, as the dynamic subsystem responses are not considered.

3.1.5 ELISSA

ELISSA stands for Environment for Life-Support Systems Simulation and Analysis and is a simulation tool from the Institute of Space Systems of the University of Stuttgart. It can be combined with two other tools, one to include reliability and the other to perform trade-offs to ease the initial selection of technologies (Detrell and Belz 2017). Overall, the focus of ELISSA is on the conceptual design of manned space missions. Regarding the level of detail within ELISSA the components can use detailed physical models but also simpler models depending on the available information. The human model uses averaged values from the literature while the modelling of other subsystems depends on TRL and available data (Detrell and Belz 2017; Detrell and Ewald 2019). The provided description suggests performance data is used for most subsystems, but this is unclear from the available literature. Since the human model uses steady state values a MCL of 3 is assigned to ELISSA. To reach MCL 4 all sub-models, including the human model, must be dynamic.

3.1.6 EcoSimPro

EcoSim Pro is a commercially available adaptive simulation tool for LSS and includes a standard library that is intended to model air loops within LSS. However, the user can define and change library components to implement more detailed models or represent other cases in the simulation (Rodriguez et al. 2006). One such example is the adaption of EcoSimPro to model the MELiSSA experiment, which includes biological components (Ordonez et al. 2004). The model for higher plants from MELiSSA in EcoSimPro uses the modified energy cascade (MEC) model (see chapter 3.3.1.1) but also tested an empirical light response plant model. According to the EcoSimPro fact sheet (EcoSimPro 2018) it is capable of modelling systems dynamically. However, it is unclear how many technologies are available as dynamic models in EcoSimPro. Only heat exchangers, pumps and valves are mentioned as library components. Therefore, the user may have to define further components to model hybrid LSS. For this reason, EcoSimPro is given a MCL of 3, as it is unclear which sub-models exist dynamically. The condition for MCL 4 is that all subsystem models must be represented dynamically, which cannot be ensured if the subsystem models do not exist yet.

3.1.7 V-HAB 1.0

The initial implementation of Virtual Habitat or short V-HAB (here called V-HAB 1.0 to discern it from the newer object-oriented V-HAB 2.x versions) reached a MCL of 6. A higher MCL was not reached due to limited information available for the sensitivities of PC technologies to the environment. (Czupalla 2011: 287) The MCL of 6 is reached because all components share a common environment and generally governing equations are used to calculate them. However, the CCAA model used only tabulated data (Roth 2012), which corresponds to an MCL of 4.



3.2 Physical/Chemical Life Support Component Models

3.2.1 Water Processing Assembly

While no complete model for the WPA with a MCL above 4 could be identified, higher MCL models for the components of the WPA exist. For the multifiltration beds a detailed model of the ion exchange and other processes verified with test data could be identified (Hokanson 2004). The model for the multifiltration beds is implemented as a combination of Visual Basic and Fortran, which is therefore not directly compatible to any of the discussed system-level analysis tools from chapter 3.1. Another important component of the WPA is the Volatiles Reaction Assembly (VRA) for which a separate model exists (Guo et al. 2005). The VRA model is a purely mathematical model, for which no direct implementation in a simulation software is discussed by (Guo et al. 2005). With the identified subsystem models the current WPA models can be improved to reach MCL 8 or potentially MCL 9.

3.2.2 Carbon Dioxide Removal Assembly

For the Carbon Dioxide Removal Assembly (CDRA) an ongoing modelling effort at the Marshall Spaceflight Center developed a predictive model of the system (Coker and Knox 2016b; Coker et al. 2015). This model is based on first principles and can calculate CO₂ and water absorption based on the current conditions in the atmosphere. This is relevant for system-level models because biological systems have a strong influence on the humidity and CO₂ in the atmosphere and the impact of this on the PC system is relevant. The model is written in COMSOL and was verified with hardware tests to prove that it could predict previously not reported behavior. It is therefore the only subsystem model to reach MCL 9.

The direct implementation of this model into any of the existing system-level analysis tools discussed in chapter 3.1 is not feasible because none of these uses COMSOL. Therefore, either an interface between COMSOL and the system analysis tool is required or a derivate model based on the presented research from (Coker and Knox 2016b; Coker et al. 2015) must be created.

3.2.3 Sabatier Reactor

A detailed 3D dynamic model for a Sabatier reactor in ANSYS CFD was developed by (Hou et al. 2016) and verified with test data. Since it was not checked whether the model can also predict previously not reported values, it is considered to reach MCL 8 with the potential to reach MCL 9 after further verification. The model couples the fluid dynamics with heat transfer and chemical reaction calculations to achieve a holistic representation of the Sabatier reactor.

3.2.4 Condensing Heat Exchanger

For the CCAA a subsystem model using performance data was developed by (Roth 2012). As the model is based on tabulated values and not fundamentals, it reaches MCL 4. However, condensing heat exchangers (CHX) are not used solely in LSS but also frequently in terrestrial applications. For these, higher fidelity models exist with an MCL of 8 to 9 (Jeong et al. 2010). While the models for terrestrial applications cannot be used directly to model the CHX for spacefaring because they are often on a different scale e.g. MW in (Jeong et al. 2010) compared to kW in the CCAA (Wieland 1998). However, the fundamental equations used to calculate the CHX are reported in detail in (Gesellschaft Verfahrenstechnik und Chemieingenieurwesen 2013) and can be used to derive a new model capable of modelling the CHX used in space applications.

3.3 Biological Life Support Component Models

3.3.1 Models for Higher Plants

For biological LSS one of the central components are higher plants, as they are the only biological component that could provide a complete diet for the crew. Although a large quantity of agricultural plant models exists (see chapter 3.3.1.4), they usually neglect some of the relevant parameters for LSS plant models. Therefore, they are not considered in the overview of higher plant models provided in Table 3.3-1. More details on the models and the applied MCL are provided in the following subchapters.

Table 3.3-1: Higher plant modelling tools for LSS.

Simulation Tool	MCL	Open Source	Source
MEC	7	Yes	(Anderson et al. 2018; Boscheri et al. 2012)
MELiSSA Higher Plant Model	9	No	(Hezard 2012; Poulet 2018)
veCROP	8	No	(Stölzle 2013; Saad 2015)

3.3.1.1 Modified Energy Cascade

The Modified Energy Cascade (MEC) model is currently a widely used plant model in the space sector because it is included in the Baseline Values and Assumptions Document (BVAD) from NASA (Anderson et al. 2018). It is an explanatory model that uses multivariate equations fitted to experimental data (Boscheri et al. 2012: 942). The model has good results especially with respect to long term tests, but in short term dynamics deviation of 30 to 50% can occur (Boscheri et al. 2012: 941). The newest iteration of the MEC model from the University of Arizona (Boscheri et al. 2012) was derived from the Lunar Greenhouse prototype that has a significant leakage rate (4.4 times the volume in 24 hours (Boscheri et al. 2012: 947)). This was accounted for in the calculations but might still have an influence on the model results. A recent analysis with lettuce also described good fitting of plant growth data and transpiration in nominal conditions, but with larger difference for off-nominal cases (Amitrano et al. 2019). While the MEC model is fitted to experimental data, the basic equations do allow it to predict plant growth and the relevant interactions dynamically without requiring additional input parameters. But as the transpiration model within the MEC model is not accurate for all conditions, it reaches MCL 7.

3.3.1.2 MELiSSA Higher Plant Model

Within the MELiSSA project, two dissertations (Hezard 2012; Poulet 2018) developed a mechanistic model for higher plants within LSS that also covers different gravity conditions. The model is currently the plant model with the highest confidence level, as the mechanistic approach and verification using parabolic flight data (Poulet et al. 2020) suggest that the model reaches MCL 9.

3.3.1.3 veCROP

The MEC model is also used in the V-HAB plant model, which is called veCROP, but an adjusted transpiration model was implemented to improve the MEC model. The transpiration model was developed in a diploma thesis in cooperation with the Kennedy Space Center (Stölzle 2013) and is based on the Food and Agriculture Organization evapotranspiration model (Allen et al. 1998). The updated model showed better results than the preceding MEC model for potato, wheat and soybeans. It was implemented in the V-HAB plant model by (Saad 2015). Overall, the MCL of veCROP is higher than for MEC model, as the part which limited the MCL was improved. The MCL of veCROP is therefore 8.

3.3.1.4 Agricultural Plant Models

Most plant models that can be found are agricultural plant models intended for modelling crops on a field on Earth. In general, the difference between agricultural plant models and those developed for LSS simulations are different objectives, scales and inputs (Czupalla 2011: 85). For example, for LSS simulations all interactions (e.g. CO₂, O₂ and transpiration) are relevant while for agriculture the primary interest is the produced biomass and everything else is considered a boundary condition. There are three primary types of plant models used on Earth: process based models,



geometric models and functional structural models. The latter strive to combine process based and geometric models (Kang et al. 2008). Examples for process based models are STICS (Constantin et al. 2015) or the FAO evapotranspiration model (Allen et al. 2015) but there are also many other examples, which are often coupled with other processes in the environment as is done for the HERMES model (Malone et al. 2017). An example for purely geometric models is PlantGL, which is an open source tool that can be used to model graphical 3D representations of different plants, from the root area to the leaf canopy (Pradal et al. 2009). Examples for functional structural plant models are the MELiSSA plant growth model (Poulet et al. 2020) or the GrapevineXL model (Zhu et al. 2018) but there are also many other models for this category (Godin and Sinoquet 2005; Kniermeyer 2008; Vos et al. 2010; Vos et al., eds. 2007). While functional structural plant models are the most sophisticated models, they are also the computationally most expensive models. Therefore, it is often challenging to scale up these models while incorporating all mechanisms:

“Despite these advances in modelling stomatal conductance, it remains challenging to simultaneously integrate detail gas exchange and water status at the leaf level while scaling to the whole plant, and even field, level.” (Zhu et al. 2018)

3.3.2 Biological Waste Processor Models

For terrestrial membrane aerated biofilm reactors, a model was identified that covers many parameters of the system (Martin et al. 2017) but the paper also states that “Biofilm models, in general, involve parameters that have high uncertainty or are system dependent.” (Martin et al. 2017: 258). And since the scale for the system considered in that research is fundamentally different than for the systems considered for LSS the model is not further studied. For the CROP system an enzyme kinetics model was developed by (Tertilt 2013) in collaboration with the DLR. The model is capable of modelling the system behavior at lower urine concentrations, but the current intended use case for CROP is to operate with pure urine. In addition, the model encountered problems when fitted to data series with different urine concentrations, as the sample size was low and is currently lacking a pH model. Therefore, the model can only be considered MCL 5.

3.3.3 Algae Reactor Models

Multiple review papers and book chapters exist that discuss the state of the art for modelling algae reactors (Bitog et al. 2011; Béchet et al. 2013; Pires et al. 2017; Losa et al. 2020). Most of these models use computational fluid dynamics (CFD) to model the multiphase flow in terrestrial reactors, where air is supplied directly into the reactor and moves up through the fluid due to gravity. For μg the gas exchange usually occurs via a membrane and this membrane currently limits the growth rates for algae reactors (Helisch et al. 2020: 103). Therefore, algae reactor models that do not include such a membrane cannot be considered applicable to μg conditions. A μg model was also validated by (Poughon et al. 2020) and can be considered the current most sophisticated model for space algae reactors. In this research a model for algae growth in membrane reactors was compared to μg and 1 g experiments and the conclusion was that models created with 1 g data were also applicable to μg conditions (Poughon et al. 2020: 64). Overall, the model uses a mechanistic approach and is validated against μg data, which allows it to reach a MCL of 8 to 9.

3.4 Human Models

One of the central elements for any life support simulation is the human model. The overarching goal of LSS is to keep the crew alive by handling the metabolic interfaces of humans and maintaining a habitable environment. Table 3.4-1 provides an overview of human models that are applicable for this purpose and are discussed in the following subchapters. Note that only human models which include detailed metabolic modelling are discussed here. Other models which focus on the thermal aspects but do not include an actual metabolic model capable of modelling the conversion of food into waste substances are not discussed here. These thermal human models include the Wissler model (WISSLER 1964) and the MetMan model (Stolwijk 1971).

Table 3.4-1: Overview of available human models.

Simulation Tool	MCL	Open Source	Source
HumMod	9	Yes	(HC Simulation 2020; Hester et al. 2011)
V-HAB	7	No	(Czupalla 2011)

3.4.1 HumMod

HumMod evolved from the quantitative circulatory physiology model of the University of Mississippi and is currently used in medical education (Hester et al. 2019). In addition HumMod is also the fundamental for the digital astronaut project of NASA (Keith Sharp et al. 2013; Summers et al. 2008) and therefore also includes gravity conditions as parameter. The model itself is based on a 160 lb male human (Hester et al. 2011). Scaling HumMod to different genders and body sizes is mentioned to be future work with a limited implementation of female physiology currently available. However, no publication with a more recent status for HumMod itself could be found. Therefore, it is assumed that this is still the current state of the model. HumMod overall is a complex validated model for physiology, which is also intended to be used for astronauts. Therefore, it reaches a MCL of 9 but the applicability to LSS analyses must be checked.

3.4.2 V-HAB Human model

A detailed full body human model was developed for V-HAB in previous research (Czupalla 2011). Most other LSS simulations rely on steady state static human models (Czupalla 2011: 79) and are therefore not applicable for detailed loop closure analysis as effects like the impact of the diet on the respiratory coefficient are not modeled. However, the V-HAB human model also has some areas that can be improved. For example, the protein metabolism and therefore also urea production (Czupalla 2011: 334) are currently not implemented. These would be required as inputs for biological waste recycling models of systems like CROP. Additionally, the system-level verification (Czupalla 2011: 333) of the human model is not finished yet. The MCL of the V-HAB human model is mentioned to be 7 (Czupalla 2011: 287).

4 Gap Analysis

Chapter 2 discussed the current state of LSS generally and shows that currently no full-scale hybrid LSS that produces the full diet for the crew exists. This can also be attributed to a lack of system analysis tools to facilitate the necessary understanding for the integration of biological components (Anderson et al. 2017a). In chapter 3 the state of the art for LSS analysis tools was discussed and no suitable tool for such a system analysis was identified. The existing tools neglect some of the relevant aspects for the analysis or are individual models of a part of the hybrid LSS like e.g. a plant model without connection to the LSS. Therefore, currently no tool exists that is capable of a holistic analysis for hybrid LSS. Chapter 4.1 discusses this gap and the necessity to close it, while chapter 4.2 discusses the tool that was selected for further study. Chapter 4.3 derives the objectives of this thesis from the defined capability gaps. The required improvements for the selected analysis tool are discussed in methodology presented in chapter 5.

4.1 Gap Identification

As discussed by (Czupalla et al. 2009) it is necessary for all sub-models to be capable of simulating the real combined system behavior. The goal for hybrid LSS and CELSS specifically is to achieve higher loop closure and to better understand the involved processes of biospherics (Salisbury et al. 1997). Improving the available models can be considered a form of learning and increasing the understanding (Jones 2009: 2). Additionally the analysis of system-level behavior for hybrid LSS can support the development of such system as both NASA experts (Anderson et al. 2017a) and European experts (Alemany et al. 2019: 10) agree. In addition, improving the cycling of e.g. nitrogen is considered a crucial future challenge (Dong et al. 2017: 86). However, current system-level models focus only on the primary substances of oxygen, carbon dioxide and water and neglect other elements like nitrogen in their analysis, as discussed in chapter 3. Therefore, a research gap is seen in the area of system-level analysis for hybrid LSS. The current limitations of hybrid LSS models are further studied in the following chapter. To identify research gaps in this area, it is necessary to have a basic understanding of the subsystems and the dependencies within hybrid LSS. For this purpose, Figure 4.1-1 provides a simplified overview of a hybrid LSS and the different dependencies and impacts.

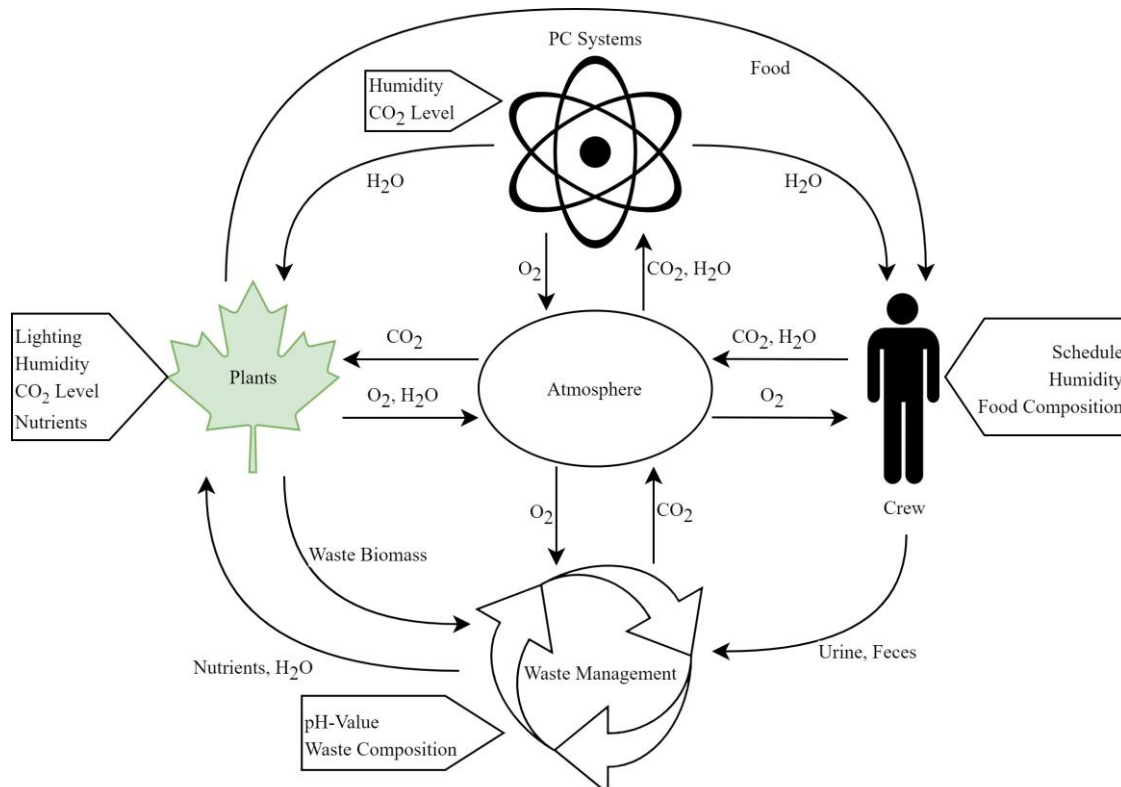


Figure 4.1-1 Simplified representation of a hybrid LSS with additional influences on the components.



In the following chapters, the research gaps are separated into system-level gaps and subsystem-level gaps. System-level gaps describe limitations in simulation tools capable of modelling a whole hybrid LSS as depicted in Figure 4.1-1 while subsystem-level gaps describe gaps in currently available, detailed subsystem models.

4.1.1 System-Level Gaps

Based on the state of the art discussed in chapter 3.1 the currently available tools that are best suited to model LSS are BioSim or V-HAB and potentially EcoSimPro depending on the availability of subsystem models. In addition, Table C-1 provides a summarized overview of the system level tools and their corresponding subsystem models. Since EcoSimPro, in principle, fulfills the required conditions for a higher MCL it will be included in this discussion. To model plant growth all three of these models use the Modified Energy Cascade (MEC) model (Kortenkamp and Bell 2003: 3; Ordonez et al. 2004; Czupalla 2011: 336). In the MEC model nutrients are currently only modelled generally as overall nutrients and it is assumed that the required composition of individual nutrients is present (Czupalla 2011: 336). To model hybrid LSS the element cycling of nutrients and potential failure cases for plants from this effect are important as it can lead to plant necrosis (Burgner et al. 2019) and a complete loss of a plant culture, which would affect the ECLSS. In addition, one fundamental aspect of dynamic system analysis is the sizing of buffers, which is not feasible without the correct nutrient dynamics. Additionally, the nutrient production of plants is of interest because one advantage of hybrid LSS is the supply of nutrients that would degrade in stored food for long duration missions (Anderson et al. 2017a). Therefore, the first identified gap is the modelling of nutrients in all currently available simulation tools.

System-Level Gap 1: Plant nutrient uptake dynamics.

Another important aspect is the simulation of the crew. In this aspect the three tools vary as they each use different human models. EcoSimPro does include a crew model, but no detailed information on it is published (Rodríguez et al. 2005). In addition, the papers that use EcoSimPro for LSS modelling do not represent the state of the art in this area as they are older than ten years. As no transient crew model is reported to exist for EcoSimPro, it must be assumed that the current crew model of EcoSimPro is still an averaged steady state model. BioSim uses a dynamic human model but the waste production does not model the waste composition in more detail as it only differentiates between water and solids (Goudarzi and Ting 1999). In addition, this part is also based on averaged steady state values. The most sophisticated human model of these three tools is available in V-HAB 1.0 as it also includes dynamic waste production and differentiates at least the larger components in the human waste streams. However, it is lacking a protein metabolism and can therefore not model the urea production for urine (Czupalla 2011: 334). Since this is part of the overall nutrient cycle, these dynamics also impact the required sizing for nutrient buffers. Therefore, the second identified gap is a human model that is able to dynamically depict waste flows and their composition.

System-Level Gap 2: Human waste production dynamics and composition.

The third part of the system is the waste management system. In BioSim solid waste is currently not handled except for incineration and waste water handling is based on percentages without dynamic effects (Kortenkamp and Bell 2003; Rodríguez et al. 2007). For EcoSimPro, no model for waste management was reported in the literature. In V-HAB 1.0 models for the UPA, WPA and other waste processing subsystems were developed, but are also based on percentage as modelling of e.g. ion exchange beds was not performed. Also the composition of urine is simplified to water, waste and contaminants as the protein metabolism was not implemented (Czupalla 2011). Overall, the waste management part of LSS simulations currently uses the least detailed models. Most models do not depict transient behavior and oversimplify the composition of the waste streams. However, especially the ion filtration used to produce potable water is ultimately a sink for elements as ions are replaced with either H^+ or OH^- ions, which then recombine to H_2O . All elements adsorbed by the multifiltration beds, for example Na^+ , are lost to the system.

System-Level Gap 3: Waste and water management system dynamics and composition of waste streams.



The fourth part of a hybrid LSS are the PC subsystems. While the most sophisticated models are available in this area, room for improvement still exists. The system-level tools discussed in chapter 3.1 often use simplified models. High-fidelity models like the one for CDRA discussed in chapter 3.2.2 are only used on subsystem-level. For example, the model for the CCAA used in V-HAB can only be considered MCL 4 due to the reliance on tabulated values (Roth 2012). However, a direct interaction between the PC subsystems and the other areas of the hybrid LSS does exist, for example the loads of the temperature and humidity control system are completely different if plants are used. Therefore, the system-level behavior can only be considered well represents if these subsystems are also able to show the relevant responses. For this reason, the fourth system-level gap is defined as the current lack in detailed PC subsystem models in system-level analysis that can be adjusted to the new requirements of hybrid LSS and are capable to predict the relevant responses.

System-Level Gap 4: PC models that are adjustable to hybrid LSS and predict the relevant responses.

4.1.2 Subsystem-Level Gaps

As discussed in chapter 3, subsystem models of high fidelity exist for many of the required subsystems. However, some aspects of hybrid LSS are currently neglected as analyzed in chapter 4.1.1. This chapter translates the system-level gaps into more specific gaps for the individual subsystem models regarding the four aspects of hybrid LSS shown in Figure 4.1-1: the human, plants, waste management and physical/chemical subsystems. Table 4.1-1 summarizes the final identified research gaps.

A frequently made wrong assumption is that a system-level model can simply be achieved by combining existing subsystem models. However, reality is not as simple as this. As (Jones 2009) discusses, subsystem models often focus on internal effects of the subsystems, but do not accurately reproduce relevant external interfaces. Therefore, either the subsystem models must be adapted to reproduce the external interfaces, or the system-level behavior must be modelled directly (Jones 2009). The advantage of the first approach is that various system-level analyses can be performed, while the second approach is specific for one ECLSS and a different ECLSS requires a completely new model. Since the objective of this thesis is to develop a tool that can support the development of various ECLSS and to analyze three different mission scenarios with different ECLSS, the first approach is chosen.

4.1.2.1 Plant Model Gaps

In this chapter only the gap with regard to the existing MEC models are discussed. The more mechanistic plant model from (Hezard 2012; Poulet 2018) discussed in chapter 3.3.1 has not been used for integrated hybrid LSS modelling and models the plants down to the gas exchange of individual leaves. As stated by (Zhu et al. 2018) this likely makes the model unsuitable for analysis of multiple plants on the relevant scale of footprints having multiple m^2 :

“Despite these advances in modelling stomatal conductance, it remains challenging to simultaneously integrate detail gas exchange and water status at the leaf level while scaling to the whole plant, and even field, level.” (Zhu et al. 2018)

The plant model from (Hezard 2012; Poulet 2018) is therefore considered too detailed for the desired system-level analysis. However, in future work the integration of this plant model into a holistic analysis shall be analyzed.

Regarding the general gap of neglecting nutrient impacts on plant growth in the currently used MEC models, the first obvious subsystem gap is a corresponding uptake mechanism model, which can describe the relation between plant nutrient content and supply solution nutrient content. In addition, plants can store nutrients (Tischner 2000: 1005) which must be included in the plant model to predict how long plants could survive nutrient deficiencies in the supply solution. The MEC model only covers edible and inedible biomass, but does not differentiate between root, shoot and leaf masses. But plants change their root to shoot ratios if nutrient deficiencies are encountered (Agren and Franklin 2003) thus it may be necessary to include this differentiation in a nutrient dependent plant model. Overall, it is necessary to derive an adjustment for the MEC model that allows the depiction of nutrient uptake, storage and allocation within the plant without making the model too complex for system-level analysis.



4.1.2.2 Human Model Gaps

In the human models the production of human waste is currently oversimplified. For example, the production of urea is part of the nitrogen cycle as it would be reprocessed into nitrate for the plants. If that is not modelled it is also not possible for the overall system-level model to depict this fundamental nutrient cycle. The simplification of the human waste output also shows an oversimplification of the metabolism model, as the protein metabolism must result in urea production if the stoichiometry of the reaction is observed (Berg et al. 2013: 695). However, if the metabolism model is adjusted to include protein metabolism, the impact of these changes on the other parts of the human model must also be included. For example, the respiratory coefficient depends on the metabolism model, and therefore the oxygen and CO₂ uptake and release mechanics are influenced by the metabolism model and must be adjusted. The separate human model HumMod identified in chapter 3.4.1 could be used to close these gaps, as it models the human in more detail than the current LSS simulation tools. However, the model was developed for a different purpose and therefore an analysis whether HumMod is applicable to a hybrid LSS analysis is required. This is discussed in detail in chapter 5.5.7.

4.1.2.3 Waste Management Gaps

The current state of PC waste management is at a TRL below 4, as discussed in chapter 2.1.3. The existing systems are on a lab scale and not sized to handle the loads associated with a large production of inedible biomass, as the assumed waste stream from (Ewert and Broyan 2013) shows. In addition, they are not well suited to recover all relevant elements for biological systems and generally have a high consumable consumption and high remaining waste production compared to biological systems as discussed by (Pickett et al. 2020). For this reason, PC waste processing technologies are not further considered in this thesis.

For biological waste treatment, multiple different options are available. However, a detailed subsystem model that is suitable as base for further studies was identified only for CROP in chapter 3.3.2. Other models are for terrestrial application and cannot be scaled directly to the different sizes required for ECLSS: “Biofilm models, in general, involve parameters that have high uncertainty or are system dependent.” (Martin et al. 2017: 258)

This also suggests that a relevant subsystem model must either be reported or access to test data must be available to develop a well fitted subsystem model. For this thesis, this is only feasible for the CROP system due to a cooperation with DLR to share test data. However, this model also has room for improvement as it is currently not possible to model the intended use case of 100% urine concentration with the existing model. (Tertilt 2013) states required improvements directly as the addition of a pH model that impacts the enzyme kinetics and the fitting of the enzyme kinetics parameters to more data sets to better depict different conditions such as high urine concentrations.

4.1.2.4 Physical/Chemical Subsystem Gaps

While detailed dynamic models of individual components for the WPA were identified in chapter 3.2.1 no complete model of the subsystem suitable for system-level analysis was identified. Since transpired water from plants would have to pass through a WPA to be considered at potable quality this is a necessary PC subsystem for hybrid LSS. In current system-level models, the waste management including waste water reprocessing is based on percentages (Kortenkamp and Bell 2003; Rodriguez et al. 2007; Czupalla 2011).

Another important aspect for hybrid LSS is the water cycling, as water is one of the most important resources within a LSS. In LSS the humidity is recovered by condensing heat exchangers (CHX) like the common cabin air assembly (CCAA) (Wieland 1998). The current implementation of a dynamic model relies on performance data (Roth 2012) and is therefore only at MCL 4. The transpiration from plants is one of the primary impacts that plants have on the habitat atmosphere. Therefore, this is a necessary system to correctly depict the system-level dynamic behavior and analyze the control logics of this system. In addition, the current systems are not sized to handle the high water load that a large plant growth chamber would produce. A model based on performance data cannot be scaled up to handle these and is therefore only of limited use in the analysis of hybrid LSS. Therefore, the calculations derived for terrestrial CHX applications (Gesellschaft Verfahrenstechnik und Chemieingenieurwesen 2013) must be adapted to model a μ -gravity cross-counter flow plate and fin CHX as it is usually used in spacecraft (Wieland 1998).

If algae instead of plants are considered for a hybrid LSS a system that can concentrate the CO₂ from the cabin air is required to supply algae with CO₂ (Detrell et al. 2020). Such a PC subsystem can also be considered an important



backup system for hybrid LSS. In addition, for hybrid LSS, where biological components do not cover the complete air revitalization, it is also a necessary PC subsystem. Therefore, a dynamic model of such a system is required for the analysis. A detailed dynamic model of the Carbon Dioxide Removal Assembly (CDRA) was identified (Coker and Knox 2016b), which is written in COMSOL. Since no available system-level ECLSS analysis tool uses COMSOL, the model must be adapted to be usable in a system-level analysis. Therefore, either a derived subsystem model should be developed that builds upon the detailed model from (Coker and Knox 2016b) or a suitable interface between COMOSL and the selected ECLSS modelling tool must be provided. As previously discussed, directly combining subsystem models into a system-level analysis usually does not work (Jones 2009) and the objective of this thesis is to derive a more general tool. Therefore, the chosen approach for CO₂ removal is to derive a simplified subsystem model based on the approach published by (Coker and Knox 2016a).

4.1.3 Summary of Research Gaps

In this chapter the identified research gaps of the previous chapters are summarized in Table 4.1-1.

Table 4.1-1: Identified research gaps.

Gap Area	Subsystem Research Gaps	Description
Plant Model	Nutrient Uptake	Current MEC model neglects the uptake rate of relevant nutrients (Anderson et al. 2018: 185)
	Nutrient Storage	Current MEC model neglects nutrient storage mechanism in the plant model (Anderson et al. 2018: 185)
	Plant Discretization	Current MEC model discretizes only edible and inedible plant biomass (Anderson et al. 2018: 186)
Human Model	Metabolism Model	Current metabolism model lacks protein metabolism and simplifies waste production (Czupalla 2011: 334)
	Urea Production	Current models do not ensure a closed nitrogen balance and neglect urea production (Czupalla 2011: 334)
	Respiratory Coefficient	Impact of nutrient uptake on respiration is only depicted partially in current models (Czupalla 2011: 334)
Waste Management Model	pH Model	Current model lacks a pH representation which impacts the enzyme kinetics (Tertilt 2013)
	different urine concentrations	The current model is not well fitted to different urine concentrations (Tertilt 2013)
Physical/Chemical Models	Water Reprocessing	Current subsystem models for system-level analysis use steady state efficiency percentages (Kortenkamp and Bell 2003: 4). Detailed models exist only on component level.
	Condensing Heat Exchanger	Only a MCL 4 model for this subsystem exists but terrestrial approaches can be used to derive a better model (Roth 2012).
	CO ₂ removal	Current subsystem is implemented in COMSOL (Coker and Knox 2016b), which requires either an interface or a derivate model to be compatible with system-level ECLSS analysis tools.

4.2 Tool Selection

This chapter discusses the general research approach of the dissertation and the selection of a suitable tool for this approach. Dynamic simulations as a tool to design ECLSS have a long standing history (Babcock et al. 1984: 263; Jones 2003: 1; Alemany et al. 2019: 10) and are also used in this dissertation. The alternative would be a hardware-based approach to gather test data from actual system tests. While this is favorable with regard to the reliability of the data, this approach is unsuitable for case and sensitivity studies and results of such tests would come too late to impact subsystem design decisions, as argued by (Czupalla 2011: 1). Simplified analyses, as they are used e.g. in equivalent system mass (ESM) or multi criteria analysis, with models based on steady state values are also not applicable to the defined research objectives. They would only provide insight into already known system behavior without being able to predict the behavior of future systems. In addition, since hybrid LSS are still in development, and not all interactions are well understood, it is not feasible to develop a system-level model using a top down approach as suggested by (Jones 2009) for ECLSS modelling. Therefore, the selected approach for this research is a bottom-up modelling approach where the selected subsystems are modelled sufficiently to represent the dynamic system-level behavior.

Chapter 3.1 introduced the existing tools capable of the intended analysis. Based on the available information chapter 4.1 identified the best suited tools for the task: BioSim, V-HAB and EcoSimPro. EcoSimPro requires licensing, for which no funding is available, so it will not be considered further. This leaves V-HAB and BioSim as potential tools for this dissertation. Of these two V-HAB was selected as tool for this thesis because it provides a broader base of subsystem models that can be adapted (e.g. better dynamic human model) and the work on V-HAB has continued at the Institute of Astronautics at the Technical University of Munich (Olthoff 2017).

4.3 Objectives

While chapter 4.1 described existing gaps in currently available research, this chapter specifies the objective of this thesis based on the identified research gaps. The primary objective of this thesis was stated in chapter 1.2:

To develop a simulation tool for hybrid life support systems that can perform dynamic, holistic, system-level simulations and predict the dynamic exchange rates of mass and energy between the subsystems.

In terms of the MCL metric, the objective is to derive a simulation tool for hybrid LSS which reaches MCL 8. Although, the definition of the term “correlated” is not defined well enough to decide when a model reaches MCL 8. This was identified as a potential area for improvement to the MCL metric by (Olthoff 2017: 250). Therefore, MCL 8 in the context of this objective shall mean: All subsystem models are validated, or in case of insufficient data verified, to the extent feasible with available data and able to model realistic interconnected system behavior.

Another aspect not well defined in the MCL metric is the degree to which a model must reproduce the real system behavior to reach MCL 8. Every model is a simplified representation of reality and will therefore only capture some aspects of the real system behavior. Developing an all-encompassing model capable of answering all possible questions is not practical because the effort is better spent on developing models that answer specific questions (Jones 2009). Therefore, the aspects which shall or shall not be included in the system representation must be defined. If the derived simulation is capable of predicting system performance with respect to these aspects, it will be considered MCL 8. For this purpose, the following limitations are placed on the simulation tool that shall be developed:

First the mass exchange between the subsystems will be limited to the most influential substances. Therefore, the focus of this thesis will be on the cycling of the elements C, H, O and N. It would be desirable to also include less impactful substances, such as iron ions which impact plant and algae growth, or the phosphorus and potassium cycles for plant nutrient, but that would exceed the scope of this research. While other substances may be considered for some aspects of the simulation, no full element cycle will be analyzed for those. With regard to energy, the dynamic exchange rates for electricity and heat are to be considered. Other energy transfers are not considered in the analysis. Also, the complete energy system is only covered for the mission scenarios two (Moon base) and three (Mars base) where it impacts the hybrid LSS. For mission scenario one (ISS) no mass exchange between the utilized battery system and ECLSS occurs. Therefore, the energy system is not modelled for this scenario.



4.3.1 Research Questions

Table 4.3-2 defines mission scenario specific research questions that are intended to highlight the desired capabilities of the tool and provide examples of design questions that can arise for the mission scenarios. If the tool is capable of answering these questions, the primary objective of the thesis is considered fulfilled.

Table 4.3-1 Research questions for the defined mission scenarios.

Scenario	ID	Research Question
One (ISS)	Q-1.1	Where is water from a plant system recovered and does this have an impact on required crew time? (Currently the ISS has a water imbalance between the Russian and the US segment. Therefore, the location where the water recovered is of interest)
	Q-1.2	Is a plant system which is open to the cabin atmosphere feasible or is a dedicated humidity control required?
	Q-1.3	What impact does a plant system have on the Sabatier reactor?
Two (Moon Base)	Q-2.1	What are the required sizes for energy and consumable storage during shadow phases?
	Q-2.2	Is the production of methane as fuel from crew CO ₂ feasible for the system?
	Q-2.3	What are the necessary conditions to integrate biological components into the system?
	Q-2.4	How does the addition of biological components affect the loop closure of the physical/chemical ECLSS with ISRU?
Three (Mars Base)	Q-3.1	Where are the break-even points based on equivalent system mass between all viable life support technologies?
	Q-3.2	Can the developed tool be used to identify previously not considered stability conditions for the ECLSS?
	Q-3.3	Can the model detect failure cases and adjust control logics of the LSS to improve fail-safe capabilities of the LSS?
	Q-3.4	What are the required buffer sizes for nutrients, water and energy to ensure that the ECLSS does not run out of consumables during nominal operation?

4.3.2 Model Requirements

In addition to the research questions, additional requirements for the tool are defined. Table 4.3-2 presents these requirements and their justification.

Table 4.3-2 Additional requirements for the tool.

ID	Requirement	Rationale
R-1	A single analysis shall require a maximum of 2-4 weeks of computation time on a personal computer	The desired analyses often require multiple different cases to be analyzed. This must be possible within a meaningful timeframe.
R-2	Dynamic models shall be used for all subsystems	To depict system-level dynamic behavior all subsystem models must be dynamic as well.
R-3	Validated models shall be used for all subsystems	Only validated models can be considered to correctly represent subsystem behavior.
R-4	A Graphical User Interface (GUI) shall be developed	Without a user interface, the application of the tool by other users is less intuitive, which would contradict the planned release of the tool as open source.
R-5	Maintain a closed mass balance and check the impact of the remaining error on the simulation	Mass balance is one of the physical principles that every system must adhere to.

5 Methodology

The methodology section is divided into five chapters. The first chapter covers the Life Support Trade Off Tool (LiSTOT), which is used for preliminary analysis of ECLSS systems. The second chapter covers the basics of Virtual Habitat (V-HAB), the simulation tool used for detailed dynamic analysis, and its improvements compared to predecessor theses. The next three chapters cover subsystem models separated into the primary categories of PC ECLSS, biological ECLSS and human modelling.

To prove the viability of the models they must be a sufficiently accurate representation of reality. Therefore it is necessary to use the methods verification and validation, as defined and described by (Olthoff 2017: 72–6). The difference between the two terms is that verification cover transformational accuracy while validation covers representational accuracy. Transformational accuracy applies to the process of transforming a conceptual model into code while representational accuracy describes how well a model represents reality. Therefore, a verification checks whether the developed code correctly represents the derived conceptual model, while validation checks whether the developed model correctly represents reality. An objective for this thesis is therefore to validate all subsystem models. However, this is not feasible for all aspects of all models. Where it is not feasible verification is therefore used instead.

5.1 Life Support Trade Off Tool

The Life Support Trade Off Tool or short LiSTOT is an Excel based analysis tool, which was initially developed in two master theses (Schreck 2017; Feigel 2019) for the analysis of a Mars transit ECLSS and a cis-lunar space station ECLSS. The tool is intended to be a preliminary analysis tool that enables the quick and easy comparison of different ECLSS architectures. The final selected ECLSS can then be analyzed in more depth within V-HAB. The tool combines a multi criteria analysis (MCA) approach with user defined weights and an equivalent system mass (ESM) analysis to compare subsystems. In a next step, the tool allows the user to combine different candidate subsystems into a complete ECLSS. Chapter 5.1.1 focuses on the changes made to LiSTOT for this thesis. The basic calculations from (Schreck 2017; Feigel 2019) are therefore not discussed again.

Chapter 5.1.2 covers the ECLSS trade-off for mission scenario three the permanent Mars base (see chapter 1.2.2.3). The ECLSS of the ISS (scenario one) is fix and the ECLSS for the Moon base (scenario two) is planned to be ISS-based with potential later biological additions (Zuniga et al. 2019). Therefore, the ECLSS composition for the first two scenarios is considered fixed and there is no need to analyze their ECLSS compositions with LiSTOT.

5.1.1 Adjustments to Previous Versions

It should be noted that the code base for LiSTOT was completely reworked for this thesis into a modular code, which is easier to maintain and adapt. Hard coded cell references were replaced with dynamic references by using the table headings to derive the position of values. This makes it easier to add values or adjust the tables and makes the code more readable as it states the column name for values and not just a single letter. Previously, a change like adding a new column to a table made all calculations invalid as the cell references in the Visual Basic for Applications (VBA) code were no longer correct. In this chapter the changes compared to previous versions are discussed.

5.1.1.1 Technology Database

The technology database of LiSTOT contains all required information about the different ECLSS technologies for the trade-off calculations. (Feigel 2019) adjusted LiSTOT to a VBA based calculation to make the calculations easier to follow and maintain. However, in this change the technology data was also moved into the VBA code, which made it difficult for the user to view and adjust it in case values had changed. To improve this, the technology database is now provided in an Excel sheet where the data for each technology is provided for the metabolic inputs and outputs of a human according to (Anderson et al. 2018: 50). These metabolic values are henceforth also referred to as a standard human. This allows the user easy access to the data to check and adjust if necessary. The convention to store the data of the subsystem per one standard human is also the basis of the new scaling approach discussed in chapter 5.1.1.3. To



more easily identify specific subsystems in the database sheet, a reference to their abbreviations was also included in the technology database.

The technology database is based on an extensive literature review performed by (Schreck 2017) and additions from (Feigel 2019). The current state was also updated for this thesis to add new technologies like the Brine Processing Assembly (BPA) (Kelsey et al. 2018) and include plant growth chambers (PGC) of different sizes based on (Anderson et al. 2018). New technologies can now simply be added in a new row of the technology datasheet, and they are automatically included in the further analysis. The only exception for this are CO₂ reprocessing technologies, which all have different chemical processes and therefore cannot be handled directly by the ECLSS composition calculation. Here it is necessary that new additions also be included in the VBA calculations and therefore newly added CO₂ reprocessing technologies are not automatically shown as valid options in the ECLSS composition GUI.

5.1.1.2 Crew and Schedule Model

The crew model in LiSTOT is also based on the nominal human metabolic values from (Anderson et al. 2018: 50). The previous implementation from (Feigel 2019) however did not check the water mass balance of the selected crew schedule and used the base values provided by (Anderson et al. 2018), which are only valid for the schedule used there. Especially exercise must be handled separately, because the water consumption of a human depends on the water output, which is heavily reliant on the amount of exercise. In (Anderson et al. 2018) only 30 minutes of exercise are assumed resulting in a potable water consumption of 2.5 kg/d (Anderson et al. 2018: 50). But because sweat and water vapor release of a human is higher during exercise (Anderson et al. 2018: 45) the daily water consumption must increase with additional exercise to ensure a closed water mass balance. This was neglected in previous versions of LiSTOT leading to a potential water deficit in the analyzed ECLSS. In the new version the additional water demand from exercise is considered by comparing the total water mass out flow of a human during exercise $\dot{m}_{H_2O,exercise} = 128.42 \cdot 10^{-4} \frac{kg}{min}$ to the nominal water out flow $\dot{m}_{H_2O,nominal} = 11.77 \cdot 10^{-4} \frac{kg}{min}$ (see (Anderson et al. 2018: 45) for the values). The difference between the water output multiplied with the duration of the exercise exceeding 30 minutes per day $t_{exercise >30}$ must then be added as water demand:

$$m_{additional\ H_2O\ demand} = (\dot{m}_{H_2O,exercise} - \dot{m}_{H_2O,nominal}) \cdot t_{exercise >30} \quad (5.1-1)$$

The first 30 minutes are not included, as they are part of the nominal schedule and therefore covered by the nominal water consumption of 2.5 kg/d.

In addition, the schedule of LiSTOT was previously limited to all crew members sleeping at the same time and only some tasks being variable. This is not flexible enough for a general trade-off tool, which should allow various combinations of subsystems and crew schedules. In addition, the previous implementation had a difficult to use drop down interface where each 30-minute slot had to be set individually. The updated schedule has no more limitations for the time at which each activity should occur, but it still enforces certain events to occur like e.g. the three meals per day. In order to ensure that the subsequent calculations are performed with the correct metabolic values, a check of the schedule and the recalculation of metabolic values must be performed before the user can continue. The schedule composition user form is shown in Figure 5.1-1. In order to achieve a simpler definition, it is possible to define time frames for the specific events and a definition order is used to override events. The events are added in the following order:

1. Sleep
2. Work
3. Exercise
4. Recreation
5. Breakfast
6. Lunch
7. Dinner
8. Hygiene

This means sleep is overwritten by all other tasks defined in the schedule. Basically, an event with a larger number from the list above takes precedence over events with lower numbers. For example, the user can define work to start at 07:30 and go to 17:00 but still add an exercise from 13:00 to 14:00 which simply overrides the work set for this time slot. Before and after sleep some fixed events are added to the schedule which also contain specific metabolic effects, e.g. urine production is placed in pre and post sleep as well as hygiene water consumption. After the schedule is defined, the user can also use copy and paste and other normal Excel editing to adjust the schedule. The metabolic flowrates for each 30-minute time step are then calculated based on the defined schedule and used to scale the systems according to the crew needs. More information on this scaling is provided in chapter 5.1.1.3.

An example of a schedule defined by the user is provided in Figure 5.1-3

Compose User Schedule Form

Enter the times for the events in the provided fields in the format 00:00

You can set multiple events by seperating the times with ; (e.g. 08:00; 11:00)

The events are added in the order they are shown here (first sleep, then work, then exercise and so on) which means you can set a work period from 08:00 to 17:00 and an exercise from 13:00 to 14:00 and the exercise will simply override the work for that time frame. Note that you can also manually adjust the schedules after you create them, you can also manually change the number of crew members for each schedule (as long as the total number of humans from the schedules match the number of humans you defined in the user interface)

Do not clear previous schedule entries

Number of crew members Defines how many humans are modelled with this schedule

Schedule Number Defines the position in the Excel Sheet for this schedule starting with schedule 1 located in column B and so on

	Start (00:00)	End (00:00)	
Sleep Time	<input type="text"/>	<input type="text"/>	Before sleep start time 1 h Pre-Sleep and after sleep end time 0.5 h Post Sleep is added to the schedule
Work	<input type="text"/>	<input type="text"/>	
Exercise	<input type="text"/>	<input type="text"/>	After exercise end time 1 h of Post Exercise is added to the schedule
Recreation	<input type="text"/>	<input type="text"/>	
	Time (00:00)		
Breakfast	<input type="text"/>	0.5 h duration	
Lunch	<input type="text"/>	1.0 h duration	
Dinner	<input type="text"/>	1.0 h duration	
Hygiene	<input type="text"/>	0.5 h duration	

Figure 5.1-1 User form to define schedules in LiSTOT.



5.1.1.3 Subsystem Scaling

The scaling of technologies to the specific crew size and schedule was previously performed individually for each technology, which made the addition of new technologies difficult as the VBA code had to be adapted in all cases. Therefore, the scaling approach was reworked to become more generalized and applicable to any new technology added to the technology database as long the following conditions are met:

- System values are provided per one standard human for:
 - Mass
 - Power
 - Volume
 - Cooling
 - Maintenance
- All system functions are defined according to the LiSTOT ECLSS function definition.

The ECLSS functions are then matched to metabolic parameters for scaling. For example, the CCAA has the functions:

- Control Atmospheric Temperature
- Remove or Add Moisture

Therefore, the CCAA scaling depends on the metabolic parameters that influence the atmospheric temperature and humidity:

- Average heat flow
- Average humidity flow
- Peak heat flow
- Peak humidity flow

To calculate the scaling factor S the current metabolic flows $\dot{m}_{k,current}$ are divided by the nominal metabolic flows $\dot{m}_{k,nominal}$ for each metabolic parameter k . Metabolic flows in this context can be either mass flows or heat flows.

$$S = \max_k \left(\frac{\dot{m}_{k,current}}{\dot{m}_{k,nominal}} \right) \quad (5.1-2)$$

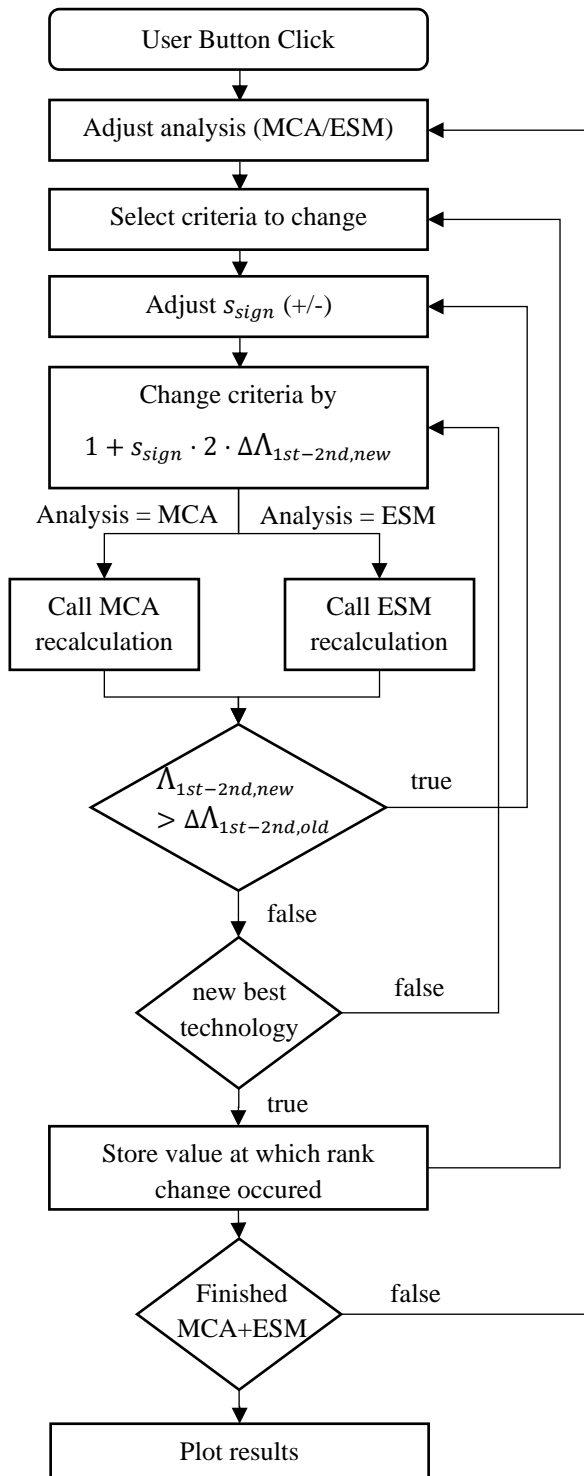
This scaling is therefore not only dependent on the number of crew members but also on the selected schedule and level of activity. For example, if all crew members exercise at the same time, as compared to all crew members exercising at different times, the average heat flow and humidity flow remain the same. But the peak flows increase significantly and would therefore become the maximum scaling parameter deciding the system size. In addition, exercise exceeding the 30-minute exercise period also increases the metabolic loads on the ECLSS, which is reflected in the scaling through this approach.

Through the automatic allocation of metabolic flows from the crew to the functionalities of the subsystem, each new technology that is added to LiSTOT is automatically scaled correctly, as long as all relevant functions and parameters are defined correctly for one standard human. For example, if an alternative to the CCAA is included in the technology sheet then it is scaled according to the produced heat and humidity as long as the two ECLSS functions ‘Control Atmospheric Temperature’ and ‘Remove or Add Moisture’ are defined for it.

5.1.1.4 Subsystem-Level Multi Criteria and ESM Analysis

The basic calculations for the MCA discussed in (Schreck 2017: 142) and (Feigel 2019: 53) for the ESM calculation defined in (Levri et al. 2003) were not changed. The basic approach for the MCA is a weighted sum model where the following equation is used to calculate the MCA score $\Lambda_{score,i}$ for each alternative i :

$$\Lambda_{score,i} = \frac{\sum_{j=1}^n w_j r_{ij}}{n} \quad (5.1-3)$$



The variable w_j is the user selected weight for criterion j . The criteria are mass, volume, power, cooling, maintenance, reliability and TRL. λ_{ij} is the performance of alternative i for criterion j . While the basic calculation remains the same, the previous code was not written in a modular manner and had the required calculations copied to multiple locations within the code, which made maintenance and changes difficult.

Therefore, a more modular approach with fewer repetitions was introduced. The ESM and MCA calculations are now performed within a subfunction, which can be called from any part of the code requiring these values. This also simplifies the criticality calculation, which was replaced with a faster and less repetitive algorithm. Figure 5.1-2 shows the flowchart for the new MCA / ESM criticality calculation.

The user starts the criticality calculation by clicking the corresponding button. Since the basic approach is identical for both the MCA and the ESM criticality, a loop is used to step through both calculations. Then the algorithm loops through all criteria and alternates between an increase and a decrease of the criteria, represented by the variable s_{sign} . This enables easy addition of further criteria because the algorithm does not require information whether an increase or a decrease is beneficial for the system. The current criteria value for the current best technology is then multiplied with the term $1 + s_{sign} \cdot 2 \cdot \Delta\Lambda_{1st-2nd,new}$. The difference in score between the first and second alternative $\Delta\Lambda_{1st-2nd,new}$ is taken into account to initially use large changes, as long as the difference between the technologies is larger. Once the difference becomes smaller, the step size also decreases to increase accuracy of the criticality calculation results. Once the criterion is adjusted the respective calculation function is called and the new difference between the first and second place is calculated and compared to the old one. If the difference increased, the current direction of the changes is wrong, and the algorithm directly goes to the next direction to reduce calculation time. If the change decreased, it checks whether a new technology is now considered best and if that is the case stores the criticality value. Once all iterations are finished, the criticality results are plotted.

Figure 5.1-2 Flow chart for the criticality analysis.



5.1.1.5 Plant Growth Chambers

The first change necessary was to add Plant Growth Chambers (PGC) as technologies to LiSTOT and include calculations for different types of PGC in the composition analysis. The following pages are largely from the publication (Kaschubek 2021), which was written by the author of this thesis. The cited content was only adjusted in formatting e.g. by adjusting the cross-references to figures and tables.

“The values for mass, power, volume and cooling of the PGC are based on (Anderson et al. 2018: 176). However, the required power for lighting is reduced to 630 W assuming LED are used as light sources based on (Zabel 2020). The electricity to light conversion efficiency assumed by (Zabel 2020) is 35% which could be further improved. The theoretic maximum conversion efficiency of red LED is 81% which together with a theoretic maximum fixture efficiency of 93% results in a maximum conversion efficiency using current technology of 75% and blue LEDs are even more efficient (Kusuma et al. 2020). The initial mass for lamps and ballasts assumed in (Anderson et al. 2018: 176) is 31.3 kg/m² with a resupply of 3.81 kg/(y m²). This means a resupply ratio of 12.17% is assumed for the high-pressure sodium lamps. Unfortunately (Zabel 2020) only adjusts the power and cooling values for the lamps, which means the mass difference between high pressure sodium lamps and LEDs is not considered. For comparison, the LED growth light GC16 from Greenception with 700 W power consumption weighs around 17.5 kg (Greenception 2021) while the Qaudra 700 Pro LED from Horizon weighs around 4.5 kg at 690 W power consumption (Horizon 2021). Since ~630 W/m² of power are required according to (Zabel 2020), the required mass for the LED lamps is between 4.5 kg and 17.5 kg. Here the more conservative value of 17.5 kg is used, which results in a required resupply of 2.13 kg/(y m²) through linear scaling. If an optimistic estimate of the life expectancy of high pressure sodium lamps (~24,000 h) compared to the LED life expectancy of the GC16 from Greenception (40,000 h) is taken into account, the resupply mass can be reduced to 1.28 kg/(y m²).¹ The life expectancy for the LED can also be considered conservative as modern LED lamps reach 50,000 h to 100,000 h (Stouch Lighting 2021). Therefore, a very optimistic estimate (using the 4.5 kg and 100,000 h) for the required resupply mass is 0.13 kg/(y m²).

The assumed mass per m² value is adjusted to assume the GC16 LED and therefore reduced by 13.8 kg/m² assuming one GC16 lamp per m². Note that the product sheet of the lamp is contradictory as the graphic within the sheet shows illumination for one m² while the text states the lamp can illuminate 1.5x1.5 m (2.25 m²). On the other hand, (Zabel 2020) states the required electric power for LEDs to be 630 W/m² and therefore one lamp per square meter is assumed here.

Another change compared to the analysis performed in (Zabel 2020) is the assumed cooling for the LEDs. (Zabel 2020) assumes only the LED power consumption as required cooling value, while LiSTOT assumes all power is required as cooling, since that is the more conservative estimate. Table 5.1-1 provides an overview of the different ESM values used by the sources and LiSTOT.

Table 5.1-1: Plant growth chamber ESM values based on (Zabel 2020; Anderson et al. 2018: 163).

Parameter	Unit	(Anderson et al. 2018: 163)	(Zabel 2020)	LiSTOT
Mass	kg/m ²	101.5	101.5	87.7
Volume	m ³ /m ²	1.03	1.03	1.03
Cooling	kW/ m ²	2.6	0.63	1.07
Power	kW/ m ²	2.6	1.07	1.07
Maintenance	h/(m ² y)	13.1	13.1	13.1
Logistics Mass	kg/(m ² y)	3.81	-	1.28

” (Kaschubek 2021)

In addition to these base values, it is also necessary to include averaged values for the mass flows the plants exchange with the ECLSS. These are calculated based on the values provided in (Anderson et al. 2018: 168) Table 4.99 and Table 4.100. The approach is simple and scalable, all values from the tables are implemented as vectors in the VBA code of

¹ $17.5 \text{ kg/m}^2 \cdot 0.1213 \text{ 1/y} = 2.13 \text{ kg/(y m}^2\text{)}; 2.13 \text{ kg/(y m}^2\text{)} \cdot 24,000 \text{ h/40,000 h} = 1.28 \text{ kg/(y m}^2\text{)}$

LiSTOT including the corresponding growth areas per crop. By multiplying the values for O₂, CO₂, H₂O and biomass with the respective growth areas, the average daily mass flows can be calculated for any PGC.

The initial approach was to implement the Exploration Life Support (ELS) PGC based on (Anderson et al. 2018: 168) using 19.5 m² (called Part ELS PGC) and 65.29 m² (called Full ELS PGC) of growth area. However, the dietary requirements changed since these crop compositions were derived. According to (Anderson et al. 2018: 134), the Full ELS PGC provides only 7.74 MJ/d while the Part ELS PGC provides 9.74 MJ/d. Therefore, the PGC must be rescaled to 51.38 m² and 164.15 m² to provide the current desired energy of 12.7 MJ/d. The very large size of the Full ELS PGC combined with the values from Table 5.1-1 results in a very expensive system. The smaller Part ELS PGC is however not designed to provide a full diet and has nutritional imbalances. For this reason, a new crop growth area composition had to be found which requires less growth area while also achieving the nutritional balance required for a full diet. The nutritional targets are based on (Anderson et al. 2018: 134) and are summarized in Table 5.1-2.

“The basic approach to optimize the crop growth area composition is an optimization under boundary conditions using the MATLAB[®] function *linprog* which solves the following equations (MathWorks[®] 2021):

$$\min f^T(x) \text{ such that } \begin{cases} \mathbf{A} \cdot x \leq b \\ \mathbf{A}_{eq} \cdot x = b_{eq} \\ l_{lower} \leq x \leq l_{upper} \end{cases} \quad (5.1-4)$$

The desired parameter to be minimized in this case is the sum of the crop growth area. Therefore x is a vector containing the individual crop growth areas for the different considered crops while $f^T(x)$ is the sum of all crop growth areas. Since the ESM values from (Anderson et al. 2018: 176) all scale linearly with the crop growth area, this approach also minimizes the required ESM for the PGC.

The nutritional value of the plants is implemented through the boundary conditions. It can either be set equal using the condition $\mathbf{A}_{eq} \cdot x = b_{eq}$ or to exceed a minimal value by using $\mathbf{A} \cdot x \leq b$. To use these conditions, it is necessary to derive a matrix \mathbf{A} which provides the produced nutritional energy, macro- and micronutrients when multiplied with the vector x . By multiplying the edible biomass produced per day and m² from (Anderson et al. 2018: 179) with the nutrient content from (U.S. Department of Agriculture 2021) a production value per m² for each nutrient and crop can be derived. These values form matrix \mathbf{A} which can then be multiplied with the crop growth areas in vector x to obtain a vector containing the produced nutrients and nutritional energy. Table 5.1-3 summarizes the required values to derive matrix \mathbf{A} . The entries for matrix \mathbf{A} are derived with equation (5.1-5).

$$a_{i,j} = \dot{m}_{i,j} \cdot c_{i,j} \quad (5.1-5)$$

Here the variable $a_{i,j}$ is the entry of matrix \mathbf{A} in row i and column j . The index j corresponds to the different plants, while the index i corresponds to the different nutritional information. $\dot{m}_{i,j}$ is the edible biomass production from Table 5.1-3 and $c_{i,j}$ is the nutritional content per edible biomass. Therefore, $a_{i,j}$ corresponds to the different nutritional information of the plants which are produced per m², e.g. the nutritional energy, fat or Fe production. For example, $a_{energy,cabbage} = 75.78 \frac{\text{g}}{\text{d m}^2} \cdot 1.03 \frac{\text{kJ}}{\text{g}} = 78.05 \frac{\text{kJ}}{\text{d m}^2}$ and $a_{Fe,cabbage} = 75.78 \frac{\text{g}}{\text{d m}^2} \cdot 4.7 \frac{\mu\text{g}}{\text{g}} = 356.2 \frac{\mu\text{g}}{\text{d m}^2}$.

Table 5.1-2 provides an overview of the different considered cases and the corresponding boundary conditions. The boundary conditions must be separated into nutrient boundary conditions which are calculated using $\mathbf{A} \cdot x \leq b$ and crop growth area boundary conditions represented by $l_{lower} \leq x \leq l_{upper}$ where the lower limit l_{lower} is simply set to 0 and the upper limit l_{upper} is either set to ∞ or the desired maximum area.

The first considered case (Case 1) uses all target values from (Anderson et al. 2018: 134) and limits the growth area for each plant to 30 m² to ensure a sufficient variety of plants. Case 2 is identical except for the area limitation which was removed for this case to see the impact on plant variety this parameter has. In Case 3 only the overall energy requirement must be achieved with a 30 m² limit for each plant, while Case 4 is identical but reduces the available growth area to 10 m² per plant. These cases are easier to achieve with plants as less variety is necessary and therefore result in lower required growth areas. Case 3 can therefore be considered the “best case” with regard to required growth area while



Case 1 is the “worst case” in this regard. On the other hand, Case 3 and 4 will require additional resupply of micronutrients. Considering only the macronutrients (carbohydrates, fats and proteins) was also considered but resulted in a very similar growth area composition as Case 1 and was therefore not included in this paper.” (Kaschubek 2021)

“In addition to the micronutrients mentioned in Table 5.1-2, vitamins targets from (Liskowsky and Seitz 2014: 587) could also be included in the analysis. However, since the initial biological life support systems will likely not provide a complete diet, and to limit the scope of the presented research, the author decided to focus on the values from (Anderson et al. 2018: 134) for this paper.

Table 5.1-2: Target values b_{eq} (=) and boundary conditions b, l_{upper} (\geq / \leq) of the optimization algorithm for the different cases.

	Unit	Target	Case 1	Case 2	Case 3	Case 4
Energy	kJ	12700	=	=	=	=
max area per crop	m ²		≤ 30	$\leq \infty$	≤ 30	≤ 10
C _x H _x O _x	g	379.42	\geq	\geq		
Protein	g	227.65	\geq	\geq		
Fat	g	40.47	\geq	\geq		
Ca	mg	1	\geq	\geq		
Fe	mg	0	\geq	\geq		
Mg	mg	0.35	\geq	\geq		
P	mg	0	\geq	\geq		
K	mg	3	\geq	\geq		
Na	mg	1.5	\geq	\geq		
Zn	mg	0.015	\geq	\geq		
Fiber	mg	10	\geq	\geq		

The other parameters used for the optimization and the sources are summarized in Table 5.1-3 on the next page.

Table 5.1-3: Plant parameters used for the optimization, edible growth rate is fresh basis from (Anderson et al. 2018: 179) page 179 for all crops except chufa and cucumber which are taken from (Fu et al. 2019: 697). Dry base carbon content (C) is from (Anderson et al. 2018: 180) page 180, except for chufa and cucumber where it was estimated based on similar crops. Nutritional data is from (U.S. Department of Agriculture 2021), $C_xH_xO_x$ describes carbohydrates.

	Edible g/(d m ²)	H ₂ O %	C %	Energy kJ/g	C _x H _x O _x mg/g	Fat mg/g	Protein mg/g	Ca mg/g	Fe μg/g	Mg mg/g	P mg/g	K mg/g	Na mg/g	Zn μg/g	Fiber mg/g
Cabbage	75.78	92	40	1.03	33	1	12.8	0.4	4.7	0.12	0.26	1.7	0.18	1.8	25
Carrots	74.83	88	41	1.73	67.8	2.4	9.3	0.33	3	0.12	0.35	3.2	0.69	2.4	28
Chard	87.5	92	40	0.79	21.4	2	18	0.51	18	0.81	0.46	3.79	2.13	3.6	16
Celery	103.27	90	40	0.57	13.7	1.7	6.9	0.4	2	0.11	0.24	2.6	0.8	1.3	16
Dry bean	11.11	10	40	13.93	351.1	8.3	235.8	1.43	82	1.4	4.07	14.06	0.24	27.9	249
Green Onions	81.82	89	40	1.12	39.4	4.7	9.7	0.52	5.1	0.16	0.25	1.59	0.15	2	18
Lettuce	131.35	95	40	0.62	15.7	1.5	13.6	0.36	8.6	0.13	0.29	1.94	0.28	1.8	13
Onions	81.82	89	40	1.66	76.4	1	11	0.23	2.1	0.1	0.29	1.46	0.04	1.7	17
Peas	12.2	12	40	3.39	87.5	4	54.2	0.25	14.7	0.33	1.08	2.44	0.05	12.4	57
Peanut	5.96	5.6	60	23.74	76.3	492.4	258	0.92	45.8	1.68	3.76	7.05	0.18	32.7	85
Pepper	148.94	93	40	0.836	46.4	1.7	8.6	0.1	3.4	0.1	0.2	1.75	0.03	1.3	17
Radish	91.67	94	40	0.67	34	1	6.8	0.25	3.4	0.1	0.2	2.33	0.39	2.8	16
Beets	32.5	80	41	3.723	67.6	1.7	16.1	0.16	8	0.23	0.4	3.25	0.78	3.5	28
Rice	10.3	12	42	14.94	687	10.8	147.3	0.21	19.6	1.77	4.33	4.27	0.07	59.6	62
Snap Beans	148.5	92	40	1.31	42.7	2.2	18.3	0.37	10.3	0.25	0.38	2.11	0.06	2.4	27
Soybean	5.04	10	46	6.14	68.5	68	129.5	1.97	35.5	0.65	1.94	6.2	0.15	9.9	42
Spinach	72.97	91	40	0.97	14.3	3.9	28.6	0.99	27.1	0.79	0.49	5.58	0.79	5.3	22
Strawberries	77.88	90	43	1.36	56.8	3	6.7	0.16	4.1	0.13	0.24	1.53	0.01	1.4	20
Sweet potato	51.72	71	41	3.59	171.2	0.5	15.7	0.3	6.1	0.25	0.47	3.37	0.55	3	30
Tomato	173.76	94	43	0.74	26.9	2	8.8	0.1	2.7	0.11	0.24	2.37	0.05	1.7	12
Wheat	22.73	12	42	14.23	626.6	19.9	106.9	0.34	53.7	0.9	4.02	4.35	0.02	34.6	127
White potato	105.3	80	41	2.88	133.1	1	16.8	0.09	5.2	0.21	0.62	4.07	0.16	2.9	24
Chufa	8.87	6.4	60	16.74	633.3	233.3	66.7	1	60	0.93	0	7.17	0	35	333
Cucumber	167.17	94	40	0.628	36.3	1.1	6.5	0.16	2.8	0.13	0.24	1.47	0.02	2	5

Note that carbon content in (Anderson et al. 2018: 180) is provided for the overall dry biomass (edible and inedible) and is used in this analysis only for the inedible biomass. But this assumption was necessary due to the lack of a better estimate for the carbon content of solely the inedible biomass. The water content is for the provided fresh edible biomass.“ (Kaschubek 2021)



“The resulting PGC growth areas from the optimization algorithm and literature values scaled to the 12.7 MJ/d energy demand assumed for this analysis are provided in Table 5.1-4.

Table 5.1-4: PGC plant growth areas. Part ELS and Full ELS are based on (Anderson et al. 2018: 181) while the Lunar Palace (LP) case is based on (Fu et al. 2019). The provided information from literature was scaled to 12.7 MJ/d energy demand for better comparability.

Crop	Case 1 m ²	Case 2 m ²	Case 3 m ²	Case 4 m ²	Part ELS m ²	Full ELS m ²	LP m ²	Manual m ²
Cabbage					0.09			
Carrots					1.41	1.35	2.00	
Chard	10.55							
Celery					0.19			
Dry bean				10.00	3.08	4.84		10.00
Green Onions					1.10	0.69	0.40	
Lettuce	30.00				0.42	0.14	4.35	2.00
Onions								
Peas					0.82			
Peanut	4.11	3.49				12.15		10.00
Pepper	14.81	17.00			0.55			
Radish						0.41		
Beets								
Rice				7.04		5.22		2.00
Snap Beans	25.59	32.13		10.00	0.18		1.52	
Soybean						116.73	4.48	
Spinach	30.00	54.24			1.44	1.60		
Strawberries							0.80	
Sweet potato				10.00	9.17	3.73		2.00
Tomato					3.19	4.13		5.00
Wheat			30.00	10.00	25.50	10.65	31.97	18.00
White potato			9.88	10.00	4.25	2.50		8.00
Chufa							7.99	
Cucumber							0.05	
Total Area	115.06	106.86	39.88	57.04	51.38	164.15	53.55	57.00

The manual case in Table 5.1-4 was not derived from the optimization algorithm. Instead, the crop growth areas were adjusted based on both the optimization results and the growth areas from literature to achieve both a small growth area and a larger variety of available crops. The supplied nutrients from the different cases are shown in Table 5.1-5 and the provided composition of macro nutrients in Table 5.1-6.

Table 5.1-5: Nutrient Supply from the different PGC.

Crop	Unit	Case 1	Case 2	Case 3	Case 4	Part ELS	Full ELS	LP	Manual
Energy	kJ/d	12700	12700	12700	12700	12699.9	12700.2	12700	12695.6
C _x H _x O _x	g/d	379.42	379.42	565.76	523.35	550.18	353.11	535.61	471.40
Protein	g/d	227.65	227.65	90.37	114.16	97.43	160.46	99.40	115.34
Fat	g/d	40.47	40.47	14.61	10.81	15.05	84.33	34.59	41.66
Ca	g/d	5.71	5.96	0.33	1.05	0.72	1.74	0.73	0.65
Fe	g/d	0.16	0.17	0.04	0.05	0.05	0.05	0.05	0.04
Mg	g/d	4.20	4.61	0.83	1.21	0.98	1.19	0.90	0.99
P	g/d	4.62	4.34	3.39	3.14	3.27	3.38	3.29	3.27
K	g/d	35.41	36.73	7.20	12.02	9.20	10.81	6.03	10.20
Na	g/d	5.10	3.49	0.18	0.58	0.59	0.50	0.30	0.36
Zn	g/d	0.03	0.04	0.03	0.02	0.03	0.02	0.03	0.03
Fiber	g/d	256.35	260.72	111.57	141.91	124.50	106.32	136.41	123.13

Table 5.1-6: Percentage of energy from macro nutrients of the different PGC.

	Unit	Case 1	Case 2	Case 3	Case 4	Part ELS	Full ELS	LP	Manual
$C_xH_xO_x$	%	50.0	50.0	74.6	69.0	72.5	46.5	70.6	62.1
Protein	%	30.0	30.0	11.9	15.0	12.8	21.1	13.1	15.2
Fat	%	12.0	12.0	4.3	3.2	4.5	25.0	10.3	12.4

Note that the values in Table 5.1-6 do not sum up to 100% because the assumed nutritional energy for $C_xH_xO_x$, proteins and fats does not match the nutritional content provided by (U.S. Department of Agriculture 2021) as the differences between different types of macro nutrients (e.g. different types of fats) are reflected in the nutritional value provided there. Therefore, the nutritional energy from (U.S. Department of Agriculture 2021) was used to calculate the overall provided energy, but for the optimization the simplification to use the averaged values of 4 calories per g carbohydrates or protein and 9 calories per g fat from (US Food and Drug Administration 2020) was chosen.

Case 1 and Case 2 are interesting results because the high yield crops like wheat, white potato and sweet potato are not used at all. Indeed snap beans provide the highest protein production index (2.7 g/m²) based on the values from Table 5.1-3 and is therefore favored to cover the protein supply target of 30 % energy of this case. Spinach provides the highest production ratio of protein compared to carbohydrates and fats, and is therefore used to achieve the 30% protein target without exceeding the total energy supply requirement. The only difference between Case 1 and Case 2 is the assumed maximum area per crop, which is unrestricted for Case 2. Therefore, fewer different crops are favored in this case reducing the total area by 8.2 m². If the micronutrients are neglected for Case 1 the required area becomes 98.28 m² with an increase of the required area for peanuts to 6.89 m² but a reduction of snap bean area to 21.24 m² and chard and peppers are no longer used at all. Case 3 and Case 4 did not require the algorithm to match macronutrients, as this led to the high total areas in Case 1 and Case 2. Case 3 therefore focused entirely on the crops with the highest energy yield per m² which is wheat followed by white potato. Without an area limitation the algorithm selects only wheat with only a small reduction in growth area to 39.26 m². Since the focus on only two plants would result in an unvaried diet, the crop growth areas were limited to 10 m² in Case 4 to promote diversity in selected crops. This resulted in a better macronutrient composition with less focus on carbohydrates as shown in Table 5.1-6. A manual optimization was then performed based on these results and the literature PGC to further optimize macro and micronutrient supply without enforcing the boundary conditions completely. The resulting diet exceeds the limit for energy supply from carbohydrates from NASA (Anderson et al. 2018: 134) but is within the range of other diets reported in literature which have been tested on humans (Fu et al. 2019; Masuda et al. 2005). While the required area is slightly larger than the part ELS diet or the LP diet, it is also more varied with respect to macro nutrients.

The manual case is slightly calcium and sodium deficient which would require supplements to cover the missing nutritional intake. The phosphorus value exceeds the NASA limits from (Anderson et al. 2018: 134) and (Liskowsky and Seitz 2014: 586), but total phosphorous intake is lower for the manual diet than for the lunar palace or full ELS diets. In addition, the phosphorous intake from the manual diet is below the 3.5 g/d upper intake limit from (Institute of Medicine 1997: 186). The manual diet also has very high dietary fiber and potassium intakes which exceed the mentioned range from (Anderson et al. 2018: 134). However, according to (Institute of Medicine 2005: 399) no upper intake limit for dietary fiber exists because no adverse effects of high dietary fiber intake could be observed. For potassium, exceedingly high levels may potentially have negative effects (Oria et al., eds. 2019: 136) but intake from natural sources like crops is deemed uncritical (Scott M. Smith et al. 2014: 58). Therefore, the derived manual diet can be considered a viable alternative to the current diets discussed in literature as it either outperforms them with regard to the required growth area or with regard to the macro and micronutrient supply.

The Full ELS focuses on soybeans also because the quality of protein received from soybeans is considered higher and it has a higher utility because multiple different food stuff can be created from it like soy milk, tofu etc.². These aspects are not considered by the optimization algorithm, which therefore focuses on dry beans or other plants as protein source.” (Kaschubek 2021)

Further detailed analysis of the different cases including a discussion which PGC is considered optimal for exploration missions can be found in (Kaschubek 2021). For the following chapters, the manual PGC is called Exploration PGC.

² Personal communication with Michael Ewert from NASA Johnson Space Center



5.1.1.6 ECLSS Composition Analysis and Trade-Off

The previous ECLSS composition analysis of LiSTOT used pre-defined ECLSS types like open-loop, partial, closed-loop and bioregenerative. In addition, the bioregenerative ECLSS was a place holder where the actual flowrates were not calculated. Since the preselection of ECLSS types limits the combinations the user can select, this calculation was completely reworked to allow any combination of systems that is possible, e.g. PGC and CAMRAS.

In addition, the implementation of PGC required additional options to e.g. incinerate inedible biomass to produce additional CO₂ and to potentially use plants for urine treatment to allow additional trade-offs. Furthermore, the carbon balance of the system must be ensured. For this purpose, the carbon content of the produced biomass is used to calculate the producible CO₂ from incinerating inedible biomass. The PGC growth area is then iteratively adjusted until carbon balance is reached resulting in smaller PGC growth areas, which depend on the used crew schedule, as the amount of CO₂ produced by the crew influences this calculation.

Figure 5.1-9 provides an example of a composition analysis from LiSTOT using all available types of technologies. In the example, the Exploration PGC is used for biomass production. The produced plant biomass is split into edible and inedible parts. The edible parts are consumed by the crew and reduce the required pre-stored food mass according to the nutritional energy content of the produced plant biomass. In addition, the potable water demand is adjusted to ensure a closed mass balance because edible plant biomass generally has a higher water content per nutritional energy than pre-stored food. If the potable water consumption is not adjusted, the human would consume more water than is produced as waste-water, which would result in an error in the water balance. It should also be noted that metabolic water generation is considered in the analysis and therefore the water mass balance over the human block does not match exactly. Inedible biomass is considered to be dried to recover about 80% of its water content but it is not further processed. The overall ECLSS water balance is added as a value inside the H₂O Storage block to give the user a quick overview whether the system composition requires additional water resupply (negative values) or if even a slight water surplus is available (positive values). A water surplus can occur because the combined water regeneration capability of all ISS water processing systems is ~98% (Kelsey et al. 2018) and additional water is introduced into the ECLSS from pre-stored food and metabolic water. The drop-down menus within the individual blocks allow the user to select alternative technologies for each subsystem based on the technologies from the technology sheet. For all systems, except the CO₂ reduction new technologies added in the worksheet are automatically added to the drop-down menu and the flowrates are calculated based on the provided efficiency values. For the CO₂ reduction subsystem this approach is not possible because the values depend on the chemical reactions of the specific reduction subsystem. For these systems the corresponding equations must first be added to the VBA code of LiSTOT.

5.1.2 Mars Base ECLSS Trade-Off Analysis

In this chapter LiSTOT is used to perform an ECLSS trade-off analysis with available subsystems for mission scenario three – the permanent Mars base from chapter 1.2.2.3. Since permanent is not a valid option to select, a mission duration of 20-years is assumed. This is on the same scale as the present total mission duration of the ISS. However, the break-even points of the individual systems are discussed individually to decide for which mission length each subsystem would be advantageous.

5.1.2.1 Assumptions

As equivalency factors for the ESM analysis the NASA values used for a Mars surface habitat are used as shown in Table 5.1-7.

Table 5.1-7: ESM equivalency factors for Mars from (Anderson et al. 2018: 23).

Parameter	Variable	Unit	Value
Shielded Volume	V_{eq}	kg/m ³	215.5
Power	P_{eq}	kg/kW	87
Cooling	C_{eq}	kg/kW	146
Crew Time	t_{eq}	kg/h	0.465

The assumed mission duration is 20-years with a crew of six. As baseline for the trade-off the ISS ECLSS consisting of the following subsystems was chosen:

- Common Cabin Air Assembly (CCAA)
- Carbon Dioxide Removal Assembly (CDRA)
- Oxygen Generation Assembly (OGA)
- Sabatier Carbon Dioxide Reduction Assembly (SCRA)
- Water Processing Assembly (WPA)
- Urine Processing Assembly (UPA)
- Brine Processing Assembly (BPA)

“Table 5.1-8 summarizes the underlying assumptions used to derive the ISS ECLSS parameters provided in Table 5.1-9 and the respective sources. The hardware replacement rates include spare parts and are based on ISS on-orbit data.

Table 5.1-8: Assumed ECLSS parameters.

Value	Unit	Value	Source
WPA Water Recovery Efficiency	%	100	(Carter et al. 2005)
UPA Water Recovery Efficiency	%	85	(Carter et al. 2019)
BPA Water Recovery Efficiency	%	80	(Kelsey et al. 2018)
WPA Nominal Processing Capacity	kg/d	141.5	(Carter et al. 2005)
UPA Nominal Processing Capacity	kg/d	9.0	(Carter et al. 2019)
BPA Nominal Processing Capacity	kg/d	0.86	(Kelsey et al. 2018)
WPA Hardware Replacement Rate	%	3.2	(Bagdigian et al. 2015)
UPA Hardware Replacement Rate	%	12.6	(Carter et al. 2019)
BPA Hardware Replacement Rate	%	< 25	(Kelsey et al. 2018)
OGA Hardware Replacement Rate	%	7%	(Bagdigian et al. 2015)
Crew Metabolic Interfaces	kg/d	See Figure 5.1-6	(Anderson et al. 2018)

Based on the hardware replacement rates the required resupply mass per kg of water or oxygen is calculated and then scaled for a crew of six to receive the values shown in Table 5.1-9. Neglecting spare part resupply mass for the physical/chemical ISS ECLSS would result in distorted performance assessment of these systems compared to the PGC values. Therefore, literature values for the resupply masses were used where available and estimates were calculated based on available data if no values were reported. The underlying assumptions of Table 5.1-9 for the individual values are summarized in the corresponding foot notes.

**Table 5.1-9: ESM values used for ISS ECLSS.**

System	Mass kg	Volume m ³	Power W	Cooling W	Crew Time h/y	Resupply kg/d	Performance -	Sources -
CCAA	112	0.4	470	470	2.3 ³	0.0186 ³	3.5 kW sensible 1.0 kW latent	(Wieland 1998)
CDRA	195.4	0.39	860	860	2.7 ³	0.061 ³	6 crew	(Hanford 2004)
OGA	676	0.79 ⁴	3210 ⁵	330 ⁶	66.48	0.34	6 crew	(Bagdigian et al. 2015)
SCRA	329	0.68 ⁷	90	361 ⁸	2.7 ⁹	0.103 ⁹	6 crew	(Junaedi et al. 2014)
WPA	930	2.4 ⁴	275.1 ¹⁰	275.1	14.95	0.3	6 crew	(Bagdigian et al. 2015)
UPA	455	0.79 ⁴	211.4 ¹¹	211.4	2.66	1.134	9 kg/d	(Bagdigian et al. 2015)
BPA	53	0.71	142	142	14 ¹²	0.22	0.86 kg/d	(Carter and Gleich 2016)

“ (Kaschubek 2021)

³ Based on the mean time between failure, component mass and number of components from Hanford (2004) Table 7.3.2 assuming a maintenance requires 5 hours of crew time.

⁴ Based on the pictures shown in Carter et al. (2017a) and the volume of an international standard payload rack of 1.571 m³

⁵ Assuming a cell voltage of 1.65 V from Takada et al. (2019) and using the Faraday equation to provide O₂ for a crew of 6

⁶ Assuming an efficiency of 89.7% based on the ratio of the ideal cell voltage 1.48 V to 1.65 V

⁷ Volume uses tank volume from Knox et al. (2005: 3) with a mass to volume ratio based on CDRA as volume values from Duffield (2001) are exceedingly low (0.01 m³).

⁸ Electric power + reaction enthalpy based on 6.24 kg of CO₂ per day and the reaction enthalpy $\Delta H = -165 \text{ kJ/mol}$

⁹ For SCRA no reliability data was available. Therefore, crew time is assumed identical to CDRA and resupply mass is scaled based on system mass from the CDRA resupply mass

¹⁰ WPA is assumed to operate 18.25 % of the time (based on the required processing capacity from Table 5.1-8 and the nominal processing capacity from Carter et al. (2005)) resulting in an average power demand of 275.11 W by using the power values from Carter (2009).

¹¹ UPA is assumed to alternately operate for 7.5 h and then being in standby for 5 h from Tobias et al. (2011) resulting in an average power demand of 211.4 W by using the power values from Carter (2009).

¹² Assumed 1 hour of crew time every 26 days when an exchange of bladders is required.

5.1.2.2 Crew Schedule

# of Crew	Schedule 1	Schedule 2	Schedule 3
time	2	2	2
	task	task	task
00:00	Sleep	Sleep	Sleep
00:30	Sleep	Sleep	Sleep
01:00	Sleep	Sleep	Sleep
01:30	Sleep	Sleep	Sleep
02:00	Sleep	Sleep	Sleep
02:30	Sleep	Sleep	Sleep
03:00	Sleep	Sleep	Sleep
03:30	Sleep	Sleep	Sleep
04:00	Sleep	Sleep	Sleep
04:30	Sleep	Sleep	Sleep
05:00	Sleep	Sleep	Sleep
05:30	Sleep	Sleep	Sleep
06:00	Post Sleep	Post Sleep	Post Sleep
06:30	Hygiene	Hygiene	Hygiene
07:00	Breakfast	Breakfast	Breakfast
07:30	Work	Work	Work
08:00	Work	Work	Work
08:30	Work	Work	Work
09:00	Work	Work	Work
09:30	Work	Work	Work
10:00	Exercise	Work	Work
10:30	Exercise	Work	Work
11:00	Post Exercise	Work	Work
11:30	Post Exercise	Work	Work
12:00	Lunch	Lunch	Lunch
12:30	Lunch	Lunch	Lunch
13:00	Work	Exercise	Work
13:30	Work	Exercise	Work
14:00	Work	Post Exercise	Work
14:30	Work	Post Exercise	Work
15:00	Work	Work	Work
15:30	Work	Work	Work
16:00	Work	Work	Exercise
16:30	Work	Work	Exercise
17:00	Recreation	Recreation	Post Exercise
17:30	Recreation	Recreation	Post Exercise
18:00	Recreation	Recreation	Recreation
18:30	Recreation	Recreation	Recreation
19:00	Dinner	Dinner	Dinner
19:30	Dinner	Dinner	Dinner
20:00	Recreation	Recreation	Recreation
20:30	Recreation	Recreation	Recreation
21:00	Pre-Sleep	Pre-Sleep	Pre-Sleep
21:30	Pre-Sleep	Pre-Sleep	Pre-Sleep
22:00	Sleep	Sleep	Sleep
22:30	Sleep	Sleep	Sleep
23:00	Sleep	Sleep	Sleep
23:30	Sleep	Sleep	Sleep

Figure 5.1-3 Crew schedule used for the trade-off.

The crew schedule selected for the mission assumes that all crew members sleep during the same time, which approximately corresponds to the Martian night. This was selected because the primary objective of a surface base on Mars would be extra vehicular activities (EVAs), which are likely only performed during daylight. Each crew member has eight hours of sleep, 7.5 hours of work, three hours of recreation and one hour of exercise within the cabin. The exercise in the cabin could be reduced if sufficient EVAs are performed, but the ECLSS design should still account for the possibility that the crew exercises inside the cabin. The exercise periods are spread over three slots per day with two crew members exercising at the same time. Aside from this, all crew members have the same schedule. The post exercise periods in the schedule are only important for metabolic reasons (increased CO₂ and H₂O output) but are considered as work or recreation based on what the remaining crew is currently doing.

Figure 5.1-4 shows the daily CO₂ production and partial pressure resulting from this schedule. This analysis only serves as preliminary dynamic analysis, as it neglects most effects the partial pressure has on the CO₂ removal technologies. But it shows that the system in principle remains within the limits set by the Spacecraft Maximum Allowable Concentration for 180 days (700 Pa) but slightly exceeds the 1000 day limit (500 Pa) (James et al. 2008).

Figure 5.1-5 shows the daily humidity, urine and wastewater production rates. LiSTOT assumes a simplified urine dynamic, where the urine production is spread between the post-sleep and pre-sleep phases. For the humidity no cabin values are calculated by LiSTOT because the removal rate depends too much on the current humidity level and the used technology and cannot be calculated with a 30-minute time step in a way that provides useful information. Therefore, only the production rates for humidity are shown as outputs.

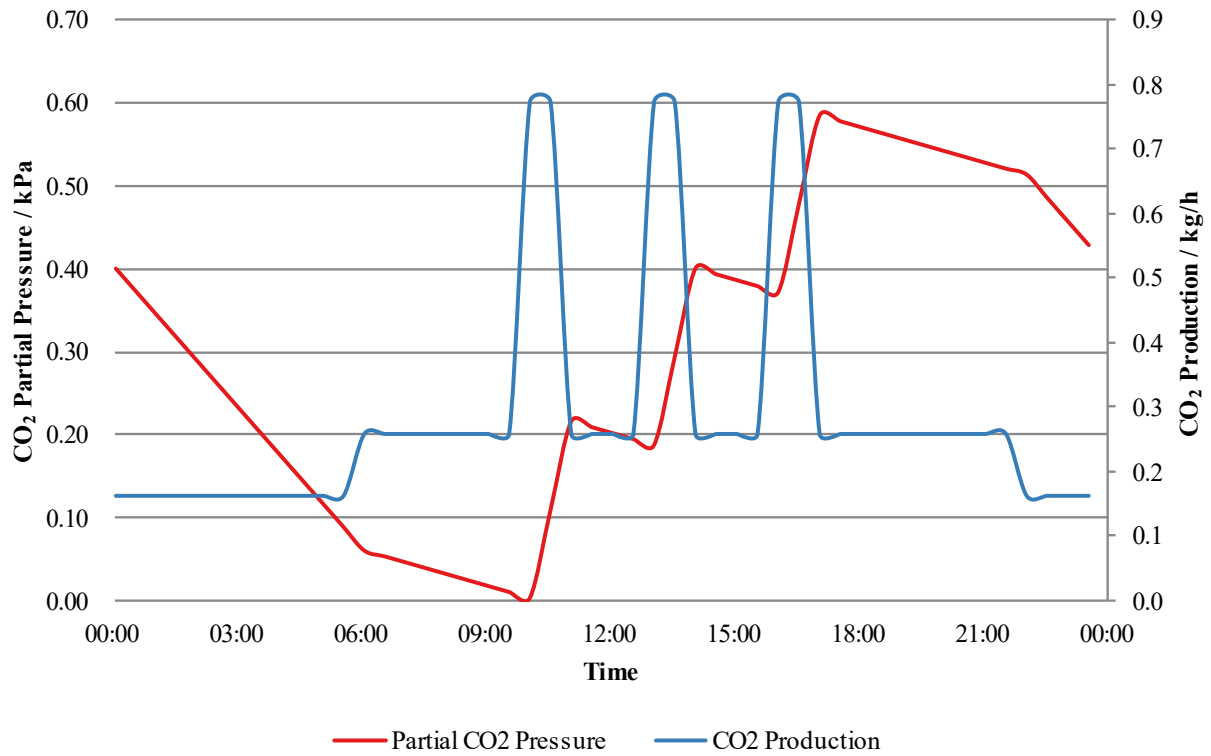


Figure 5.1-4 Daily CO₂ partial pressure and production in LiSTOT. Since all systems are scaled to achieve the same average CO₂ removal, these results are independent of the selected subsystems.

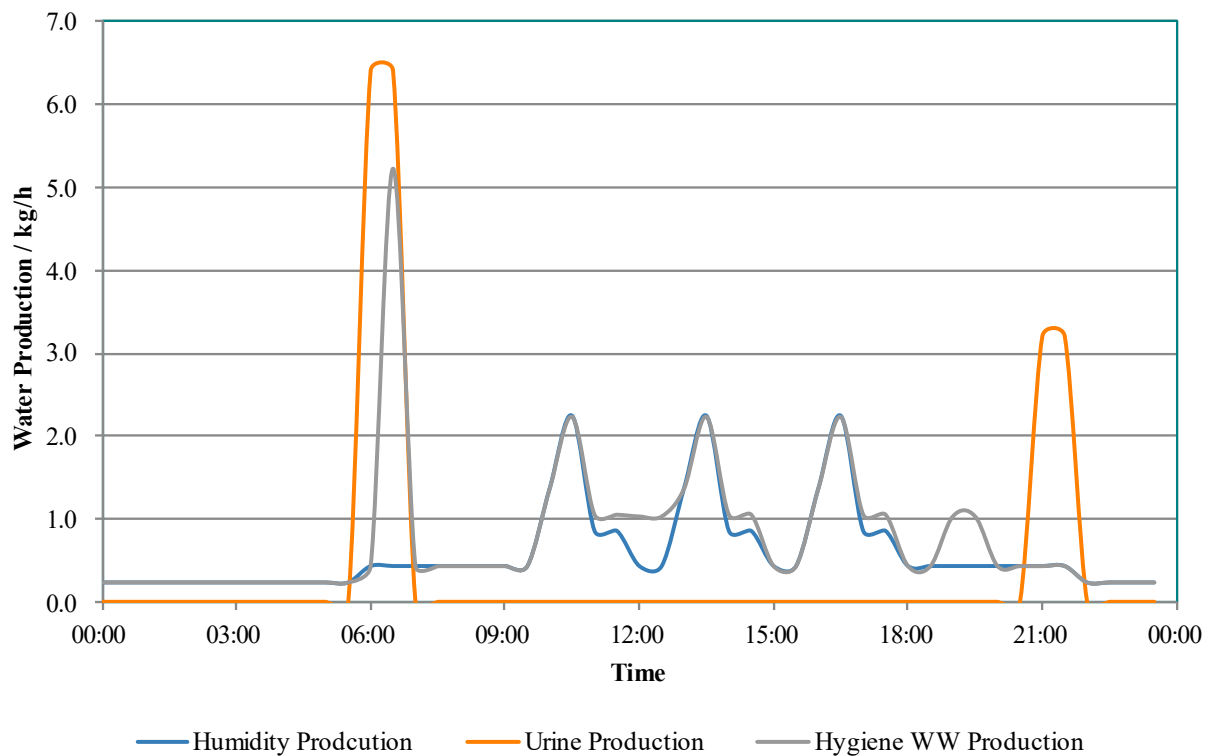


Figure 5.1-5 Daily humidity, waste-water and urine production in LiSTOT.

5.1.2.3 Subsystem MCA and ESM Analysis

The Multi Criteria Analysis (MCA) and Equivalent System Mass (ESM) analysis is an important step in the selection of subsystems as it allows the comparison of different system criteria in a single parameter. In LiSTOT, these two analyses are performed independently of each other and the ESM is not used as input to the MCA. Since the ESM factors can also be considered weights for the different criteria the user can define the weights for the MCA to the corresponding ESM factors. This approach provides the same result as if the ESM would be used as input for the MCA. Since that option exists, the calculations are left separate to give the user more freedom and make comparisons of different weights to a baseline ESM analysis easier.

The limitation of this step is that it is only performed on subsystem-level for individual ECLSS functions such as CO₂ removal. This means that especially biological systems, which perform multiple functions, are underrated compared to PC technologies, which only perform one specific function. Therefore, the ECLSS composition analysis is necessary to include the full effect of these technologies on the ECLSS. Due to this limitation, this analysis step is not as important for the analysis of a permanent Mars base, as the mission duration is so long that biological systems will have potential savings not shown in this subsystem trade-off. For this reason, the MCA analysis is only performed exemplary for one function and the focus is placed on the composition analysis.

Furthermore, the objective of the analysis is to compare biological systems to PC systems and to compare different options of biological systems (different plant growth areas, crop compositions and algae systems) to each other. Therefore, the current ISS ECLSS was selected as baseline PC ECLSS to which the other systems are compared.

In this chapter only the CO₂ reduction system is discussed because of the mentioned assumptions and limitations. Table 5.1-10 provides an overview of the MCA and ESM values for the possible technology options. Note that LiSTOT includes additional technologies from the ones considered in chapter 2 because it includes non-regenerable options, which are not considered for hybrid LSS. Sodasorb and Superoxides represent non-regenerable options, which have very high masses because of the long mission duration. The Photo Bio Reactor (PBR) and PGC options have high ESM values compared to the remaining three PC options. However, plants handle multiple function (oxygen generation food production etc.) while the PC system only provide the CO₂ reduction functionality. This becomes apparent especially when the Part ELS PGC and the Full ELS PGC are compared. Both cases in this table correspond directly to the crop growth areas mentioned in (Anderson et al. 2018: 181) and therefore correspond to 19.5 m² and 65.29 m² of plant growth area. In terms of CO₂ reduction, they are comparable but the Full ELS PGC is designed to supply more food and therefore requires more than three times the ESM. It should be noted that the CO₂ electrolysis and Sabatier reactor do not have reliability values, because no literature information on this could be found also in other trade-off analysis by NASA (Jones 2017: 16).

Table 5.1-10: MCA and ESM values of CO₂ reduction options.

Parameter	Mass	Volume	Power	Cooling	Maint.	Rel.	TRL	MCA	ESM
Unit	kg	m ³	W	W	h	-	-	-	kg
Bosch Reactor	595	1.1	2,233.5	613.2	292	0.90	6	0.56	1156.6
CO ₂ electrolysis	151.1	0.2	3,420.9	750.2	-	-	5	0.28	444.6
Sabatier Reactor	284.6	0.5	87.8	453	-	-	9	0.57	471.6
Sodasorb	248,146	0.9	98.4	-	-	1	6	0.23	248,339
Superoxides	409,853	535.1	3.4	-	3243.3	1	9	0.40	526,671
PBR	9,755.2	15	19,880.6	16,567.2	21.6	-	5	0.30	16,231.9
Part ELS PGC	16,901.9	138.2	14,933.6	12,444.7	1728.8	0.36	5	0.30	71,774
Full ELS PGC	55,273.8	457.6	500,008	416,674	5788.4	0.36	5	0.06	237,861

Based on the MCA the Sabatier reactor and Bosch reactor perform nearly identical, but the Sabatier is better in terms of ESM. However, at this stage in the analysis the higher oxygen recovery of the Bosch reactor is not yet considered. Therefore, both options must be compared in the composition analysis to select the best option. The CO₂ electrolysis is the best solution with regard to ESM but due to the low TRL and unknown reliability does not perform well in the MCA. Since the other two system are better known and the difference in ESM compared to the Sabatier is not that large, CO₂ electrolysis is not further considered. All three biological options will be further studied in the composition analysis,



because it is difficult to compare them without taking the full system into account. From just the subsystem analysis it seems that the PBR is the best option, but food production is only possible in limited quantities (10 g to 30 g) using a PBR because of palatability issues (Waslien and Oswald 1975: 141).

5.1.2.4 ECLSS Composition Analysis

The ECLSS composition analysis combines different subsystems to an ECLSS capable of meeting the crew requirements. The analysis provides averaged daily mass flow rates per crew member as an overview of the ECLSS and to help the user understand the relations between the systems. Figure 5.1-6 shows the LiSTOT ECLSS composition chart for the ISS ECLSS, which also serves as baseline to which the other compositions are compared.

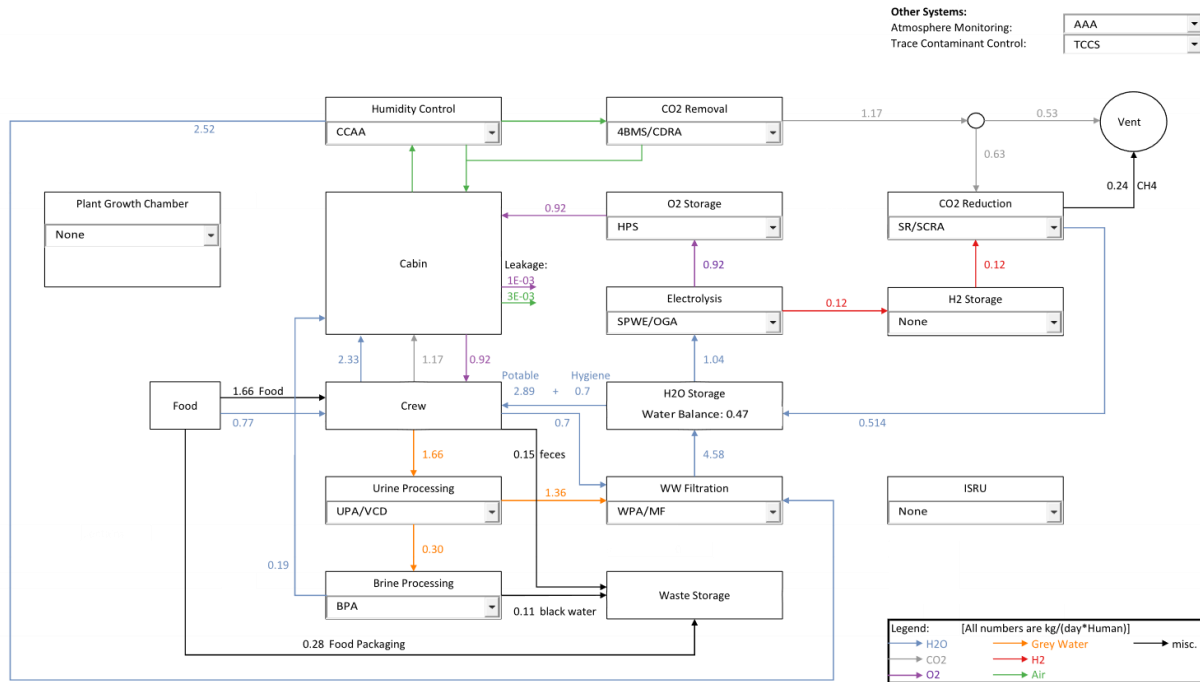


Figure 5.1-6 ISS ECLSS composition.

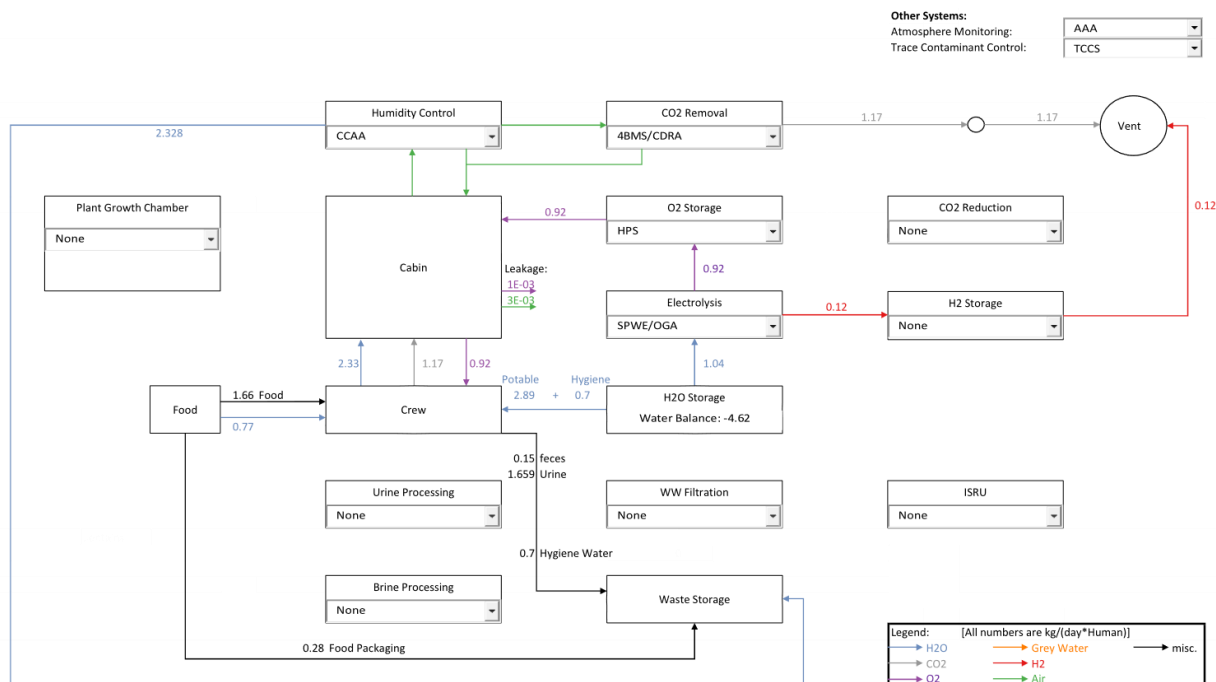


Figure 5.1-7 ISS based Open-Loop ECLSS composition.

Figure 5.1-7 shows the first alternative, a very simple open-loop design without water processing. This serves as comparison for open-loop cases. The required water for consumption is provided from storage tanks in this case.

The other alternative options change individual subsystems without changing the complete ECLSS. Therefore, only the changed sections from the ISS ECLSS composition analysis are shown for the following compositions. Figure 5.1-8 shows the Bosch reactor (BR) and PBR as alternatives to the ISS CO₂ reduction system SCRA (a Sabatier reactor).

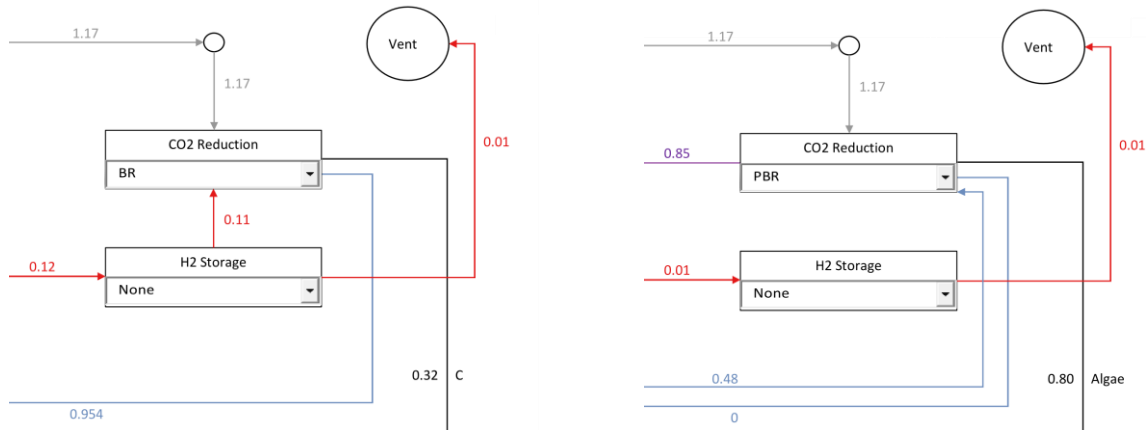


Figure 5.1-8 Alternative CO₂ reduction options. Left Bosch reactor with higher oxygen recovery than SCRA. Right PBR which directly produces oxygen without requiring hydrogen.

Compared to the SCRA the BR can recover up to 100% of the oxygen within the CO₂, while the SCRA would require additional hydrogen to process all of the CO₂. The BR recovers 0.95 kg of water, which covers more than 90% of the required water for oxygen production. The remaining difference is due to the respiratory coefficient of the humans, as not exactly one mol of CO₂ is released per mol of O₂ consumed. However, when combined with the water recycling subsystems, this advantage is limited, as the ISS ECLSS already has a water surplus of 0.47 kg/d. Therefore, the BR only increases this surplus to 0.91 kg/d. In addition, the methane produced by the Sabatier could be used as rocket fuel, while the carbon produced by the Bosch does not have a direct potential application.

The PBR can directly produce O₂ from the supplied CO₂ and therefore reduces the required electrolyzer size significantly as it supplies about 90% of the required O₂. The PBR requires additional water for algae growth, which is then converted to algae biomass. However, the overall system still has a water surplus of 0.43 kg/d because of the reduced electrolyzer demand. Figure 5.1-9 provides an overview of different PGC options.

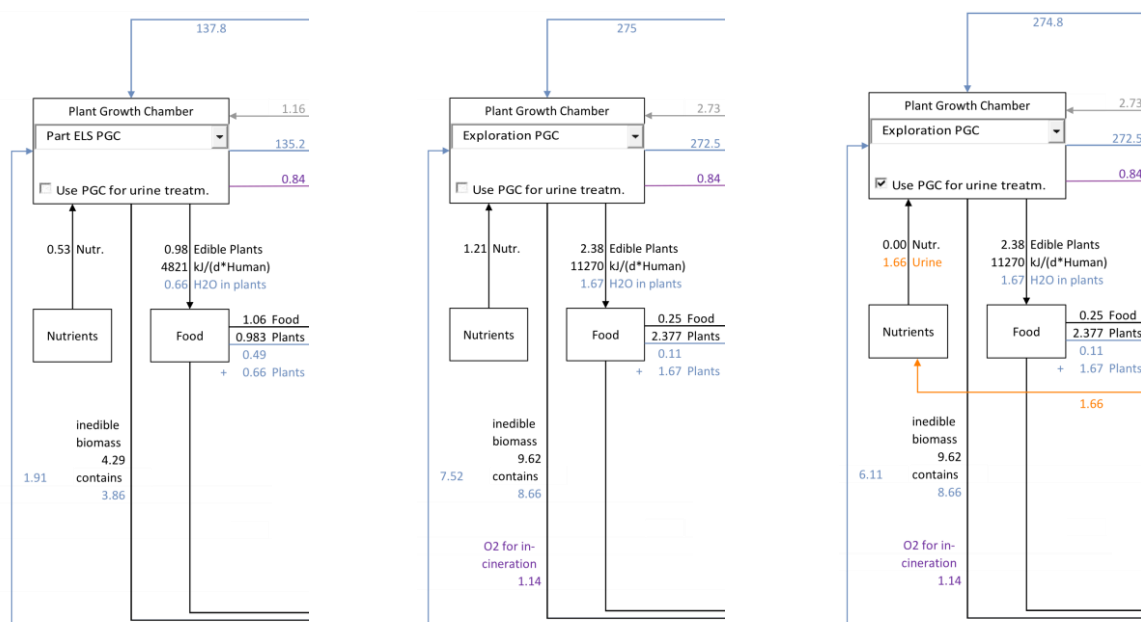


Figure 5.1-9 PGC options for ECLSS composition.



The Part ELS PGC refers to the 19.5 m² crop growth area compositions from (Anderson et al. 2018: 181). It only provides a part of the diet and also does not process all of the crew CO₂. The Exploration PGC is the manual optimization case from Table 5.1-4. It is considered as option with and without urine processing, as urine usage by plants poses additional challenges as previous research with both direct urine usage (Salisbury et al. 1997; Zolotukhin et al. 2005b) and microbial trickle filters (Zabel et al. 2019) shows. The Exploration PGC growth area is reduced to 50.6 m² to achieve carbon balance. This is also the reason why it does not provide a full diet for the crew and 0.25 kg/d of stored food per crew member are required. These PGC were selected to analyze different levels of biological loop closure within the PC ECLSS.

Based on the required consumables, the Exploration PGC with plants as urine treatment seems the most promising candidate from the PGC options. The full composition analysis for this case is therefore shown in Figure 5.1-10.

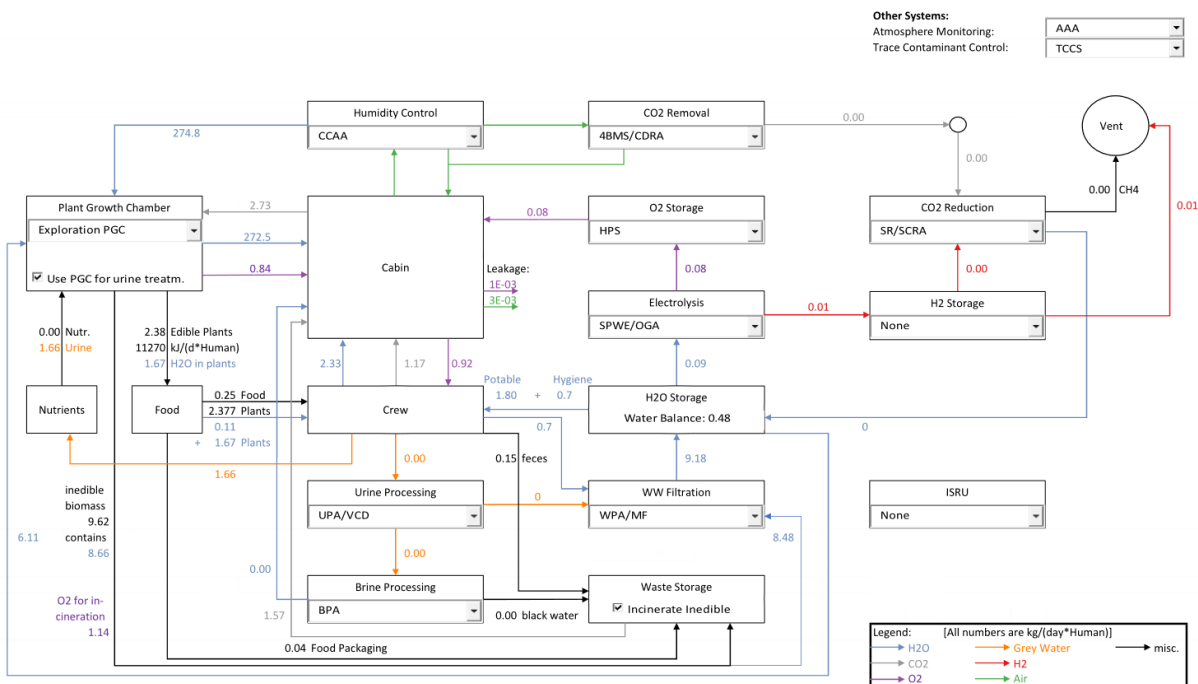


Figure 5.1-10 Exploration PGC with urine treatment composition analysis.

Notably, the high water content of the fresh biomass reduces the potable water demand of the crew compared to Figure 5.1-6 and the PC systems for CO₂ removal and reduction are no longer required. The O₂ generation operates at a much lower flowrate and is still required to achieve O₂ balance in the system. On the other hand, the waste-water filtration system receives an additional input of 8.66 kg/d from the inedible biomass but no longer has to process the 1.36 kg/d from the UPA, as all urine processing is assumed to be handled by the PGC in this case. The overall water balance is therefore slightly positive, with about 0.48 kg/d of water as surplus.

In the next chapter the break-even points between the different compositions are discussed.

5.1.2.5 Trade-Off Results

The results of the trade-off analysis for the different ECLSS compositions are summarized in Figure 5.1-11.

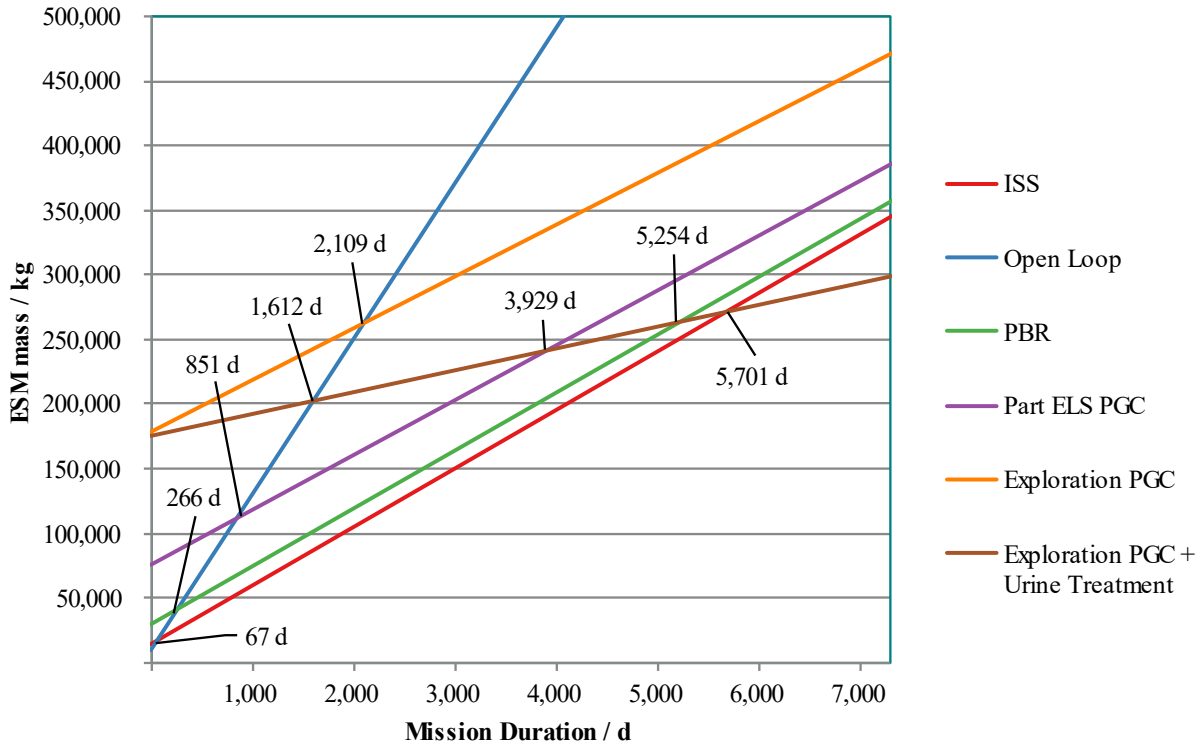


Figure 5.1-11 ESM results over time for the different ECLSS compositions including the break-even times.

To better interpret these results, Table 5.1-11 shows the individual resupply masses of the subsystems.

Table 5.1-11: Resupply masses of the different ECLSS options.

Resupply Mass	Unit	ISS ECLSS	Open Loop	Bosch	PBR	Part ELS PGC	Exploration PGC	Exploration PGC + Urine Treatment
Clothes/misc.	kg/d	2.06	2.06	2.06	2.06	2.06	2.06	2.06
H ₂ O	kg/d		27.74					
Food	kg/d	11.64	11.64	11.64	11.64	7.40	1.72	1.72
CO ₂ removal	kg/d	0.41	0.41	0.41	0.41			
CO ₂ reduction	kg/d	0.12						
Water filtration	kg/d	0.88	0.36	0.88	0.88	0.99	2.02	1.76
Urine Processing	kg/d	1.07	0.71	1.07	1.07	1.07	1.07	
Brine Processing	kg/d	1.69	1.12	1.69	1.69	1.69	1.69	
Electrolysis	kg/d	0.39	0.39	0.39	0.03	0.03	0.03	0.03
PGC	kg/d					3.60	8.32	1.06
∑ Resupply	kg/d	18.25	44.43	18.14	17.78	16.84	16.92	6.64
∑ Resupply ESM	kg/d	45.27	120.33	45.15	44.80	42.45	40.06	16.88

For the Bosch reactor and the PBR no information on required spare parts was available and therefore the CO₂ reduction resupply for these alternatives is zero. This is in fact the only advantage the Bosch reactor provides compared to the ISS ECLSS as the ISS ECLSS already achieves a water surplus as Figure 5.1-6 shows. Therefore, the Bosch is not included in Figure 5.1-11, as the plot for it almost coincides with the ISS ECLSS. The PBR directly produces O₂ and therefore allows a downsizing of OGA, which is a realistic advantage of this system. Neglecting required spare parts of the PBR favors this option, but on the other hand algae are not considered as food in this analysis, which is a



disadvantage for it. Overall, the PBR has a very long break-even time of 31,904 days when compared to the ISS ECLSS, which is not favorable. The PGC systems without urine treatment through the plants also result in very long breakeven times (21,692 days for the Part ELS PGC and 31,522 days for the Exploration PGC), because of the required nutrient solution resupply shown in Figure 5.1-9. As Table 5.1-11 shows the required resupply for these PGCs is almost as high as the required food resupply. A break-even within the considered 20-year period is only possible if the PGC also handles urine treatment and receives the required nutrients from urine. These results allow two major conclusions. The first conclusion is that a PGC is a feasible alternative to PC ECLSS within the considered 20-year period. The second conclusion is that PGC can only be considered favorable if the urine treatment is no longer performed using PC systems as the nutrient resupply for the PGC would become too expensive.

Figure 5.1-12 shows the subsystem ESM distribution for the different options. The open-loop system is dominated by resupply masses for food and water, as nothing within the system is recycled. For the ISS ECLSS, regardless if the Bosch or PBR option are used, food is the highest total mass for the 20-year time frame.

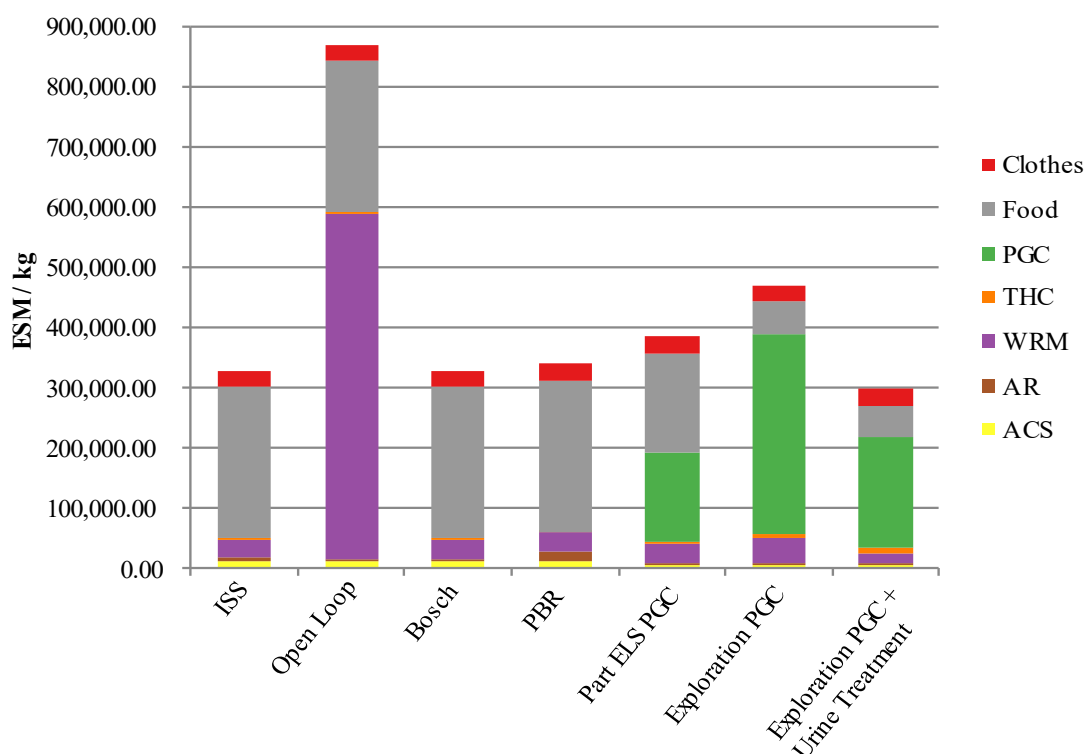


Figure 5.1-12 ECLSS subsystem ESM allocation for the different considered options excluding spares.

5.1.2.6 Sensitivity Analysis

As discussed in chapter 2.2.2 the performance values of algae reactor are susceptible to the underlying assumption of the required algae volume to support a human. The most optimistic values are from (Ruck et al. 2019). However, even with the optimistic values the algae reactor has a break-even time with the ISS ECLSS of 20,331 days. While this is significantly better than the non-optimistic 31,904 days it still shows that a PBR as pure air revitalization option is not favorable even under optimistic assumptions.

For the Exploration PGC the nutrient solution accounts for 7.26 kg of resupply mass while spares for the lamps account for the remaining 1.06 kg/d. If the optimistic logistics value of 0.13 kg/(y m²) is used the resupply for spares can be reduced to 0.108 kg/d. However, the more significant portion of resupply are nutrients. Therefore, significant improvement in break-even time is only possible if the plants also take over urine processing as shown in Figure 5.1-11.



5.1.3 Summary

The Life Support Trade Off Tool (LiSTOT) was reworked to become more flexible with regard to the selectable crew schedules and ECLSS compositions. In addition, the user interface was simplified. Plant growth chambers (PGC) and their averaged daily flowrates now interact with the remaining ECLSS, allowing compositions analysis that calculate the impact of PGC on other ECLSS. Thus, enabling a whole system ESM analysis for PC, hybrid and bioregenerative ECLSS. Through such an analysis the earliest break-even time for a PGC was calculated to 5,701 days or 15.6 years compared to an ISS ECLSS but only if the plants also handle urine treatment instead of the PC systems. If the plants are only used for air revitalization and food production, they require more than 31,900 days to outperform the ISS ECLSS, which corresponds to more than 87 years. This option is therefore not considered a realistic alternative.

For plant system the following conclusion is drawn for the remainder of this thesis:

A plant growth system must also provide urine processing capabilities, either directly or through a simple and cheap additional pretreatment, to be a viable alternative to physical/chemical systems.

In (Zolotukhin et al. 2005b) using urine and human feces to supply plant nutrition is discussed. This requires periodic desalination of the plant nutrient solution. A similar conclusion is drawn in (Zabel et al. 2019) when using CROP solution, a biological pretreatment option for urine that was discussed in chapter 2.2.3. As discussed in chapter 3.3.2 a detailed model for CROP as pretreatment is already available, and the alternatives from chapter 2.2.3 do not provide pretreatment for a plant nutrient solution but produce potable water. Therefore the CROP system will be studied as pretreatment option for urine to supply plant nutrients in this thesis.

5.2 Virtual Habitat

Virtual Habitat or short V-HAB was initially developed by (Czupalla 2011) in MATLAB®. The original code was a mixture of different coding styles and Simulink® as well as MATLAB® code, which is the reason why it was completely reworked into an object oriented MATLAB® framework by (Olthoff 2017) with support from another PhD student Jonas Schnaitmann. An overview of the development status is provided in (Pütz et al. 2019). This chapter will also cover the status discussed in the paper but in more depth and including more recent additions and changes to V-HAB. The following cited content from (Pütz et al. 2019) was primarily the contribution of the author of this dissertation Daniel Kaschubek (né Pütz) to the paper.

5.2.1 Basic Structure

V-HAB is designed to be a modular framework that can be adapted to any type of ECLSS simulation. To model a new ECLSS the user only requires knowledge of the ECLSS-Model part of the pyramid shown in Figure 5.2-1. This limits the complexity and increases the usability of V-HAB. This level is also covered by a user interface, which is discussed in more detail in chapter 5.2.6. If a new subsystem model shall be developed, more understanding of V-HAB is required. This approach is intended to enable the usage of V-HAB without requiring detailed understanding of all layers.

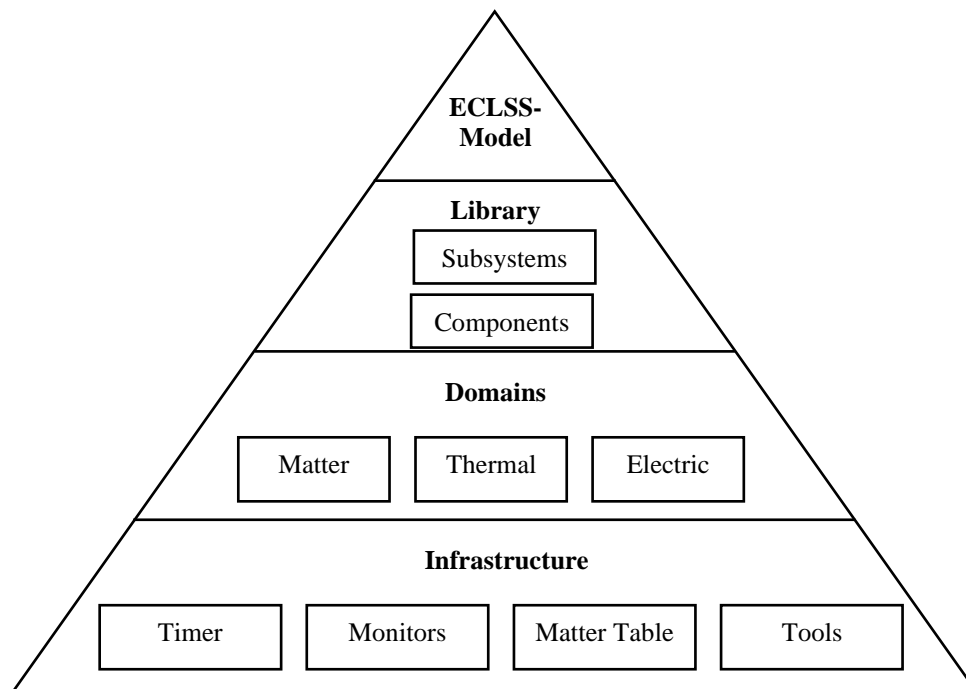


Figure 5.2-1 Basic structure of V-HAB (Pütz et al. 2019).

“The pyramid symbolizes that each of the upper layers builds upon the layers below and has according dependencies. The lowest level is the infrastructure, which provides the basic framework for any simulation in V-HAB. It includes the general definitions of a V-HAB simulation and provides an object-oriented structure as a foundation for the other levels. The domains contain the required classes and calculations for the corresponding physical domain. For example, the matter domain includes classes to model a gas phase with a specific pressure and mass, as well as classes to change this mass in a defined manner. Additionally, it includes the solver necessary to calculate the corresponding mass changes. The same is true for the thermal and electric domain, but they model thermal energy and heat flows or charge and current accordingly. There are certain dependencies between the different domains. For example, the matter domain provides the information of the current mass, which the thermal domain uses to calculate the total heat capacity. However, these interfaces are kept to a minimum to simplify the debugging of a simulation. At the same time the basic structure of the three domains shares commonalities. Each of the domains consists of stores (mass, thermal energy, charge) and flows (mass flows, heat flows, current) and this commonality is exploited to define an abstracted common layer between the three domains. This reduces the necessary code to implement the different domains and increases the

maintainability as changes to the basic framework have to be performed only once and are inherited by the three domains.

The infrastructure together with the domains provide the framework necessary to model (but not calculate) any physical process. The difference between model and calculation is that these two layers only provide a framework and basic calculations for the flow rates between the stores. They do not include more specific calculations, such as the adsorption of CO₂ into a zeolite. These specific models are included in the library, which contains pre-defined models of specific components, processes or entire subsystems. The final layer is the actual ECLSS model as defined by the user. The ECLSS model uses an arbitrary combination of library models or newly defined specific models to simulate the ECLSS dynamically in the required level of detail. The following subchapters will discuss the individual parts in more detail.

The modeling approach chosen for V-HAB is a bottom-up approach as shown in Figure 5.2-2. When creating new models for ECLSS components and technologies, modelers are instructed to begin with models based on first principles as much as possible. These basic models can then be merged into models that represent the technology or component, which in turn can be incorporated into full system models. The resulting models are of very high fidelity and accordingly the speed with which they can be simulated is very slow. Depending on the needs for an individual study, the results from these high-fidelity models can be used to generate simpler mathematical models. Although these are only accurate for a certain set of input parameters, they enable considerably shorter execution times, and thus long duration simulations of habitat life support systems or simulations for rapid design space exploration. If the study's requirements allow or mandate it, the models can even be abstracted to a point where most of the dynamic interactions are replaced by static or linear interdependencies to maximize simulation speed. This is achieved, for example, by creating look up tables for the system behavior which are then used in very simple but fast models.

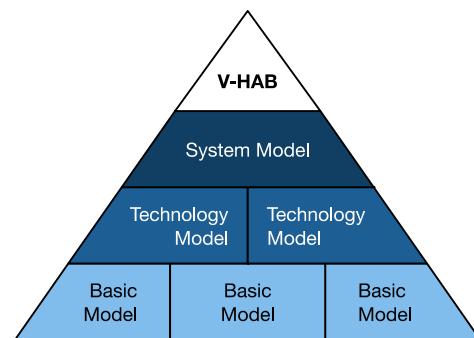


Figure 5.2-2 V-HAB modelling philosophy.

Whenever a model or its results are presented, a reader or listener will usually ask “Does the model include X?” This implies that the inclusion of X has an impact on the results. This kind of question drives modelers to create ever more complex and inclusive models, like the ones made possible by V-HAB. It has been argued, for example by (Jones 2009), that this holistic approach sacrifices clarity and understanding in order to gain completeness and plausibility. Jones also maintains that (system) models can never display emergent properties and behavior if these have not been explicitly included into the models. This argument, however, is made with the assumption that the chosen modeling approach is top-down. As was shown by (Czupalla 2011) this is not necessarily the case when modeling from bottom up. Jones is correct in that V-HAB is a complex system that can be difficult to fully understand, but it is this complexity that enables simulation behaviors to be observed that were not explicitly modeled and are unexpected. Of course, not all emergent behavior which such a system would show in a real-world test is represented by the model. But through coupling of several non-linear calculations into individual subsystem models and then coupling these subsystem models into one overall ECLSS model, the interactions become complex as well. For example, the humidity in the spacecraft cabin is controlled with condensing heat exchangers, but the impacts on humidity in a spacecraft cabin come from the crew and their state (e.g. exercise leading to increased water vapor production from the crew). Furthermore, the CO₂ removal system often impacts the humidity, either because it dehumidifies the air prior to CO₂ adsorption, and re-humidifies it after adsorption (as is done in CDRA (Coker et al. 2015)) or because it releases humidity during the desorption process (as is done for example in ACLS (Bockstahler et al. 2015)). If plants are present in the system as well, they transpire water based on the current environmental conditions and lighting conditions etc. Additionally, other systems like intra-modular-ventilation, which decide how the air is distributed through the system also impact the humidity in the individual spacecraft cabins. Overall, this means that the individual impacts on the humidity must be modeled into the subsystems, but the overall behavior of the parameter in the spacecraft is a combination of these non-linear subsystem simulations and can therefore show unexpected behavior, even though this behavior is not specifically modelled on the supra-system scale. For example, in a V-HAB analysis regarding plant chambers on a cis-lunar space station the result of an analysis with V-HAB was that it is more efficient to use open loop plant chambers without internal humidity

removal up to a certain size of the plant growth chamber compared to crew size and instead perform humidity removal only in the cabin (Pütz et al. 2018). In another example of a full scale bioregenerative ECLSS where one generation of plants was assumed to die the oxygen levels initially rose after the death of the plants because the algae system received more CO₂ and could overcompensate the missing oxygen.

Of course, models can be wrong and shown behavior by a model might not be the actual behavior of the real system. The model can therefore not replace the engineers and scientist who evaluate them and shown off-nominal or unexpected behavior should always be analyzed to see if it is the result of modelling errors or an actual effect.” (Pütz et al. 2019)

In order to minimize the possibility of errors within V-HAB a combination of test cases is defined which can be executed and compared to previous results to identify unintended changes and errors.

5.2.2 Infrastructure

5.2.2.1 Timer

“One of the primary parts of the infrastructure is the timer, which controls the execution of the simulation and handles the time progression of the simulation. Different from the previously overall fixed time step of 60 seconds used in V-HAB 1.0 the new release allows different time steps for every component in the simulation. This is achieved by calculating individual time steps based on stability conditions or user inputs in each component of the simulation. The individual time steps are recalculated in each simulation step based on the current conditions. This makes the model slow but accurate while relevant changes are occurring but allows high time steps and fast calculations during periods of near steady state system behavior.

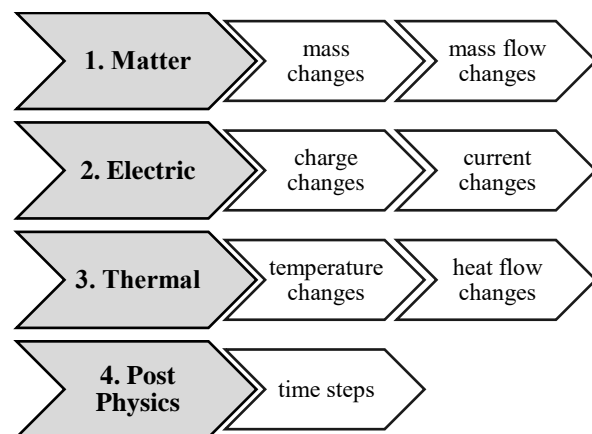


Figure 5.2-3 Overview of execution order in V-HAB.

The timer controls the execution of the individual components and decides what must be calculated at the current time. However, it is also necessary to ensure a controlled execution order between different parts of the V-HAB simulation while allowing this dynamic time step. Therefore, the execution of one time-step in V-HAB was separated into two parts. During the first part all values that need to be re-calculated are collected and in the second part the actual calculations are performed in a fixed execution order. Figure 5.2-3 shows the current execution order within V-HAB. It is important to note here that matter is executed before the other domains, because the electric and thermal domain calculate some of their properties (like the total heat capacity) based on the current masses. By executing the matter domain first, the correct masses for the calculations are used.

5.2.2.2 Monitors

The monitors include additional observers for a simulation. There are three basic monitors which are used in every simulation: the matter observer, the logger and the execution control. The matter observer continually checks the simulation for any errors regarding the conservation of mass. For this purpose, the total mass inside of the simulation is summed up at the beginning of the simulation and then compared with the total mass currently inside the simulation. By subtracting these two values a mass balance for simulation can be calculated.

The amount of possible data points inside of a larger simulation model exceeds the levels that are easy to handle. Therefore, the user must select the data points that are of interest and add them to the second basic monitor, the logger. Only values, which are added to the logger, are stored for every time step of the simulation, thus reducing the amount of data that is stored in the model. For large models the logger can write these log files to the hard drive in order to free up space in the random-access-memory.



The execution control monitor enables pausing and restarting of a simulation during the execution. It also enables restarting a simulation that was previously saved to the hard drive.

Additional optional monitors are primarily used for debugging. For example, a monitor to identify the component with the smallest time step within a simulation can be used to find “bottlenecks” regarding simulation speed. Another observer tracks mass balance issues and identifies the location at which the mass balance was violated.

5.2.2.3 Matter Table

A common issue in dynamic physical calculations is the calculation of matter properties such as the specific heat capacity, thermal conductivity or density of substances. For V-HAB a variable and expandable look-up table was created containing matter data from any source and formatted as comma separated values. Currently the matter data used in V-HAB is from (Linstrom 1997). The stored data is loaded into V-HAB and converted to matrices, which are stored inside of the matter table class. When for a specific substance at a specific condition a matter property is requested from the matter table a linear interpolation between the datapoints is performed. This interpolation is stored inside the matter table at the first access and preserved over multiple simulations increasing the access speed of the look-up table significantly.

If a user wants to model matter in V-HAB there are therefore two different options to achieve this. The most common approach is to use existing substances to model a new substance. For example, air is modelled as a combination of nitrogen, oxygen, carbon dioxide, water and any other trace gases the user wants to model. However, often new substances, which are not mixtures of existing ones, are used in new ECLSS technologies. For these, the user can simply add the matter properties to the look up table, either as static reference with one value per substance, or with multiple data points to allow dynamic temperature and pressure dependent calculations.

5.2.2.4 Tools

V-HAB considers an entity as a tool if it is an independent program that does not rely on the rest of the class architecture to function. Most tools are helper functions that ease implementation of programming tasks. However, two larger tools will be discussed in the following, because they are an integral part of the overall usability of V-HAB. The post processing tool is used to create well formatted figures from the data generated by a simulation. MATLAB[®] already includes many functions for this purpose. However, the usability of V-HAB would be fairly low if it only provided a matrix of the log values as outputs. For this reason, the post processing tool was introduced. It enables the user to define values that should be plotted together and automatically creates the corresponding legend and axis titles necessary to create a meaningful plot. A functionality to save the created plots in a user specified size and format allows easier export of the figures into written publications. Otherwise, the size of saved plots often depends on the current size of the window on the screen, which would be cumbersome to use and yield inconsistent image sizes.

Another important tool is the import script to convert xml files created by draw.io into executable V-HAB simulations. More details on this feature will be discussed in the separate chapter 5.2.6.” (Pütz et al. 2019)

5.2.3 Domains

“As the basic structure of the domains is identical, we first discuss the common structure and then more in-depth the individual domains. As previously mentioned, a commonality between the three domains is that there are stores, which contain the corresponding mass or energy, and flows between these stores. The basic principles of mass and energy conservation must be enforced in all cases during the simulation. However, energy cannot be stored without a corresponding mass to store the energy. For example, thermal energy cannot be stored without heat capacity or phase change enthalpy, and both require a mass. The same is true for electricity as batteries and other energy storage options all have an associated mass. Therefore, V-HAB implements a store on the matter side of the calculation and the thermal and electrical “stores” are connected to a corresponding matter domain element. For the flow part of the calculation this is not always true. For example, radiative thermal energy transfer is massless. On the other hand, if mass flows from one store to another it always transports a certain thermal energy. Therefore, other domains do not always require flows. Only where necessary a corresponding thermal pendant for the matter domain flow is automatically created.

5.2.3.1 Matter

The basic components to store matter are called *stores*, which are containers that seal matter inside. Inside of a *store* different *phases* can be present. Currently V-HAB includes a gas, liquid, solid and mixture *phase* type. The mixture type is used for example to model the adsorption of CO₂ (gas) into a zeolite (solid). Each of the phase types additionally has three subclasses, a *boundary phase*, a *flow phase*, and a normal *phase*. The *boundary phase* assumes an infinitely large volume and mass that does not change, no matter how much mass is taken from or added to it. However, the user can set the properties of the phase to mimic measured data from hardware tests if necessary. The mass balance for *boundary phases* is checked by logging how much mass was taken from it or added to it and including it in the analysis as a valid mass source/sink. On the other hand, the *flow phase* is modeled as an infinitely small volume that does not contain a mass. This approach is useful to model small volumes inside specific systems, such as the gas phase inside of an absorber, say a LiOH canister. The normal *phase* is considered to have a finite volume and finite mass that can change during the simulation. This type of *phase* is usually used to model the cabin atmosphere for example.

Currently, there are two methods to move mass from one phase to another. The first one is called a *branch* and connects *phases* between different *stores*. A *branch* can only specify a flow rate and always removes mass according to the current composition of the source *phase*. Therefore, a *branch* basically represents piping. On the other hand, it is necessary to model e.g. the uptake of CO₂ into zeolite, where a specific substance is removed from a stream of air. This can be done by using a *phase to phase processor* (P2P). These *processors* can only be used inside of one store to connect different *phases* and can be used to model phase changes like condensation, adsorption or other substance specific processes.

In order to provide a general framework to model pressure losses inside of piping, an arbitrary number of *flow to flow processors* (F2F) can be added to each branch. The most basic of these F2Fs would be a pipe that calculates its pressure loss. For example, a simple model for a fan pumping air from one module of the ISS into another module would look like shown in Figure 5.2-4.

Furthermore, it is necessary to model chemical equations such as the Sabatier reaction. To represent this in V-HAB the *manipulator* component is used which allows the user to change one substance into another within one *phase*.

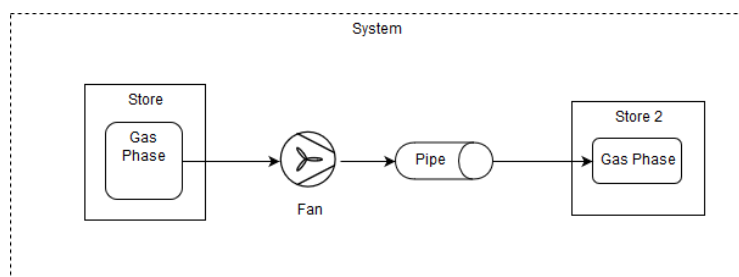


Figure 5.2-4 Basic V-HAB model. Branches are represented as arrows with the arrow indicating the positive flow direction of the branch.

In addition, a common problem within ECLSS modelling are changing compositions of matter types. For example, the water content of urine is not constant but variable. In order to correctly model this but still have the capability of discerning between different masses. E.g. if different edible plants are modelled, V-HAB must be able to discern the water content of each plant individually even if they are stored together. For this purpose compound masses were created in V-HAB. They allow the user to define a new matter type as a combination of any of the available base substances, like for example urine as a combination of water, urea and sodium chloride. This information is stored within V-HAB as a quadratic matrix where each row contains the composition of the compound mass corresponding to this row. By changing the entries within the matrix, the composition of the compound mass can be varied. This allows the model to discern between different compound masses while varying their composition.

5.2.3.2 Thermal

In order to increase code maintainability and reduce bugs some of the structure between the thermal and the mass domain is identical and based on the same base classes. A *phase* from the matter domain is associated with a *capacity* that models the thermal energy storage of the corresponding *phase* mass. To transfer thermal energy from one *capacity* to another, *thermal branches* are used, which represents the energy transfer based on mass transfer or radiation, conduction and convection through the use of *conductors*. *Conductors* have the same role as F2Fs in the mass domain and it is possible to place an arbitrary number of them into a *thermal branch*. To reduce the necessary definitions for a

model, every *mass branch* automatically generates a corresponding *thermal branch* calculating the thermal energy transfer.

Additionally, it is necessary to model sources and sinks within a capacity. This is achieved through a component called *heat source*, which can have positive and negative heat flow rates and can therefore act as a source or a sink despite the name.

5.2.3.3 Electric

The electrical domain is again structured similarly to the other two domains. There is an *electrical store* that can be used to model anything that contains electrical energy, e.g. batteries or capacitors. Voltage and current sources are also modeled as stores and similarly to the *boundary phases* in the matter domain, their properties can be set to be constant. To transfer electricity from one *store* to another there are *electrical branches* that include *electrical flows* and *electrical components*. The latter are equivalent to the F2F *processors* in the matter domain and are used to model parts like resistors, inductors, and switches. Similar to *flow phases* in the matter domain, there are *electrical nodes* that do not contain electrical energy, but rather represent nodes in an electrical diagram.“ (Pütz et al. 2019)

5.2.4 Solvers

“The *branches* in the domains are used as a basic framework for the transfers, while the actual calculation of that transfer is performed by solvers, which can be selected for each *branch* individually, allowing a wide range of utility.

5.2.4.1 Matter Solvers

Currently four basic solver types exist in the matter domain. The simplest solver is a manual solver where the user can specify the flow rate either directly as a mass flow rate, a volumetric flowrate, or a mass transfer over time. Additionally, a residual solver can be used which ensures that the mass change of a normal *phase* remains zero over the course of the simulation. These two solvers are not based on physical calculations, instead they rely on known values for flow rates. The actual physics-based solvers use the pressure differences calculated by the F2Fs to ensure a force balance between the momentary pressure differential across the *branch* and the pressure differences from the F2Fs. This amounts to a momentary steady state assumption. However, in the next time step the pressures of the connected *phases* will have changed resulting in different conditions for which a new steady state solution can be found thus resulting in a dynamic calculation. We also used solvers that do not use this assumption and calculate the acceleration of fluid in a *branch*. However, compared to the increase of information that was gained, the increased calculation time was excessive. In addition to this steady state assumption, V-HAB assumes that fluids are incompressible because *branches* do not store mass and therefore cannot represent a change in mass inside the branches. Therefore, the mass that enters the *branch* on one end must emerge instantly at the other end.

Based on these assumptions, two solvers can be used to calculate flow rates, the interval solver and a network solver. The interval solver uses a nested interval approach to solve a single *branch*, while the network solver can be allocated multiple *branches* and it will calculate all of them at once by creating and solving a linear system of equations. Since the delta pressure from the F2Fs depends on the mass flow rate passing through them, both solvers require iterations. The following figures show an example system (Figure 5.2-5) and the resulting linear system of equations for the network solver (Equation (5.2-1)).

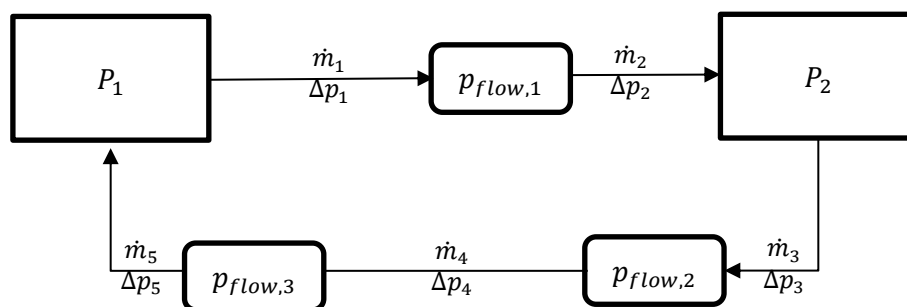


Figure 5.2-5 Example system for the matter network solver.



Lower case p represents flow phase pressures, which are calculated by the solver, while a capital P represents the pressure in normal *phases* or *boundary phases*, which at a given time step are assumed not to change in value and hence act as boundary conditions in the solver. The vector holding the variables the solver is looking for therefore consists of the mass flows (\dot{m}_i) and the *flow phase* pressures ($p_{flow,i}$). The matrix of the linear system of equations consists of two distinct sets of equations, the pressure equations where the pressure differential across the *branches* must be equal to the pressure difference between the two *phases* on either side of the *branch* (grey background) and the mass balance of *flow phases* (blue background):

$$\begin{pmatrix} -1 & -\Delta p_1 & 0 & 0 & 0 & 0 & 0 & 0 \\ 1 & 0 & -\Delta p_2 & 0 & 0 & 0 & 0 & 0 \\ 0 & 0 & 0 & -1 & -\Delta p_3 & 0 & 0 & 0 \\ 0 & 0 & 0 & 1 & 0 & -1 & -\Delta p_4 & 0 \\ 0 & 0 & 0 & 0 & 0 & 1 & 0 & -\Delta p_5 \\ 0 & 1 & -1 & 0 & 0 & 0 & 0 & 0 \\ 0 & 0 & 0 & 0 & 1 & 0 & -1 & 0 \\ 0 & 0 & 0 & 0 & 0 & 0 & 1 & -1 \end{pmatrix} \cdot \begin{pmatrix} p_{flow,1} \\ \dot{m}_1 \\ \dot{m}_2 \\ p_{flow,2} \\ \dot{m}_3 \\ p_{flow,3} \\ \dot{m}_4 \\ \dot{m}_5 \end{pmatrix} = \begin{pmatrix} -P_1 \\ P_2 \\ -P_2 \\ 0 \\ P_1 \\ 0 \\ 0 \\ 0 \end{pmatrix} \quad (5.2-1)$$

The boundary conditions in this example only consists of the non-*flow phase* pressures (P_i) but can in general also include other *branches* not solved by the network as boundary conditions for the mass balance.

The solvers were verified by comparing them to calculations from ANSYS in (Busch 2019) for a pipe with a specified pressure difference. A comparison of V-HAB and ANSYS for different cases is shown in Figure 5.2-6 to Figure 5.2-9. In general, the results for smaller diameters fit the ANSYS calculation quite well. For larger diameters the difference increases because there the incompressible assumption of the solvers no longer hold true as the flow speed reaches fairly high values. However, these flow regions should not be reached in ECLSS simulations.

Table 5.2-1 Percentage errors in the comparison of V-HAB and ANSYS from (Busch 2019).

	Smooth	0.001	0.01	0.1	1	Mean
5	2.2%	2.0%	5.2%	2.6%	58.4%	14.1 %
10	29.5%	26.6%	22.6%	9.4%	24.0%	22.4 %
50	66.2%	64.9%	59.9%	51.7%	36.1%	55.8 %
100	77.0%	75.1%	71.3%	64.8%	53.8%	68.4 %
Mean	42.1%	39.8%	32.1%	43.1%	43.7%	40.2 %

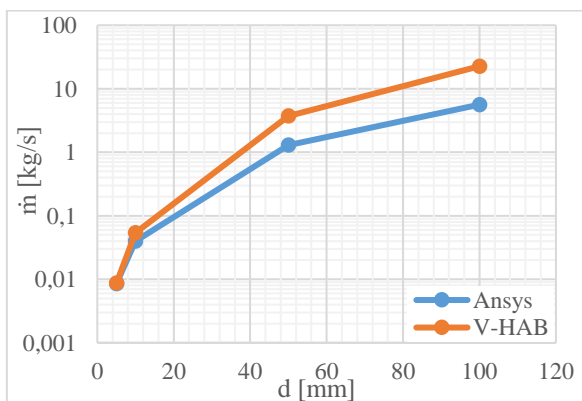


Figure 5.2-6: Mass flow for a roughness of 0.001 mm ($\Delta p = 1$ bar) (Busch 2019).

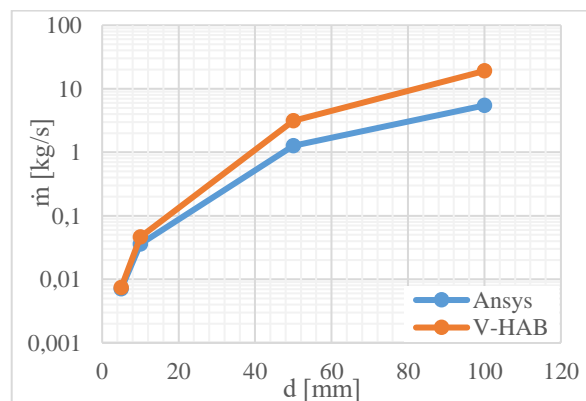


Figure 5.2-7: Mass flow for a roughness of 0.01 mm ($\Delta p = 1$ bar) (Busch 2019).

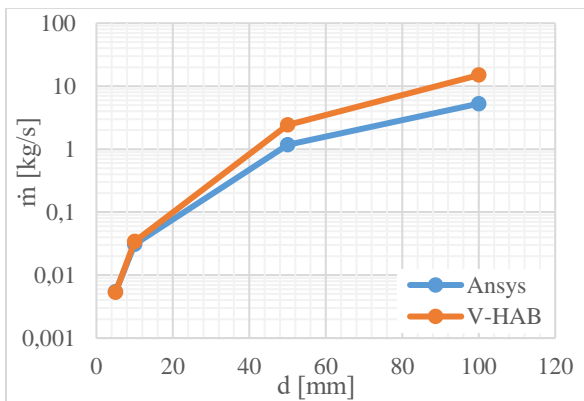


Figure 5.2-8: Mass flow for a roughness of 0.1 mm ($\Delta p = 1$ bar) (Busch 2019).

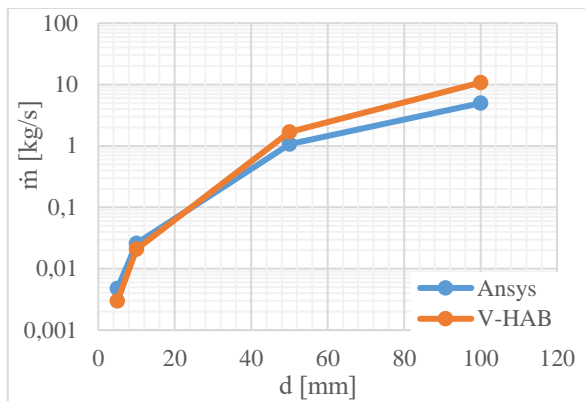


Figure 5.2-9: Mass flow for a roughness of 1 mm ($\Delta p = 1$ bar) (Busch 2019).

5.2.4.2 Thermal Solvers

The thermal solvers are based on the basic Peclet and Fourier Laws and calculate an overall thermal resistance for *thermal branches* with *conductors*. The calculations are based on chapter 3 from (Polifke and Kopitz 2009). For *thermal branches* that represent mass bound energy transfer the specific heat capacity, the mass flow rate from the *matter branch*, and the temperature difference of the *phases* is used to calculate the corresponding heat flow.” (Pütz et al. 2019)

Other solvers can be used for specific use cases, e.g. a dedicated infinite conduction solver that models a perfect thermal coupling of two phases was written to enable quick calculations for some specific use cases.

The thermal domain also uses a thermal network solver, which can solve multiple branches at the same time. Two different types of network solvers are implemented. The *basic* multibranch solver is the basis for other thermal multibranch solvers, which inherit from this base class. Figure 5.2-10 shows a simple example for the thermal domain, which is used to discuss the solvers.

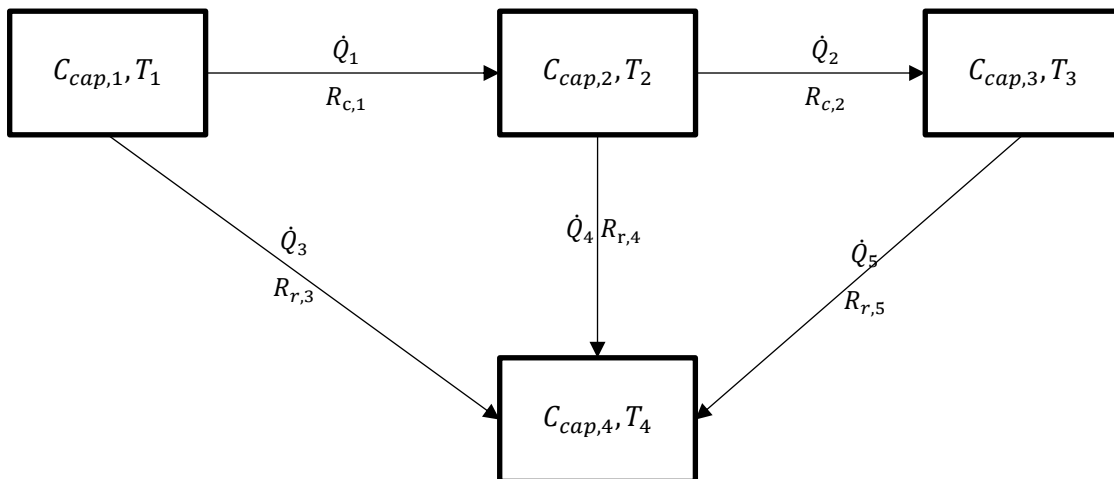


Figure 5.2-10 Example system for the thermal network solver.

$C_{cap,i}$ represents the capacity and T_i the temperature for each *capacity* i in the example. \dot{Q}_j represents the heat flows and $R_{x,j}$ the thermal resistance for each *thermal branch* j . The index x for the resistances indicates whether the resistance is radiative or conductive/convective. The differentiation is necessary because radiative heat transfer scales with T^4 .

The *basic* solver only calculates the heat flows between the phases based on the system of equations shown in equation (5.2-2) for the example provided in Figure 5.2-10.

$$\begin{pmatrix} \frac{1}{R_{c,1}} & -\frac{1}{R_{c,1}} & 0 & 0 \\ 0 & \frac{1}{R_{c,2}} & -\frac{1}{R_{c,2}} & 0 \\ \frac{1}{R_{r,3}} & 0 & 0 & -\frac{1}{R_{r,3}} \\ 0 & \frac{1}{R_{r,4}} & 0 & -\frac{1}{R_{r,4}} \\ 0 & 0 & \frac{1}{R_{r,5}} & -\frac{1}{R_{r,5}} \end{pmatrix} \cdot \begin{pmatrix} T_1 \\ T_2 \\ T_3 \\ T_4 \end{pmatrix} = \begin{pmatrix} \dot{Q}_1 \\ \dot{Q}_2 \\ \dot{Q}_3 \\ \dot{Q}_4 \\ \dot{Q}_5 \end{pmatrix} \quad (5.2-2)$$

In the *advanced* solver this functionality is combined with the MATLAB® *ode45* solver, which uses an explicit Runge-Kutta (4,5) formula. The *ode45* is used to calculate the temperature change from the heat flows and internally recalculates the heat flows to provide more stable solutions. This requires the solver to set the *capacity* temperatures directly and therefore made a new type of *capacity*, the *network capacity* necessary. In other cases, V-HAB does not allow the setting of temperatures directly as a temperature change is only possible through a corresponding heat flow.

5.2.5 Generalized pH-Model

“In biological systems the pH value is often crucial. Therefore, a pH calculation module was added to V-HAB in (Ruck 2018) and generalized afterwards. It calculates the pH assuming ideal dilute solutions (neglecting activities). In the following, this module is described for the calculation of a phosphate buffer, which is neutralized with NaOH. The basis for the calculation is the dissociation constants of the individual reactions and of water (K_i). They describe the relation between the different substances with the following equation.

$$K_{H_3PO_4} = \frac{c_{H_2PO_4^-} \cdot c_{H^+}}{c_{H_3PO_4}} \quad (5.2-3)$$

Using these equations for every involved substance and adding a molar balance for the PO_4 group, as well as a mass balance over all involved substances and a charge balance, results in the following non-linear system of equations. Since NaOH is considered to be a strong base, we assume that it completely dissociates into Na^+ and OH^- :

$$\begin{pmatrix} K_{H_3PO_4} & -c_{H^+} & 0 & 0 & 0 & 0 & 0 \\ 0 & K_{H_2PO_4^-} & -c_{H^+} & 0 & 0 & 0 & 0 \\ 0 & 0 & K_{HPO_4^{2-}} & -c_{H^+} & 0 & 0 & 0 \\ 1 & 1 & 1 & 1 & 0 & 0 & 0 \\ 0 & 0 & 0 & 0 & 0 & c_{H^+} & 0 \\ M_{H_3PO_4} & M_{H_2PO_4^-} & M_{HPO_4^{2-}} & M_{PO_4^{3-}} & M_{H_2O} & M_{OH^-} & M_{H^+} \\ 0 & -1 & -2 & -3 & 0 & -1 & +1 \end{pmatrix} \cdot \begin{pmatrix} c_{H_3PO_4} \\ c_{H_2PO_4^-} \\ c_{HPO_4^{2-}} \\ c_{PO_4^{3-}} \\ c_{H_2O} \\ c_{OH^-} \\ c_{H^+} \end{pmatrix} = \begin{pmatrix} 0 \\ 0 \\ 0 \\ c_{initial PO_4} \\ K_{H_2O} \\ m_{ges}/V \\ -1 \cdot c_{Na^+} \end{pmatrix} \quad (5.2-4)$$

K_i : Dissociation constant for substance i

M_i : Molar mass for substance i

c_i : Concentration for substance i

$c_{initial PO_4}$: Sum of the initial concentrations of all substances that contain a PO_4 group

m_{ges} : Total initial mass of all substances

V: Volume of the liquid

As the system is non-linear, it must be solved iteratively. For this purpose, a nested interval approach is used to calculate the concentration of H^+ . While the system shown here only includes phosphoric acid and its dissociations, it is modelled such that more reactions are easy to add. The currently implemented pH calculation also includes carbonic acid and ethylene-diaminetetraacetic, which is relevant for algae growth media. The calculation was verified by comparing the

pH calculated by the V-HAB module with a titration curve found in (Binnewies et al. 2016), as is shown in Figure 5.2-11.” (Pütz et al. 2019)

The mean difference between the calculated values and the literature values is 10.4% and the overall behavior is well represented. The initial model from (Pütz et al. 2019) showed oscillation at high pH values because the concentration of H^+ became very small. This was resolved by using the concentration of OH^- for high pH values.

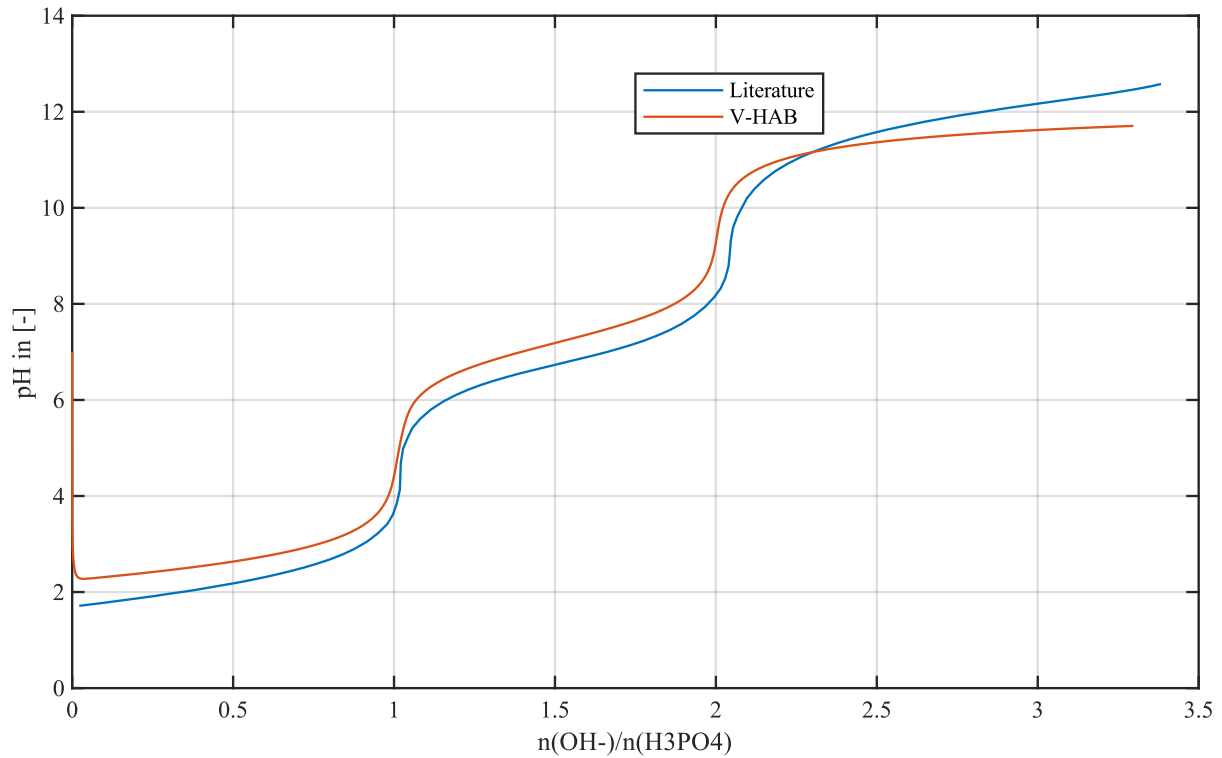


Figure 5.2-11 Comparison of V-HAB pH calculation for a titration curve of H_3PO_4 with $NaOH$.

5.2.6 User Interface

“An important aspect for the usability of a tool is the user interface and the ease of creating a new simulation using existing components. Previously, this was one of the main disadvantages of V-HAB, because simulations could only be created in text-based MATLAB programs. In the new release V-HAB enables the creation of simulations from xml files drawn into the open source program draw.io using a library of existing components. Because the existing drawing functionality of draw.io could be used, this approach did not require the programming of a completely new user interface. Only a converter for the generated xml file had to be created. Parameters for the different components can be added to the objects in draw.io and are imported as input parameters into the V-HAB system. Since this approach generates the required code to run the V-HAB system, any functionality not covered by the user interface can still be accessed in the code. Overall, the interface is intended to ease the creation of basic simulations and the initial contact with V-HAB, but the full functionality will always only be accessible with a text based coding approach. The current draw.io library consists of the components shown in Figure 5.2-12.

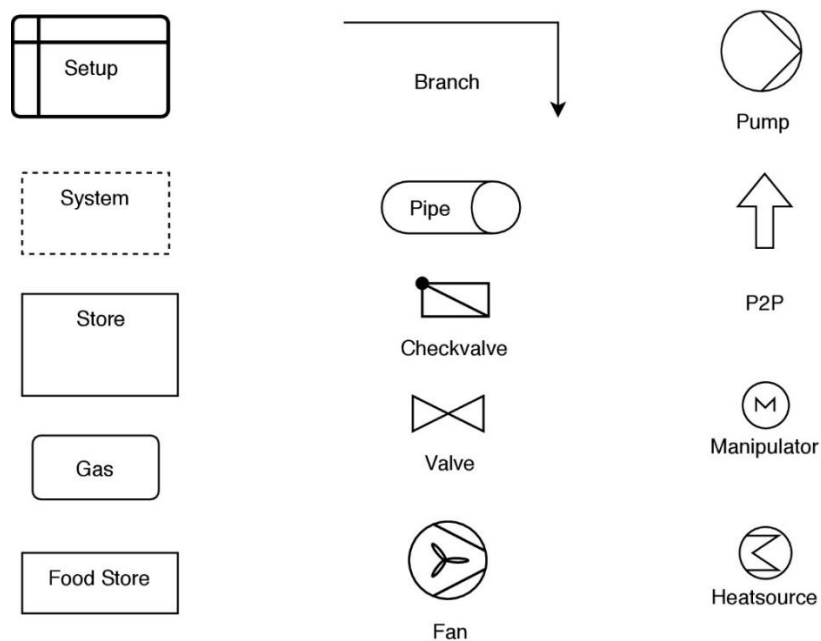


Figure 5.2-12 V-HAB draw.io library.

The setup block contains basic information, such as the supposed simulation time. That block is necessary to enable the execution of simulations without having to code anything. The created code from the xml is already executable.

In addition, the mentioned subsystems that are already defined in V-HAB are also added to the library. Overall, the simulation of a basic ECLSS system using the user interface could look like what is shown in Figure 5.2-13.” (Pütz et al. 2019)

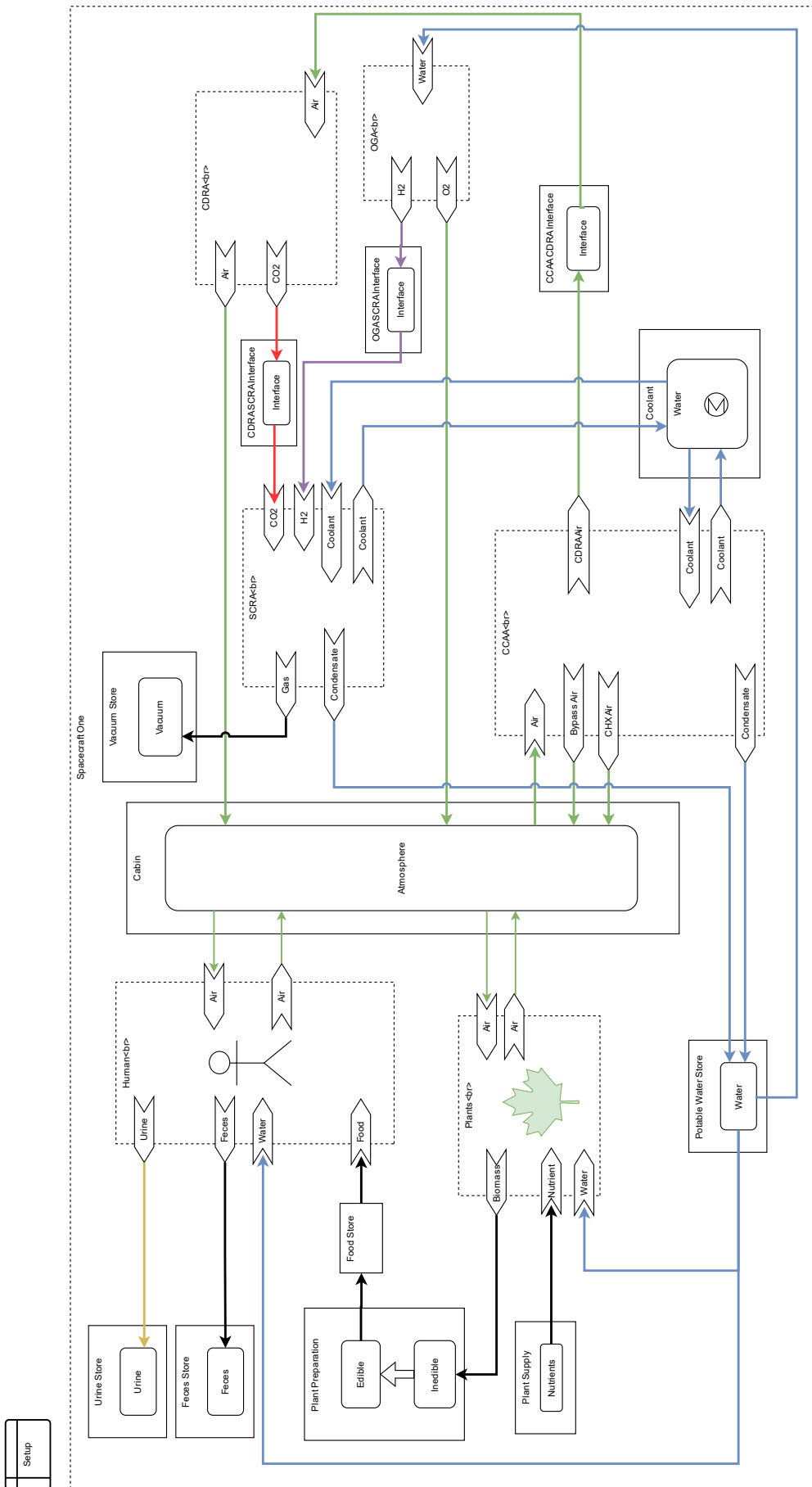


Figure 5.2-13 Example ECLSS model created with draw.io (Pütz et al. 2019).

5.3 Physical/Chemical Life Support Models

5.3.1 Selection of Subsystems

The decision which subsystems shall be modelled in more depth is based on the results of chapter 5.1.2, which showed that the ISS ECLSS is superior to e.g. a system where the Sabatier reactor is replaced with a Bosch reactor or a PBR. Furthermore, the ISS ECLSS is considered state of the art with regard to ECLSS and was therefore chosen as PC ECLSS that is modelled in depth in this thesis. In addition, for the Moon base the option of an In-Situ Resource Utilization (ISRU) reactor is considered based on (Kaschubek et al. 2021).

5.3.2 CDRA

5.3.2.1 Modelling Approach

The following description is largely from the publication of the author of this thesis (Pütz 2017) but was updated to include more recent changes to the model, which were left as future work in the publication.

The CDRA model “employs a modelling approach that is derived from the linear driving force (LDF) approach that better reflects the actual physical behavior. Previously the model used performance data that was curve fitted to CDRA test data. The linear driving force equation according to (Coker et al. 2014) can be written as

$$\frac{\delta q}{\delta t} = k_m \cdot (q^* - q(t)) \quad (5.3-1)$$

Using the factor k_m to describe the kinetics of the adsorption and desorption process which was obtained from (Coker et al. 2015) for this model. $q(t)$ is the loading of the absorber material in kg of CO₂ or water per kg of absorber material at the time t . q^* is the equilibrium loading which is defined as the loading that is reached after an infinite amount of time for the current temperature and partial pressure conditions. The equilibrium loading for competitive adsorption between water and CO₂ is calculated based on the Toth equation from (Coker et al. 2013) with values for the different adsorber material from (Coker et al. 2014). Using the assumption that the equilibrium loading q^* does not change during one time step the basic behavior of adsorption kinetics for time differences Δt approaching zero or infinite is:

$$\lim_{\Delta t \rightarrow 0} q(t + \Delta t) = q(t) \quad (5.3-2)$$

$$\lim_{\Delta t \rightarrow \infty} q(t + \Delta t) = q^* \quad (5.3-3)$$

In between these two extremes the linear driving force results in an exponential behavior of the adsorption flowrate. While the LDF equation (5.3-1) could be used directly to calculate the flowrate that is being absorbed by assuming $q(t)$ is constant for each time step this would limit the time step significantly since the LDF equation does not reflect the correct behavior for large timesteps as described by equations (5.3-2) and (5.3-3). Therefore, a slightly different calculation approach was chosen in this model to allow higher time steps and therefore higher simulation speeds. It uses the following analytical solution for equation (5.3-3) which will be called exponential approach from now on, to calculate the new loading after a time step of Δt :

$$q(t + \Delta t) = q^* - (q^* - q(t)) \cdot \exp(-k_m \cdot \Delta t) \quad (5.3-4)$$

The exponential approach is based on studies performed in (Portner 2013) and was adapted for the current CDRA model.” (Pütz 2017)

The value Δt can be used to describe the time step or alternative to describe the time the gas is in contact with the zeolite in the corresponding cell (also called empty bed contact time or EBCT). Since V-HAB uses a variable time step it is difficult to estimate the next execution time. For that reason, the EBCT is used for Δt . It can be calculated based on the current flow speed of the fluid and the length of the cell as described in equation (5.3-5).

$$t_{EBCT} = \frac{\epsilon \cdot V_{cell}}{\bar{V}} \quad (5.3-5)$$

Figure 5.3-1 shows “a comparison of a calculation with constant equilibrium loading for a LDF calculation using small time steps (blue line) and for the exponential approach using only 1/100th of the time steps (yellow line). The red line shows the calculation using LDF with the same time step as the exponential approach. As can be seen the exponential approach results in the same loading for each time step as the LDF calculation with a smaller step size. Only between the steps differences between the two calculation can be seen. On the other hand the linear driving force using the larger time steps oscillates and even exceeds the equilibrium loading resulting in an entirely different dynamic behavior.

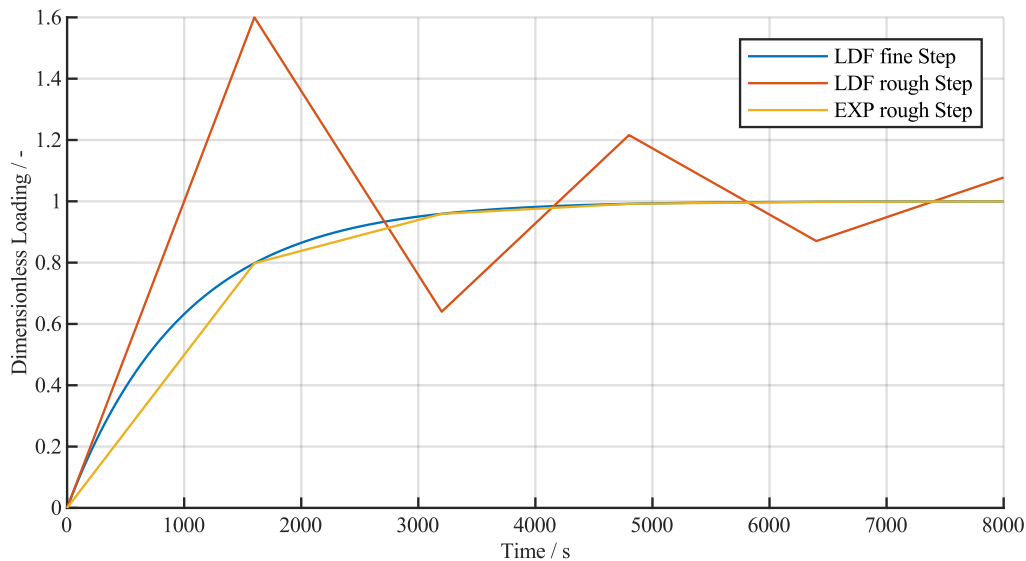


Figure 5.3-1: Comparison of LDF calculation at different step sizes with the exponential approach.

However, equations (5.3-2) and (5.3-3) only describe the limits of the adsorption process correctly if the properties of the gas phase, especially the partial pressure of the substances being absorbed, are assumed to be constant.” (Pütz 2017)

Therefore, the changes the adsorption process has on the resulting phase partial pressure must be included in the analysis. To limit the error from these effects the Toth equation, which is used to calculate the equilibrium loading q_i^* of the different substances i , from (Coker et al. 2013; Coker et al. 2014) shown in equation (5.3-7) is linearized to a parameter K .

$$q_i^* = \frac{a_i \cdot P_i}{(1 + (\sum_i b_i \cdot P_i)^{tr})^{\frac{1}{tr}}} = K \cdot P_i \quad (5.3-6)$$

This linearization is then used to estimate the partial pressure at which an equilibrium is achieved. An iterative calculation then calculates the adsorption and desorption flowrates while including the variance in both the partial pressure of the gas phase and the adsorbed masses in the solid phase. Through this iterative calculation no oscillations occur because the actual limits are maintained. The iterative calculation uses a simple nested interval scheme where the upper limit for the adsorption flowrates is estimated by ignoring all changes in gas and solid phase values and the lower value is assumed to be zero.

Additionally, a thermal model of CDRA was included that uses the basic lumped parameter thermal network solver discussed in chapter 5.2.4.2 to calculate the temperature exchange between the different nodes. The basic structure of the overall model is shown in Figure 5.3-2.

“In the model, each different absorber can be split into several cells creating a one-dimensional representation of CDRA. Each of the cells will consist of a solid phase and a gas phase with the solid phase containing the absorber material while the gas phase contains the air flowing through CDRA. The gas phases are connected with each other by air flows from one cell to the next while the solid and gas phase exchange matter based on the adsorption/desorption calculation

explained above. Additionally, heat flows are exchanged between the solid phases of each absorber material through conduction and heat is lost to the cabin air from the solid material. There is no heat flow between the solid phase and the gas phase because in the thermal model these two are combined into one thermal mass using the assumption that the thermal contact between the gas phase and the solid phase is ideal within each cell. This is a valid assumption because the absorber material has a very large surface area. The composition of the beds and the masses of the absorber material within each bed is based on the values provided in (Coker et al. 2015). One of the Zeolite 5A beds is connected to the vacuum during each cycle and desorbs CO₂. For this process electrical heating is used to increase the temperature using a maximum electrical power of 980 W (Coker et al. 2015). Once the cycle changes a selector valve switches the Zeolite 5A beds and the one that was desorbing is connected to the airflow cycle. The flow direction of the air flow through the Zeolite 13x and Sylobead beds is reversed. Since the temperature of the absorber material in the 5A bed is still at 204 °C (Coker et al. 2015) the air flow to the 13x and Sylobead downstream of the 5A bed will have a higher temperature which initiates the desorption of the humidity that these beds had adsorbed in the previous cycle. Additional each adsorption or desorption process is associated with a heat flow per mol of absorbed substance for which values are provided in (Coker et al. 2014) Table 1.” (Pütz 2017)

Heat sources in the solid phases represent the adsorption heat flow which is calculated after the flowrates are calculated.

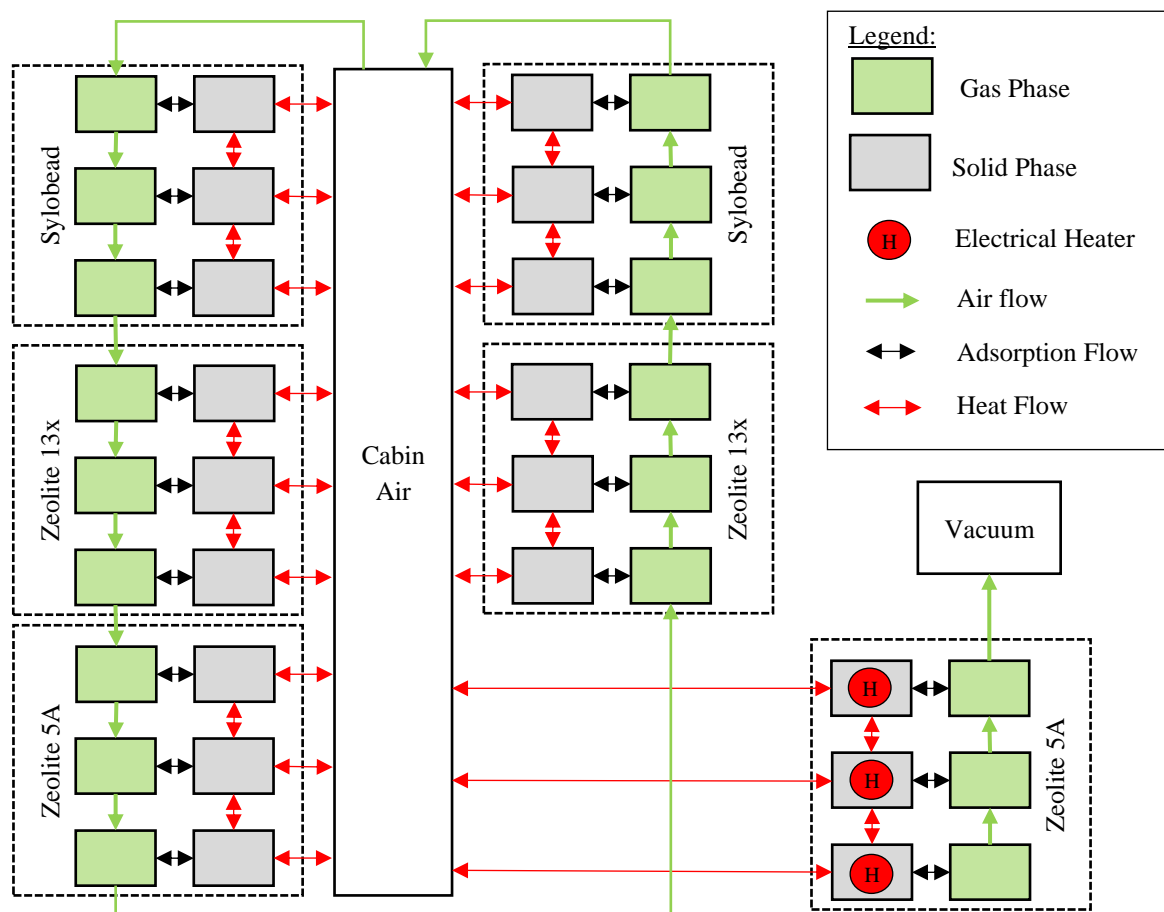


Figure 5.3-2 CDRA model structure.

5.3.2.2 Validation

In order to validate the developed model the test data from (Knox 2000) was digitized using the software from (Rohatgi 2020). Since the test data are provide in Torr, the simulation data were converted to Torr as well. The operating conditions described in (Knox 2000) are used in the simulation to match the test conditions as closely as possible. Figure 5.3-3 shows the resulting partial pressure of CO₂ for a model using ten cells per adsorbent bed. The initial flat CO₂ level in the test was due to an error in the hardware test. This period is included in the simulation to precondition the model. The actual validation therefore can be considered from hour ten onward. While the simulation results show a higher

CO₂ partial pressure than the test data with an average difference of 0.27 Torr the mean squared error of 0.09 Torr is relatively low. Since the model overestimates the CO₂ level it can be considered conservative. However, the basic behavior of the CO₂ level for the different load cases is well depicted as the difference between test data and simulation is nearly identical for all three load cases of the test.

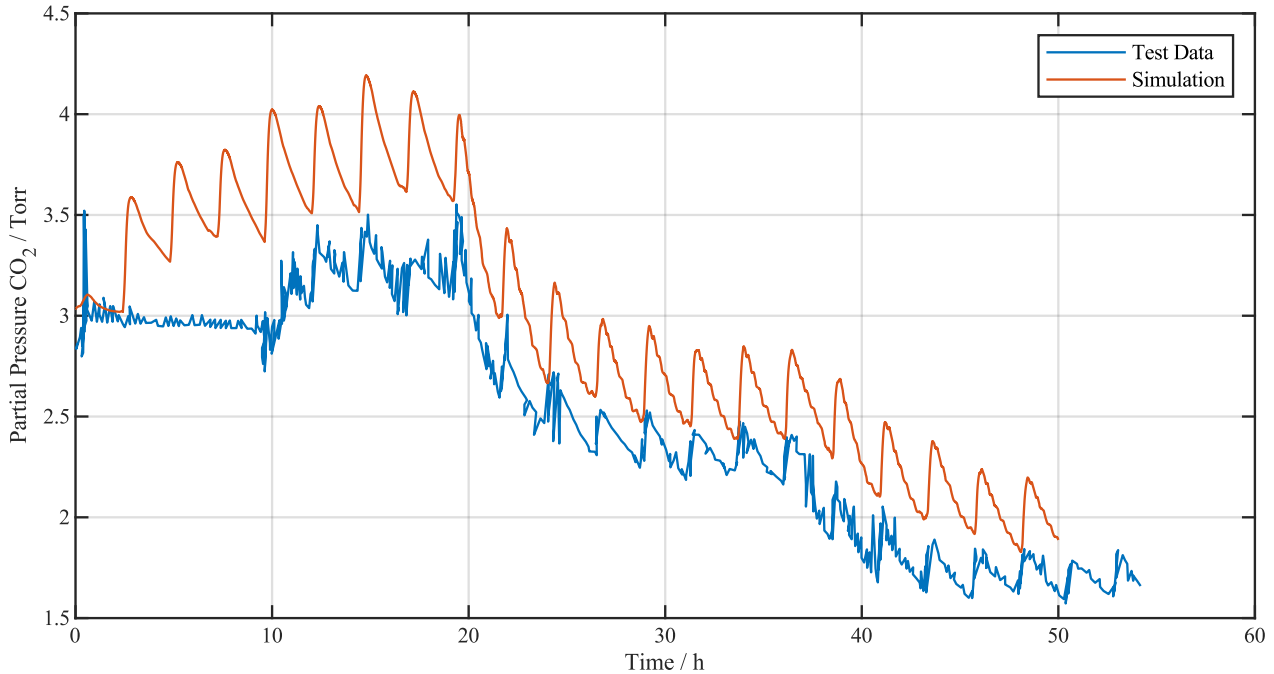


Figure 5.3-3: CDRA model comparison to test data from (Knox 2000).

To further study the errors of this model, a convergence analysis was performed. The number of cells representing each adsorber bed was adjusted from two to 90 cells. The case with 90 cells therefore results in a model with 540 cells in total for CDRA. While it is possible to use more cells for the model, the simulation becomes exceedingly slow. Figure 5.3-4 shows the results of this convergence analysis. A general trend towards smaller errors for better discretization is observable. Although a medium number of cells seems to be less favorable compared to either ten cells or 70 cells and more. It is not entirely clear why this is the case, but the increase of the error is relatively small and therefore might be a result of perturbations, which can be expected of such models. If a better representation of reality is desired, the model can be discretized with more than 70 cells, although this severely impacts the computational performance. For this reason, the subsystem model of CDRA is generally defined with ten cells per adsorber bed.

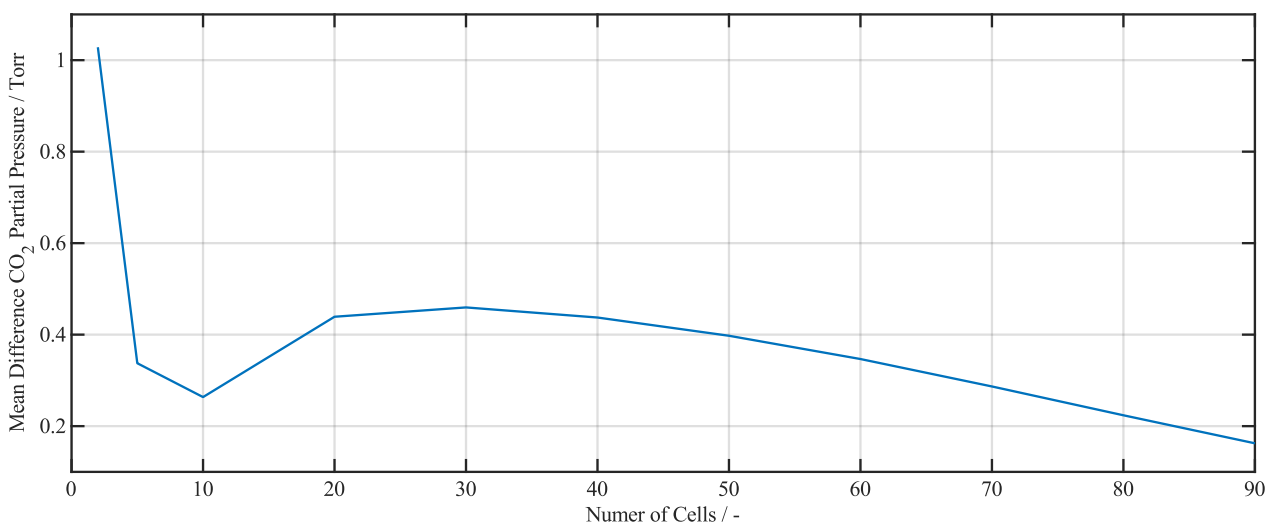


Figure 5.3-4 Convergence analysis of the CDRA model showing the mean difference in CO₂ partial pressure. Since the difference between model and test data is generally positive, the mean squared error shows the same basic behavior.

5.3.3 SCRA

5.3.3.1 Modelling Approach

The Sabatier Carbon Reduction System (SCRA) is used on the ISS to convert CO₂ into H₂O and CH₄:



This principle is also applied in ESAs Life Support Rack (LSR) (formerly Advanced Closed Loop System (ACLS)) (Bockstahler et al. 2017). Therefore, it is the only PC technology currently at TRL 9 which can recover O₂ from CO₂. A detailed schematic of the SCRA is provided in (Knox et al. 2005) and was used to develop the subsystem model for V-HAB, which is shown in Figure 5.3-5. To make the model compatible with different systems (e.g. high-pressure hydrogen tanks) a pressure regulator was added to the hydrogen inlet. All branches are calculated using the multibranch solver, except for the condensate outlet, which uses a residual solver, and the CO₂ reactor supply and bypass, which use manual solvers. The manual solvers are used to regulate the CO₂ supply to the reactor, and to vent excess CO₂ if the pressure in the accumulator exceeds a specific pressure. While the control logic for the SCRA CO₂ supply to the reactor is not known in detail, Table 1 from (Knox et al. 2005) shows the basic operating rules depending on the accumulator pressure. The maximum and minimum accumulator pressures are estimated based on these values. The accumulator volume is stated to be 0.73 ft³, which is equal to 0.02 m³ (Knox et al. 2005). As the volume of other components is small in comparison their volume is considered negligible and flow phases are used in the model to represent them.

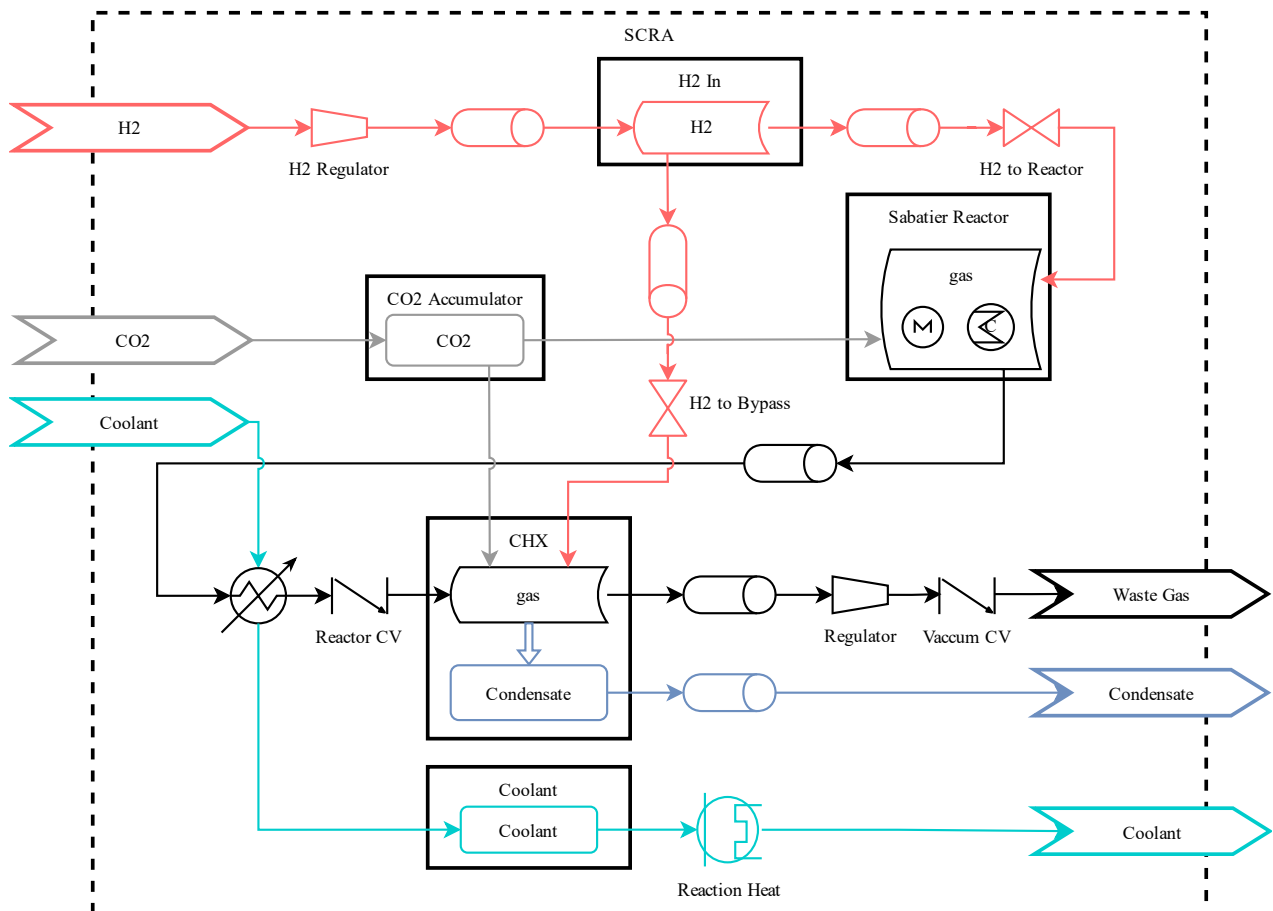


Figure 5.3-5 SCRA model structure.

The produced heat of the Sabatier reaction together with the required heat flows to maintain the reactor temperature is set as heat flow for the “Reaction Heat” F2F heater, which directly heats up the coolant water after the condensing heat exchanger. The amount of CO₂ supplied to the reactor is calculated based on the current H₂ supply to the reactor, to

ensure a lean operating mode, where the molar ratio of CO_2 to H_2 is about 1 to 3.5. The conversion is calculated stochastically with an assumed efficiency of 88%, which is based on the values provided in (Knox et al. 2005).

5.3.3.2 Validation

To validate the SCRA model the test conditions from (Knox et al. 2005) are reproduced in a simulation. The test duration was 16.1 h but the simulation requires an initial period during which the CDRA is conditioned to the test setpoints and therefore runs for an additional CDRA half cycle of 144 min. Figure 5.3-6 shows the resulting accumulator pressure and the cumulative produced and vented masses of the system. A small portion of CO_2 is vented initially since the SCRA accumulator is initialized to full and then additional CO_2 from CDRA is added. However, since more CO_2 can be consumed for the corresponding H_2 stream, the venting only occurs for a very short duration. Towards the end of the test case the reactor reaches starve times for a total of three periods, as indicated by the flat pressure levels in the accumulator pressure and produced water.

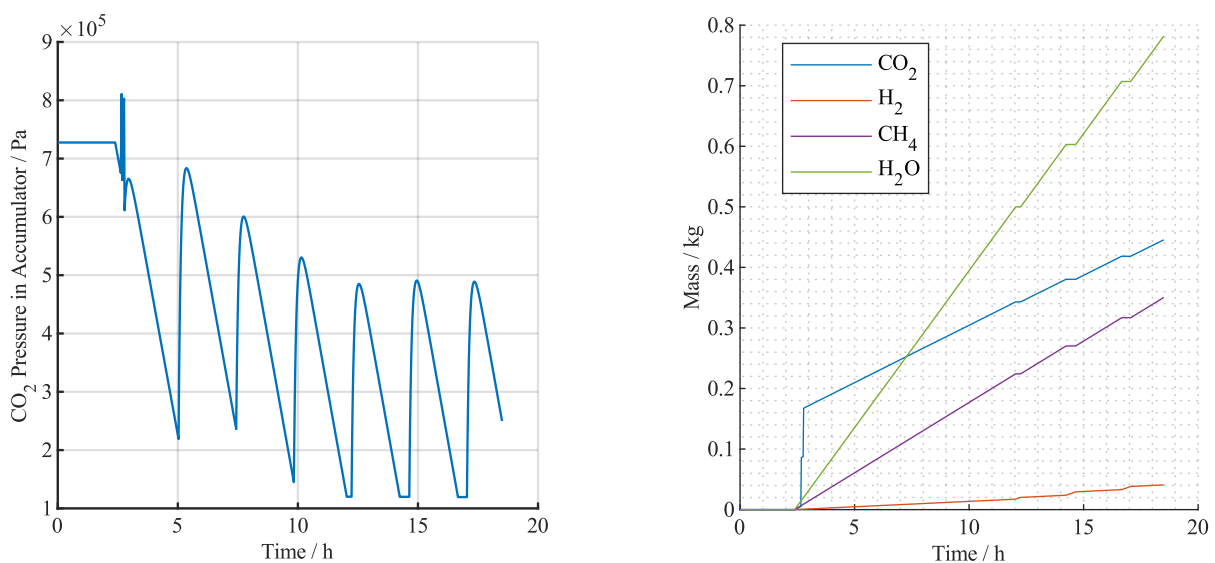


Figure 5.3-6 SCRA accumulator pressure and cumulative produced (H_2O) and vented (all other) masses for the simulation.

Figure 5.3-7 shows the flowrates within SCRA. The dynamic effect of the CO_2 release from the CDRA can be observed in this figure, which also impacts the behavior of the SCRA accumulator pressure. The starve times are also visible as the CO_2 supply flowrate to the reactor becomes zero during starvation, which results in higher hydrogen vent rates.

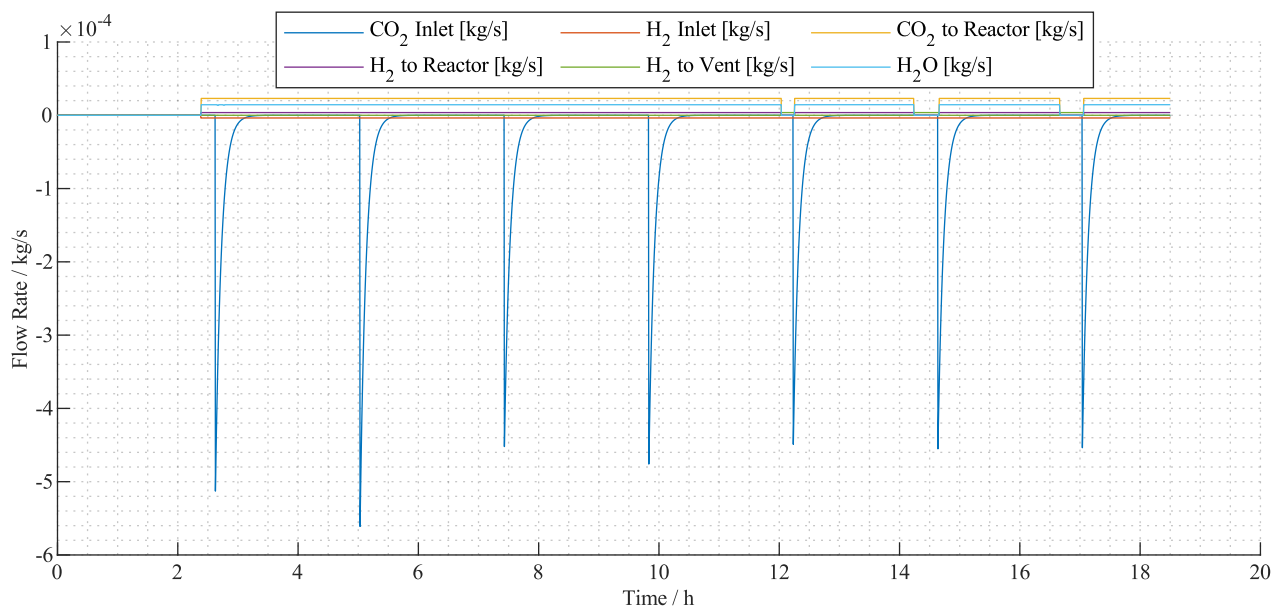


Figure 5.3-7 Flowrates within the SCRA during the validation case.

Table 5.3-1 provides a comparison of the test results and the simulation results including the starve time of the reactor. Overall, the simulation matches the expected results. Since the SCRA model is not as detailed as other models, as it does interact with downstream systems, the conversion is not dynamic but set to a static 88%. The simulation results reflect this as they reach 87.44% conversion. The specific control logic for the CO₂ supply to the reactor is not known, therefore some deviations between the starve time and compressor runtime are expected. This is also the case in the results, but the simulation reflects the actual system, especially with regard to the water production capability.

Table 5.3-1: SCRA validation results compared to test results from (Knox et al. 2005).

Parameter	Unit	Test	Simulation
Test Duration	h	16.1	16.1
Maximum Theoretic Water Production	g	939.85	893.43
Actual Water Production	g	876.34	781.25
Efficiency of Water Production	%	93	87.44
Starve Time of Reactor	min	15	62.14
Compressor Runtime	min	168	257.6

5.3.4 CCAA

5.3.4.1 Modelling Approach

The basic implementations for the Common Cabin Air Assembly (CCAA) model were derived by (Alexander Schmid 2018) and (Fabian Lübbert 2018). However, adjustments were necessary due to erroneous assumptions. For example, (Fabian Lübbert 2018) assumed the Condensing Heat Exchanger (CHX) used in the CCAA was a multi-pass parallel flow heat exchanger. This means the water flow and the air flow pass through parallel channels and flow in the same direction. Actually, it is a single pass for the air flow and a multipass one for the water flow, with counterwise water and air flows. The picture showing the CHX in (Wieland 1998: 107) is not explicit regarding the air flow, but it is stated, that the CCAA CHX is based on the Spacelab CHX, which is mentioned to use a single air pass in (Burns and Ignatonis 1974: 5). The modelling principle is the calculation of local heat flows and condensate flows as described by (Alexander Schmid 2018) in discretized cells of the CHX. The flowpath for air and water can then be implemented as the exchange between different cells. In a cross-counter flow CHX, it is not possible to solve this directly, as the air inlet is in contact with the water outlet and vice-versa. Therefore, an iterative solution is required to solve the counter flow CHX. The resulting temperature distribution in this CHX is shown in Figure 5.3-8.

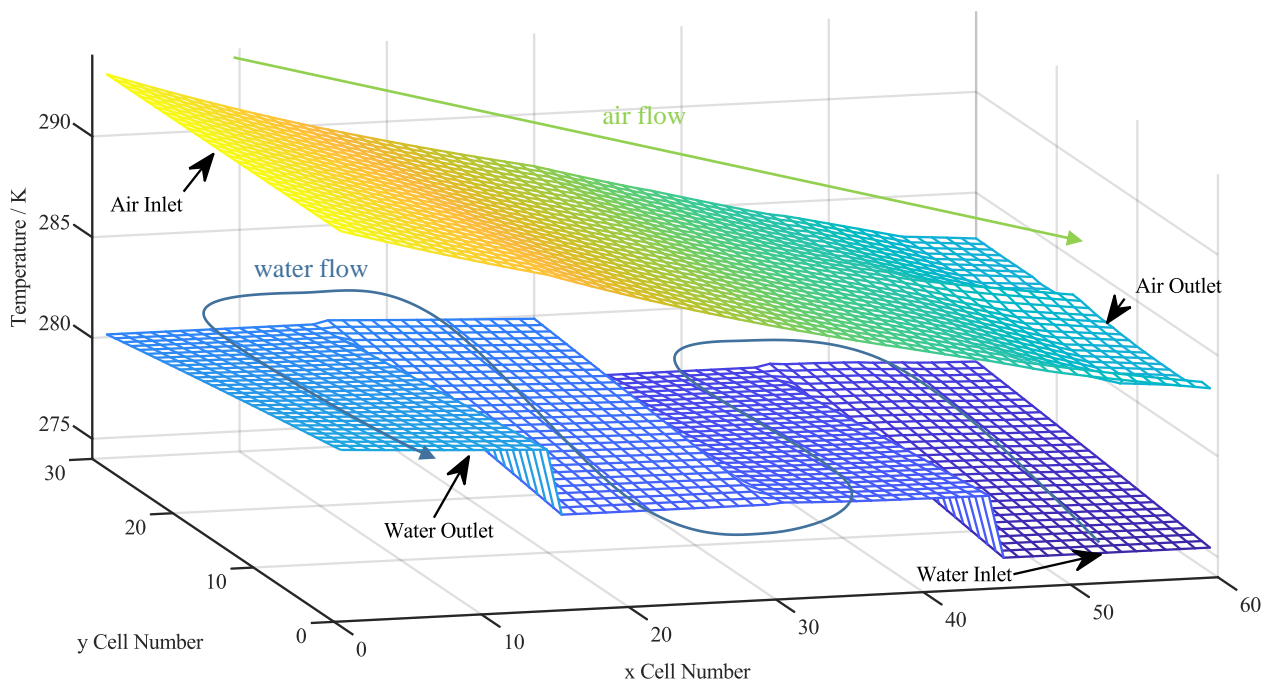


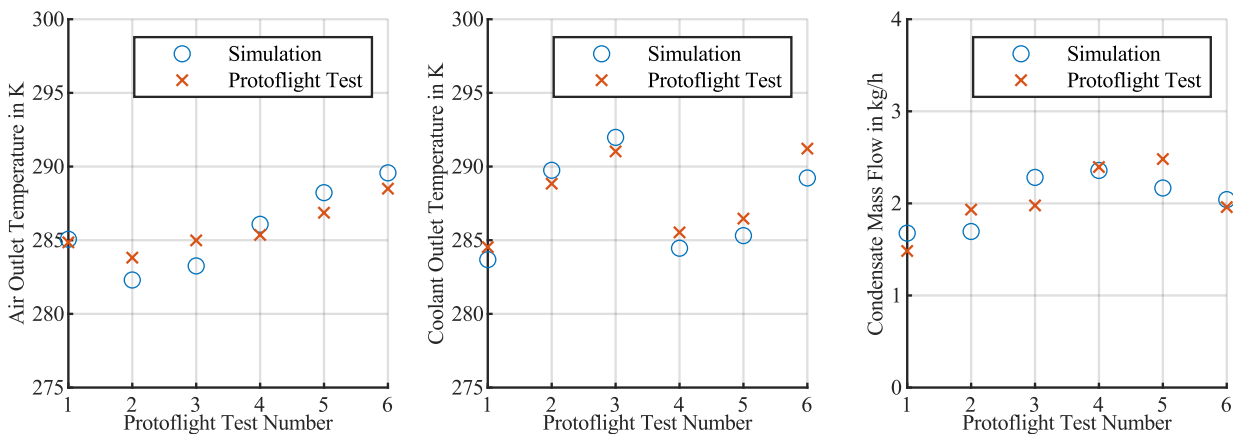
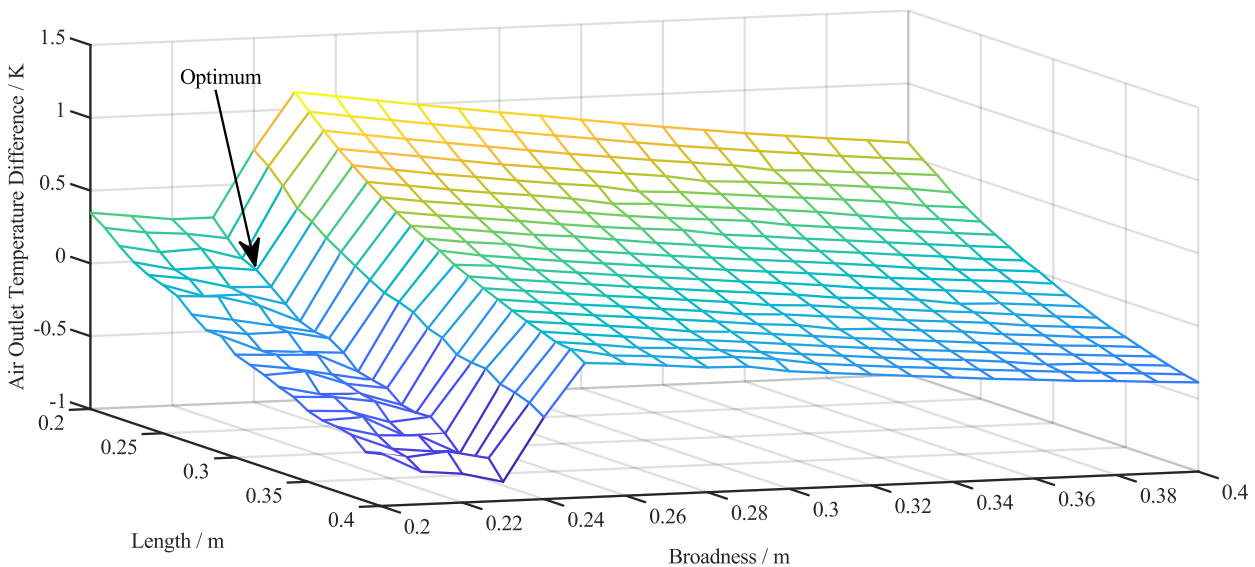
Figure 5.3-8 Cell temperatures inside the CCAA condensing heat exchanger for the water and air flow.

5.3.4.2 Validation

To validate the model proto-flight test data from Table 6-1 of (Roth 2012) is used since the original proto-flight test is not available publicly. By comparing the table with the raw data of the thesis, which is available at the institute of astronautics, some errors in the information were identified and fixed. For example, the Temperature Control and Check Valve (TCCV) Angle of Test 1 is stated to be 5° while the raw data shows that the value should be 40° . The corrected proto-flight test data is provided in Table 5.3-2. For validation, six CCAAs operating at the specified test conditions are simulated. Figure 5.3-9 shows the resulting outlet temperatures and condensate rates compared to the tests. The average difference in condensate production is -1.6 g/h, the average difference for the outlet temperatures is 0.02 K for air and 0.54 K for coolant. Figure 5.3-10 shows the parameter fitting that resulted in 0.23 m for both dimensions as lowest error.

Table 5.3-2: Proto-flight test setpoints used for CCAA validation.

Set Point Conditions	Unit	Test 1	Test 2	Test 3	Test 4	Test 5	Test 6
Air Inlet Flow	m^3/s	0.20	0.20	0.20	0.20	0.20	0.20
TCCV Angle	$^\circ$	40.0	5.0	5.0	40.0	40.0	40.0
Air Inlet Temperature	$^\circ\text{C}$	18.16	18.01	20.81	20.87	25.78	25.78
Air Inlet Dew Point	$^\circ\text{C}$	13.06	12.81	14.65	14.77	14.51	15.01
Coolant Inlet Flow	g/s	145.15	74.27	75.13	146.66	145.28	74.68
Coolant Inlet Temperature	$^\circ\text{C}$	6.44	5.61	5.72	6.01	6.00	5.64
ARS Blower Flow	m^3/s	35.64	35.64	35.64	35.64	35.64	35.64


Figure 5.3-9 CCAA simulation results compared to proto-flight test data.

Figure 5.3-10 CCAA parameter fitting for the average air outlet temperature difference over the six proto-flight tests.

5.3.5 WPA

5.3.5.1 Modelling Approach

The WPA model of V-HAB was derived in (Mühlhaus 2017) and is based largely on (Hokanson 2004). For the work performed by (Mühlhaus 2017) not all of the features mentioned in chapter 5.2 were implemented in V-HAB already. For example, the flow phases and corresponding matter network solver as well as the pH model were not available at that time. Therefore, the model was reworked to utilize these features and improve the performance to a level where it is feasible to perform system-level simulations with this component. Figure 5.3-11 shows an overview of the model, which consists of a total of three discretized filtration beds.

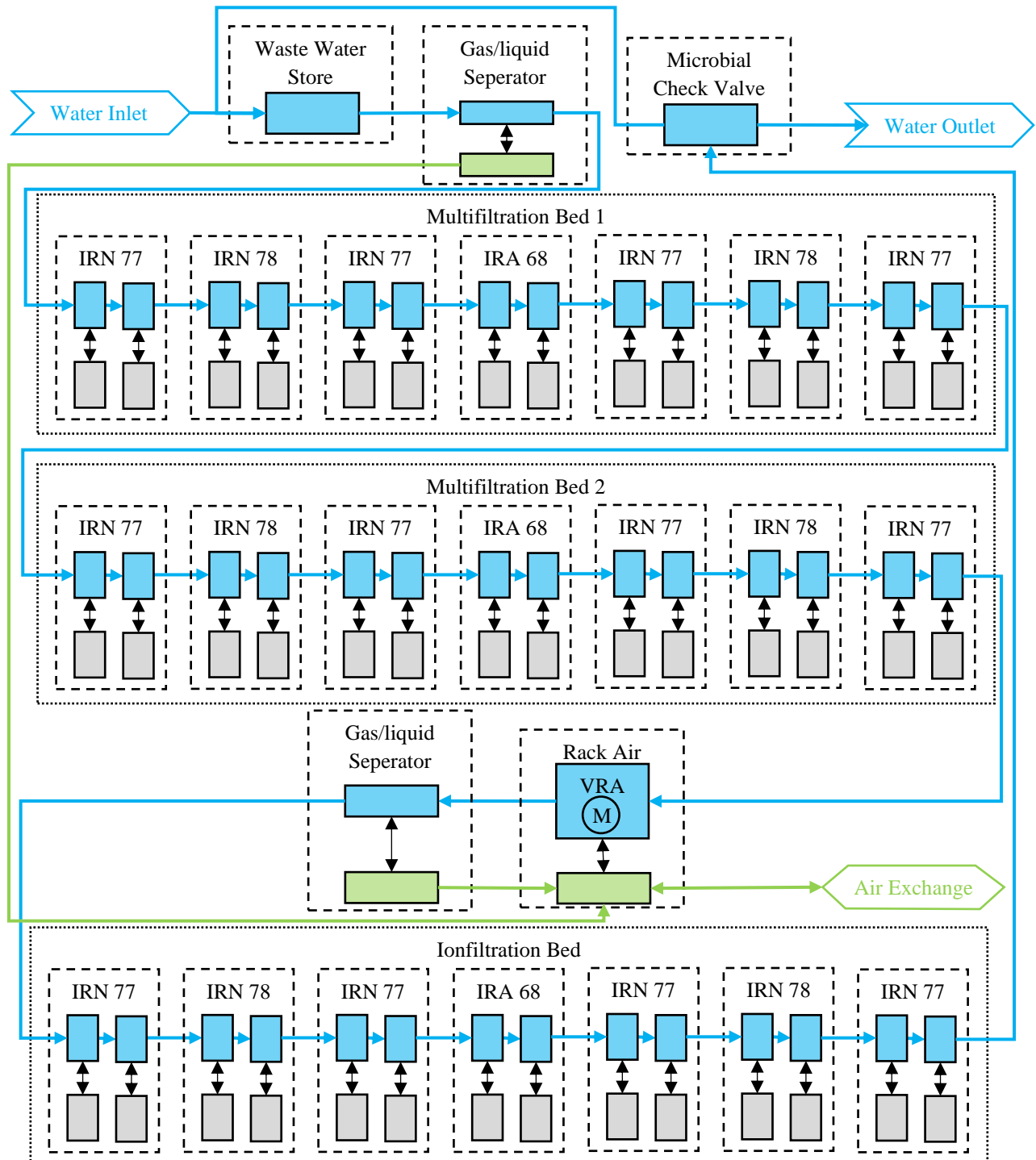


Figure 5.3-11 WPA model structure showing only two cells per resin. Resins are manufacturer names from (Hokanson 2004).

The composition of the multifiltration beds is modelled according to (Hokanson 2004: 1) while the overall structure of the WPA is modelled according to (Carter et al. 2017a). The abbreviations IRN 77, IRN 78 and IRA 68 are producer labels for the different ion exchange resins used in the filtration beds. The Volatiles Removal Assembly (VRA) is a catalytic reactor used to oxidize organic contaminants. According to (Tobias et al. 2011) the WPA starts a process cycle once the waste water tank reaches 65% of its capacity and then processes waste water until the tank reaches 4% of its capacity. The capacity of the waste water tank is stated to be 68 kg and the nominal flowrate for the WPA is 5.9 kg/h according to (Carter et al. 2005). These parameters are used as control logic for the WPA together with the power demand of the WPA of 414 W during operation and 224 W during standby from (Carter 2009).

The air exchange shown in Figure 5.3-11 is primarily a supply of oxygen to the VRA, which combusts organic contaminants. The produced gases from VRA are also released to the habitat atmosphere via these air branches. In order to minimize the required interfaces of the WPA subsystem, a common gas interface is used for both gas/liquid separators.

The primary function of the WPA is to remove contaminants from the water stream. In the multifiltration beds this is achieved through ion exchange. The ion exchange is solved for each cell in the model using the MATLAB® *ode45* solver for the following differential equation from (Hokanson 2004: 181).

$$\frac{\delta q_i}{\delta t} = \frac{\dot{V} \cdot C_{i,0} - \dot{V} \cdot \left[\frac{C_{T,C} \cdot q_i}{\sum_{j=1}^{n_{cation}} \alpha_j^i \cdot q_i} \right]}{m_{resin} + \epsilon \cdot V_{cell} \cdot \left[\frac{C_{T,C} \cdot \sum_{j=1, j \neq i}^{n_{cation}} \alpha_j^i \cdot q_i}{\sum_{j=1}^{n_{cation}} \alpha_j^i \cdot q_i} \right]} \quad (5.3-8)$$

q_i	loading of ion i	α_j^i	separation factor between ion j and i
\dot{V}	volumetric flowrate	m_{resin}	mass of ion exchange resin in cell
$C_{i,0}$	initial concentration of ion i	ϵ	void fraction of resin
$C_{T,C}$	total concentration of cations	V_{cell}	volume of cell

While equation (5.3-8) is specifically for cations, the same approach can also be used for anions in which case the summation is over all present anions. Whether cations or anions are removed depends on the type of ion exchange resin of the current bed. The *ode45* solver calculates the change from the current time and loading up to the empty bed contact time (EBCT), which depends on the flowrate and geometry of the beds and is provided in (Hokanson 2004: 1).

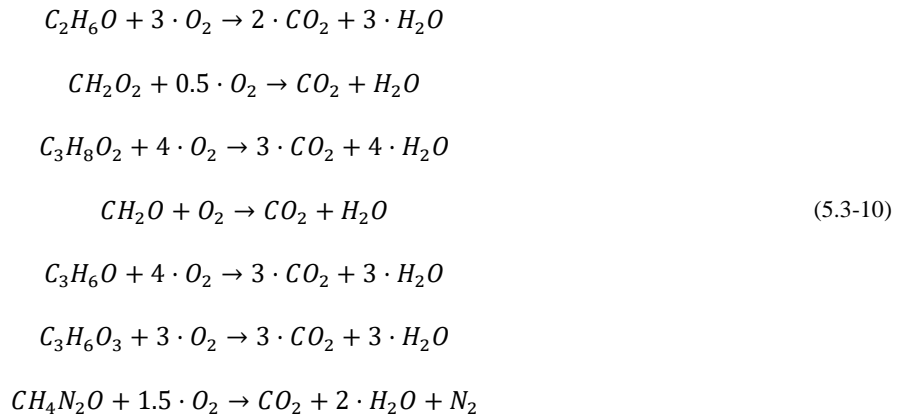
For anions a second adsorption mechanism is used in some beds. These do not use the strong ion adsorption described in equation (5.3-8) but instead use a weak base anion exchange, which can be described using the following equation (Hokanson 2004: 234).

$$\frac{\delta C_{i,e}}{\delta t} = \frac{\dot{V} \cdot C_{i,0} - \dot{V} \cdot C_{i,e}}{m_{resin} \cdot \left[\frac{\left(1 + C_H \cdot \sum_{j=1, j \neq i}^{n_{anion}} \alpha_j^i \cdot C_i\right) \cdot \left(q_T \cdot \alpha_i^i \cdot C_H\right)}{\left(1 + C_H \cdot \sum_{j=1}^{n_{anion}} \alpha_j^i \cdot C_i\right)^2} \right] + \epsilon \cdot V_{cell}} \quad (5.3-9)$$

$C_{i,e}$	outlet concentration of ion i	C_H	concentration of H^+
q_T	total loading over all ions		

Equation (5.3-9) is also solved with the *ode45* solver but in this case it calculates the outlet concentration of the ions. The required adsorption flows are then calculated to achieve the desired outlet concentration for the ions.

Another primary function is performed by the VRA where organic contaminants are combusted through catalytic oxidation. A detailed model of the VRA is discussed in (Guo et al. 2005). The model implemented in the V-HAB WPA model is simplified to model the relevant interactions with the remaining ECLSS. The implemented combustion is assumed to occur stoichiometrically and completely combust the contaminants to water and CO_2 and potential other gases, like nitrogen in the case of urea combustion. The heat of reaction is considered negligible and therefore neglected. The implemented combustion reactions are:



The ratio of oxygen within the reactor that can be utilized to react contaminants according to (5.3-10) is calculated based on equation (5.3-11) from (Guo et al. 2005):

$$U_{O_2} = 1 - \exp\left(\frac{3 \cdot r_{O_2} \cdot \Psi_b}{r_b \cdot \rho_{O_2} \cdot v_b}\right)
 \tag{5.3-11}$$

U_{O_2}	oxygen utilization	r_b	average bubble radius
r_{O_2}	rate of oxidation	ρ_{O_2}	density of oxygen
Ψ_b	average sphericity of bubbles	v_b	average velocity of bubble

The required parameters for equation (5.3-11) can be calculated dynamically. However, for the simplified model the parameters calculated by (Guo et al. 2005) were used as static variables in the model. Table 5.3-3 provides an overview of the used parameters for the model. To calculate the oxygen mass consumption potential $\Delta m_{O_2,pot.}$ the oxygen utilization U_{O_2} is multiplied with the oxygen injection rate \dot{m}_{O_2} and the residence time of water in the reactor t_w .

$$\Delta m_{O_2,pot.} = U_{O_2} \cdot \dot{m}_{O_2} \cdot t_w
 \tag{5.3-12}$$

Based on $\Delta m_{O_2,pot.}$ the model calculates how much contaminants can be oxidized according to equation (5.3-10).

Table 5.3-3: VRA parameters used in the WPA model

Parameter	Symbol	Unit	Value
reactor length	l_{VRA}	m	1.12
rate of oxidation	r_{O_2}	g/m ²	0.515
average sphericity of bubbles	Ψ_b	-	0.5
average bubble radius	r_b	m	0.07
density of oxygen	ρ_{O_2}	kg/m ³	4.28
average velocity of bubble	v_b	cm/s	0.18

5.3.5.2 Validation

Validation of the WPA is based on the experiments performed by (Hokanson 2004) but since the reported test data points were limited, the V-HAB simulation is compared to the model developed by (Hokanson 2004). All ions modelled by (Hokanson 2004) are also modelled in the V-HAB simulations, but for brevity only one cation and one anion is shown for validation. The remaining ions all show similar behavior to the two ions discussed in this section.

Figure 5.3-12 shows the results for sodium ions (Na⁺). Since the V-HAB model uses flow phases to model the water in the WPA some dynamic effects are neglected like the slight initial ramp up of the breakthrough and the overshooting at the end of the breakthrough. The V-HAB model also has a higher apparent capacity than the model from (Hokanson 2004) as the breakthrough occurs later for all considered ions. The cause for this are the simplifications used to achieve higher simulation speeds. In the originally developed V-HAB model from (Mühlhaus 2017) the dynamic effects like

the ramp ups are modelled correctly and the capacities also match better with the results from (Hokanson 2004) as shown in Figure 5.3-13. Nevertheless, the current implementation of the WPA is necessary to model it in a complex system-level simulation due to the slow computation of the previous implementation. Multiple different approaches to improve the accuracy of the model were tested:

- modelling the individual cells with mass
- model the water mass within each resin in a single normal phase after the flow cells for each bed
- various different combinations of the cells and the pH module of V-HAB (include a pH-manip in each cell, including it only in the normal phase after the flow cells from the previous example etc.)

All of these approaches did not produce a better combination of well-matched results and high simulation speeds. The planned simulations of this dissertation will not be long enough to have a breakthrough in the WPA. Therefore, the impact on this work was deemed small enough. The relevant aspect of modelling the exchange of ions and the removal of some substances like sodium from the overall system is captured by the model. This was the primary goal for this model and is sufficient for the intended studies in this research.

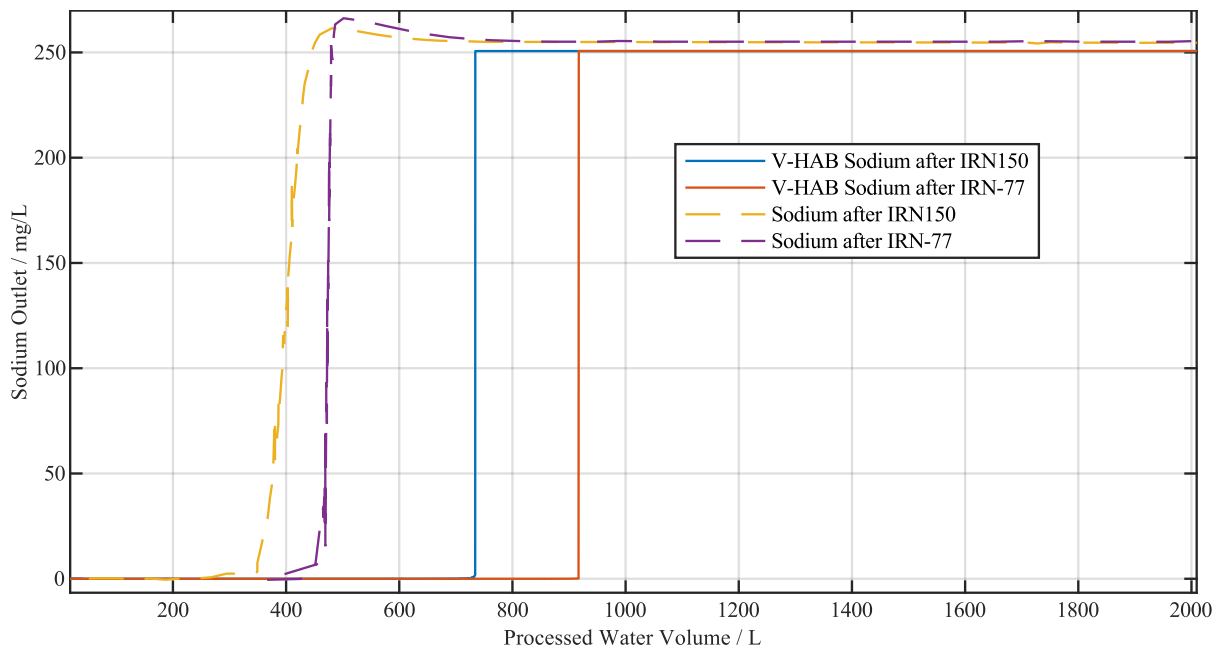


Figure 5.3-12 Comparison of sodium breakthrough from (Hokanson 2004: 287) (dashed lines) with the V-HAB model.

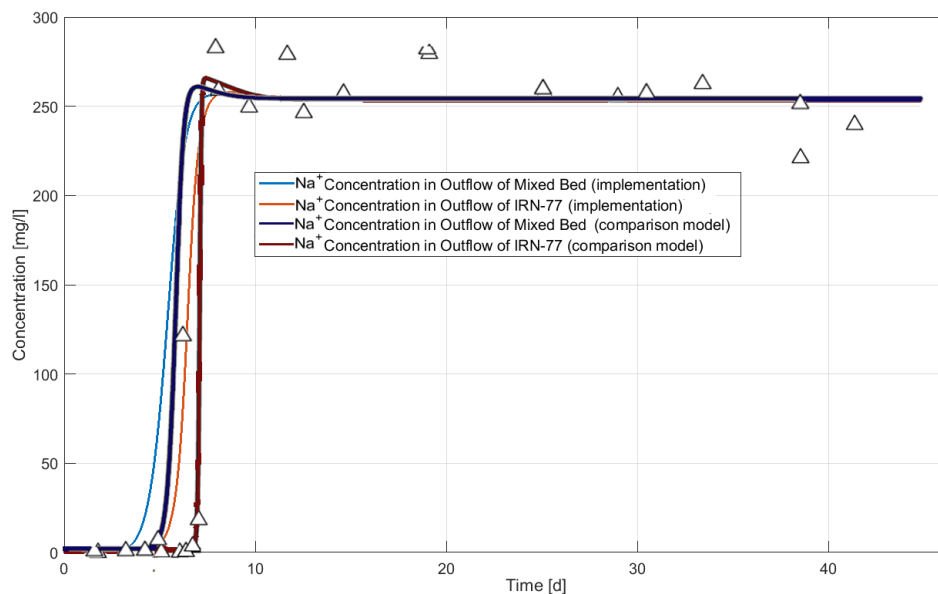


Figure 5.3-13 Comparison of sodium breakthrough from (Mühlhaus 2017: 30).

Figure 5.3-14 shows the result for acetate (CH_3COO^-). The results for the IRA-68 bed show an overall different behavior as it uses a different adsorption mechanic, the weak base anion exchange described in equation (5.3-9).

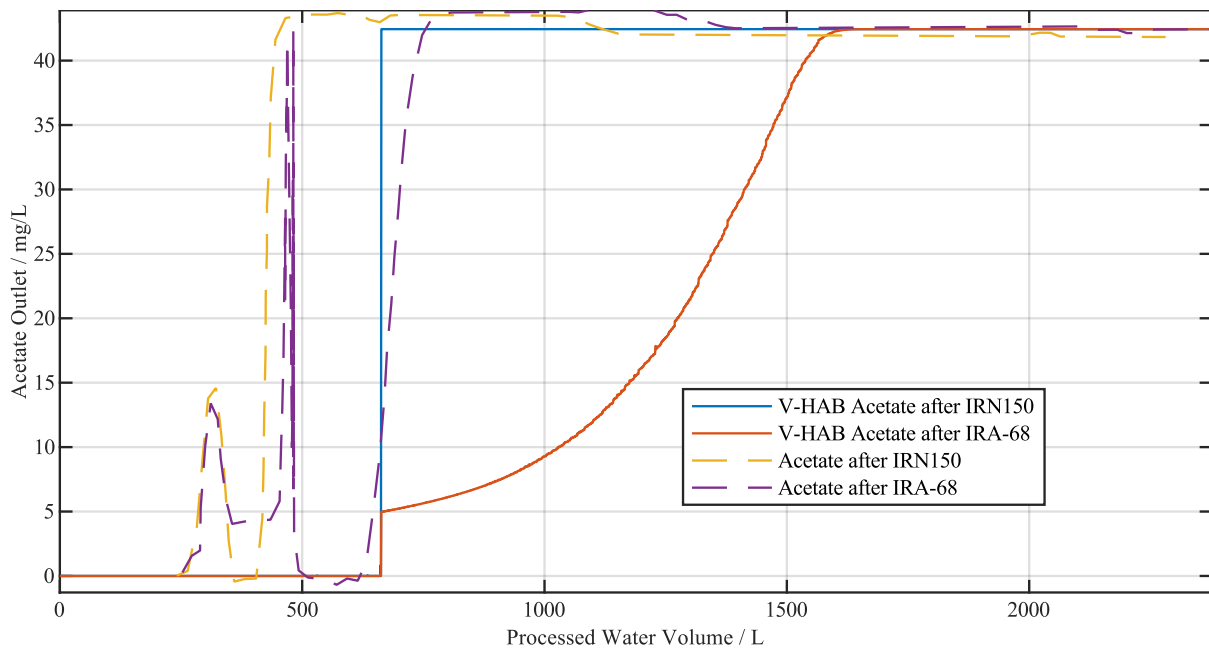


Figure 5.3-14 Comparison of acetate breakthrough from (Hokanson 2004: 289) (dashed lines) with the V-HAB model.

5.3.6 UPA

5.3.6.1 Modelling Approach

The UPA is modelled based on the schematic provided in (Carter et al. 2017a). The model is simplified compared to the biological processing options because it is only used for comparisons with regard to the water production capability. The impacts of the system on the cabin atmosphere and the produced contaminants for the waste-water are not modelled in-depth. Figure 5.3-15 provides an overview of the implemented V-HAB structure for the model. The urine produced by the crew is created as a compound mass (see chapter 5.2.3.1), which consist of water and other components (like urea and sodium chloride). The produced water by UPA is assumed to be pure water, which is not realistic, but suffices for the simpler calculations performed with this model.

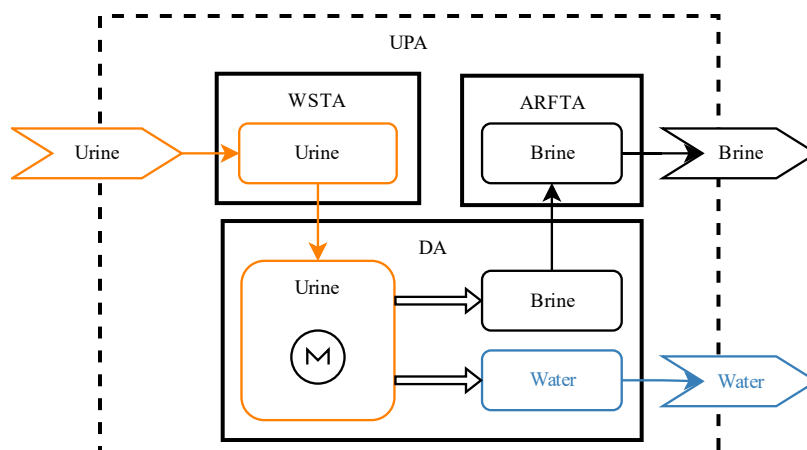


Figure 5.3-15 UPA model structure.

The manipulator in the Distillation Assembly (DA) of the UPA model separates the water from the compound mass and creates brine from the remaining mass. This means the brine composition produced by the UPA depends on the input it receives from the human. If the human produces urine with a higher urea content, the brine will also have a higher urea content. The efficiency of the water recovery is not modelled in detail and is assumed to be 85% according

to (Carter et al. 2019). The produced water is not of potable quality and must be processed by the WPA before it can be considered potable. The urine supplied to the UPA is stored in the Wastewater Storage Tank Assembly (WSTA). The UPA starts processing a batch once WSTA is at 70% capacity and the remaining amount after processing is 8%. One batch requires 7.5 h to process followed by 5 h of cooldown according to (Tobias et al. 2011: 7). No direct mention of WSTA capacity was found during literature research. Figure 2 from (Tobias et al. 2011) shows a spreadsheet calculation of water balance operations including system loads and WSTA tank capacity percentages, the capacity was estimated to 13 l. The brine produced by the DA is stored in the Advanced Recycle Filter Tank Assembly (ARFTA), which has a capacity of 22 l according to (Pruitt et al. 2015).

5.3.6.2 Validation

In order to validate the UPA it was simulated for a period of 60 days. Figure 5.3-16 shows the dynamic results which are then compared to the known operation parameters of UPA for validation.

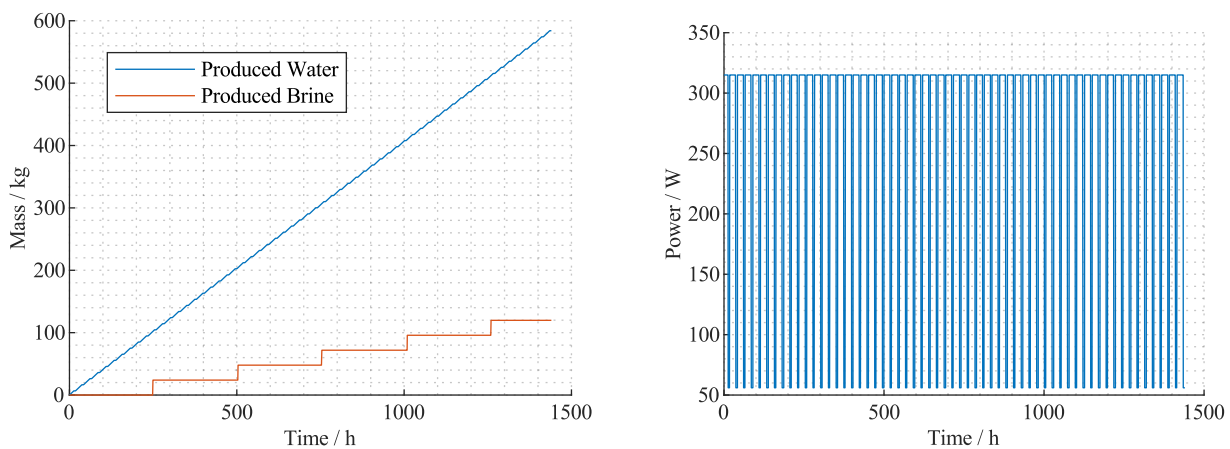


Figure 5.3-16 UPA validation simulation over 60 days.

The UPA produced a total amount of 584 kg of water which corresponds to 9.73 kg/day. The design flowrate of UPA is 9 kg/day which corresponds to a crew of six (Carter et al. 2017a). The slight increase is a result of the continuous urine supply, where the downtime is minimized to exactly the five hours required. This cannot be achieved in a real system. The power profile also shows the cycle behavior with 7.5 hours of operation followed by five hours of standby and the corresponding power demands which are based on (Carter 2009).

5.3.7 BPA

5.3.7.1 Modelling Approach

The BPA uses a membrane distillation approach where the water in the brine evaporates through a semipermeable membrane into an air stream. The water is then released as humidity in the cabin and recovered by humidity control systems like the CCAA. The BPA is able to recover 22.5 l over a period of 26 days with a water recovery efficiency of 80%. (Kelsey et al. 2018)

From a modelling perspective the BPA is similar to the UPA as the brine is modelled as compound mass (see chapter 5.2.3.1) consisting of water and other substances. The manipulator within the bladder removes water from this compound mass, which is then transported into the gas flow via a P2P. The air stream is modelled as gas exchange with the cabin atmosphere and therefore introduces additional humidity into the attached cabin. Currently the created concentrated brine is stored within a disposal store within the BPA model, as no further processing for this is considered. In reality, the dried bladders containing the concentrated brine are switched out completely and burn up as trash on a cargo vehicle reentry. But for the model, it is of interest to calculate the total produced mass and the number of cycles, as that allows the estimation of required bladders and crew time.

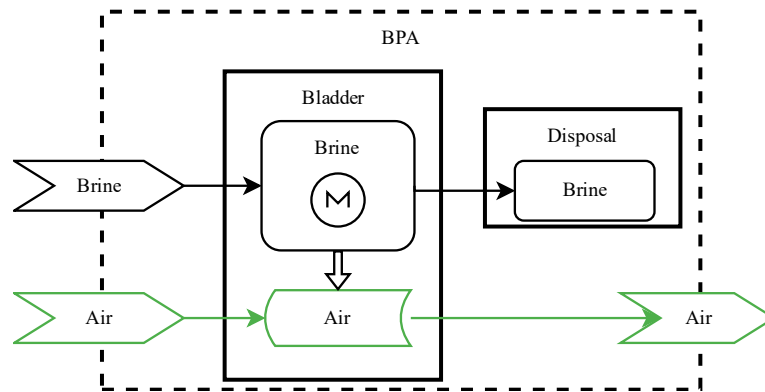


Figure 5.3-17 BPA model structure.

5.3.7.2 Validation

Since the BPA requires brine from the UPA as input both systems were modelled together for validation of the BPA. The simulation period was again 60 days and in addition to the ARFTA store in the UPA a brine store in the parent system (called Brine Storage in Figure 5.3-18) was added. This was necessary since the UPA is designed for a crew of six while the BPA is designed for a crew of four (Kelsey et al. 2018).

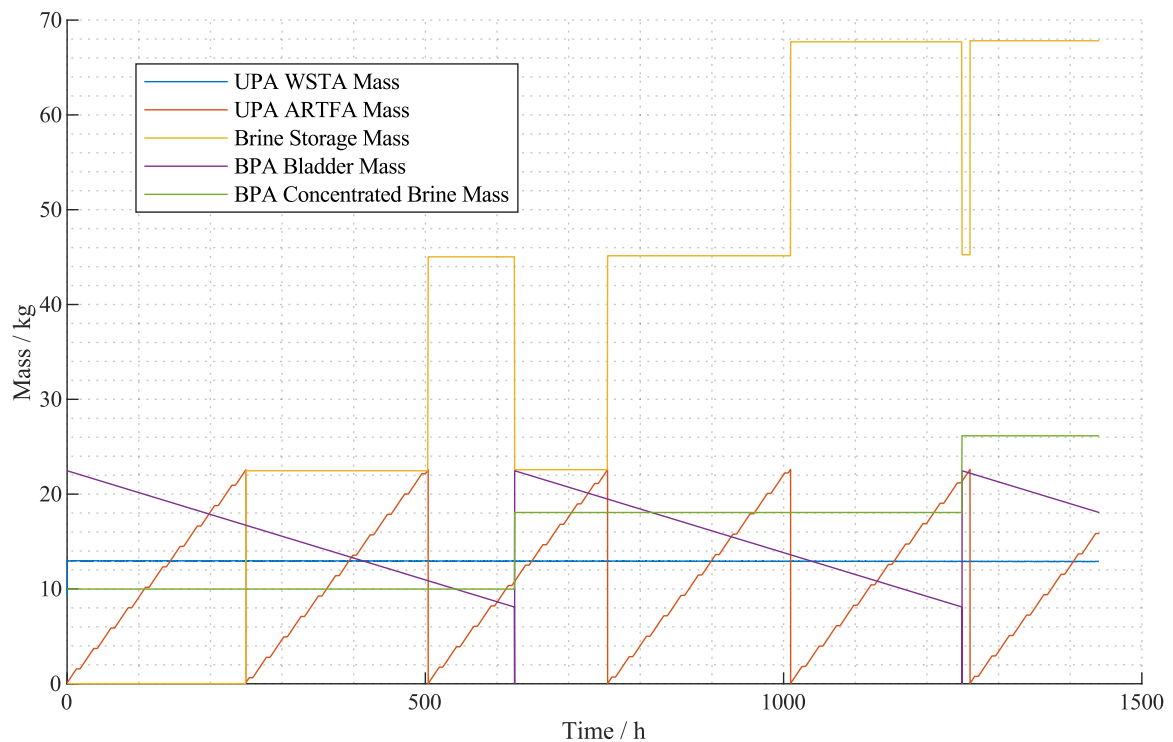


Figure 5.3-18 BPA validation simulation over 60 days.

The UPA produces 44.5 kg of brine over a 26-day cycle, which is more than the BPA can handle. The BPA produced 33.15 kg of water over the 60-day period, which corresponds to 552 g of water per day. In order to check this value, it is first necessary to estimate the water content of the brine after the UPA. According to (Anderson et al. 2018: 63) urine consists of 0.06 kg of solids and 1.6 kg of water initially. The UPA removes 85% of the water, which leaves 240 g of water and 60 g of solids. This corresponds to 80% of initial water content. Therefore, the BPA bladder with an overall capacity of 22.5 l contains 18 l water. With 80% recovery rate, a total of 14.4 kg of water are recovered over 26 days. This corresponds to 553 g of water recovery per day, which is almost identical to the value from the simulation. Therefore, the model is considered a valid representation of the real BPA.

5.3.8 Electrolyzer

Another frequently used component in PC ECLSS is an electrolyzer to produce oxygen, see also chapter 2.1.1.2. In combination with a fuel cell an electrolyzer can also be used as a regenerative fuel cell system (RFCS) to store energy. In both roles, the electrolyzer is often required to produce the gases at elevated pressure. Therefore, a model for the electrolyzer that reflects the influence of temperature and pressure on the required energy is necessary. The efficiency of the electrolyzer influences the required storage sizes for O₂ and H₂ and is therefore also of interest, as stated in the research questions from Table 4.3-1. Due to the better availability of data a Proton Exchange Membrane (PEM) electrolyzer is modelled here.

5.3.8.1 Modelling Approach

The basic equation used to calculate both electrolyzer and fuel cells is the law of Faraday:

$$\dot{m}_k = \frac{M_k \cdot I}{z_k \cdot F} \quad (5.3-13)$$

It calculates the produced mass flow \dot{m}_x of a substance k using the current I , the molar mass of the substance M_k , the charge number z_k and the Faraday constant F . For water electrolysis two electrons must be exchanged per mol of water or hydrogen (Falcão and Pinto 2020). Therefore, the charge number z_k is two. If the current of an electrochemical device is known, the mass flow rates of reactants can be calculated from the law of Faraday. To model electrochemical devices like fuel cells and electrolyzer, the basic approach is to calculate the required voltage per cell by combining the thermoneutral voltage with multiple overpotentials (Falcão and Pinto 2020). The current can then be calculated using the voltage and the electrical power of the device. The thermoneutral voltage or open circuit voltage U_{OC} of an electrolyzer can be calculated using the Nernst equation according to (Falcão and Pinto 2020):

$$U_{OC} = U_{rev}^0 + \frac{RT}{2F} \left[\ln \left(\frac{p_{H_2} p_{O_2}}{p_{H_2O}} \right) \right] \quad (5.3-14)$$

The reversible cell voltage U_{rev}^0 is used in most modelling approaches (Awasthi et al. 2011; Abdin et al. 2015; Han et al. 2016; Ruuskanen et al. 2017; Moradi Nafchi et al. 2019) discussed by (Falcão and Pinto 2020). The other parameters are the ideal gas constant R , the temperature T and the pressure of the involved substances p_i . For U_{rev}^0 multiple calculation approaches are discussed by (Falcão and Pinto 2020). The most promising equation to include all relevant relations is equation 13 from (Falcão and Pinto 2020), as it includes pressure dependencies. However, after checking the provided references no original reference for this equation could be found. Therefore, the following commonly used equation for U_{rev}^0 is selected here:

$$U_{rev}^0 = 1.229 \text{ V} - 0.9 \cdot 10^{-3} \frac{\text{V}}{\text{K}} \cdot (T - 298 \text{ K}) \quad (5.3-15)$$

The modelled overpotentials consist of the ohmic U_{Ω} , kinetic U_{kin} , and mass transport $U_{transport}$ overpotential. U_{Ω} is calculated based on equation 22 from (Falcão and Pinto 2020), which is originally from the publication (Springer et al. 1991).

$$U_{\Omega} = \frac{\delta}{\sigma_{elec}} \cdot I \quad (5.3-16)$$

The membrane thickness δ is an electrolyzer specific value, with smaller values representing better performance. The membrane conductivity σ_{elec} for Nafion is calculated using the following empirical equation, which is also stated by (Falcão and Pinto 2020) but originally from (Springer et al. 1991).

$$\sigma_{elec} = \left(0.005139 \frac{\Omega}{\text{cm}} \cdot \lambda - 0.00326 \frac{\Omega}{\text{cm}} \right) \cdot \exp \left[1268 \text{ K} \left(\frac{1}{303 \text{ K}} - \frac{1}{T} \right) \right] \quad (5.3-17)$$

The water content of the membrane λ is assumed ideal in the current model, which means the value $\lambda = 14$ is used. The kinetic (or activation) overpotential $U_{kin.}$ is calculated based on equation 6 from (Zhang et al. 2012).

$$U_{kin.} = \frac{\alpha_A + \alpha_C}{\alpha_A \alpha_C} \frac{RT}{2F} \ln \left(\frac{i}{i_0} \right) \quad (5.3-18)$$

Where α_A and α_C are the transfer coefficients of anode and cathode respectively, which are $\alpha_A = 0.5$ and $\alpha_C = 1$. The current density i is divided with the exchange current density i_0 , which can be calculated as follows:

$$i_0 = 1.08 \cdot 10^{-17} \frac{A}{cm^2} \cdot \exp(0.086 \frac{1}{K} \cdot T) \quad (5.3-19)$$

The equation for $U_{kin.}$ differs from the ones mentioned by (Falcão and Pinto 2020) because the selected equation better reflected the results of a temperature and pressure dependent electrolyzer studied by (Suermann et al. 2016). This was selected as verification case because it provides sufficient data over a variety of pressures and temperatures. However, equation (5.3-19) is still insufficient to correctly represent the pressure behavior of $U_{kin.}$. Therefore, it had to be adjusted with a correction factor ξ_{kin} based on the operating pressure p .

$$\xi_{kin} = \left(\frac{1}{\frac{p}{10^5 Pa}} \right)^{0.025} \quad (5.3-20)$$

ξ_{kin} is multiplied with $U_{kin.}$ to receive a pressure corrected $U_{kin.,cor.}$, which is used as kinetic overpotential in the model.

$$U_{kin.,cor.} = U_{kin.} \cdot \xi_{kin} \quad (5.3-21)$$

The mass transport overpotential $U_{transport}$ can also be calculated using the Nernst equation according to (Falcão and Pinto 2020) with C the concentration of oxygen or hydrogen at the interface between membrane and electrode and a reference concentration C_0 .

$$U_{transport} = \frac{RT}{2F} \left[\ln \left(\frac{C}{C_0} \right) \right] \quad (5.3-22)$$

To accurately depict C the model would require a detailed discretization and therefore a relation using current densities is often used as simplification. However, the simplification is not able to depict the pressure dependency shown in (Suermann et al. 2016) for $U_{transport}$. Since the model developed here is intended for system-level analysis of larger ECLSS a detailed model that depicts the interface concentration C is not feasible. For this reason a new empirical equation is derived based on the data from (Suermann et al. 2016) using the Nernst equation as basis. For low current densities $U_{transport}$ is small and often neglected, therefore a simple linear equation is used up to current densities of $i_{inflection} = 1.5 \text{ A/cm}^2$. The value is called $i_{inflection}$ because the inflection point of the sigmoid function used for higher densities is set to be at this value. (Mohamed et al. 2016) adjusted the Nernst equation with an additional transfer coefficient $\alpha_{transport}$, which is used as additional fitting parameter and set to 0.075 for this model.

$$i < i_{inflection}: U_{transport} = \frac{RT}{2 \alpha_{transport} F} \left(\frac{i}{2 i_{inflection}} \right) \quad (5.3-23)$$

For higher current densities, the sigmoid function was found to be a better fit for the behavior and is therefore used instead of the natural logarithm.

$$i \geq i_{inflection}: U_{transport} = \frac{RT}{2 \alpha_{transport} F} \frac{e^x}{e^x + 1} \quad (5.3-24)$$

Using the following empirical equation for x with the maximum current density i_{max} :

$$x = \frac{i - i_{inflection}}{2(i_{max} - i_{inflection})} \cdot 12 \quad (5.3-25)$$

While these equations were able to depict the behavior at 1 bar sufficiently accurate, the pressure and temperature dependency of the value is not yet included. Therefore, a correction factor $\xi_{transport,p}$ for the pressure dependency and a correction factor $\xi_{transport,T}$ for the temperature dependency are also necessary.

$$\xi_{transport,p} = 1 - \frac{p}{10^7 Pa / 3.84} \quad (5.3-26)$$

The temperature factor is more complex to better reflect the behavior at different current densities and temperatures.

$$\xi_{transport,T} = \left(0.65 + 0.6 \cdot \frac{343.15 K - T}{40 K} \right) \cdot \left[\left(\frac{\left| i - \frac{i_*}{2} \right|}{\frac{i_*}{2}} - 1 \right) \cdot 0.44 + 1 \right]^a \quad (5.3-27)$$

$$\text{with } a = -\frac{1}{20 K} \cdot (T - 323.15 K), a \in [0,1]$$

i_* is a fitting parameter and was set to 2.5 A/cm² in this model. The corrected $U_{transport,cor.}$ is calculated as:

$$U_{transport,cor.} = \xi_{transport,T} \cdot \xi_{transport,p} \cdot U_{transport} \quad (5.3-28)$$

Overall, the cell voltage of the electrolyzer is calculated as:

$$U_{cell} = U_{OC} + U_{\Omega} + U_{kin.,cor.} + U_{transport,cor.} \quad (5.3-29)$$

The subsystem model of the electrolyzer receives the electrical power P_{el} as input. A nested interval approach between the maximum current density of the electrolyzer i_{max} and $i_{min} = 10^{-8} A/m^2$ is used to find the correct cell voltage for the provided P_{el} value. First U_{cell} for the interval boundaries is calculated. With U_{cell} a current density is calculated from the following equation using the number of cells of the electrolyzer n_{cells} and the membrane area $A_{membrane}$.

$$\frac{I}{A_{membrane}} = \frac{P_{el}}{n_{cells} U_{cell}} \quad (5.3-30)$$

The difference between the initial current density for the interval boundary and the one calculated from equation (5.3-30) is used as error in the nested interval approach and decides which side of the interval should be replaced. The advantage of this algorithm is a guaranteed convergence as long as the value is within the initial limits of the interval. This holds true for all cases except where the power is set to 0 W, which is handled separately.

Figure 5.3-19 shows the V-HAB model structure of the electrolyzer.

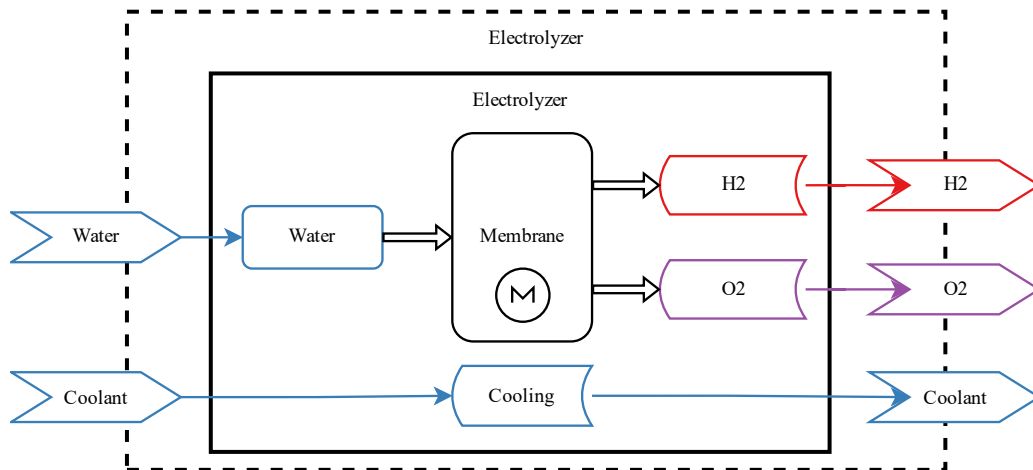


Figure 5.3-19 V-HAB model structure of electrolyzer.

5.3.8.2 Validation

In order to validate the system behavior, the values from (Suermann et al. 2016) are compared to the simulation at different pressures and temperatures. The open circuit voltage is not shown in these figures, but as equation (5.3-14) shows the open circuit voltage, and therefore also the required power for electrolysis, increases with increasing gas pressures and increasing temperature. Therefore, even if the following figures show a potential decrease in overpotentials for higher pressures, the overall required energy will still increase with increasing gas pressures. Figure 5.3-20 shows the behavior of overpotentials for different current densities and pressures.

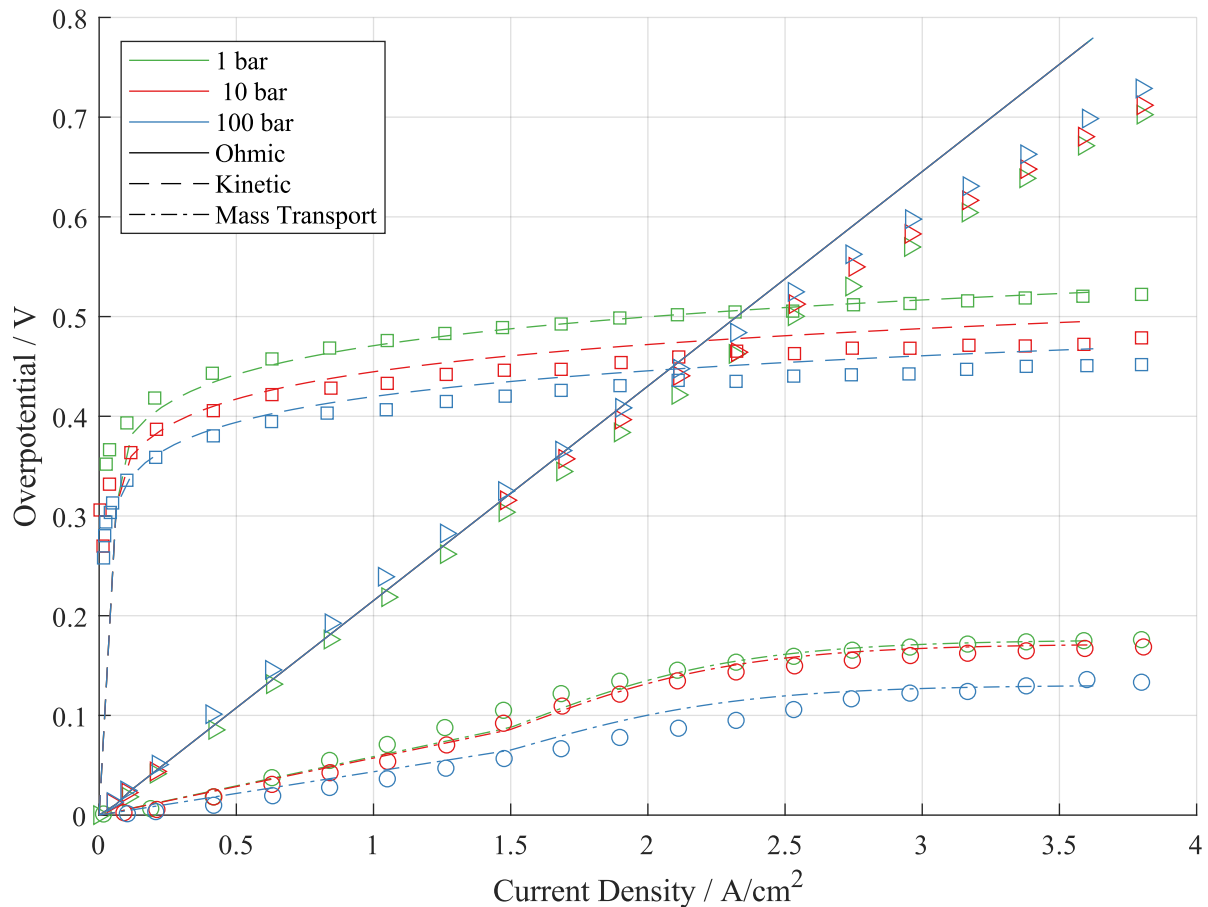


Figure 5.3-20 Overpotentials in the electrolyzer model at different pressures compared to data (squares, triangles and circles for the respective overpotentials) from (Suermann et al. 2016).

While Figure 5.3-21 shows the relation between temperature and the overpotentials at different current densities.

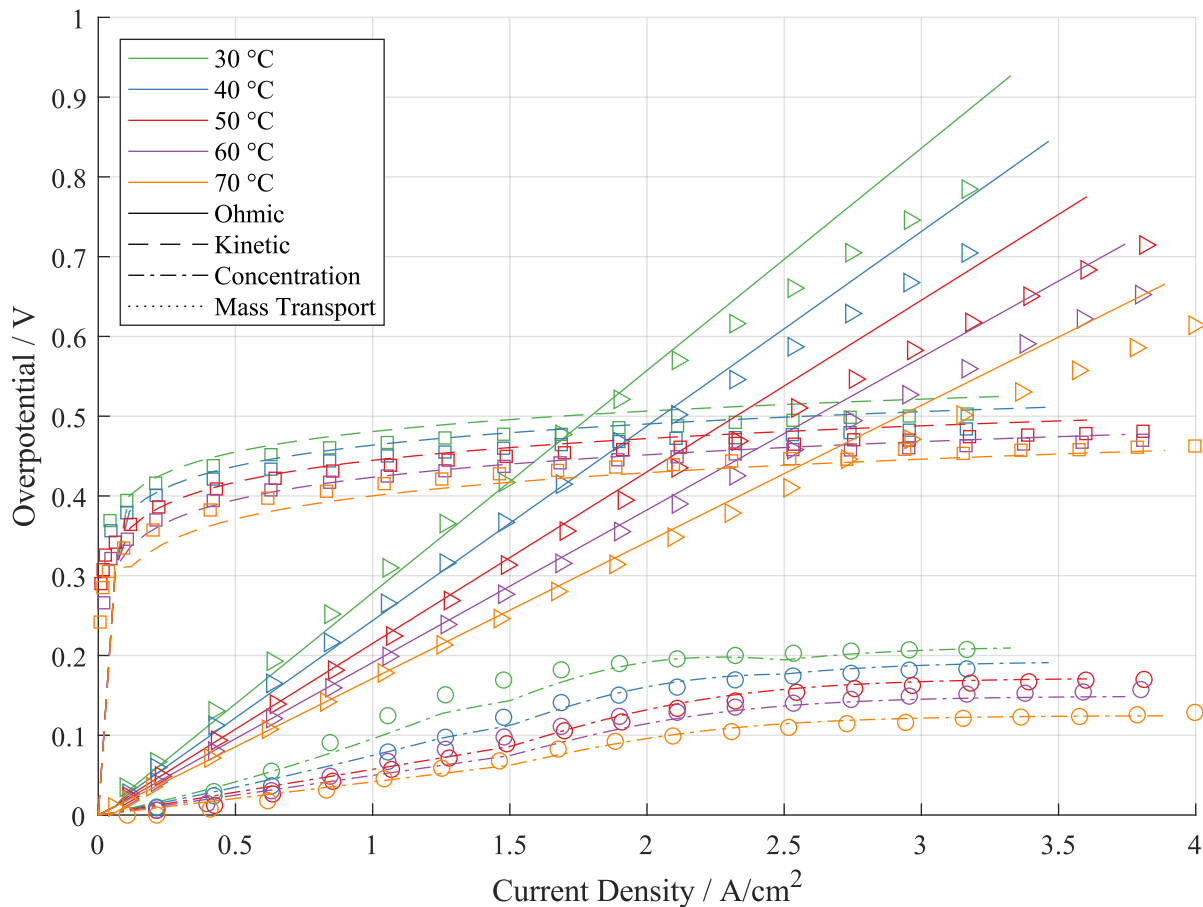


Figure 5.3-21 Overpotentials in the electrolyzer model at different temperatures compared to data (squares, triangles and circles for the respective overpotentials) from (Suermann et al. 2016).

In both Figure 5.3-20 and Figure 5.3-21 the ohmic overpotential is modelled accurately at current densities below 2 A/cm^2 but for higher current densities the ohmic overpotential deviates slightly from the linear behavior modelled by the ohmic law. In addition, the impact of pressure on the overpotential shown in Figure 5.3-20 was deemed too small to be included in the model. Therefore, the ohmic overpotential is overestimated at high current densities. This is not considered an issue as the model is usually operated at lower current densities and for higher current densities the model is conservative, as the overpotential is overestimated. The kinetic overpotential is well represented by the model with regard to pressure. For high temperatures, the kinetic overpotential is underestimated slightly. This could be adjusted by introducing another correction factor, but the differences are considered small and therefore the current simpler implementation is deemed sufficient. Overall, the basic behavior and relation between temperature and pressure for the kinetic overpotential is modelled correctly. The mass transport overpotential required the most complex modelling approach, as the currently used equations to model this overpotential (see (Falcão and Pinto 2020)) do not include pressure and would result in an increasing mass transport overpotential for increasing temperatures. Overall, the mass transport overpotential from the model for both pressure and temperature influences matches the data well.

5.3.9 Ilmenite Hydrogen Reduction Reactor

The selection of the ISRU reactor process and the derivation of the reaction kinetics model was performed by Laura Grill and is described in (Kaschubek et al. 2021). The following sub-chapters are also from this publication and were only adjusted in formatting to this thesis. The cited passages in this chapter were the contribution of the author of this thesis to the paper and describe the model developed based on the reaction kinetics.

5.3.9.1 Modelling Approach

“The ISRU reactor model combines the reaction kinetics reaction model with solvers for mass and thermal flows to provide a holistic subsystem model in V-HAB. A simplified Condensing Heat Exchanger (CHX) model recovers the generated water from the gas loop and calculates the temperature change of the coolant water as a thermal load for the ECLSS. In addition, the required electrical energy of the ISRU reactor at different operating times and the water production rate interface with the ECLSS and RFCS. A 1-D model consisting of 10 cells represents the regolith and gas within the reactor. All view factors are calculated analytically based on (Gesellschaft Verfahrenstechnik und Chemieingenieurwesen 2013).

We assumed the lunar surface to be in thermal equilibrium at 250 K without the reactor. A cylinder with 10 m diameter and 10 m depth represents the lunar surface, where the first cell has the same diameter as the reactor and the remaining cells are equally spaced. The boundary condition to the remaining lunar surface was set to a constant temperature of 250 K. Figure 5.3-22 provides an overview of the reactor model with three instead of ten cells.

As a first step, we derived the optimum operating conditions for the reactor, assuming the same thermal insulation and reactor shell thickness for all cases. The geometry of the reactor was set to minimize the area to volume ratio. For this purpose, the equation for the height of the reactor based on the regolith mass and reactor radius,

$$H_{Reactor} = \frac{m_{Regolith}}{\pi \cdot r_{reactor}^2 \cdot \rho_{Regolith}} \quad (5.3-31)$$

is combined with the equation for the surface area of a cylinder:

$$A_{Reactor} = 2 \cdot \frac{m_{Regolith}}{\rho_{Regolith}} \cdot \frac{1}{r_{reactor}} + 2 \cdot \pi \cdot r_{reactor}^2 \quad (5.3-32)$$

Differentiating this equation and setting it to zero results in the following equation for the optimal radius:

$$r_{reactor} = \sqrt[3]{0.5 \cdot \frac{m_{Regolith}}{\pi \cdot \rho_{Regolith}}} \quad (5.3-33)$$

” (Kaschubek et al. 2021)

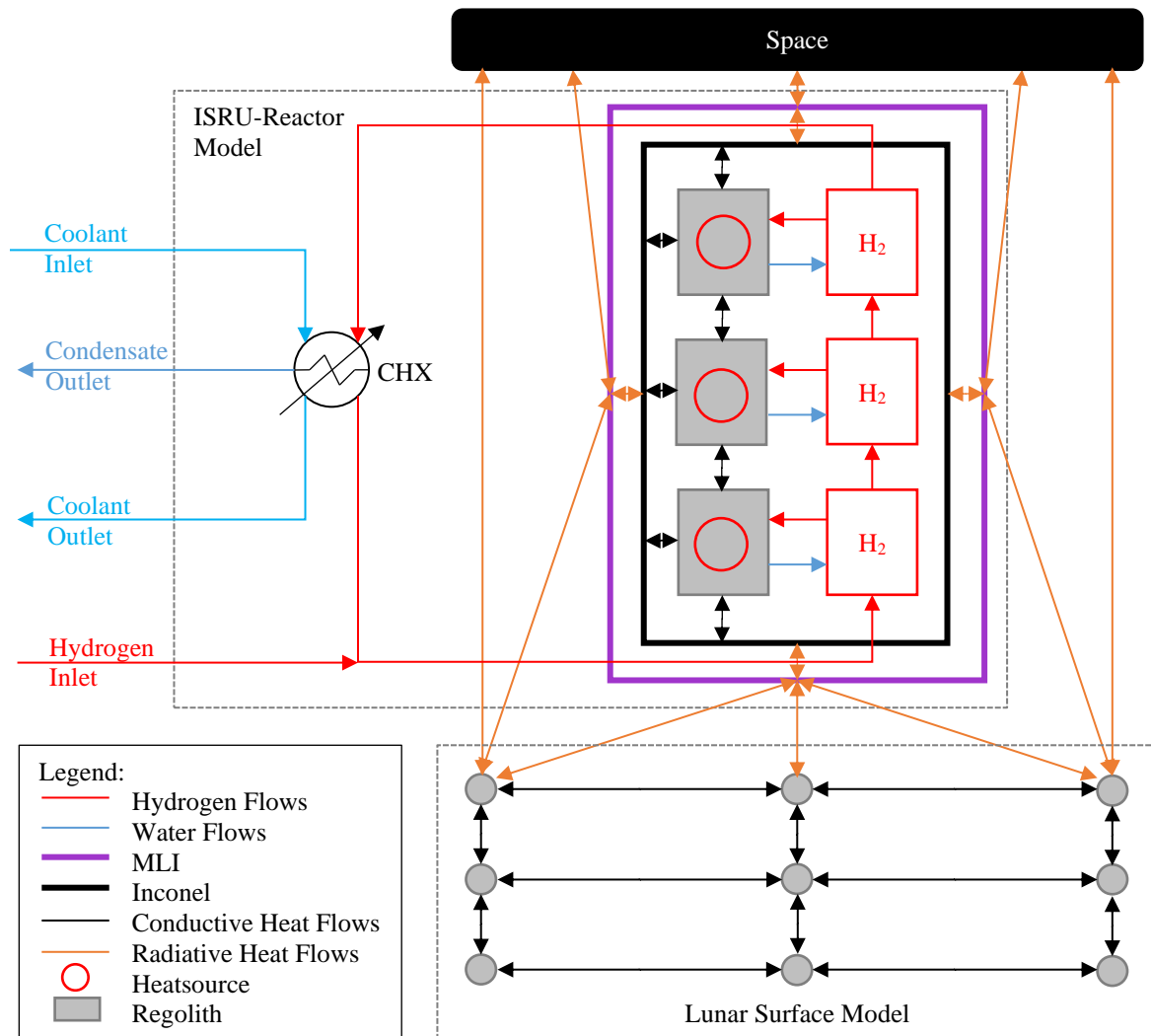


Figure 5.3-22 Overview of the ISRU reactor model. The number of cells is reduced to three compared to 10 in the model. (Kaschubek et al. 2021)

The reaction kinematics from equation (8) of the paper are used “...to calculate the theoretic time to reach 90% conversion by solving it for the time t . An iterative calculation then estimated the possible number of batches per day based on the time to reach conversion, the required pre-heat time and the time to refill and empty the reactor per batch. The required preheat time is calculated with the following equation.

$$t_{preheat} = m_{Regolith} \cdot c_{p,Regolith} \cdot \frac{T_{Reactor} - T_{Regolith}}{P_{Heater} - \dot{Q}_{Loss}} \quad (5.3-34)$$

Where the heat losses to the environment \dot{Q}_{Loss} are estimated using the equation.

$$\dot{Q}_{Loss} = ((T - \Delta T_{insulation})^4 - 3^4) \cdot A_{Reactor} \cdot \frac{\sigma}{\frac{1 - \epsilon_{Shell}}{\epsilon_{Shell}} + \frac{1 - \epsilon_{Regolith}}{\epsilon_{Regolith}}} \quad (5.3-35)$$

The parameter $\Delta T_{insulation}$ represents the temperature difference between the outer shell and the inside of the reactor and was set to 420 K. At this value, the heat loss of the simplified calculation is close to the heat loss in the detailed discretized calculation. The estimation of the required reactor size before the parameter study results in a more comparable water production for the different considered reactor set points.



To select the optimal operating conditions we calculated the ESM of the reactor for the different operating conditions with the ESM equation and equivalency factors for the Moon from (Anderson et al. 2018: 23). We are aware that the ESM factors provided there are not specifically for the selected system combination proposed in this paper, but we used them as the baseline ESM values used by NASA to compare individual subsystem for the lunar surface. In addition, we performed a sensitivity analysis of the results to decide if we should further scrutinize the ESM factors. The reactor mass was calculated from the mass of the shell based on the shell thickness and material values from Table 5.3-4 and the reactor geometry from equations (5.3-31) and (5.3-33). The model shown in Figure 5.3-22 calculates the required cooling for the CHX and the heat losses to environment as well as electrical power demand of the ISRU reactor. We averaged these values after a simulation period of one day and used them for the ESM calculation.

Table 5.3-4 provides an overview of the parameters for the optimization of the ISRU reactor. The parameters which are changed during the optimization are the maximum available heater power P_{Heater} in the range of 3,500 W to 7,500 W and the operating temperature of the reactor $T_{Reactor}$ in the range of 1,000 K to 1,450 K.” (Kaschubek et al. 2021)

Table 5.3-4: Parameters used for the ISRU reactor optimization. (Kaschubek et al. 2021)

Set Point Conditions	Unit	Value
Shell Material	-	Inconel
Shell Thickness	m	0.05
Effective Emissivity MLI ϵ_{MLI}	-	0.005
Emissivity Outer Reactor Shell ϵ_{Shell}	-	0.1
Emissivity Regolith $\epsilon_{Regolith}$	-	0.8
Density of Regolith $\rho_{Regolith}$	kg/m ³	1,450
Heat Capacity of Regolith $c_{p,Regolith}$	J/kg·K	800
Moon Surface Temperature $T_{Regolith}$	K	250
Reaction Enthalpy	kJ/mol	+40.6
Ilmenite Ratio	wt%	80
Activation Energy	kJ/mol·K	156
Pre exponential factor	1/s	661
Volume ESM Factor V_{eq}	kg/m ³	9.16 ¹³
Power ESM Factor P_{eq}	kg/kW	76
Cooling ESM Factor C_{eq}	kg/kW	102

¹³ The volume equivalency factor is for unshielded inflatable volume. The mass of the reactor shell is considered separately by assuming an Inconel shell with the provided geometry parameters. Therefore, this relatively low equivalency factor accounts only for lightweight additional packaging around the reactor and its electronics, excluding the reactor shell.

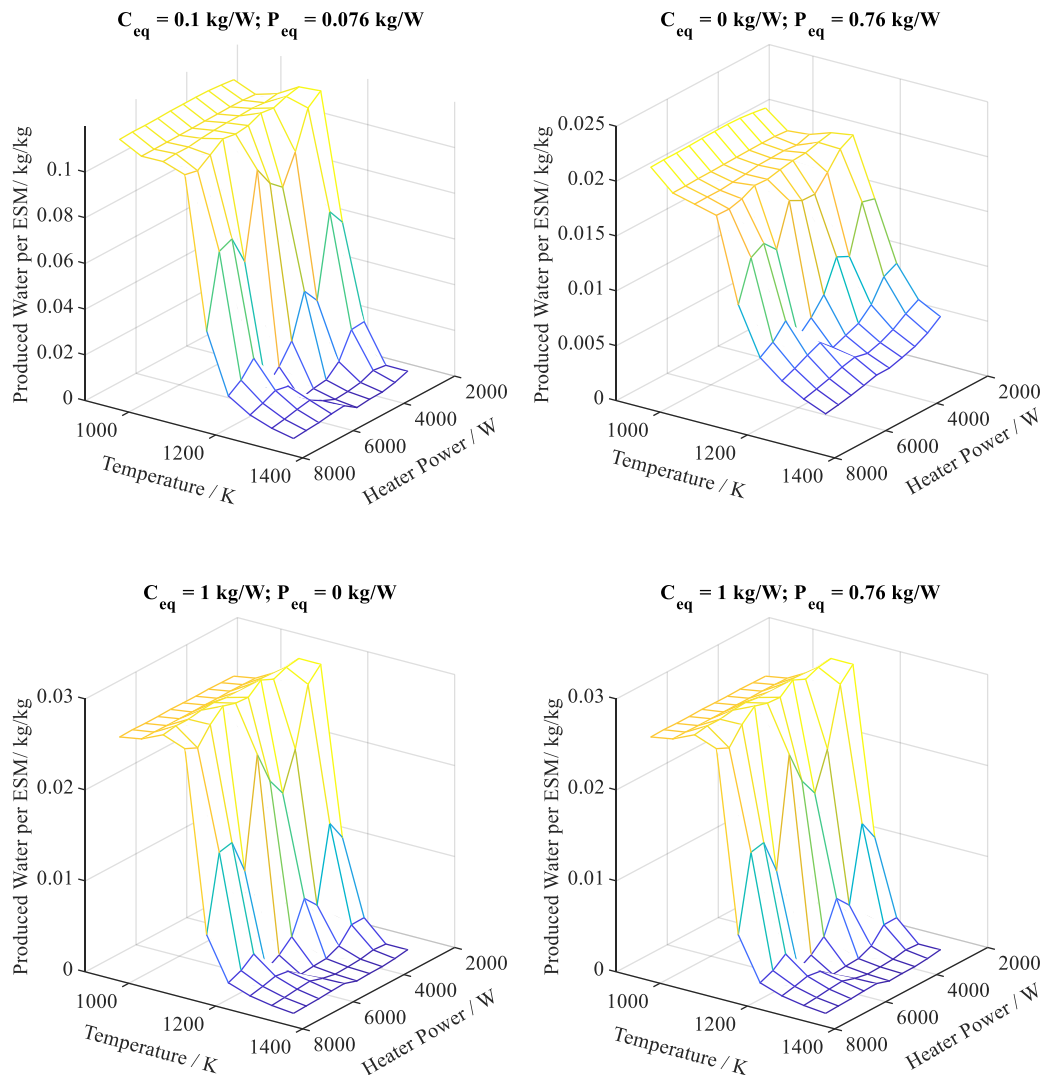


Figure 5.3-23 Results of ISRU reactor optimization in produced water per day per ESM with different equivalency factors for power and cooling. (Kaschubek et al. 2021)

Figure 5.3-23 “shows that temperatures below 1,150 K result in better water-per-ESM values than higher temperatures even though the necessary reactor size increases with lower temperatures. In addition, this behavior is insensitive to the selected ESM factors, as varying them between 0 and 10 times the initial value still favors lower temperatures. The absolute optimum is located at 3,000 W and 1,150 K. The differences between values in the range of 950 K to 1,100 K and 3,000 W to 7,500 W is minimal with an average of 0.1115 kg/kg and a deviation of +/- 0.007 kg/kg (or 6.3 %) for the nominally selected ESM factors. At 1,150 K values are similar, but at that location only heater powers below 3,500 W result in favorable values. Because the differences are small, we did not further consider ESM factors for this analysis and did not derive specific ESM factors for the overall system used in the design. Temperatures lower than 1,000 K were included but are not considered valid options since the reaction kinetics become unfavorable at low temperatures and the data on which the kinetic model is based on is limited to 1,073 K (see also Figure 5 from (Kaschubek et al. 2021)).

The reactor operating conditions were set to 5,500 W and 1,000 K for the following analysis because with these values the reactor is in a stable close to optimal operating point. We did not choose the absolute optimum of 3,000 W and 1,150 K because it is very close to large performance limitations in case of small temperature fluctuations. Based on Figure 4 from (Kaschubek et al. 2021) the required C/D ratio for the Mount Kocher and Shackleton South East site is 50 %. Since the reactor is designed to supply the required oxygen for a crew of six (i.e. 0.816 kg/(CM·d) (Anderson et

al. 2018: 63)), the respective mass of water that the reactor should produce is 5.5 kg/d. For contingency it is increased to 6 kg/d and together with the C/D ratio of 50 %, the reactor shall produce 9 kg/d of water.

For the selected reactor operating conditions of 1,000 K reaction temperature and 5,500 W heater power and the daily water production of 9 kg/d the ideal geometry is calculated to 34.74 cm diameter and height using equations (5.3-31) and (5.3-33).” (Kaschubek et al. 2021)

5.3.9.2 Verification

As no actual system exists which is modelled in the case of the ISRU reactor, a validation where the simulation is compared to test results is not possible. For this reason, a verification was instead performed to ensure that the model is a realistic representation of a potential system. Figure 5.3-24 and Figure 5.3-25 show the temperature of the reactor itself and of the modelled lunar surface. The lunar surface temperature was assumed to be 250 K and the reactor temperature set-point was assumed to be 1,000 K. Therefore, the results of the model are within the expected results.

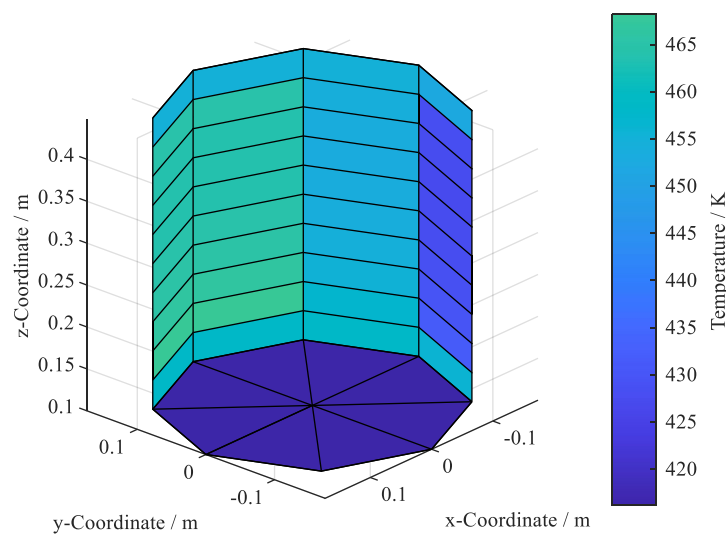


Figure 5.3-24 Outer temperature of the ISRU reactor. The warmer front side points towards the sun. (Kaschubek et al. 2021)

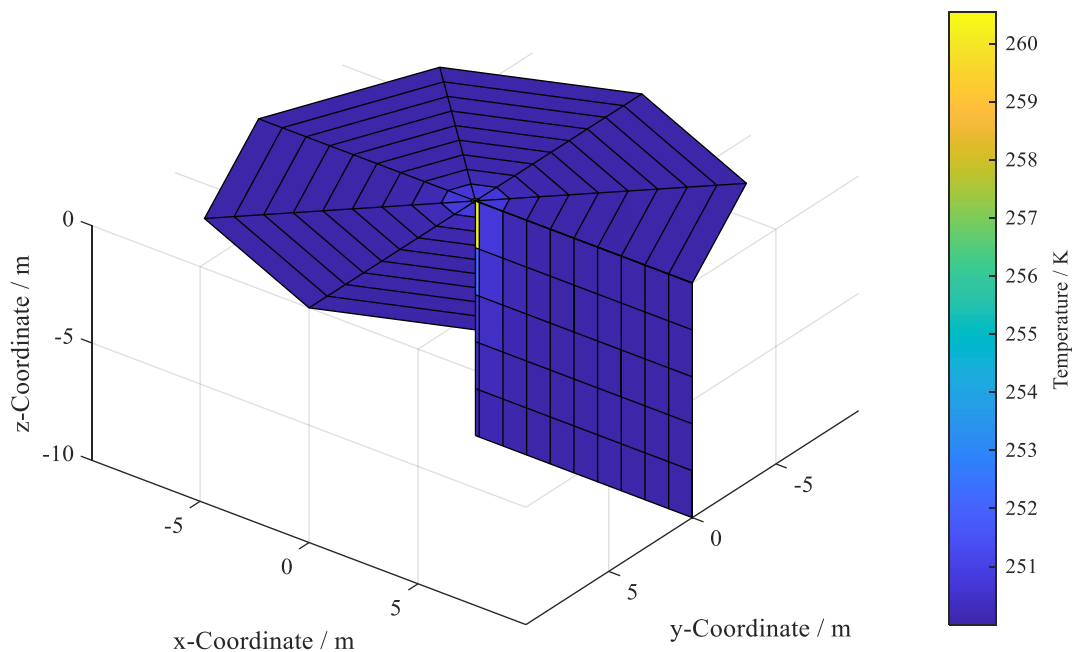


Figure 5.3-25 Temperature of the lunar surface below the reactor. The shadow of the reactor is not considered. (Kaschubek et al. 2021)

As Figure 5.3-25 “shows, only the surface directly below the reactor heats up by a significant amount. The lunar surface temperature farther away than the modelled cylinder is therefore not included in the model. For the view-factors between the reactor and the lunar surface an infinite flat surface is assumed to stretch out from the outer most cell which also receives the corresponding heat flow from the reactor.” (Kaschubek et al. 2021)

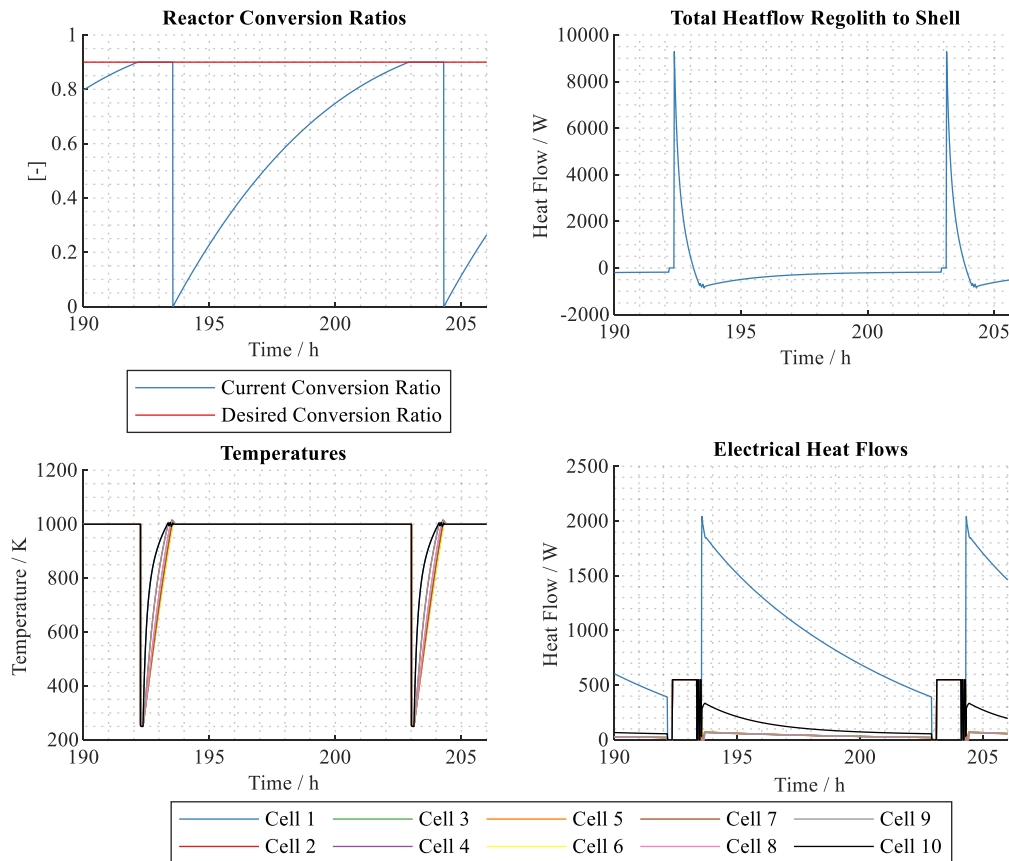


Figure 5.3-26 ISRU reactor values. Top left corner shows the current conversion ratio of ilmenite in blue and the desired conversion ratio of 0.9 in red. The top right corner shows the total heat flow between the regolith and the reactor shell. Bottom left corner shows the temperatures of the cells in the reactor and bottom right corner shows the heat flow of the electrical heaters within the reactor cells. (Kaschubek et al. 2021)

Figure 5.3-26 “shows that the time to process one batch of regolith with 47.75 kg of regolith containing 80% of ilmenite is 10.77 h. The average daily water mass produced by the reactor is 9.18 kg and the average electrical power consumption is 2,000 W. These values are used in the next chapter to size the ECLSS and RFCS.” (Kaschubek et al. 2021)

With regard to the verification Figure 5.3-26 also shows that the electrical heat flows remain positive and within the expected values as does the reactor temperatures. Overall, the verification is therefore considered successful as all parameters remain within the expected range.

5.4 Biological Life Support Subsystem Models

5.4.1 Plant Model

The plant model of V-HAB is based on the modified energy cascade (MEC) model initially described by (Cavazzoni 2004) and later adjusted by (Boscheri et al. 2012). The MEC model is also described in (Anderson et al. 2018: 185–93) as the basic plant model used by NASA for ECLSS analysis. Chapter 3.3.1 includes a comparison of the model with other plant models but as chapter 4.1.2.1 discusses only the MEC model is further considered. The limitations of the model with regard to produced humidity, which chapter 3.3.1.1 mentioned, were resolved through a new algorithm implemented into the model by (Stölzle 2013) and (Saad 2015).

5.4.1.1 Modelling Approach

The MEC model is a so called “explanatory crop model”, which means it is not developed on first principles like e.g. the plant model from (Poulet et al. 2020) but is fitted to experimental data of the modelled crop species. It uses the basic assumption that plant growth can be separated into three phases:

- Time of canopy closure t_A
- Time of onset of canopy senescence t_Q
- Time of crop maturity t_M

Figure 5.4-1 shows the daytime CO_2 exchange during these phases in the MEC model. The CO_2 exchange is directly proportional to the photosynthesis and the crop growth rate. During the initial phase, the crop leaf canopy is not yet closed, which allows exponential growth, as new leaves result in additional area for photosynthesis. After the time of canopy closure new leaves overshadow already existing leaves, which means the growth becomes linear, as the available area for photosynthesis and therefore also the growth rate and CO_2 exchange becomes constant. After the time of canopy senescence, the photosynthesis declines linearly up to the time of crop maturity at which the crop is harvested.

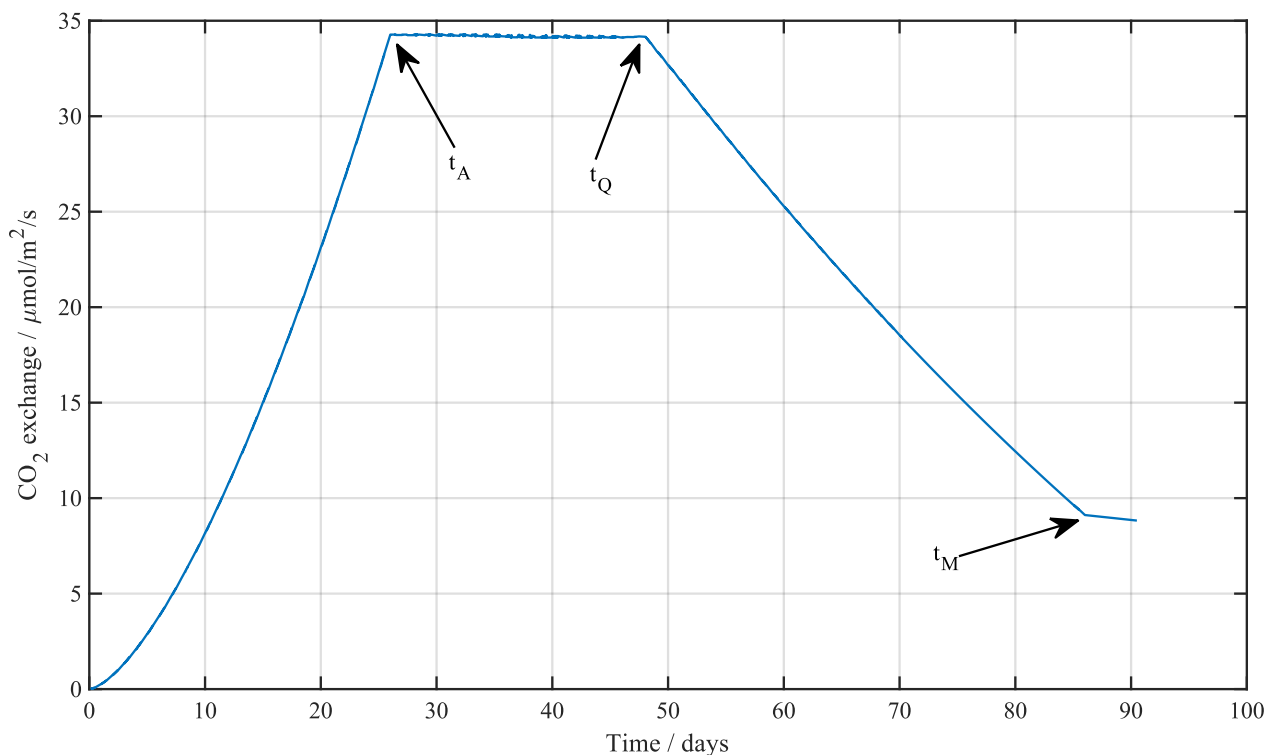


Figure 5.4-1 Exemplary daytime CO_2 exchange for the MEC model.

The required parameters to model the different plants in the MEC model are from (Anderson et al. 2018: 185–93) and were not adjusted for the V-HAB model.

Here the basic calculations of the MEC model will not be discussed further, as they are identical to the cited literature. Instead, this chapter will now discuss the addition of nutrient uptake mechanics to the MEC model. In a basic version the nutrient consumption was added to the original MEC model by (Boscheri et al. 2012) based on the crop growth rate of the MEC model and a nutrient consumption fraction per dry biomass. While this approach is sufficient to calculate the required mass of nutrients for the ECLSS it is not sufficient to depict the behavior of plants during varying nutrient supply conditions as the basic assumption that nutrients are non-limiting remains. In this research the objective is to predict whether dynamic changes in nutrient supply, due to the effects of a biological recycling system like CROP, inhibit or limit plant growth. For this purpose, a first principle nutrient uptake model must be included in the MEC model. This was achieved by (Nikic 2017) for the V-HAB plant model in a basic initial implementation of nitrate uptake dynamics for tomatoes with a Michaelis-Menten kinetic (Nikic 2017: 65).

$$\dot{n}_{nutrient} = \frac{J_{max} \cdot (C - C_{min})}{K_m + (C - C_{min})} \quad (5.4-1)$$

$\dot{n}_{nutrient}$	molar uptake of nutrient	J_{max}	maximum molar influx
C	molar concentration in solution	C_{min}	minimum molar solution concentration for uptake
K_m	Michaelis-Menten Parameter		

Another aspect is the separation into structural nutrients, which are incorporated in the grown biomass, and stored nutrients, which are stored in vacuoles of root and shoot cells (Tischner 2000: 1005). If a nutrient deficiency occurs the growth is limited by the ratio ζ_{growth} of available nutrients from either nutrient uptake or from storage $m_{nutrient,available}$ to the required structural nutrients for nominal plant growth $m_{nutrient,required}$ (Nikic 2017).

$$\zeta_{growth} = \frac{m_{nutrient,available}}{m_{nutrient,required}} \quad (5.4-2)$$

The implementation from (Nikic 2017) had to be adapted to be used in larger simulations, as the nutrients consumed by the plants were placed in completely separate phases, which were not emptied during harvesting. This is not a problem as long as only one generation is modelled. However, if multiple generations are modelled, the nutrients from the previous generation would remain to supply the next generation. In addition, the earlier implementation lacked a mechanism to reduce the night-time transpiration if the growth of the plants was limited by nutrient deficiencies. This resulted in high transpiration rates during the night phase even if no plants had grown due to a lack of nutrients. Furthermore, despite the previous nutrient uptake limitations, no other effects were considered after the first occurrence. This was caused by reducing plant growth only for the time when the nutrient deficiency occurred, but not tracking how this deficiency affected overall plant growth. For that reason, an additional parameter was implemented that tracks the potential inedible biomass without nutrient deficiency $m_{inedible,ideal}$ and compares it to the current actual inedible biomass $m_{inedible,actual}$. The ratio ζ_{global} between these two values is used to reduce the overall growth.

$$\zeta_{global} = \frac{m_{inedible,actual}}{m_{inedible,ideal}} \quad (5.4-3)$$

$m_{inedible,actual}$ is calculated by integrating the MEC flowrate without nutrient deficiency over the growth time of the culture and is reset while the culture is harvested. Through this approach, all effects except the nutrient limitation are included in the value of $m_{inedible,actual}$ and the ratio ζ_{global} only includes effects from nutrient limitations. The basic logic for this approach is, that plants which had limited nutrient supply grew smaller and therefore also have reduced growth and other exchange values later on. This is a simplification, but as the objective of the model is to identify potential issues in plant nutrient supply and not to model the plant behavior during nutrient limitation correctly, this is deemed sufficient for the proposed model.

Another aspect which was not yet included in the nutrient model of (Nikic 2017) are the nutrients required for edible biomass. For each plant, information on how much protein the edible part contains is available from (U.S. Department of Agriculture 2021), which is included in the model now. For each mol of protein, which is modelled as $C_3H_7NO_2$ (see chapter 5.5.2) one mol of nitrogen is required. This consumption is added to the model to ensure the nitrogen cycle is

depicted correctly. In order to model varying levels of nutrients, a more detailed plant model would be required, which would result in a completely new development for a plant model. Since the objective of this research is not to accurately depict what occurs during deficiency, but rather to predict whether deficiencies occur at all, the chosen implementation is sufficient for the proposed studies.

Figure 5.4-2 provides an overview of the plant model implementation in V-HAB. The exchange of gases with the atmosphere is handled via a flow phase that interacts with the environment in which the plants are placed. The nutrient solution similarly passes through a flow phase in the plant module, allowing the plants to remove the required nutrients and water. The whole nutrient uptake initially enters the storage phase, but the required structural nutrients are directly passed on to the balance phase for plant growth. The balance phase serves as location in which a manipulator converts all substances to the desired biomass, which is then stored in the plants phase.

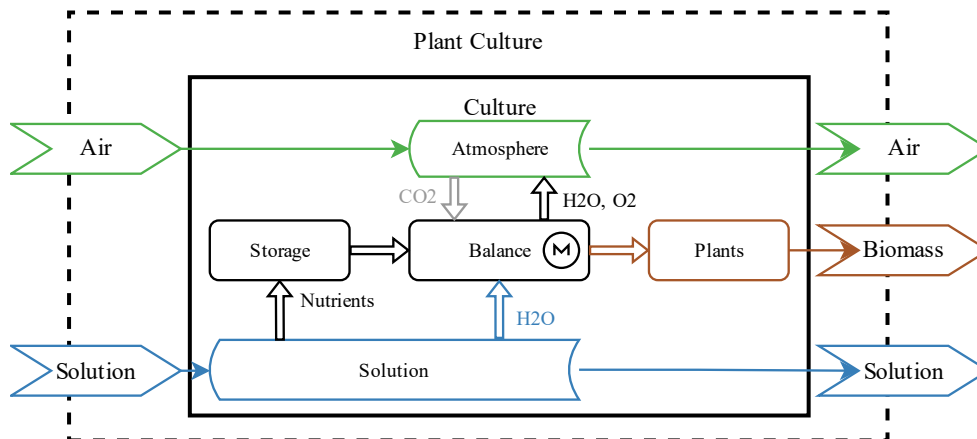


Figure 5.4-2 Overview of plant model in V-HAB.

The actual calculations for the plant growth are placed in two separate function files, which are called by the exec function of the plant subsystem. One function is used to calculate the MEC model flowrates without adjustments and the second function includes the nutrient dependency and other V-HAB related functionalities.

Since the MEC model does not differentiate between the growth of different inedible plant parts, like roots, stems and leaves, the effect of nutrient deficiency on changes in root biomass to other biomasses cannot be considered in the plant model.

Another important advantage of using the MEC plant model is the option to quickly calculate plant growth under ideal assumptions. For this purpose, the user can specify the number of days for which plant growth shall be assumed before the start of the simulation. The function containing the MEC calculations is then called with a time step of one hour using fixed values for the atmosphere to calculate the plant growth flowrates under ideal conditions with the specified photon flux and other parameters defined for the plant culture. The calculated values for biomass and inedible biomass are then used to calculate the structural nitrate mass and with that value the storage nitrate mass under luxurious nutrient supply. These values, together with the current plant time at the start of the simulation, are then used as inputs for the plant model to initialize the phases with the corresponding masses. This allows V-HAB to model only the critical phases of a biological ECLSS in detail, as the phases where plants have little impact can be quickly estimated using this approach. With plant growth times of more than 100 days for some plants, this severely reduces the required simulation time for case studies and enables a quick analysis of various cases. If a more complex plant model is used, aside from the additional time required for its calculation, it would also likely require a complete simulation of the growth cycle to function properly. Therefore the MEC model is the plant model of choice for this research, as it enables quick comparison of different cases within the desired simulation time as defined by Table 4.3-2. Analyzing the difference in results between the MEC model and a more sophisticated plant model is however still an interesting research objective, but this is considered future work and not part of this thesis.

5.4.1.2 Validation

The validation is performed without nutrient deficient conditions, which are discussed in chapter 5.4.1.3. For validation two different approaches are used. The first approach is to simulate the plants over multiple generations and compare the resulting average values for oxygen production, carbon dioxide consumption, transpiration and biomass growth with the provided values from (Anderson et al. 2018: 179). Figure 5.4-3 summarizes the results of this validation. For all plants except wheat and soybean the plant model underestimates the produced biomass compared to (Anderson et al. 2018: 179) while the values for oxygen production, carbon dioxide consumption and transpiration match the data. The differences in biomass production are likely due to the constant 90% water content assumed for the inedible biomass. Since dry biomass growth is proportional to carbon dioxide consumption, which is better matched, the dry biomass will also show a better overlap. Here the fresh basis was chosen for validation, as it highlights one weak spot of the model, the constant water content of the biomass. Soybean and wheat, where the growth rate and the carbon dioxide consumption are overestimated, are part of the more detailed dynamic validation and will be further discussed with more insights gained from Figure 5.4-4.

The tendency to underestimate biomass growth also showed in experiments performed with a plant growth chamber at the institute, which are further discussed in chapter 5.4.1.4. A limiting factor regarding this validation is the missing information on the CO₂ level during the experiments used as basis for (Anderson et al. 2018: 179). For the validation a constant level of 1,000 ppm CO₂ was assumed since this corresponds to multiple plant tests performed by NASA (Wheeler et al. 1993; Wheeler et al. 1998; Wheeler 2006) and is also within the nominal growth area of the model.

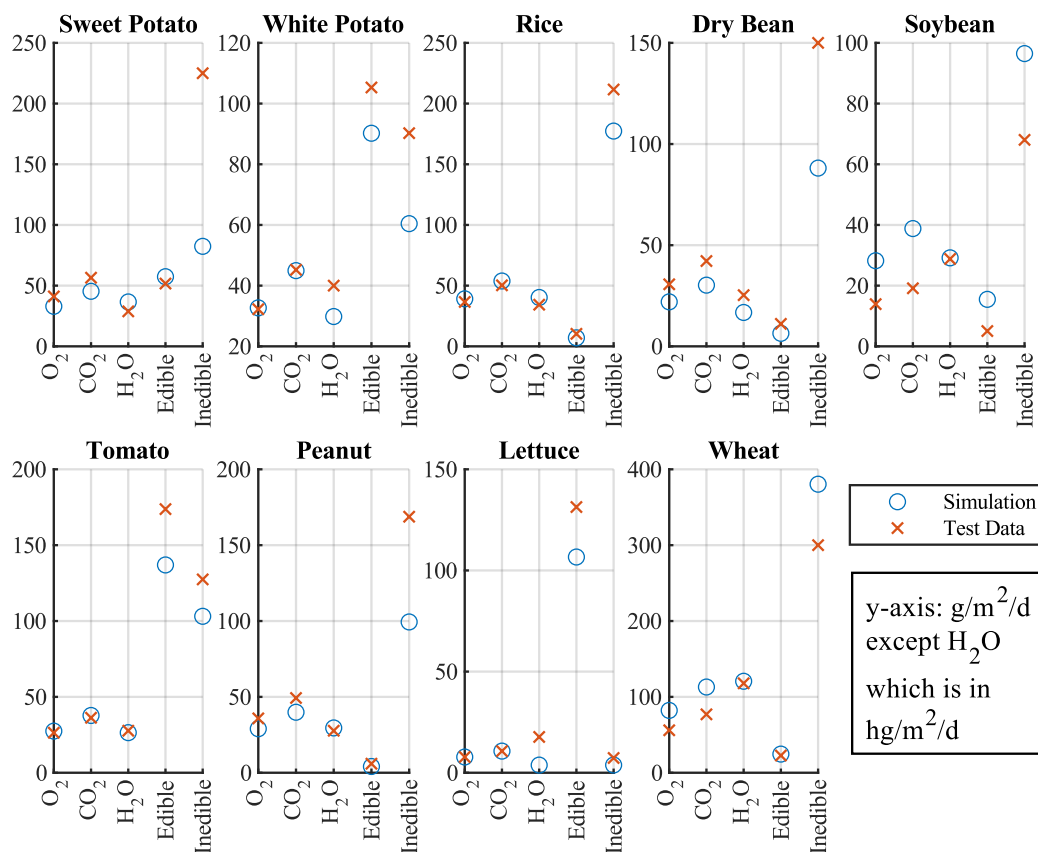


Figure 5.4-3 Average daily flowrate validation for oxygen production (O₂), carbon dioxide consumption (CO₂), transpiration (H₂O) and biomass growth (edible and inedible) of plant model (simulation) compared to test data from (Anderson et al. 2018: 179). Transpiration is in hector-gram per m² and day while all other values are in gram per m² and day.

Figure 5.4-4 shows the results for the dynamic validation, which was performed where suitable data was available. The data used in this validation is the same as used by (Stölzle 2013) and was taken from the available raw data of the master thesis. For soybeans the model matches the data for CO₂ exchange very well. The transpiration is slightly underestimated in Figure 5.4-4. This contradicts the overestimation of the average daily value, which is 2.91 kg/m²/d

for the V-HAB model compared to $2.88 \text{ kg/m}^2/\text{d}$ from (Anderson et al. 2018: 179) as shown in Figure 5.4-3. Therefore, the transpiration for soybean is likely modelled correctly even though Figure 5.4-4 suggests an underestimation. For wheat the time to maturity used in the MEC model is obviously different from the test data. In the model wheat is assumed to reach maturity after 62 days (Anderson et al. 2018: 194) while it requires more time in the test data from (Wheeler et al. 1993). Therefore, the CO_2 and H_2O exchange after the time of maturity are severely underestimated while they are overestimated beforehand. However, since the time to maturity is not a constant but depends on the growth conditions, the value from (Anderson et al. 2018: 194) is kept in the model, as the goal is not to match one specific test of plant growth but provide a general representation of it for different systems. The exchange rates for wheat are still within reasonable bounds and show that the dynamic behavior is not completely off. For potatoes the transpiration rate is underestimated in both the averaged and the dynamic data. Overall, the transpiration model is more accurate than the initial transpiration model used in the MEC model by (Cavazzoni 2004; Boscheri et al. 2012) as is also discussed in detail by (Stölzle 2013: 23–31). However, the model still has room for improvement as the validation data here shows. Since plants have a relatively high variation in productivity however, the values vary significantly between different experiments. Therefore, the current implementation of the plant model is deemed sufficiently accurate, if somewhat conservative for the proposed analysis.

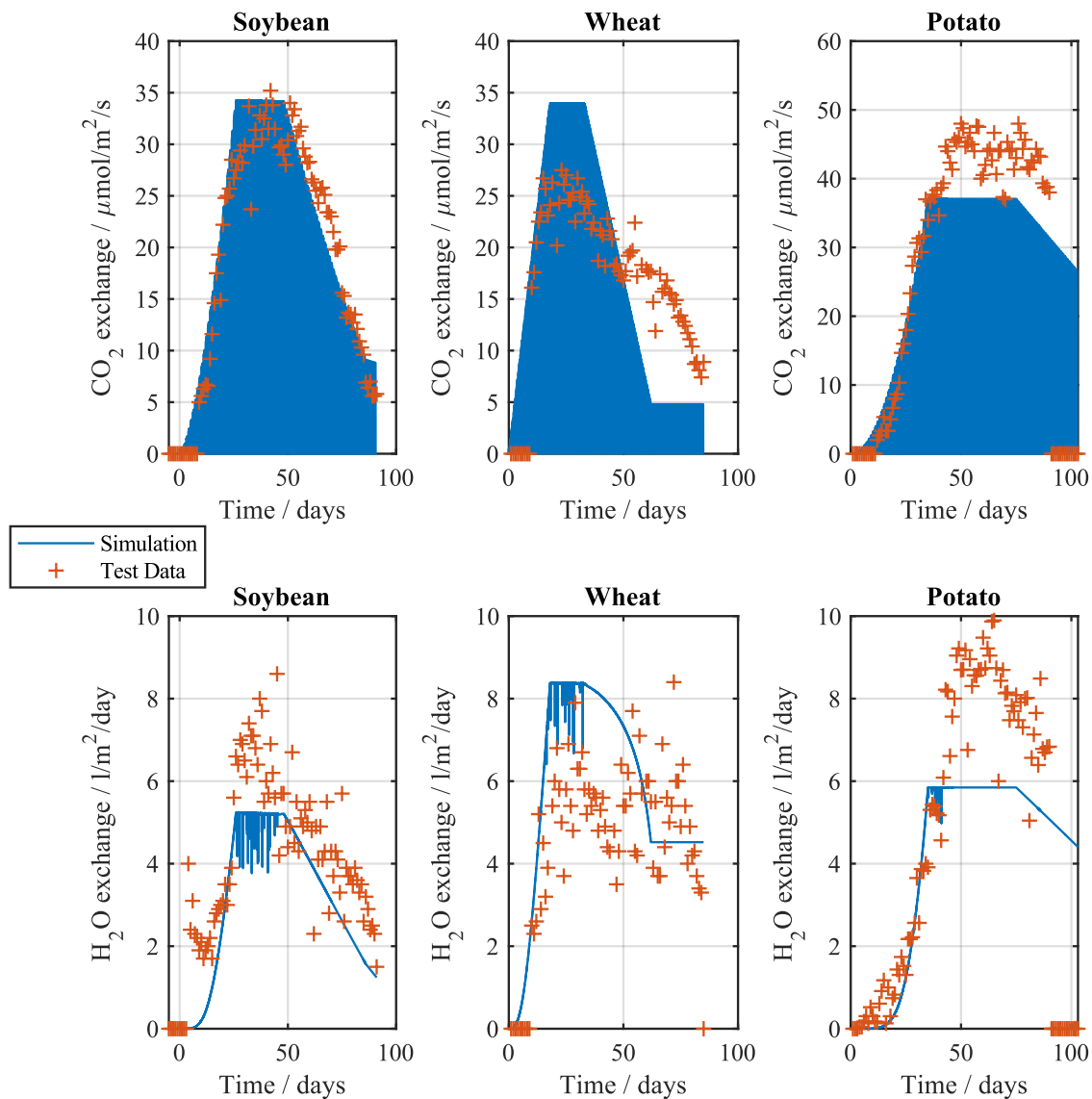


Figure 5.4-4 Dynamic validation of carbon dioxide exchange and transpiration compared to test data from the following sources: Soybean (Wheeler et al. 1998), Wheat (Wheeler et al. 1993) and Potato (Wheeler 2006).

5.4.1.3 Verification

Since an actual validation with test data was not possible for the nutrient dependency of the plant model, especially for all different plants, a qualitative verification of the implemented nutrient dependency is performed instead. For this purpose, lettuce and sweet potato, as a crop with a short harvest cycle and another with a long cycle, are simulated and the nutrient supply is turned off after 80 days. Figure 5.4-5 shows the results of this analysis. For lettuce two generations can be harvested before the nutrient supply is turned off. The nutrient storage is almost sufficient to maintain growth up to the third harvest at 90 days, therefore this generation is likely still useable, if somewhat reduced in growth. For sweet potato the nutrient storage is sufficient to cover the 40 days to harvest at day 120, as only a small amount of structural nitrate is required since the majority of the plant had already grown. The sharp decline at day 120 is the effect of harvesting the potatoes, which shows that this aspect of the model also works as intended.

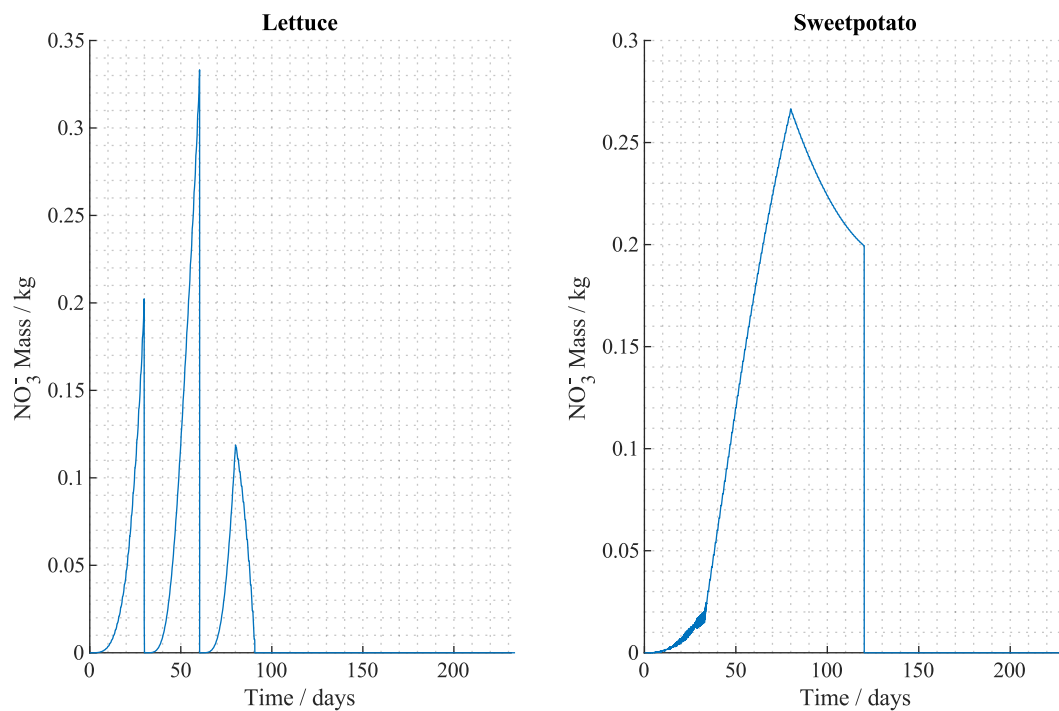


Figure 5.4-5 Nitrate mass in the storage compartment of the plant model with nutrient supply turned off after 80 days.

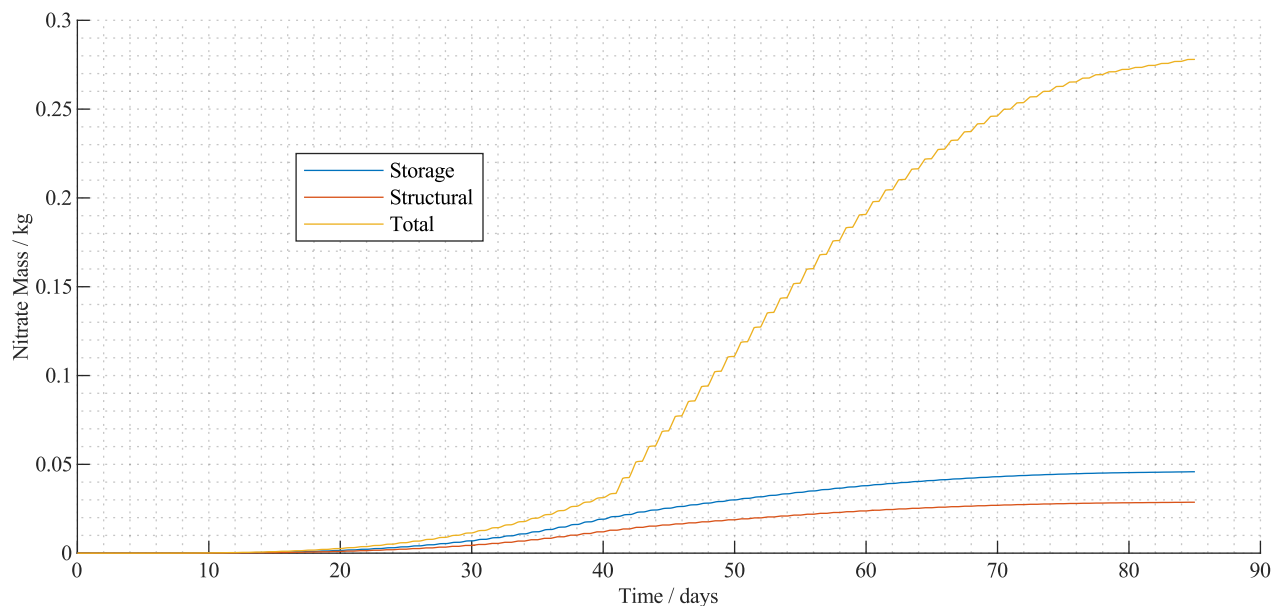


Figure 5.4-6 Nitrate Mass in the different compartments of a tomato plant without nutrient deficiency. Total mass includes nitrogen required for edible biomass and the storage and structural mass contained in the inedible biomass.

Figure 5.4-6 allows a more quantitative comparison to values from (Zhang et al. 2015) for tomato plants. (Zhang et al. 2015) discuss the uptake rate of different nutrients for tomato plants without deficiency and show that a fully grown tomato plant has an uptake rate of nitrate of between 10 and 25 meq/plant/week, which can be transformed to 0.62 to 1.55 g/plant/week by using the molar mass of nitrate of 62 g/mol. The MEC model assumes a planting density of 6.3 tomato plants per m² with 5 m² modelled here. Therefore, the simulation corresponds to 31.5 tomato plants. The uptake after the onset of edible biomass (shortly after day 40 in Figure 5.4-6), where the plants can be considered fully grown, corresponds to an average uptake of 38.89 g/week, which is therefore 1.23 g/plant/week. This is within the range mentioned by (Zhang et al. 2015) and shows that the model is able to predict nutrient uptake realistically. The general behavior of the curves also matches qualitative plant nutrient uptake behavior as discussed by (Nikic 2017: 72).

5.4.1.4 Validation with Hardware Setup

In addition to available data from literature a plant growth chamber for lettuce was built in cooperation with multiple student theses (Bosch 2018; Blank 2019a, 2019b). Figure 5.4-7 shows the developed PGC with an open front side. (Blank 2019b) provides an overview of the chamber and more details on the test setup, which will therefore not be discussed here. In addition to measuring the values for the plants, the test set-up also measures the environmental parameters, which are then used in the simulation to reflect reality as closely as possible. This is the primary advantage of this setup compared to using literature data, where only reported data points can be included in the analysis and dynamics in the environmental conditions are often not reported.

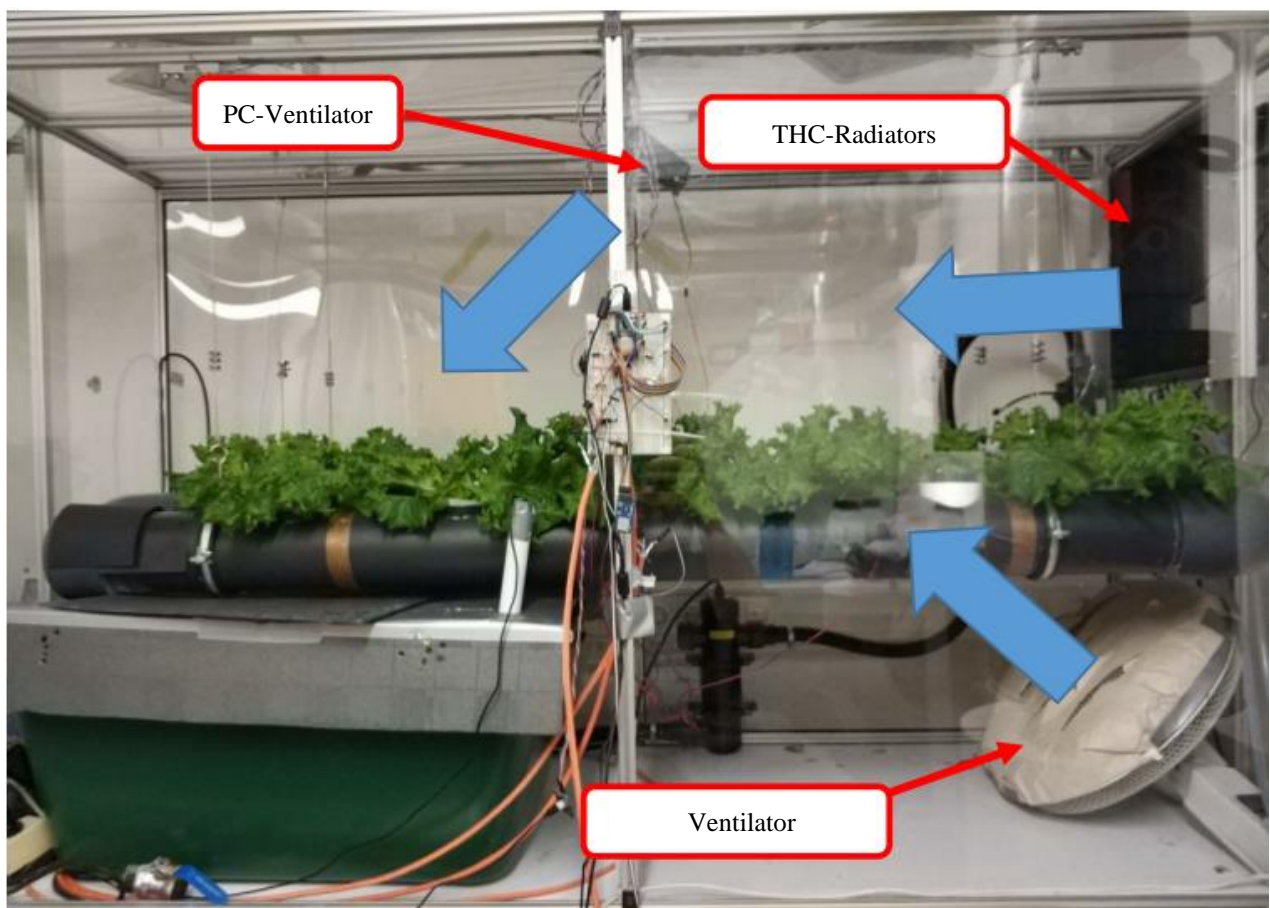


Figure 5.4-7 Picture of the plant growth chamber with an overview of the ventilators and airflows translated from (Blank 2019b: 36).

Overall, four generations of lettuce could be grown in the chamber where the first three generations had various growth limiting effects and the fourth generation had optimal growth (Blank 2019b: 64–9). However, as Figure 5.4-8 shows the plant model accurately predicts the growth for the first three generations while underestimating the growth for the

fourth. This supports the results from chapter 5.4.1.2 that the model is conservative and likely underestimates plant growth. Or using a different viewpoint, it models plant growth under less than optimal conditions.

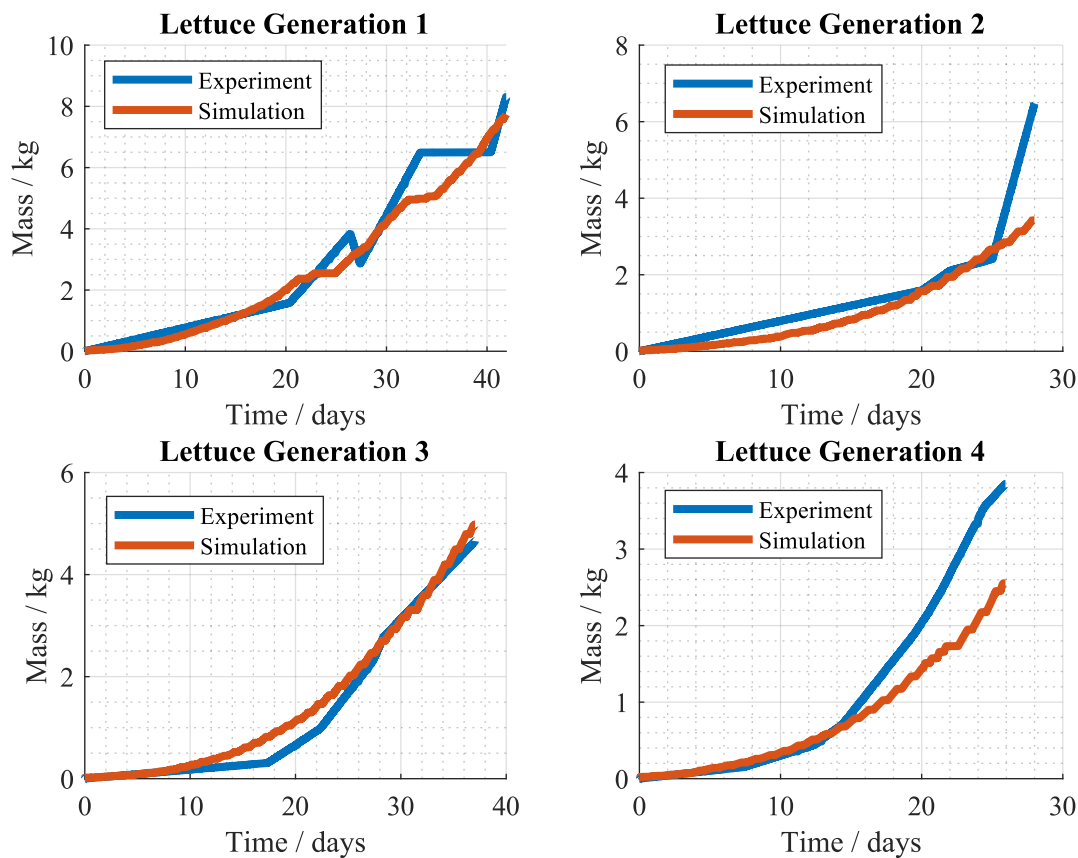


Figure 5.4-8 Biomass from experiment in plant growth chamber compared to simulation. (Blank 2019b: 96)

In addition to the biomass measurements, CO₂ draw down tests were also performed for generations three and four. Since the chamber could not be built completely airtight, the idea for this approach was to measure the conditions inside the chamber and outside the chamber and to model the leakage in the simulation using this data. By then adjusting the leakage rate with the correction factor β_{leakage} the actual leakage during the test is included in the simulation. The CO₂ exchange of the plants was also adjusted using the correction factor β_{CO_2} to fit the draw down profile, which was split into a day phase (light on), followed by a night (light off) and a second day phase (light on). Initially it was unclear whether it is possible to fit the two factors, which depends on the relation between plant CO₂ removal and leakage. By checking the impact each correction factor has on the results (Blank 2019b: 92) proved that only a variation of both factors leads to an overlap between experiment and simulation. This means the information level of the experiment is sufficient to fit both parameters and calculated the impact of both the leakage and the CO₂ exchange of plants on the experiment. Figure 5.4-9 shows the fitted draw down curves for the performed tests while Table 5.4-1 provides an overview of the used correction factors. (Blank 2019b)

The draw down test results also support the conclusion that the plant model underestimates plant growth, as β_{CO_2} factors for almost all cases are higher than one, which means the modelled CO₂ consumption of the plants had to be increased to fit the measurement data.

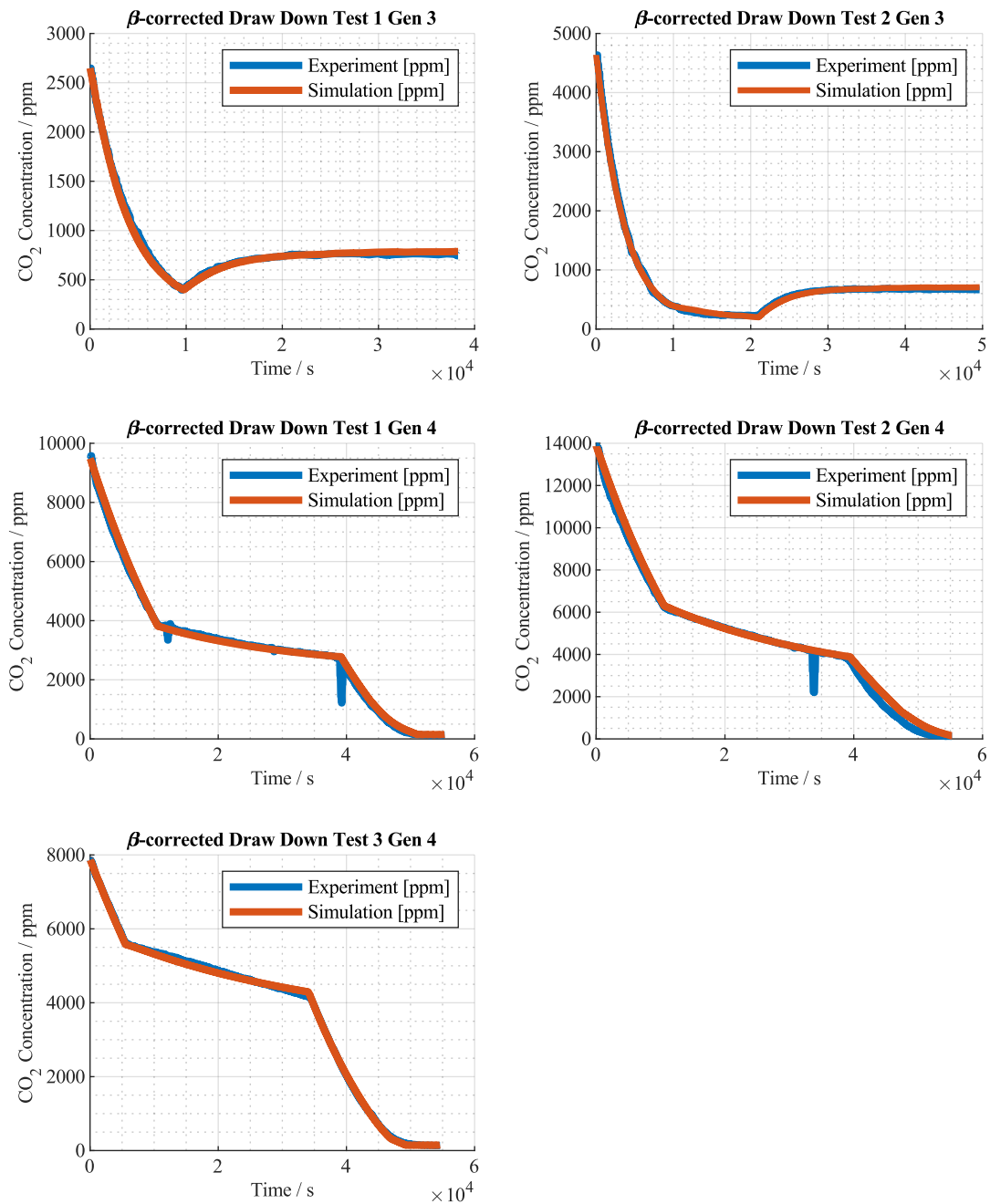


Figure 5.4-9 β corrected CO₂ draw down tests comparison between experiment and simulation. (Blank 2019b: 99).

Table 5.4-1: β correction factor of CO₂ drawn down tests for the PGC adjusted from (Blank 2019b: 100).

CO ₂	β_{CO_2}						$\beta_{leakage}$		
	>1300 ppm	>330 ppm	>150 ppm	>1300 ppm	>330 ppm	>150 ppm			
	day			night			day 1	night	day 2
Generation 3 Test 1	0.95	0.80	-	-	2.83	-	0.64	0.65	-
Generation 3 Test 2	1.28	1.16	1.04	-	2.78	2.78	2.69	2.91	-
Generation 4 Test 1	1.46	1.21	1.10	1.48	-	-	1.71	1.48	1.70
Generation 4 Test 2	1.55	1.25	1.01	1.24	-	-	1.71	1.79	1.01
Generation 4 Test 3	1.33	1.31	0.97	1.53	-	-	1.03	1.03	1.99

5.4.2 Algae

The V-HAB algae model was developed by (Ruck 2018) in cooperation with Tobias Niederwieser from the CU Boulder during a Master's thesis and the results of the modelling are published in (Ruck et al. 2019). In this chapter only the adjustments to the model are discussed, as the basic algae model was not changed.

5.4.2.1 Modelling Approach

The model is separated into two systems, the algae model, which models the growth of *Chlorella vulgaris* algae, and the photo bio reactor (PBR) model, which is used to grow the algae. Figure 5.4-10 provides an overview of the models and their connections.

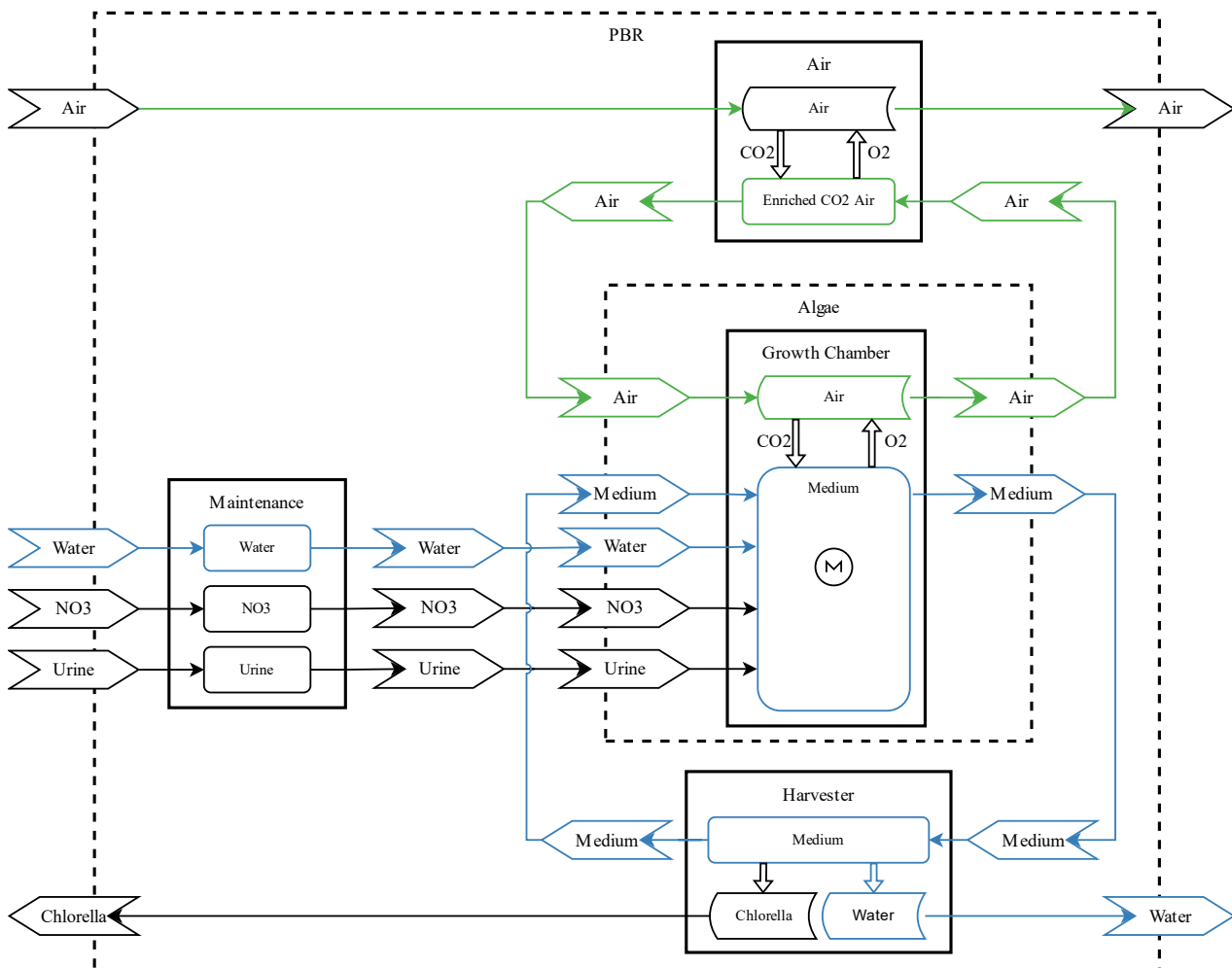


Figure 5.4-10 Model overview of the V-HAB photo bio reactor and algae models.

In the model of (Ruck 2018) the PBR system did not yet have interfaces for nitrate and water supply, as these were supplied from internal buffer stores. To model the nutrient cycling in this research, the interfaces were added to allow the parent system to supply the required nitrate and water. This also required the addition of control logics for this resupply. A minimal operating mode was also added to the PBR. In this minimal mode, the growth rate of algae is not maintained at maximal conditions but rather at minimal conditions. Thus, the algae are kept alive while only consuming minimal amounts of CO_2 . This simplifies the addition of the PBR into a system with a plant growth chamber, which should primarily receive CO_2 during low CO_2 conditions. The basic assumption for algae growth is the Gompertz growth model where the current achievable biomass growth rate depends on the maximum concentration of biomass (Ruck 2018: 15–20). Since different literature values for the maximum concentration and growth rates can be found, which highly impact the required volume and other parameters of the PBR as discussed by (Niederwieser and Klaus 2018), an assumption is necessary. Here, the optimistic but realistic assumption of $3.89 \cdot 10^{-4} \text{ kg}/(\text{m}^3\text{s})$ maximum

growth rate and 18.15 kg/m^3 of maximum biomass concentration from (Ruck 2018: 115) are chosen for the PBR in this research. Figure 5.4-11 shows the resulting growth curves and maximum biomass concentration of the Gompertz model for these assumptions. Since the goal is to maintain optimal growth rate, the PBR tries to operate at the point of maximum biomass increase from the lower diagram of Figure 5.4-11. If the PBR is set to minimal mode, the lighting is reduced, which results in a decrease of *C. vulgaris* concentration and therefore also in a decreased growth rate.

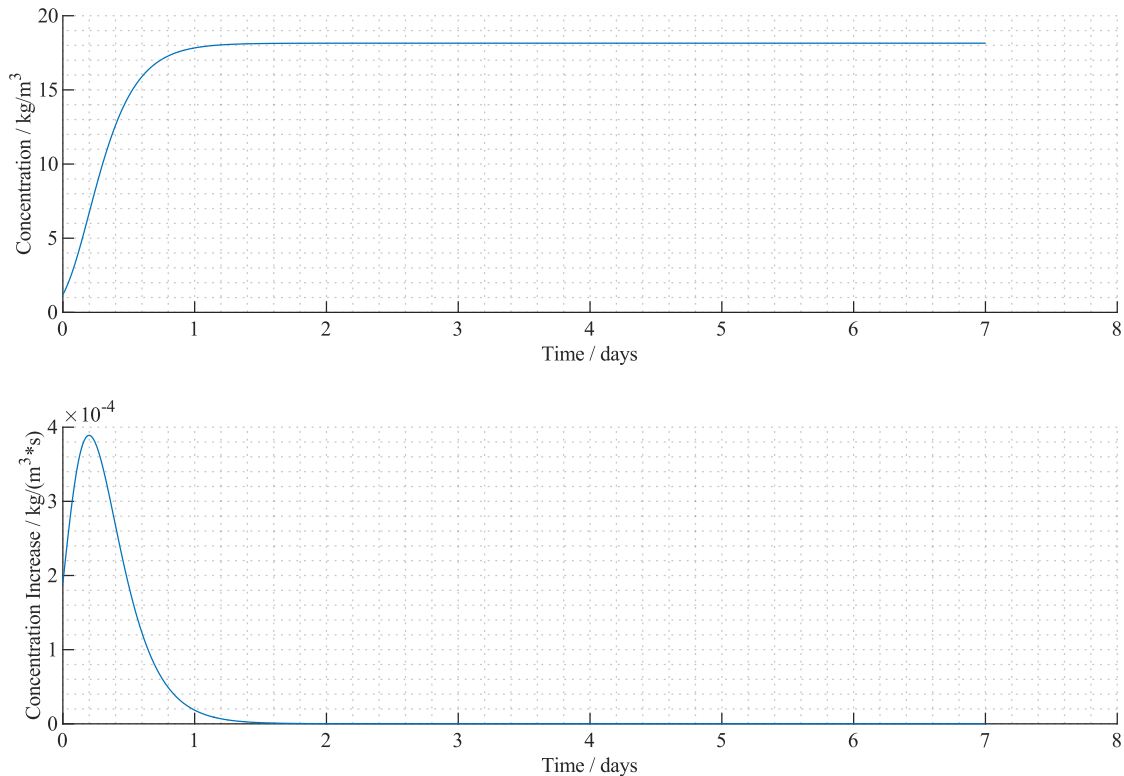


Figure 5.4-11 Reference Gompertz model biomass concentration and concentration increase.

Another change to the model was required to achieve compatibility between the produced chlorella mass and the newly implemented human model discussed in chapter 5.5. (Ruck 2018) assumed a chlorella composition of $\text{C}_1\text{H}_{1.75}\text{O}_{0.42}\text{N}_{0.15}\text{P}_{0.008}$ but neglected the phosphorus since that is not implemented in the simplified human model used for the analysis. The issue with combining this chlorella composition with the new human model is, that the human model requires a compound mass of proteins, fats and carbohydrates to metabolize. However, while the relative contribution of atoms is accurate in the implemented chlorella model, the overall molar mass is much smaller than for a compound mass consisting of macronutrients. The solution chosen here is to use the molar mass and composition derived by (Ruck 2018) internally in the algae model, but then convert the produced chlorella to a macronutrient composition based on (Belz et al. 2014: 172).

(Ruck 2018) provides further detailed information on the modelling assumptions of the algae and their implementation, which were not adjusted for this thesis and are therefore not discussed in detail here.

5.4.2.2 Verification

Since the developed PBR model is a conceptual model of a future PBR it cannot be validated. Instead validation was performed for individual aspects of the model by (Ruck 2018: 80-104) and here only a verification to check if the PBR operates as intended is performed. For this purpose, a simulation with four humans inside a 65 m^3 cabin is used to analyze the PBR. As Figure 5.4-12 shows the PBR is able to maintain the O_2 level in the cabin, although the CO_2 levels rises. This is a result of the difference between the respiratory coefficient of algae, and the respiratory coefficient of the crew. While the crew has a respiratory coefficient (which is calculated as mol produced CO_2 per mol consumed O_2) of about 0.92 or lower, depending on the food supply (Anderson et al. 2018: 63), the algae with urine as nutrient have an assimilation coefficient (mol consumed CO_2 per mol produced O_2) of 0.7 (Ruck 2018: 39-40). This means if the

required amount of O_2 for the crew is produced with algae using urine as nutrient source, the algae consume less CO_2 than the crew produces. In a finalized ECLSS this can be handled by using an additional CO_2 removal system to maintain the CO_2 level in the cabin. For this verification the effect resulting from this difference in respiratory coefficient and assimilation coefficient is intentionally shown. Therefore, as Figure 5.4-12 shows, the PBR is sized sufficiently to provide oxygen for a crew of four.

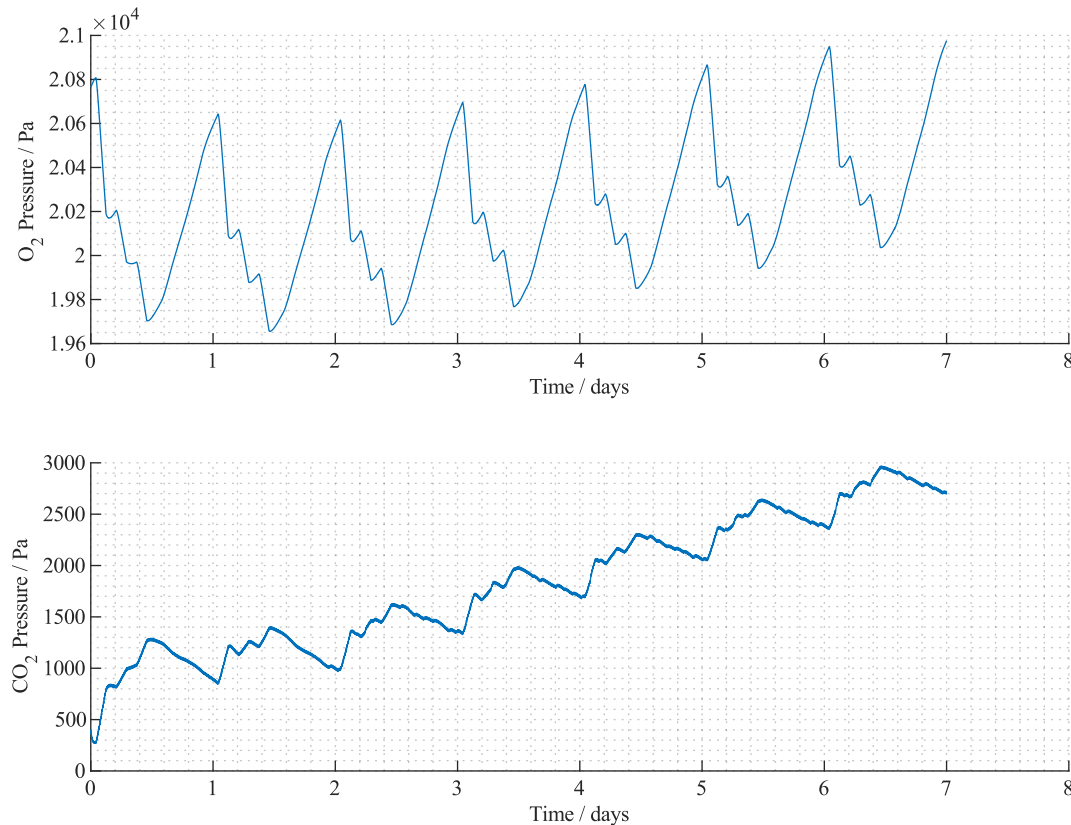


Figure 5.4-12 Partial pressure of oxygen and carbon dioxide in 65m³ cabin with PBR.

Figure 5.4-13 shows the various factors used to adjust the theoretically possible algae growth rate to the various environmental influences. For the selected case of high biomass concentration, the shading of the algae results in a growth limitation as shown by the Photosynthetic Active Radiation (PAR) influence in the figure. In addition, the high oxygen yield also results in a further limitation from the high oxygen concentration in the growth medium. The other factors are maintained by the system to keep the algae within optimal growth conditions, for nitrogen availability only short reductions in growth occur directly before a refill of either urine or nutrient solution. Figure 5.4-13 shows that the added control logics are functional and provide the required growth conditions for the algae.

Figure 5.4-14 provides an overview of the cumulative consumed or produced masses of the PBR. The daily O_2 production amounts to 4.18 kg/d while the daily CO_2 consumption is 4.42 kg/d. This corresponds to an assimilation coefficient of 0.77, which is a result of a mixed nitrate and urine supply of the algae. Since the PBR prioritizes urine as nitrogen source, all urine from the crew is consumed and processed. The water content of the urine is removed from the PBR and provided as output to the parent system. However, the urea content of the urine is not sufficient to provide the required nitrogen and is therefore complemented by nitrate. The assimilation coefficient for algae growth using nitrate is 0.83 (Ruck 2018: 39–40), and therefore the average assimilation coefficient of the PBR is higher than with pure urine supply.

Overall, this verification shows that the PBR model works as intended and is capable to supply the required O_2 for four crew members while removing the according amount of CO_2 .

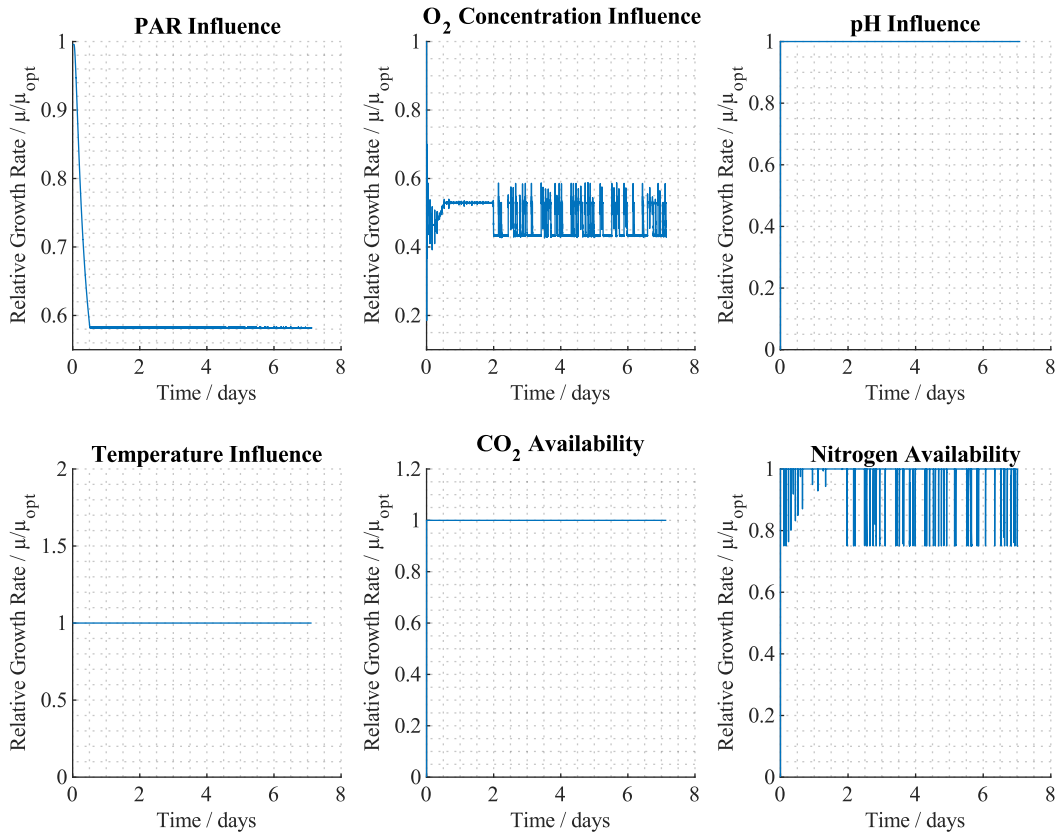


Figure 5.4-13 Factors impacting algae growth for the modelled PBR test case.

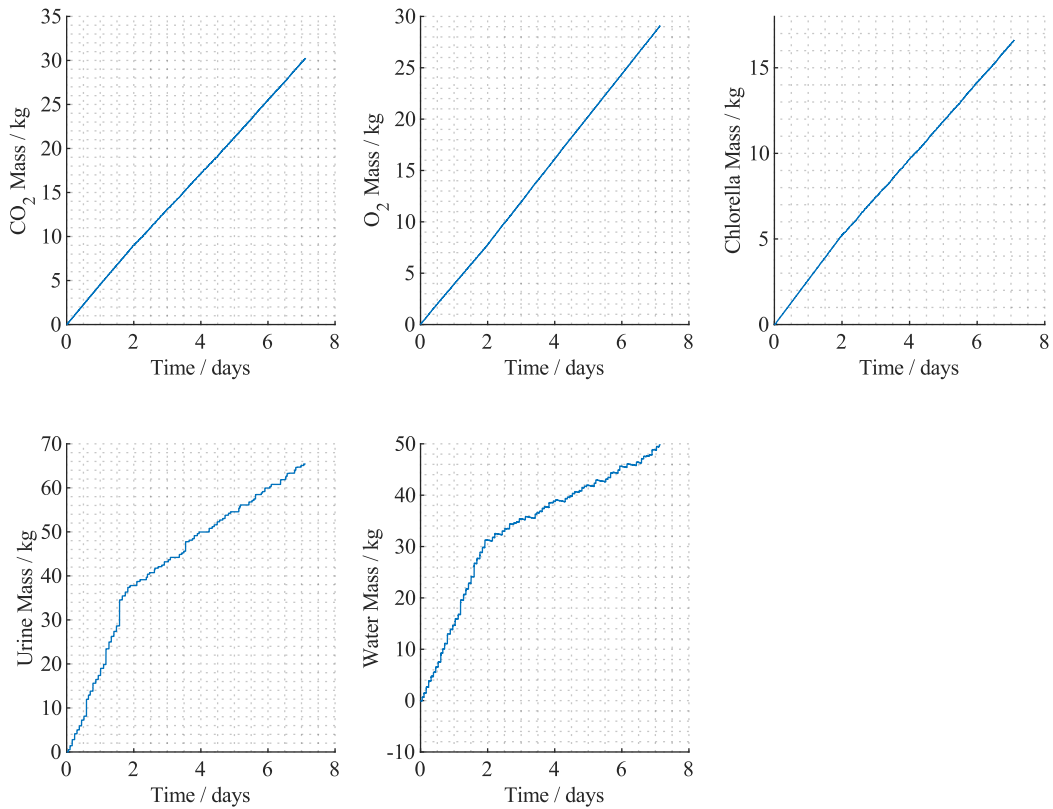


Figure 5.4-14 Consumed masses (CO₂ and Urine) and produced masses of the PBR.



$$v_{tot} = \begin{pmatrix} K_{exter}^A & K_{exter}^B & K_{exter}^C & K_{exter}^D \\ K_{inter}^A & \mathbf{0} & \mathbf{0} & \mathbf{0} \\ \mathbf{0} & K_{inter}^B & \mathbf{0} & \mathbf{0} \\ \mathbf{0} & \mathbf{0} & K_{inter}^C & \mathbf{0} \end{pmatrix} \cdot \begin{pmatrix} v^A \\ v^B \\ v^C \\ v^D \end{pmatrix} \quad (5.4-11)$$

$$K_{inter}^A = \begin{pmatrix} -1 & 0 & -1 & 0 & 0 & 0 & 1 & 0 & 0 \\ 1 & -1 & 0 & -1 & 0 & 0 & 0 & 0 & 0 \\ 0 & 0 & -1 & -1 & 0 & 0 & 0 & 0 & 0 \\ 0 & 0 & 1 & 0 & -1 & 0 & 0 & 0 & 1 \\ 0 & 0 & 0 & 1 & 1 & -1 & 0 & 0 & 0 \\ 0 & 1 & 0 & 0 & 0 & 0 & 0 & -1 & 0 \\ 0 & 0 & 0 & 0 & 0 & 0 & 1 & 0 & -1 \end{pmatrix} \quad (5.4-12)$$

$$K_{inter}^B = \begin{pmatrix} -1 & 0 & -1 & 0 & 0 & 0 & 1 & 0 & -1 & 0 & 0 & 0 & 0 \\ 1 & -1 & 0 & -1 & 0 & 0 & 0 & 0 & 0 & 0 & 0 & 0 & 0 \\ 0 & 0 & -1 & -1 & 0 & 0 & 0 & 0 & 0 & 0 & 0 & -1 & 0 \\ 0 & 0 & 1 & 0 & -1 & 0 & 0 & 1 & 0 & -1 & 0 & 0 & 0 \\ 0 & 0 & 0 & 1 & 1 & -1 & 0 & 0 & 0 & 0 & 0 & 0 & 0 \\ 0 & 1 & 0 & 0 & 0 & 0 & -1 & 0 & 0 & 0 & 1 & 0 & 0 \\ 0 & 0 & 0 & 0 & 0 & 1 & 0 & -1 & 0 & 0 & 0 & 0 & 1 \\ 0 & 0 & 0 & 0 & 0 & 0 & 0 & 0 & 1 & 0 & -1 & -1 & 0 \\ 0 & 0 & 0 & 0 & 0 & 0 & 0 & 0 & 0 & 1 & 0 & 1 & -1 \end{pmatrix} \quad (5.4-13)$$

$$K_{inter}^C = \begin{pmatrix} -1 & 0 & -1 & 0 & 0 & 0 & 1 & 0 & 0 \\ 1 & -1 & 0 & -1 & 0 & 0 & 0 & 0 & 0 \\ 0 & 0 & -1 & -1 & 0 & 0 & 0 & 0 & 0 \\ 0 & 0 & 1 & 0 & -1 & 0 & 0 & 1 & 0 \\ 0 & 0 & 0 & 1 & 1 & -1 & 0 & 0 & 0 \\ 0 & 1 & 0 & 0 & 0 & 0 & -1 & 0 & 0 \\ 0 & 0 & 0 & 0 & 0 & 0 & 1 & 0 & -1 \end{pmatrix} \quad (5.4-14)$$

$$K_{exter}^A = \begin{pmatrix} 0 & -1 & 0 & 0 & 0 & -1 & 0 & 0 \\ 0 & 1 & 0 & 0 & 0 & 1 & 0 & 0 \\ 0 & 0 & 0 & 0 & 0 & 0 & 0 & 0 \\ -1 & 0 & 0 & 0 & -1 & 0 & 0 & 0 \\ 0 & 0 & 0 & 0 & 0 & 0 & 2 & 2 \\ 0 & 0 & 0 & 0 & 0 & 0 & 0 & 0 \\ 0 & 0 & 0 & 0 & 0 & 0 & 0 & 0 \end{pmatrix} \quad (5.4-15)$$

$$K_{exter}^B = \begin{pmatrix} 0 & \mathbf{1} & 0 & 0 & 0 & \mathbf{1} & 0 & 0 & 0 & 0 & 1 & 0 & 1 \\ 0 & 0 & 0 & 0 & 0 & 0 & 0 & 0 & 0 & 0 & 0 & 0 & 0 \\ 0 & -1.5 & 0 & 0 & 0 & -1.5 & 0 & 0 & 0 & 0 & -1.5 & 0 & -1.5 \\ 0 & 0 & 0 & 0 & 0 & 0 & 0 & 0 & 0 & 0 & 0 & 0 & 0 \\ 0 & 0 & 0 & 0 & 0 & 0 & 0 & 0 & -1 & -1 & 0 & 0 & 0 \\ -1 & 0 & 0 & 0 & -1 & 0 & 0 & 0 & 0 & 0 & 0 & 0 & 0 \\ 0 & 0 & 0 & 0 & 0 & 0 & 1 & 1 & 0 & 0 & 0 & 0 & 0 \\ 0 & 0 & 0 & 0 & 0 & 0 & 0 & 0 & 0 & 0 & 0 & 0 & 0 \end{pmatrix} \quad (5.4-16)$$

$$K_{exter}^C = \begin{pmatrix} 0 & 0 & 0 & 0 & 0 & 0 & 0 & 0 & 0 \\ 0 & 0 & 0 & 0 & 0 & 0 & 0 & 0 & 0 \\ 0 & -0.5 & 0 & 0 & 0 & -0.5 & 0 & 0 & 0 \\ 0 & 0 & 0 & 0 & 0 & 0 & 0 & 0 & 0 \\ 0 & 0 & 0 & 0 & 0 & 0 & 0 & 0 & 0 \\ 0 & 0 & 0 & 0 & 0 & 0 & 0 & 0 & 0 \\ -1 & 0 & 0 & 0 & -1 & 0 & 0 & 0 & 0 \\ 0 & 0 & 0 & 0 & 0 & 0 & 1 & 1 & 0 \end{pmatrix} \quad (5.4-17)$$

$$K_{exter}^D = (-1 \ 0 \ 0 \ 0 \ -1 \ -1 \ 0 \ 0)^T \quad (5.4-18)$$

Changes in the matrices are marked red. In addition, the decomposition of ammonia to ammonium is now modelled by the generic pH model discussed in chapter 5.2.5. Therefore, the equilibrium constants for these conversions are set to prevent additional conversion during these calculations. The matrices K_{inter}^I for the respective reaction I always represent the general enzymatic inhibition model of equation (5.4-4) whereas the matrices K_{exter}^I represent the equations (5.4-5) to (5.4-9). Originally it was planned to adjust the derived equilibrium parameters from (Sun 2016) to additional data for 100% urine solution, as that is the intended operating point for CROP. However, the data did not become available in time for this thesis and therefore the parameters from (Sun 2016) are still used in the model. The V-HAB model implementation from (Sun 2016) and (Schalz 2019) was adjusted to utilize the new general pH model and allow easier integration of a CROP subsystem into larger simulations. Figure 5.4-15 provides an overview of the current CROP model structure.

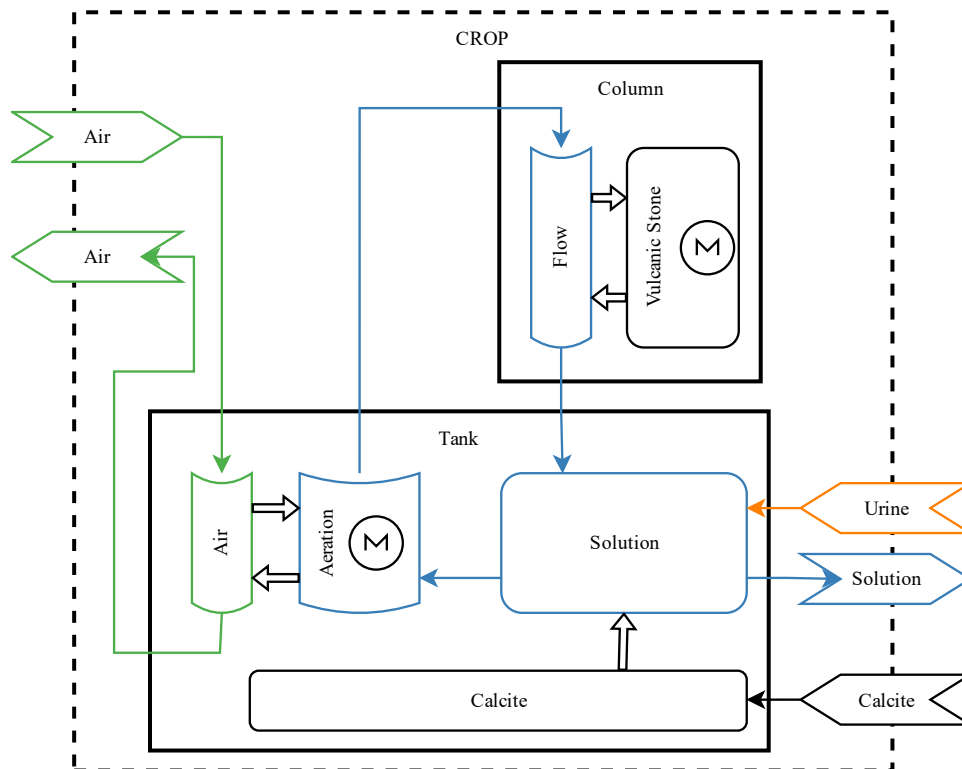


Figure 5.4-15 Overview of CROP V-HAB model structure.

One change to the model structure was to separate the calcite buffer of CROP into a separate phase. The previous models only considered one cycle and therefore this was not necessary. However, if multiple cycles are modelled, the solution phase will be emptied and filled with fresh urine. If the calcite is completely dissolved in this phase, it would also be removed. In the real system the calcite is present as a solid at the bottom of the tank and therefore not exchanged with the urine. Another change is connecting the CROP subsystem to another air phase, which was previously only done internally. This enables the outgassing of CROP to influence the habitat atmosphere in which it is placed. The change to place the aeration phase into the tank as a flow phase before the column was necessary to increase the simulation speed of CROP. If the pH manipulator is placed in the solution phase, it limits the possible time step severely, but if it is placed in a flow phase the outlet of that flow phase will directly have the correct pH and composition without any limits regarding the time step. The impact on the solution phase itself will be delayed and its compositions will not be completely correct, as the conversions related to the pH value do not take place in this phase. If the solution is used in another system, for which the pH is of interest, another generic pH manipulator can be used in that location.

Another modelling change to CROP was the removal of the enzyme compounds, e.g. the enzyme substrate compounds, from the matter table. These substances are only present as intermediate substances and are therefore only modelled as values within the enzyme kinetic manipulator in the volcanic stone phase. If these are modelled as actual substances in V-HAB they would be present in the solution phase and then enter the next system. This system would have to convert these substances, which contradicts the modularity of V-HAB. Another adjustment is the use of the *ode45* solver from



MATLAB® to solve the system of differential equations, which allows larger time steps of the overall system while still resulting in stable calculations for the conversion rates. Basically, the previous model calculated conversion flowrates directly to calculate the mass changes, while the new model uses the *ode45* solver for the elapsed time since the last execution to calculate the new masses of the different substances. The flowrates are set according to the calculated mass changes, which is a more stable solution for larger time steps while the detailed effects of the smaller time scales are still reflected correctly within the *ode45* calculation.

5.4.3.2 Verification

Only limited data on 100% urine solution was available as discussed in (Sun 2016), and additional data did not become available in time for this work. Therefore, only a verification is performed and no comparison to test data. The test data for 100% urine solution also shown in (Sun 2016) did not show a significant increase in nitrate mass over the time, but urea was converted to NO_2^- . The conversion of urea (CH_4N_2O) occurred over a time of about 80 days. It is unclear whether the production of nitrate would occur at a later stage in the test data or if some issue in the few tests available prevented the nitrate reactions from occurring. In the current model the conversion of urea requires 2000 hours or ~81.5 days as shown in Figure 5.4-16. In the developed simulation, no effect is present that prevents the production of nitrate, and therefore the desired nitrate is produced. This must be validated with additional test data once it becomes available. For this work, it basically represents the underlying assumption that the CROP system works and does produce the desired end product nitrate. Another effect shown in Figure 5.4-16 is the regular resupply of calcite ($CaCO_3$) to maintain the pH value. The pH value remains at levels where nominal enzymatic reaction kinetics are maintained. The changes in CO_3 value and oscillations occurring are an effect of the pH calculation where CO_3 is converted ultimately to CO_2 . A smoother curve could be observed with smaller time steps, but the general behavior of the system in the relevant other aspects matches the expectations and therefore the time step is deemed adequate for the overall simulation.

Figure 5.4-17 shows the enzymatic kinetic flowrates within CROP including the different overall conversion rates of the primary substances but not the internal enzymatic substances like the enzyme substrate complex. Figure 5.4-18 on the other hand shows the cumulative masses exchanged between CROP and the calcite phase or parent system.

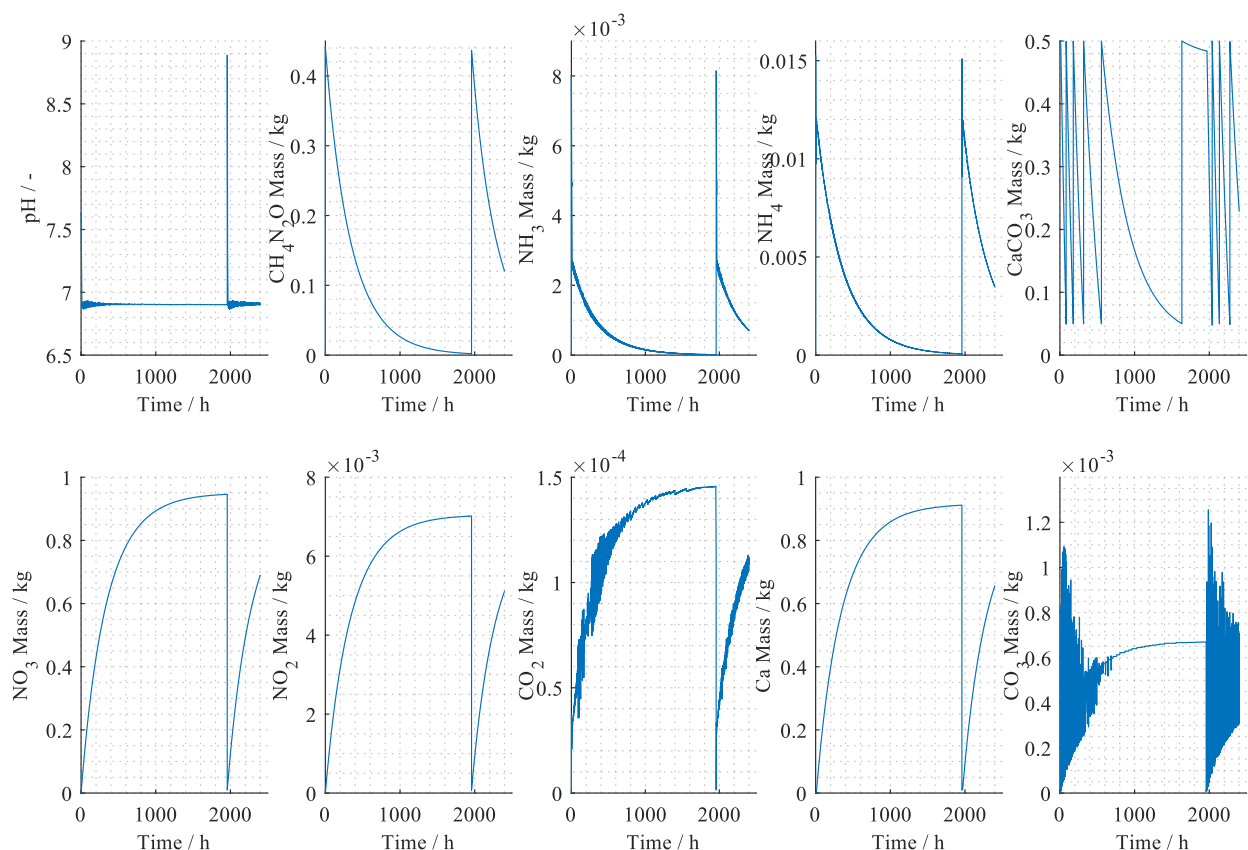


Figure 5.4-16 pH Value and masses in the CROP solution during a simulation.

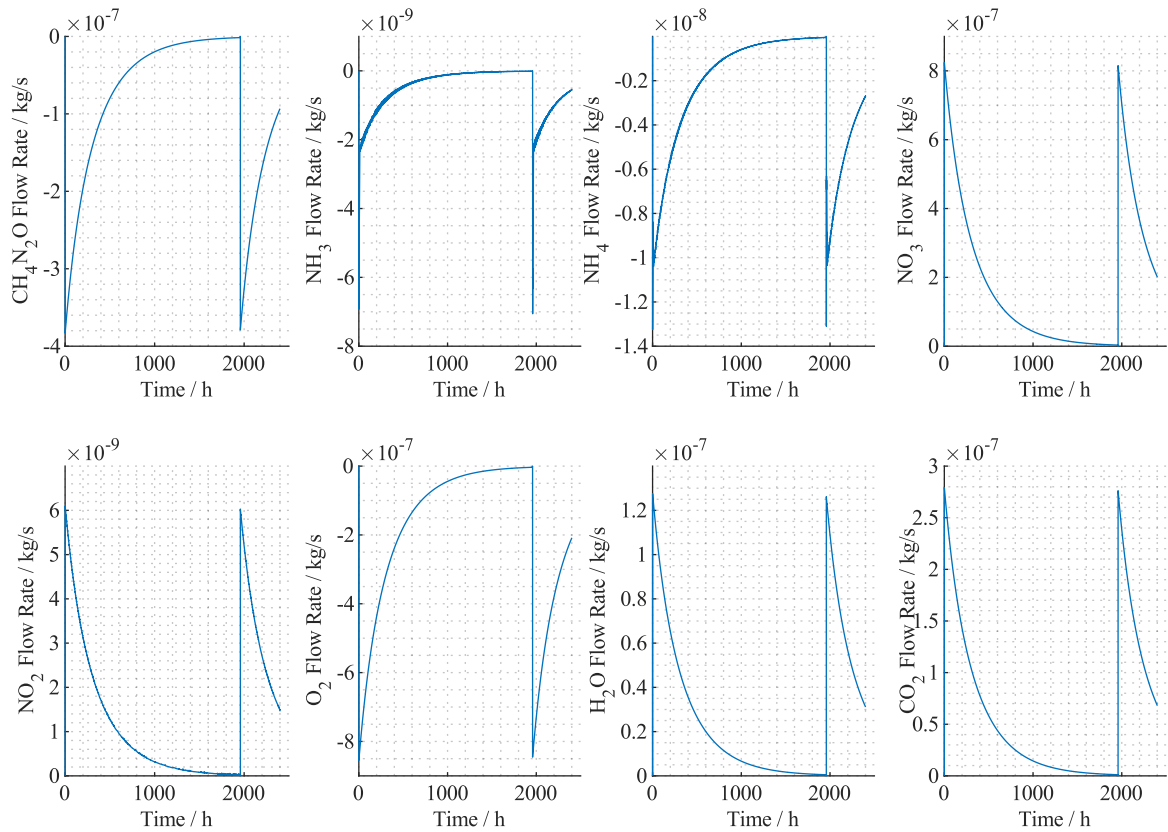


Figure 5.4-17 Enzymatic kinetic flowrates of the different substances within CROP.

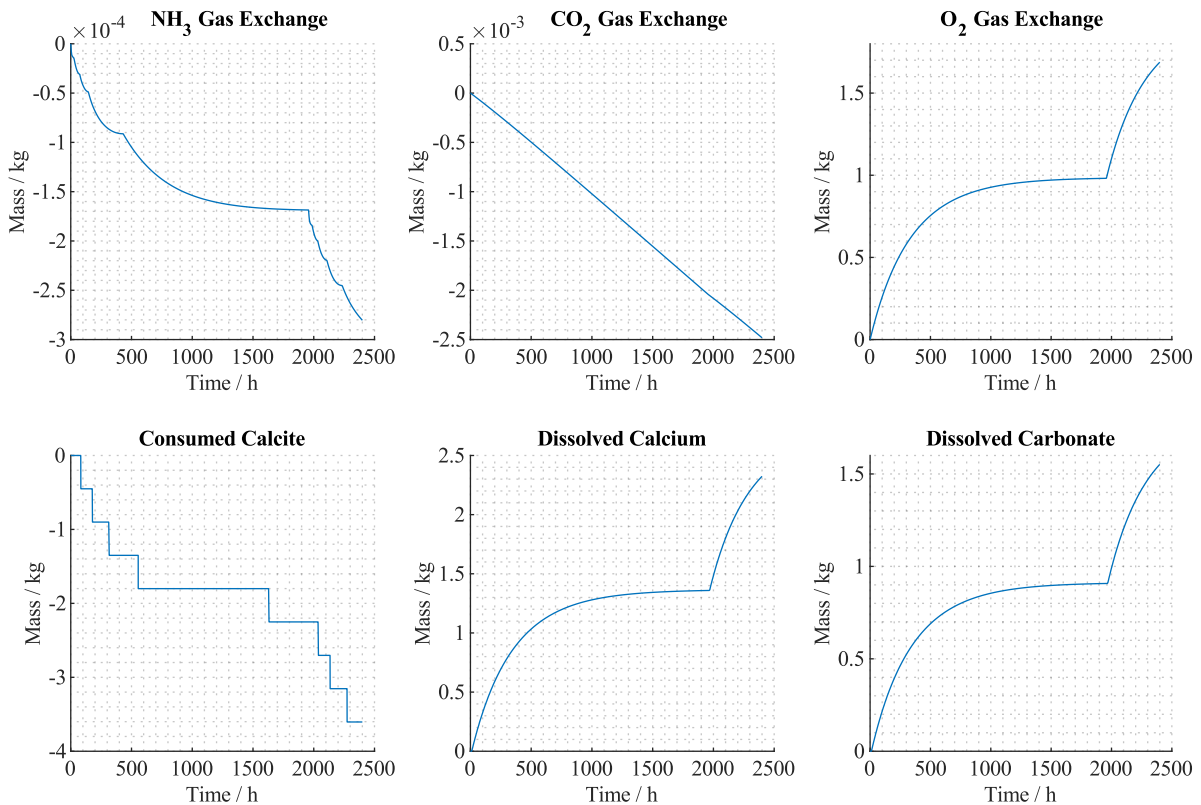


Figure 5.4-18 Cumulative exchanged masses of CROP, positive values represent an uptake of CROP while negative values represent a production of that mass by CROP. Dissolved masses represent the uptake from the calcite mass within the system while consumed calcite is the cumulative supply via the calcite interface.

5.5 Human Model

The V-HAB human model was created by (Czupalla 2011) and combined the work of multiple bachelor and master theses to a complete model of a generic human. However, in the following rework of the basic V-HAB structure performed by Jonas Schnaitmann and Claas Olthoff the human model was not migrated. Only the development of the thermal layer continued. Since this dissertation requires a human model, the initial question was, whether the original V-HAB human model should be reworked and adapted for V-HAB 2.X or whether the better solution would be to implement a different model. In the literature survey for human models, see also chapter 3.4, HumMod (Hester et al. 2011) was identified as the currently most capable and openly accessible alternative (available at <http://hummod.org/>). The justification to rework the original model instead of providing an interface between V-HAB and HumMod was the basic philosophy of V-HAB to maintain control over all solved aspects and to maintain the independent capability to model the impact of humans on the ECLSS. In addition, while analyzing the results of HumMod severe differences between the expected metabolic outputs of a human and the outputs of HumMod were identified, as discussed in chapter 5.5.7. These differences resulted in the final decision to improve and implement the V-HAB human model as HumMod is not considered a valid alternative for ECLSS analysis.

The V-HAB human model consist of six layers:

- Cardiovascular Layer
- Metabolic Layer
- Water Balance Layer
- Respiratory Layer
- Digestion Layer
- Thermal Layer

These layers are connected as described in Figure 5.5-1:

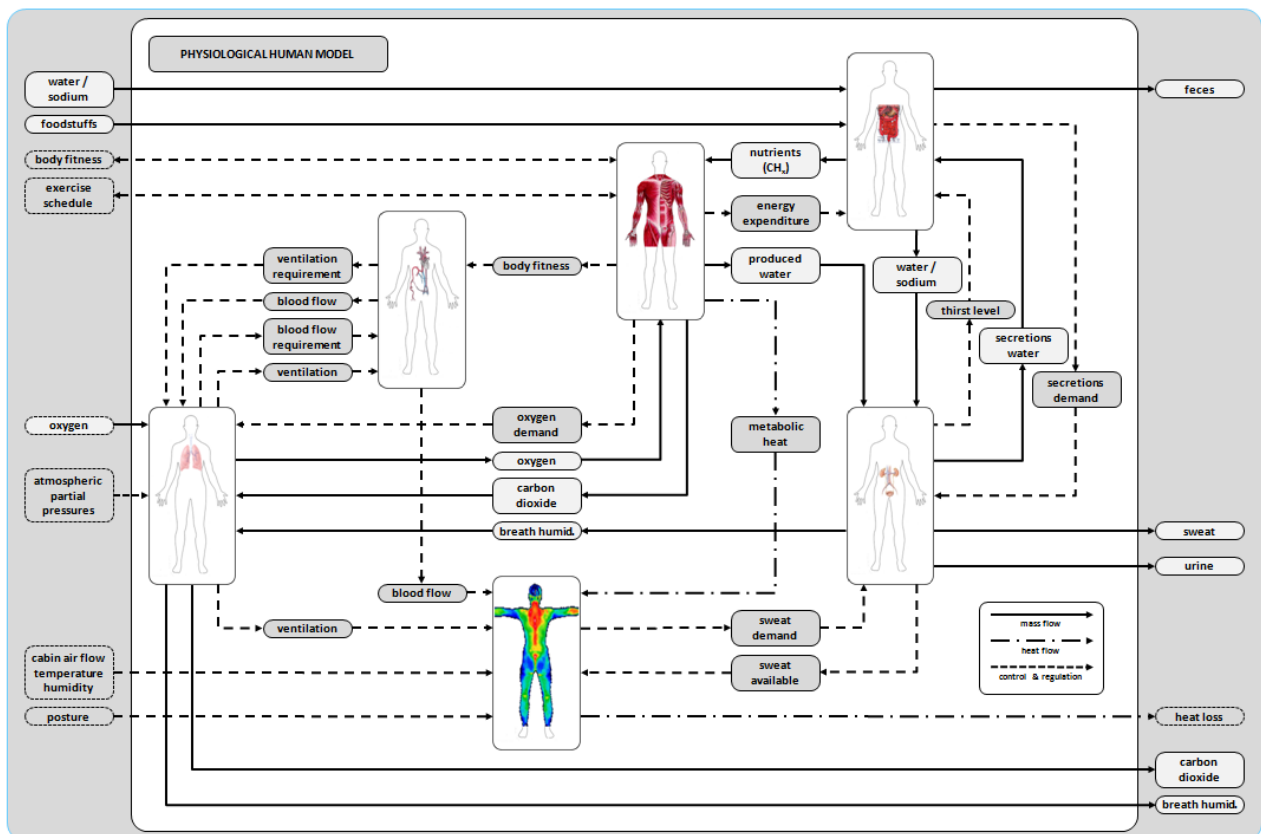


Figure 5.5-1 Connections in the V-HAB human model. (Czupalla 2011: 164)

This structure and the connections between the layers were not changed during the rework and are still valid. However, it should be noted that in the code the respiratory and cardiovascular layer are implemented as a single layer because of their high interconnection.

5.5.1 Respiration and Cardiovascular Layer

The respiration and cardiovascular layer of (Czapalla 2011) was converted to a V-HAB 2 model, but the principal structure remains identical. The previous calculations also remain identical except for those related to blood flow mixing. The basic V-HAB 2 phase calculations now handle these calculations. All other calculations are implemented as described by (Czapalla 2011) as methods in the class architecture of this layer. Figure 5.5-2 provides an overview of the V-HAB structure of the new implementation. The outlet flow phases are required because of the underlying assumption that normal phases are ideally mixed in V-HAB. To model the gas exchange of the tissue with the blood it is more accurate to assume a high oxygen concentration at the inlet and a high carbon dioxide concentration at the outlet. By using a flow phase, this is modelled more accurately. The normal phases are still required to represent the blood volume within these body parts, which would not be modelled if only flow phases were used. Therefore, a combination of flow and normal phases was chosen to best depict the behavior.

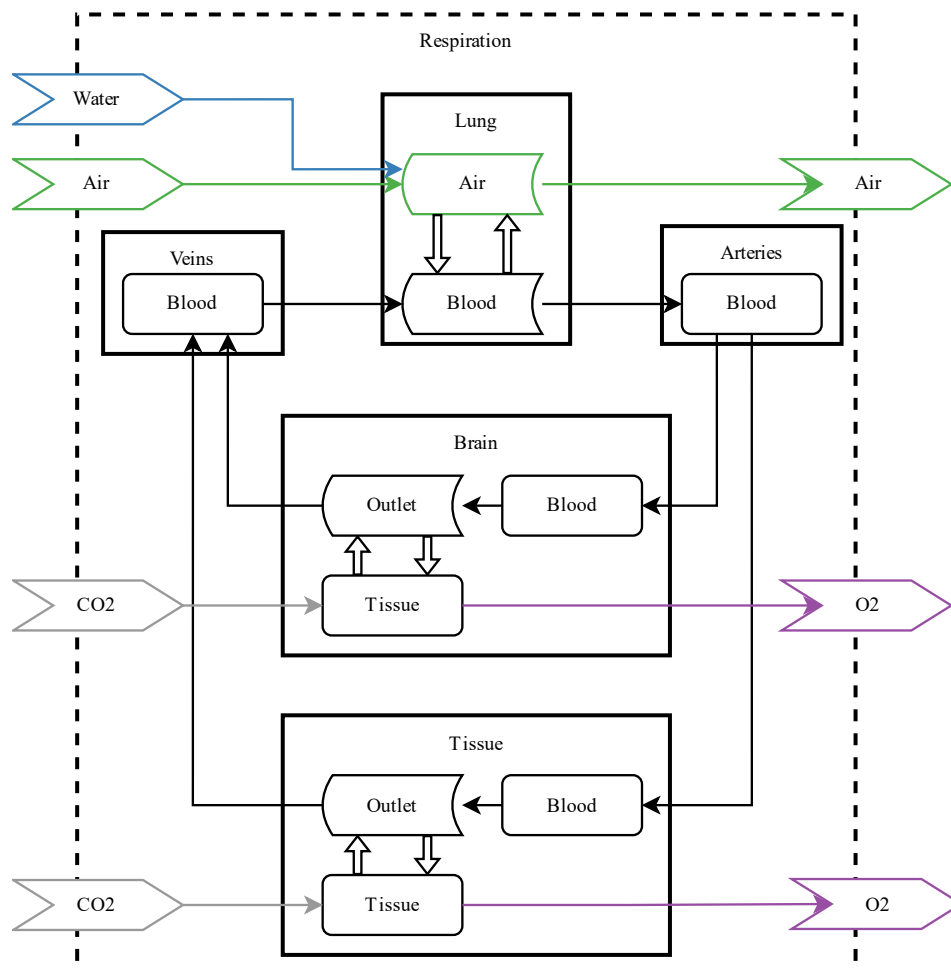


Figure 5.5-2 V-HAB model structure of the respiration and cardiovascular layer.

5.5.2 Metabolism Layer

The metabolic layer of the human model required the most extensive rework. Not only because the protein metabolism and resulting urea production were not yet implemented in the original V-HAB human model (Czapalla 2011: 334) but also because the knowledge of the human metabolism changed over the years and, consequently, multiple biochemical textbooks changed e.g. the amount of adenosine triphosphate (ATP) produced during glucose oxidation. While the original V-HAB human model assumes the old value of 36 mol of generated ATP per mol of glucose (Matthias Pfeiffer 2007: 117) newer textbooks all state 32 mol of ATP per mol of glucose (McArdle 2015: 151; Berg et al. 2013: 559). The replacement of the 36 mol ATP value with 30 or 32 mol ATP is also explained in more detail in (Berg et al. 2013: 559).

Another difference is the ATP Energy yield, which is 7.3 kcal/mol according to (Berg et al. 2013: 434; Lodish op. 2016: 62) instead of 12 kcal/mol (Czupalla 2011: 362). However, since the consumed food stated in (Czupalla 2011) was accurate, the conversion of mechanical energy expenditure and food energy overall was correct. To adjust the ATP energy yield to the correct value, the mechanical efficiency of the human model was adjusted from 25% to 41.1% in order to maintain the overall conversion value while using the correct energy yield for ATP.

Furthermore, some incorrect assumptions in the original metabolic layer were found while reworking it. For example, the original model assumed that glycogen could be generated from fats by the human body and even encountered negative glycogen masses in the model. It assumed these were all right if the metabolic pathway of fat to glycogen is implemented in the future (Matthias Pfeiffer 2007: 170–1). However, this is actually not possible for animals, including humans, as they can only convert the glycerin part of fats to glycogen (Berg et al. 2013: 663). For these reasons, a full rework of the metabolic model became necessary, which is discussed in this chapter.

Some conventions from biochemical textbooks are applied in this chapter. For example, only the abbreviations are used for the substance adenosine diphosphate ($C_{10}H_{12}N_5O_{10}P_2^{3-}$) or ADP and adenosine triphosphate ($C_{10}H_{12}N_5O_{13}P_3^{4-}$) or ATP in the chemical reactions. While this makes checking the atom balance a bit more complex, it keeps the equations short and easier to understand. However, different from the textbooks, no hydrogen atoms or phosphate groups are neglected in the reactions. Therefore, the atom balance can be checked by just replacing these two abbreviations with the mentioned chemical formula. The atom balance may not be important for the biochemical textbooks, where the focus is on the reader to understand the metabolic pathways and processes. However, for an engineer developing a numerical model, which has the requirement to maintain a closed mass balance, it is of paramount importance. The practice to further simplify the reactions therefore made the adaption of this layer a challenge.

For this reason, the derivations provided in Appendix D are very detailed to make it easier to check the steps for errors and help engineers and other readers without biological background to understand the reactions. Chapter 5.5.2.1 provides an overview of the resulting net-reactions that are used in the model without the derivations for those readers who are either already familiar with the metabolic pathways, or who are not interested in the detailed derivation.

Figure 5.5-3 shows the new model structure of the metabolic layer within V-HAB. The metabolic nutritional storage compartments are now modelled as phases, and therefore the mass balance within this layer is now checked. The manipulator is used to convert the food nutrients received from the digestion layer and models the conversion of the nutrients and oxygen to energy, water and carbon dioxide as described in the next subchapter.

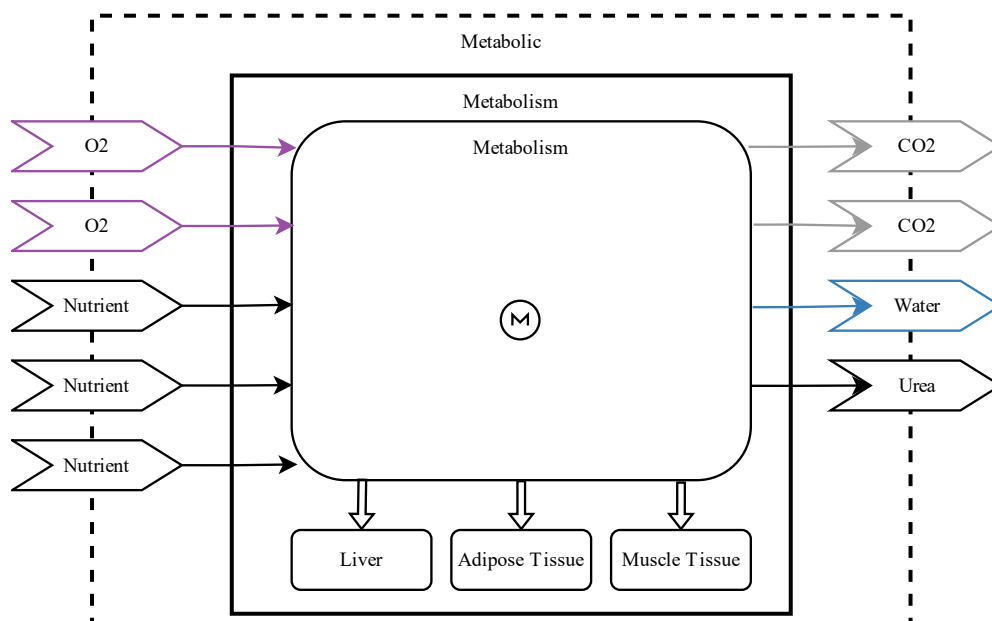


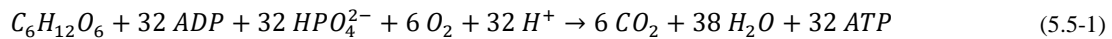
Figure 5.5-3 V-HAB model structure of the metabolic layer.

5.5.2.1 Overall Net Reactions

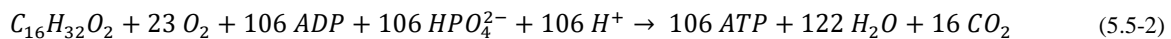
To summarize the results of the derivations from Appendix D, the overall net-reactions are listed in this subchapter, both with the corresponding ATP reactions and without.

Reactions with ATP:

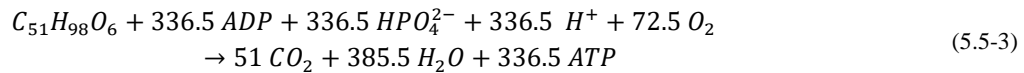
Glucose oxidation:



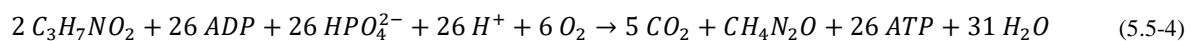
Fatty Acid oxidation:



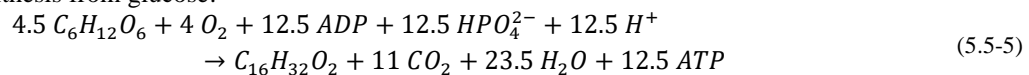
Triacylglycerol oxidation:



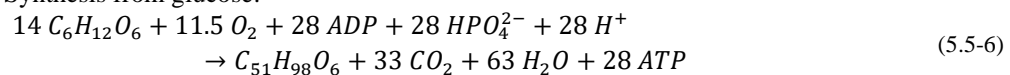
Protein oxidation:



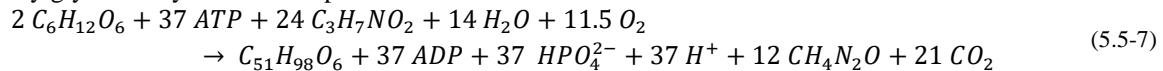
Fatty Acid Synthesis from glucose:



Triacylglyceride Synthesis from glucose:

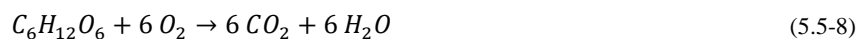


Triacylglyceride Synthesis from protein:

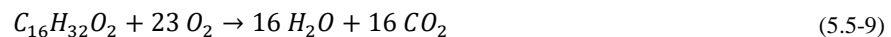


Reactions without ATP:

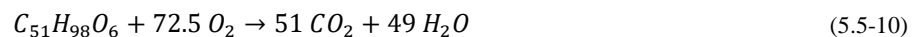
Glucose oxidation (+32 ATP):



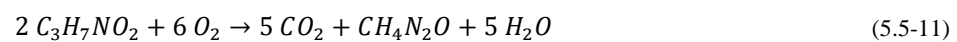
Fatty Acid oxidation (+106 ATP):



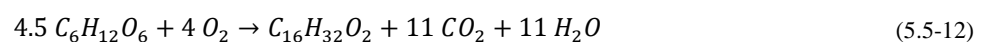
Triacylglycerol oxidation (+336.5 ATP):



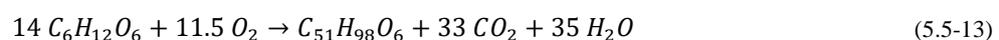
Protein oxidation (+26 ATP):



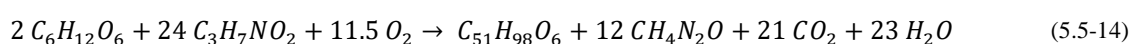
Fatty Acid Synthesis from glucose (+12.5 ATP):



Triacylglyceride Synthesis from glucose (+28 ATP):



Triacylglyceride Synthesis from protein (-37 ATP):





5.5.2.2 Discussion of Differences Between Previous and Updated Metabolism Model

Because there are some quite significant differences between the previous metabolic layer and the new one, the most sever differences are summarized here and their impact on the model is discussed.

ATP yield:

New insights of human metabolism result in reduced ATP generation for the different metabolic pathways:

- One mol of glucose previously produced 36 ATP (Czupalla 2011: 360), now it produces 32 ATP (McArdle 2015: 151; Berg et al. 2013: 559).
- One mol of triacylglycerol generated 407 ATP (Czupalla 2011: 360), now it generates 336.5 ATP .

For further derivations of the difference in ATP yield of triacylglycerol see equation (D.4-12). These differences in ATP yield affect the food consumption of the model, as more food must be consumed to generate the same amount of ATP. As the produced carbon dioxide and consumed oxygen depend on the consumed food, which in return depends on the ATP demand, this change also affects the respiration layer of the human model. The stoichiometric conversion ratios for these gases per mol consumed nutrient did not change, but more mol of the nutrients must be converted to produce the same energy now.

Protein Metabolism:

The protein metabolism is now implemented. Previously proteins were converted into fat using the nutritional energy attributed to fat (9 kcal/g) and proteins (4 kcal/g) (Matthias Pfeiffer 2007: 137), which maintains energy balance but removes mass and therefore does not lead to a closed mass balance.

The implementation of protein metabolism results in a closed energy and mass balance of the human model. The conversion using the stated nutritional energy would mean 1 g fat or triacylglycerol (or 1.17 mmol) are equivalent to 2.25 g (or 25.83 mmol) of protein/alanine. Therefore, for each 2.25 g or protein consumed by the human 1.25 g of mass were previously deleted in the model. With a consumption of 91.3 g/d of protein per human the previous simplification resulted in a daily mass balance error of 50.7 g/d. In addition, as equations (5.5-3) and (5.5-4) show, the conversion of 1.17 mmol of fat results in 88.34 mmol of oxygen consumption and 59.57 mmol carbon dioxide production. While the equivalent conversion of 25.83 mmol of proteins results in 77.49 mmol oxygen consumption and 64.575 mmol carbon dioxide production. Therefore, the respiratory loads from protein consumption were previously off by +14% for oxygen and -7.8% for carbon dioxide, which also leads to a different respiratory coefficient.

Metabolic Water Generation:

The previous V-HAB human model from (Markus Czupalla 2011) produced >1 kg of metabolic water, which is more than 2.5 times the value mentioned in (Anderson et al. 2018).

The reason for this difference is that not 36 mol of H_2O are generated in the body for each mol of glucose that is consumed. The original model made this assumption, as can be seen in Fig.: 8-12 of (Matthias Pfeiffer 2007: 119), which resulted in a metabolic water production of over 1 kg per day. As stated in (Anderson et al. 2018: 50) the metabolic water production should be closer to 0.4 kg per day. The mistake which lead to this discrepancy is also discussed in (Horiike et al. 1996) and can be attributed to the fact that the equation contains the reaction of ADP to ATP but not the reaction where ATP is converted back to ADP, which is described in equation (D.1-7). As can be seen in equation (5.5-1) the water yield if ATP generation is considered is much higher than for equation (5.5-8) without the ATP generation. Since the implemented original model did not include the back-and-forth conversion of ADP and ATP this aspect was missed. While the new model also does not include ADP and ATP as modelled substances, the model uses the net reaction without the ADP to ATP conversion from equations (5.5-8) to (5.5-14). This approach is also consistent with (Volk and Rummel 1987: 141).

5.5.3 Water Balance Layer

The water balance layer of the human model was translated to V-HAB 2 but the basic equations from (Czupalla 2011) remain identical and will therefore not be discussed again here. However, it should be noted that the changes to the metabolic layer also affect this layer. Since less metabolic water is produced more water uptake is required by the model. Figure 5.5-4 shows the current model structure of the water balance layer in V-HAB. The water interfaces are for metabolic generated water, secretion and reabsorption from the digestion layer. An overview of the connections is provided in Figure 5.5-6.

An adjustment of the water balance layer was necessary for the kidney model, which previously assumed 100% as the maximum efficiency for the glomerulotubular balance, which is controlled by the sodium level in the water layer. This is fine if the human consumes adequate amounts of salt. However, for cases where the primary diet consists of fresh vegetables, the sodium level in the human drops due to the high water and low salt uptake. For low salt concentrations, the kidney model previously reabsorbed 100% of both water and salt, which resulted in a built-up of water as no urine was produced anymore. (Thomson and Blantz 2008) state that the glomerulotubular balance is a stochastic process, which cannot become 100% efficient. Therefore, it was limited to 95% efficiency, which solves this issue. The specific value was defined by testing various maximum efficiencies with fresh vegetable diets and analyzing the human model water in- and outputs.

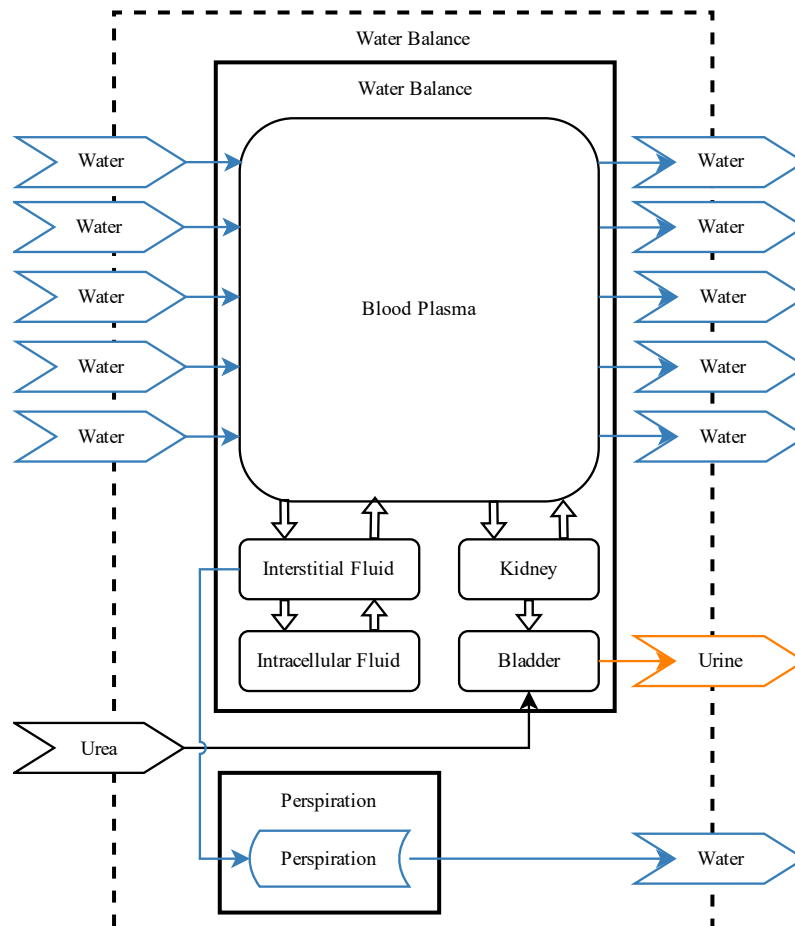


Figure 5.5-4 V-HAB model structure of the water balance layer.

5.5.4 Digestion Layer

The digestion layer had to be adjusted during the translation into V-HAB 2. Previously the mouth was also modelled as a separate compartment, but due to the small size, this would result in severely limited time steps for the human model. Therefore, the secretion and reabsorption flows of the mouth were added to the calculations of the stomach in the new model. In addition, the previous human model received macronutrients directly, not a variety of different foods like tomato, lettuce etc. Therefore, a manipulator was added to the stomach that converts the food consumed by the

human into the different nutrients based on the values stored in the compound mass of the respective foods. This allows V-HAB to model different kinds of food like different types of vegetables and supply them directly to the human model. Figure 5.5-5 provides an overview of the current V-HAB implementation of the model. The connection of the interfaces for this layer to the other layers are shown in Figure 5.5-6.

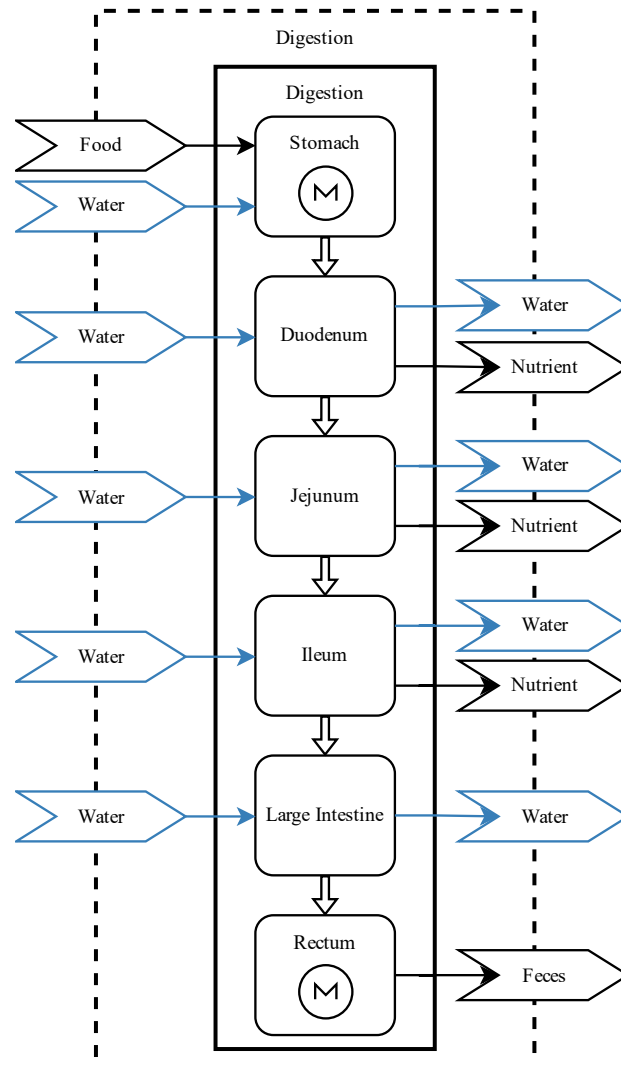


Figure 5.5-5 V-HAB model structure of the digestion layer.

5.5.5 Thermal Layer

(Czupalla 2011) implemented a detailed multi node thermal layer. This was migrated to V-HAB 2 and further improved by (Weber and Schnaitmann 2016) and (Olthoff 2017: 90). However, detailed thermal modelling of the crew is not the focus of this thesis. Instead, the general impacts like overall produced heat and water are sufficient. Therefore, a simplified representation of the thermal layer was derived for this thesis. The heat flow contributions of the human were separated into respiratory loads, trans-epidermal water loss (TEWL), sweat and sensible heat flow. For respiratory loads, the model assumes that the air flow calculated by the respiratory layer is heated up to the body core temperature of the human and is saturated with humidity. For the TEWL a value of 300 to 400 ml per day is stated by (Honari and Maibach 2014). However, (Anderson et al. 2018: 63) state a total water production of 1.695 kg/d for a nominal human. The respiration water production for this case only accounts for 0.95 kg according to initial modelling tests with the human model. Therefore, the TEWL was increased to 750 ml/d to match the data from (Anderson et al. 2018: 63). For sweating the difference between the basic metabolic heat flow, and the metabolic heat flow during activity, which are

calculated by the metabolic layer, are used to calculate the overall additional heat load from activity. Based on data from (Anderson et al. 2018: 45) the ratio of heat load from sweat is calculated:

$$\dot{Q}_{sweat} = \frac{653.33 \text{ W} - \dot{Q}_{respiration} - \dot{Q}_{TEWL}}{826.11 \text{ W}} \cdot (\dot{Q}_{metabolic,activity} - \dot{Q}_{metabolic,base}) \quad (5.5-15)$$

The remaining additional heat flow from activity is represented as sensible heat flow in the thermal model.

5.5.6 Overview of new V-HAB Human Model

The following figure provides an interconnected overview of the different human model layers within V-HAB 2. The thermal layer is not shown here, as it only controls some of the flows between the other layers or sets heat flows within phases but does not interact directly with the other layers.

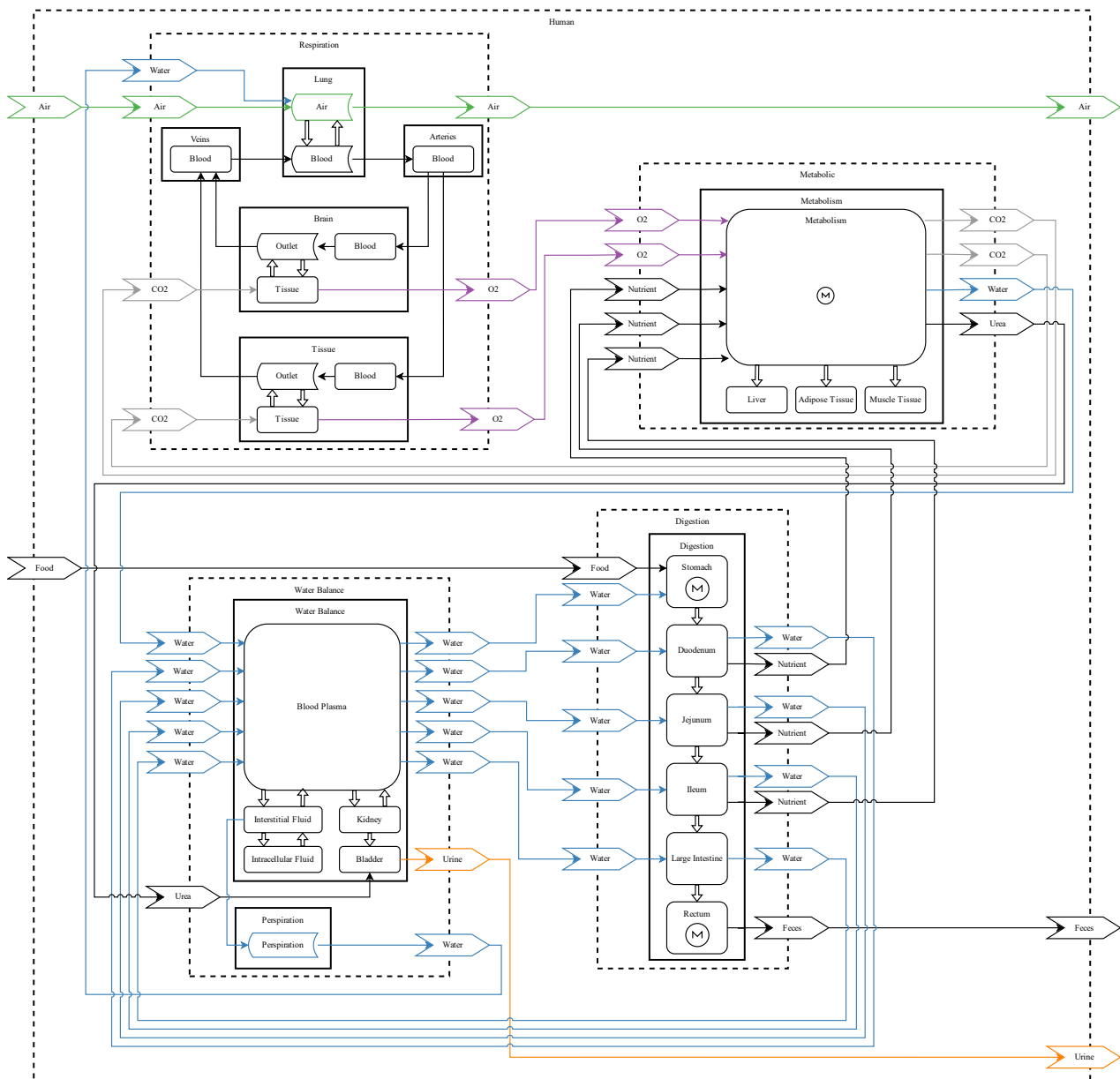


Figure 5.5-6 Overview of the new V-HAB human model with all connections between the different layers. The thermal layer is not shown here, as it does not have mass flow interfaces with the other layers and only controls thermal heat flows and sweat production. Sweat production is shown here as the water branch connected to respiration, as all sweat is assumed to evaporate.



5.5.7 Human Model Validation

The main difficulty for the human model validation is the variability in human physiology. Since the model is currently not capable of modelling a large variety of humans these variations are also not depicted. The available data for comparison also varies depending on the analyzed subject. Therefore, the model is compared to two other models for human physiology. The first is the Baseline Values and Assumptions Document (BVAD), which lists nominal human interfaces for space missions used by NASA (Anderson et al. 2018: 50). The other is HumMod (HC Simulation 2020), a physiological human model developed at University of Mississippi Medical Center.

5.5.7.1 Validation Set Points

Since the data from (Anderson et al. 2018) is not available as an executable human model, the basic assumptions for the human, like exercise per day, food composition etc., from (Anderson et al. 2018) are used as baseline for HumMod and the V-HAB human model for the comparison. These assumptions also depict the conditions for space life support systems quite well. The assumed diet is based on the recommendation from (Liskowsky and Seitz 2014: 586) and consists of 52.5 % carbohydrates, 17.5 % proteins and 30 % fat. A 30 minute exercise at 75 % $\dot{V}_{O_{2,max}}$ is used as specified in (Liskowsky and Seitz 2014: 360). These values are replicated in the V-HAB human model and HumMod to the best possible degree. HumMod lacks some of the necessary setpoints. For example, it is not possible to specify the amount of water in the consumed food and the exercise load can only be defined in Watts, not in $\dot{V}_{O_{2,max}}$. Therefore, the specified 3.69 l/min oxygen consumption assumed in (Liskowsky and Seitz 2014: 360) had to be converted using the assumption of a caloric value for oxygen of 4.9 kcal/l according to (Hofmann 1979: 577):

$$0.75 \cdot 0.045 \frac{l}{kg \min} \cdot 82 \text{ kg} \cdot 4.9 \frac{kcal}{l} = 13.56 \frac{kcal}{min} = 946 \text{ W} \quad (5.5-16)$$

According to the description in HumMod, the exercise value is only motion. Since the human is not 100% efficient, the motion also results in produced heat. The value from equation (5.5-16) is the overall metabolic load, which consist of both the motion and heat. Therefore, according to the description from HumMod, 3.55 W of heat have to be added to each motion Watt to calculate the overall metabolic load. To derive the required motion load for HumMod, the calculated value from equation (5.5-16) is therefore divided with 4.55. Since HumMod only allows 10 W steps for this value, 210 W are finally selected. The resulting oxygen consumption in HumMod with this value is ca. 2.25 l/min. This is less than the 75 % value of $\dot{V}_{O_{2,max}}$ defined in equation (5.5-16), which would be 2.78 l/min. To reach this value of oxygen consumption, an exercise level of 260 W would be required in HumMod. However, this cannot be set, because HumMod would go into ventricular fibrillation at normal CO₂ levels with this exercise level. Table 5.5-1 provides an overview of the remaining selected conditions for the validation case.

Table 5.5-1: Validation Case Set Points. – Represents Values for which no Information was available

Set Point Conditions	Unit	NASA	HumMod	V-HAB
Pressure	kPa	70.3	70.9	70.3
Oxygen Partial Pressure	kPa	-	14.9	14.8
Carbon Dioxide Partial Pressure	Pa	-	0	40
Temperature	°C	21	21	21
Dew Point	°C	10	10.1	10
Gravity	g _{Earth}	0	0	1

For HumMod the total pressure and relative humidity could not be set more accurately, resulting in slight variations for the partial pressures and dew point. The HumMod GUI states that the partial pressure for CO₂ is zero, but most likely it internally calculates with a partial pressure composition of normal air (0.04% CO₂), as the GUI can only show 0.1% steps for the partial pressures. In the V-HAB human model it is currently not possible to define gravity conditions. Since the model is generated based on 1 g_{Earth} data, the model is assumed to be at 1 g_{Earth}.

5.5.7.2 Validation Results

The following table summarizes the validation results. Note that feces are not implemented in HumMod, at least it was not possible to locate any variable referring to it in the GUI of HumMod or the produced solution data file. The water balance view of the GUI does not mention any water loss due to feces (only the case of diarrhea is available). HumMod does not discern between water consumed in food or water in liquid form, therefore the dietary water intake was assumed to represent both of these values.

Table 5.5-2: Human model validation. The differences are always relative to the NASA (Anderson et al. 2018) values. The balance column indicates whether a value is consumed (+) or produced (-) by the human. Feces are not available as parameter in HumMod.

Value	Balance	NASA	HumMod	V-HAB	Difference HumMod	Difference V-HAB
Unit		kg/d	kg/d	kg/d	%	%
Oxygen	+	0.816	0.537	0.88	-34.2	+8.2
Water	+	2.5	2.32	2.44	-27.5	-2.3
Water in Food	+	0.7		0.79		+13.8
Food	+	1.5	1.289	1.57	-14.1	+4.7
Metabolic Water	+	0.345	0.319	0.42	-7.6	+22.1
Carbon Dioxide	-	1.04	0.591	1.04	-43.1	+0.5
Humidity	-	1.9	1.22	1.79	-35.8	-5.5
Urine Water	-	1.6	1.44	1.77	-9.7	+10.7
Urine Solids	-	0.059	0.063	0.04	+7.6	-31.4
Feces Water	-	0.1		0.09		-11.1
Feces Solid	-	0.032		0.04		+17.2

Most notable is the difference of oxygen and carbon dioxide data where HumMod has differences of more than 30 % compared to the NASA values. It should be noted, that HumMod does not directly provide mass values for these parameters, only ml/min values are available. However, it is not documented at what conditions (e.g. what density) these volumetric values are provided. Therefore, the best possible assumption, which led to the lowest differences was chosen. This is the case for standard conditions of 1 bar and 0 °C, as they have the highest density and therefore the highest mass value of all possible conditions for the conversion.

In addition, HumMod seems not well suited to simulate higher CO₂ partial pressure conditions. If a partial pressure of 280 Pa CO₂ is assumed, the human goes into ventricular fibrillation during the 30-minute exercise period followed by cardiac arrest. It seems unlikely that this is a realistic outcome since the partial pressure of CO₂ in spacecraft is frequently above that value.

To study the influence of gravity on HumMod, the same simulation was also performed with 1 g_{Earth} settings. The only differences larger than 2% in the simulation results were for the produced urine solids and the urine water flow. The urine solids showed the most significant difference with only 25.41 g of solids per day in 1 g_{Earth}, compared to 63.48 g of solids per day in 0 g_{Earth}. The produced urine water per day for 1 g_{Earth} was 1.56 kg with a difference of 114.8 g compared to the 0 g_{Earth} case. This can be explained by the increased output of proteins and calcium from bone and muscle loss in 0 g_{Earth}. Since the V-HAB human model does not include this, the urine solids also show the highest deviation compared to the BVAD values.

Compared to HumMod, the V-HAB human model corresponds much better to the NASA values. Most deviations are below 15% with the larger differences occurring for the internally calculated metabolic water and the relatively small masses of urine and feces solids. The metabolic water of the new model was derived in detail in Appendix D and is based on the state of the art of metabolic physiology. Therefore, an improvement of this value cannot be achieved for the current model. The solids of urine and feces depend on the modelled salts and the fiber content of the food. Since the V-HAB human model currently only includes sodium as salt the solids production is underestimated. Overall, this chapter proves that the V-HAB human model is better suited to ECLSS analyses than HumMod.



6 Mission Scenario Case Studies

In this chapter the three mission scenarios defined in chapter 1.2.2 are analyzed in detail. In the first chapter, general limitations of the simulations are discussed, which apply to all cases. Subsequently, each mission scenario is discussed in detail in a separate chapter.

6.1 Limitations

The general limitations and simplifications for V-HAB and the overall models of the mission scenarios are summarized in the following bullet points:

- V-HAB assumes ideally mixed phases.
- V-HAB assumes the matter within a branch is incompressible (no mass can be stored in branches).
- The used subsystems have limited accuracy, see the individual validation and verification chapter from chapter 5 for the accuracy of the various subsystem models.
- The UPA and BPA subsystem models are based on percentages and are assumed to produce water without further contaminants.
- The human model metabolism does not model all different types of macronutrients. E.g. all fats are assumed to be tripalmitin ($C_{51}H_{98}O_6$), all proteins are assumed to be alanine ($C_3H_7NO_2$) and all carbohydrates are assumed to be glucose ($C_6H_{12}O_6$).
- Only the nutrient cycle of nitrogen is considered in the models. Other substances, e.g. phosphor and potassium, are currently not included in all relevant subsystem models and therefore not correctly depicted in the overall system.
- Trace contaminants in the atmosphere and their removal are not modelled. For a list of potential trace contaminants view (Anderson et al. 2018: 68).
- Sweat is assumed to evaporate completely without time delay. This increases the direct humidity load during exercise, which would be less pronounced without this assumption.

6.2 Parallelization of Simulations

To more efficiently perform the case studies for this chapter, two different options to parallelize V-HAB simulations were developed for different types of available computation systems. The first approach is based on the parallelized execution script using the parallel computing toolbox of MATLAB for the V-HAB test cases written by Claas Olthoff. This script was adapted and generalized for any V-HAB simulation. The basic approach remains identical. A “for” loop assigns each V-HAB simulation defined by the inputs of the script to a worker in the parallel computing toolbox. This works well on desktop computers with multiple cores. For example, on the compute cloud of the Leibniz Rechenzentrum where nodes with ten cores are available for simulations.

Recently, a high-performance computer with a batch software became available at the Institute of Astronautics. In order to utilize this resource, a suitable docker file for V-HAB simulations was written, which assigns each simulation as a batch job to the high-performance computer. The base class of V-HAB had to be adjusted slightly to add batch job specific properties, which enable writing a zip file of the simulation outputs using the job ID. This is necessary because the docker file cannot know the time stamp usually used by V-HAB to create the output folder. Therefore, in order for the docker to correctly know which file to transfer and still maintain a unique file name for each simulation output, an interface to provide the job id to V-HAB was required.

Using these two parallelization approaches, a parallel execution of multiple V-HAB simulations is possible on all available computational resources, significantly reducing the required time for case studies.

In addition to the ISS ECLSS shown in Figure 6.3-1 an International Standard Payload Rack (ISPR) based plant growth chamber (PGC) was implemented and the impact on the ISS analyzed. Figure 6.3-2 provides an overview of the assumed growth areas and volumes for that PGC. Each of the four lettuce (green) and tomato (red) compartments is modelled as a separate plant culture to distribute the harvest times over multiple occasions for both vegetables. The harvest time for lettuce is 30 days and for tomato it is 80 days. Therefore, the plant cultures of lettuce are assumed to grow with 7.5 days in between each culture while the tomato cultures are assumed with 20 days in between each culture. In addition, the plant growth is initialized to assume 78 days of previous plant growth. See chapter 5.4.1.1 for a description how this initialization is achieved. This results in the first culture of tomato being harvested during the simulation period of one week. This also coincides with the highest humidity production by the PGC and was therefore chosen for the simulation.

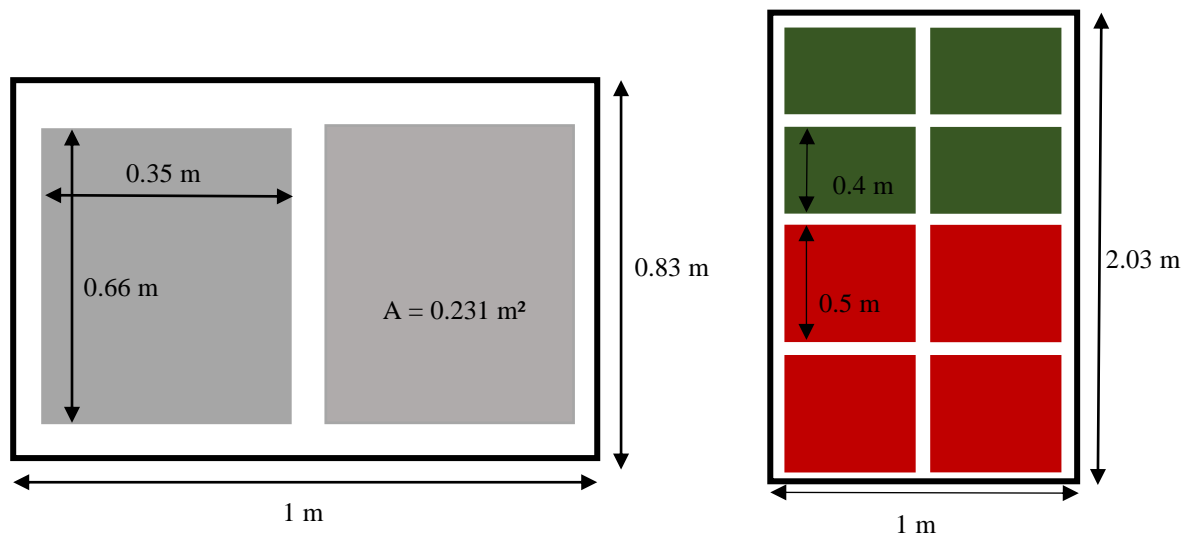


Figure 6.3-2 Top view (left) and front view(right) of an ISPR based plant growth chamber with lettuce (green) and tomato (red) compartments. The area size in grey is used for all crop growth compartments. (Pütz et al. 2018)

Within this case study for the ISS the location of the PGC and its impact is studied. While this was already performed in (Pütz et al. 2018) with simplified models of e.g. the CCAA, the analysis presented here uses the detailed models discussed in chapter 5. Another change was to deactivate the CCAA in the US Lab because only one CCAA in the US part is nominally operated. To analyze the effect of the location, the PGC is placed into different modules for this case study and each case is named after the module in which the PGC is located.

6.3.2 Results

Initially the results for the overall ISS without a PGC are discussed. Figure 6.3-3 shows the partial pressure of CO₂ for the different modules of the ISS. The daily schedule including sleep and exercise periods are clearly visible in the CO₂ level with the sleep coinciding with the low CO₂ level occurring every 24 hours and the exercise being visible as peaks in CO₂ in Node 3 where the exercise is performed. The additional oscillations of the CO₂ in SM and Node 3 are a result of the CO₂ removal systems in these modules. In Columbus, the time when the crew member returns from exercise to Columbus is also clearly visible for each day as a peak in CO₂ level resulting from the increased CO₂ production after exercise. Since both the CDRA and the Russian Vozdukh are assumed to operate, the CO₂ level is overall lower than expected if only CDRA is used. Overall, the CO₂ level remains within the desired area although it slightly exceeds the new exploration target of 300 Pa, because CDRA was not designed for lower partial pressures and removes less CO₂ at lower partial pressures. The effects of the IMV are also visible in the plot, as the CO₂ oscillations from Node 3 propagate into PMM and Node 1. The further away the module is from the exercise and CO₂ removal systems, the less pronounced are these oscillations as is observable in JEM and Columbus. In JEM the effect of the crew member returning after exercise is almost unnoticeable due to the significantly larger volume of JEM compared to Columbus.

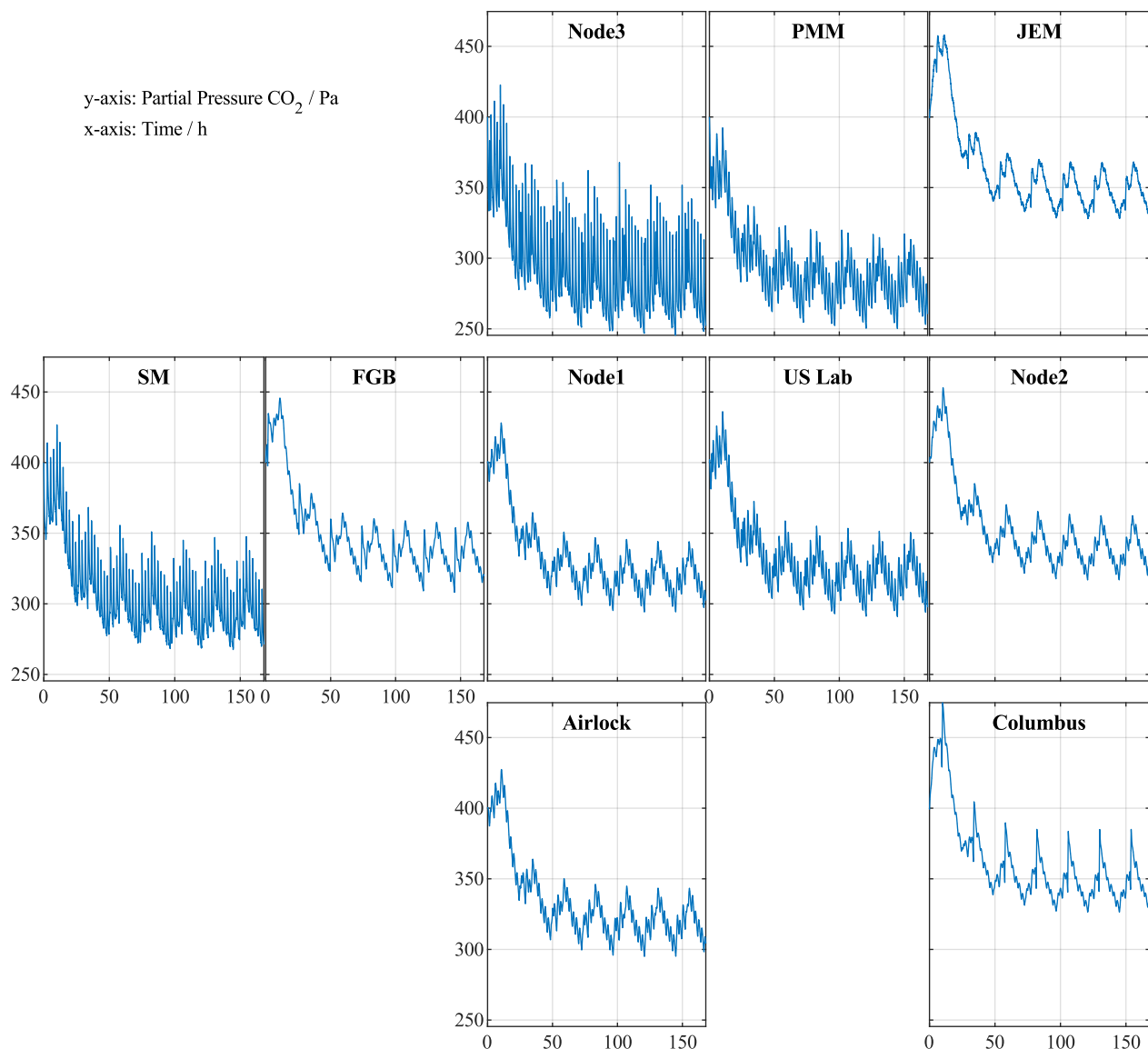


Figure 6.3-3 Partial pressure of CO₂ on the ISS without a plant growth chamber.



Figure 6.3-4 shows the relative humidity within the ISS. The humidity overall remains within the desired range of 25% to 75% with some slightly lower levels in some modules e.g. the FGB and Node 1. The humidity also shows the day and night cycle of the crew as there is a high humidity level followed by a low humidity level for each day in each module. In addition, the exercise is also visible as three distinct peaks in the modules, which can be clearly seen in e.g. the FGB. The peaks in humidity for an individual exercise period, which are visible in the FGB and Columbus, are also due to a crew member returning to this module after exercise. The modules without active humidity control system have a lower relative humidity compared to modules with an active CCAA. This may be confusing at first, however, if the dew point in Figure 6.3-5 is viewed, the values are higher in the modules without CCAA. This is due to the different temperatures in the modules, as the active CCAA also reduces the temperature, the modules with CCAA have a lower temperature than the other modules. For higher temperatures, the relative humidity is lower if the partial pressure of water is identical.

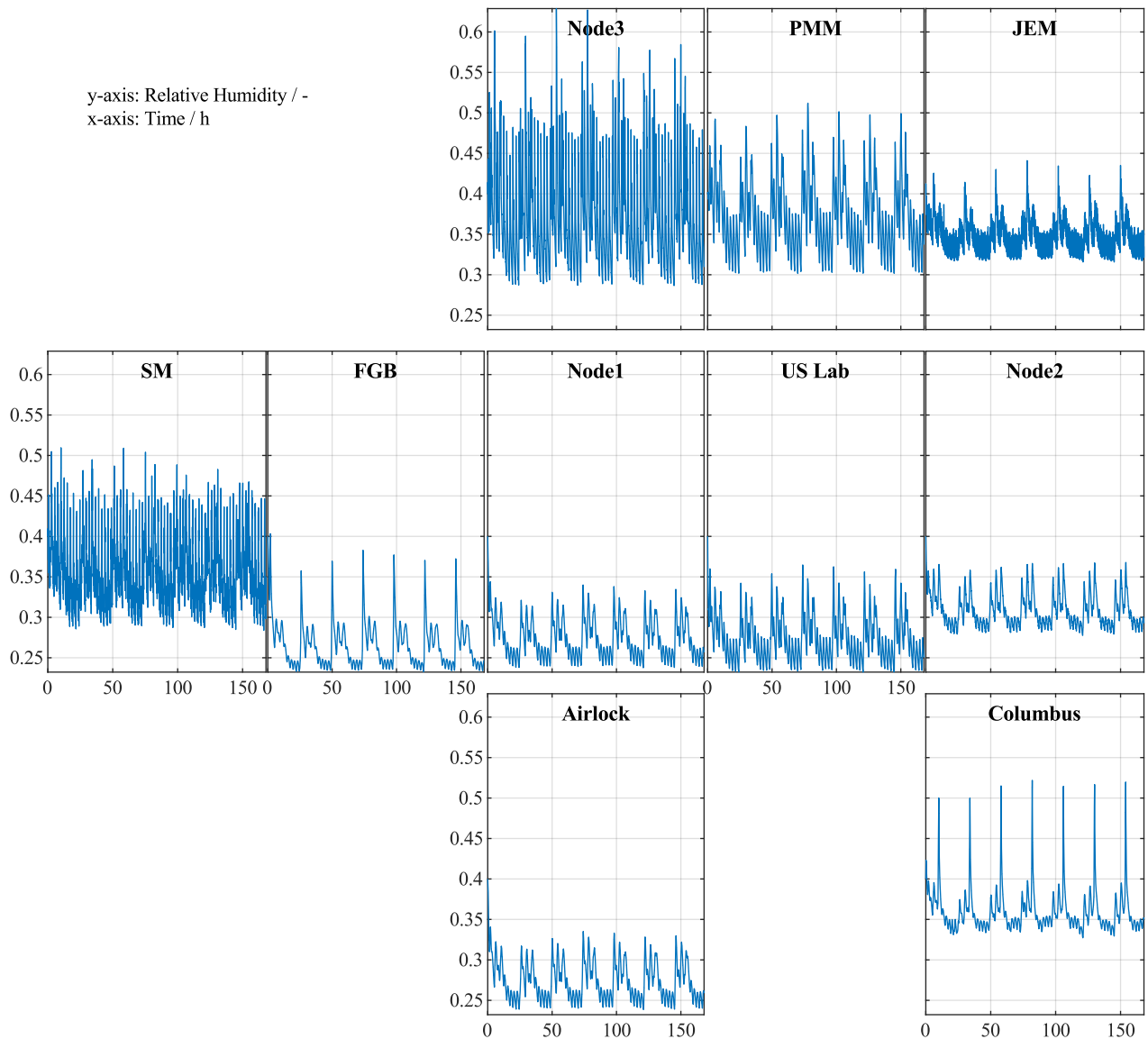


Figure 6.3-4 Relative humidity on the ISS without a plant growth chamber.

Figure 6.3-5 also shows that the dew point remains low enough to prevent condensation.

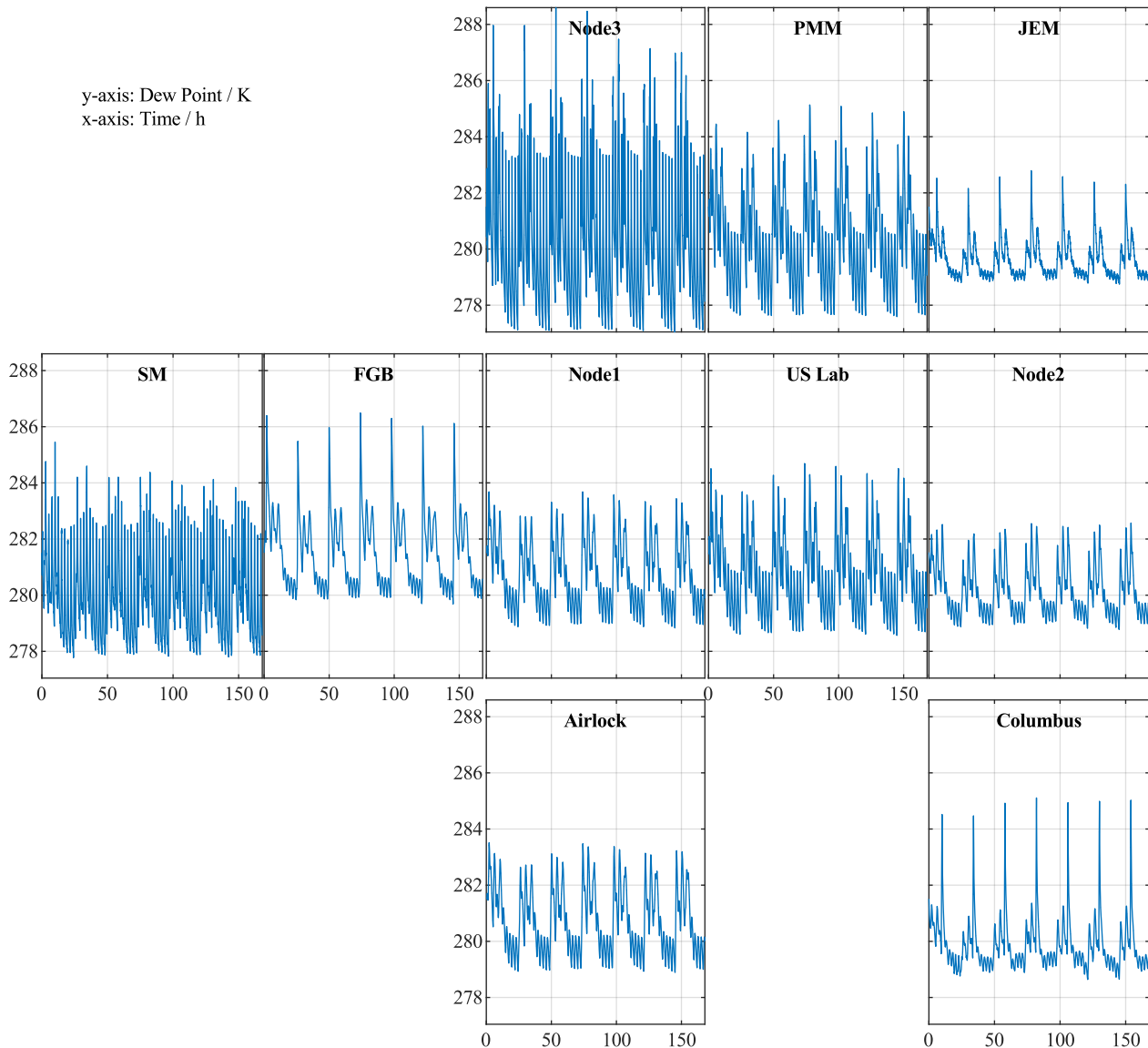


Figure 6.3-5 Dew Point on the ISS without a plant growth chamber.

Figure 6.3-6 shows the masses within the water processing systems of the ISS as well as the food mass for the case without PGC and for the PGC installed in Columbus (Columbus case). The Water Storage System WSS was recently added to the ISS as primary storage for potable water (Carter et al. 2019). It therefore represents the currently available potable water mass. The top left part of Figure 6.3-6 shows that the PGC initially consumes additional water but due to most consumed water being transpired by the plants (as is also shown in Figure 6.3-8) the WSS potable water mass reaches similar levels just with a different dynamic as in the case without PGC. The overall water surplus of the ECLSS, which was discussed in chapter 5.1.2, can also be observed here. The initial reduction in water mass is due to the WPA waste water tank filling up before the first processing cycle. After that period the WSS potable water mass reaches its previous value even though more waste-water is stored in the WPA, meaning that overall more water is available at the end of the simulation. As discussed previously, this effect is due to metabolic generated water and the water content of the food supplied to the ISS. Another interesting result can be observed from the two bottom plots of Figure 6.3-6. After about 50 h the first plant generation is harvested, introducing new edible mass. Since plant biomass is prioritized for consumption, this edible biomass is then consumed by the humans, which impacts the urine production. This can be seen by the divergence of the dashed line (the case with PGC) and the solid lines (no PGC) of the UPA WSTA mass in the bottom right plot.

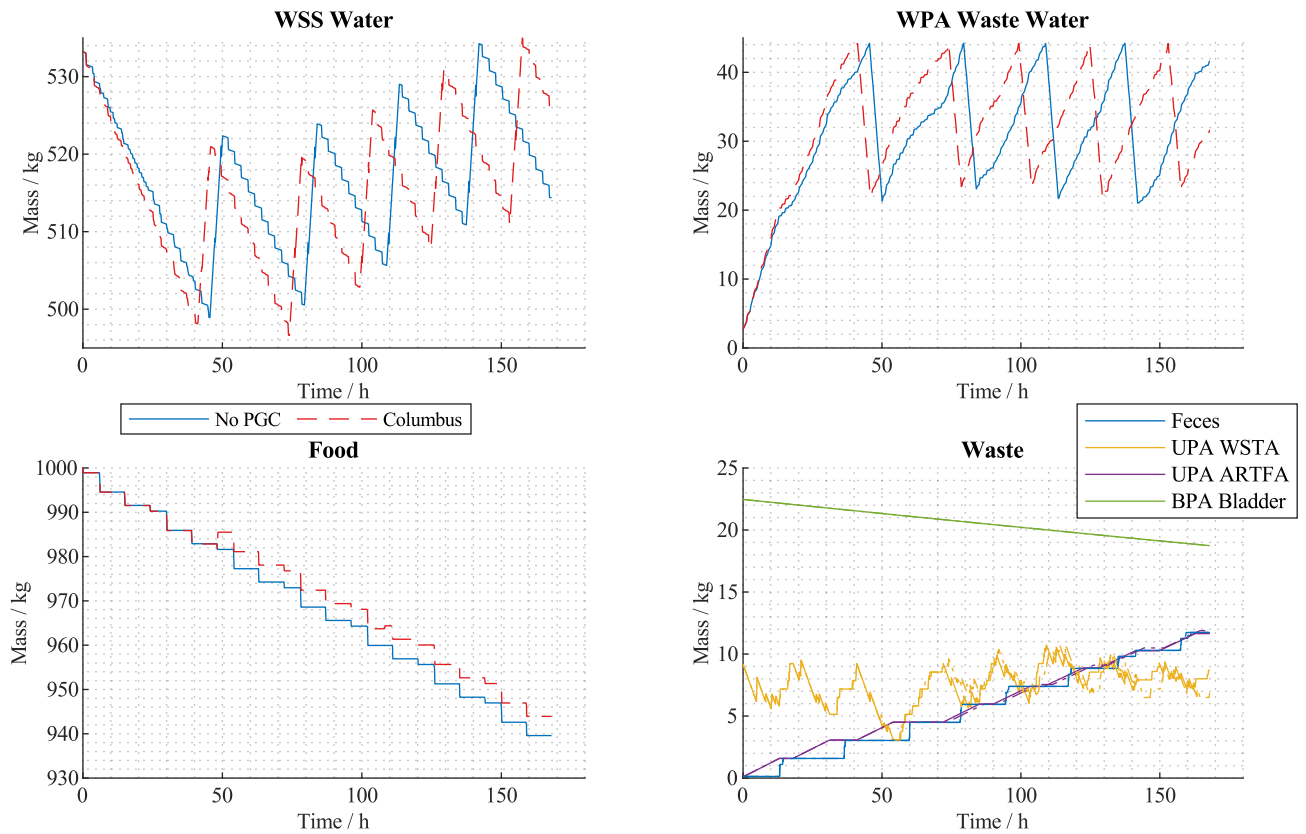


Figure 6.3-6 Overview of different masses in the ISS ECLSS. Top left: Water Storage System (WSS) potable water mass. Top right: WPA waste-water tank mass. Bottom left: food storage mass. Bottom right: waste processing system masses. For the bottom right figure, dash-dotted lines represent the Columbus case, while solid lines are the case without PGC.

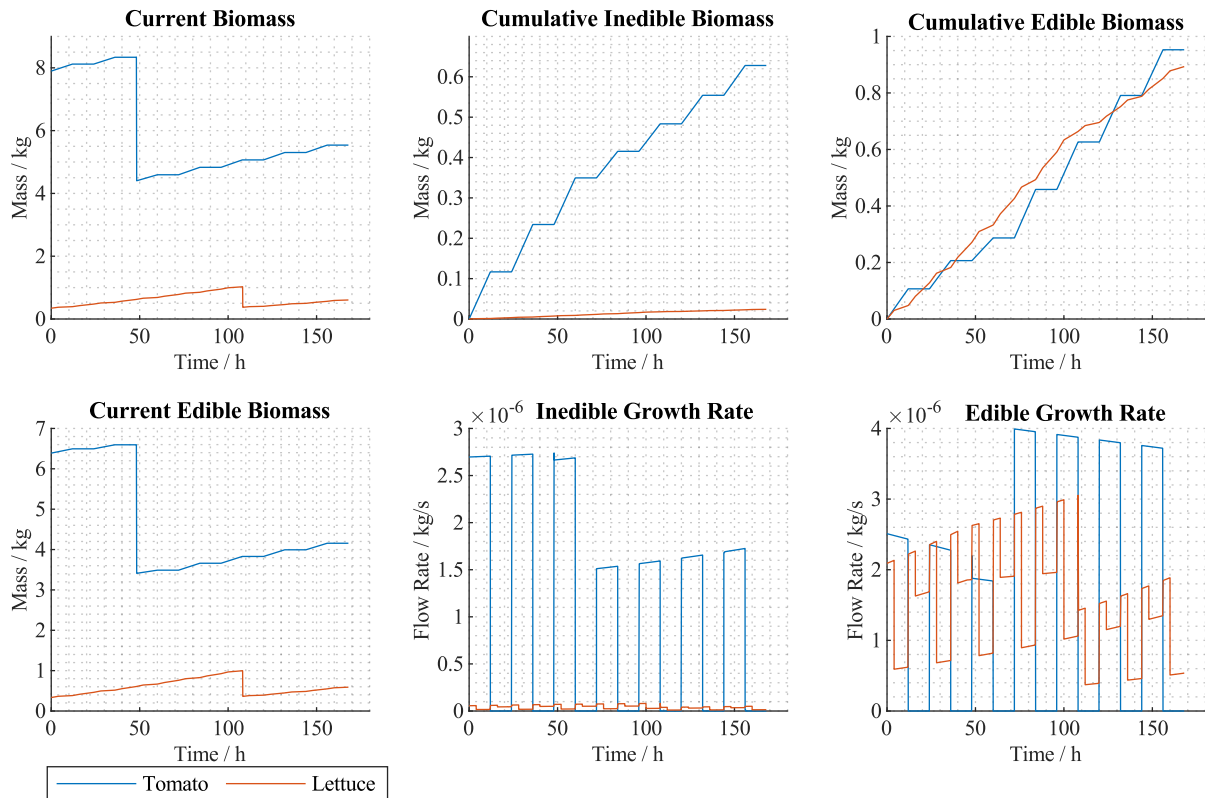


Figure 6.3-7 Overview of PGC biomass values. The values are the summation over the four cultures for each crop. Cumulative values represent the integral of the corresponding flowrates.

The results shown in Figure 6.3-7 to Figure 6.3-9 are for the US Lab case. The other PGC cases are not shown, as the values for the PGC itself do not differ significantly between the cases.

Figure 6.3-7 shows the biomass for both crop types used in the PGC. The values are shown as the sum of all four cultures for each crop for conciseness and the drops in biomass and edible biomass show the time plants are harvested. Since the PGC is initialized with 78 days of previous growth, tomatoes are harvested two days after the start of the simulation.

Figure 6.3-8 shows the different interactions of the PGC with the ECLSS, both as flowrate and as cumulative mass, which is the flowrate integrated over time. By comparing the water uptake and the transpiration it is obvious that most water consumed by the plants is transpired again and then recovered by the ISS ECLSS. From the oxygen and CO₂ exchanges it is also obvious that the PGC does not have any significant impact on the oxygen and CO₂ levels.

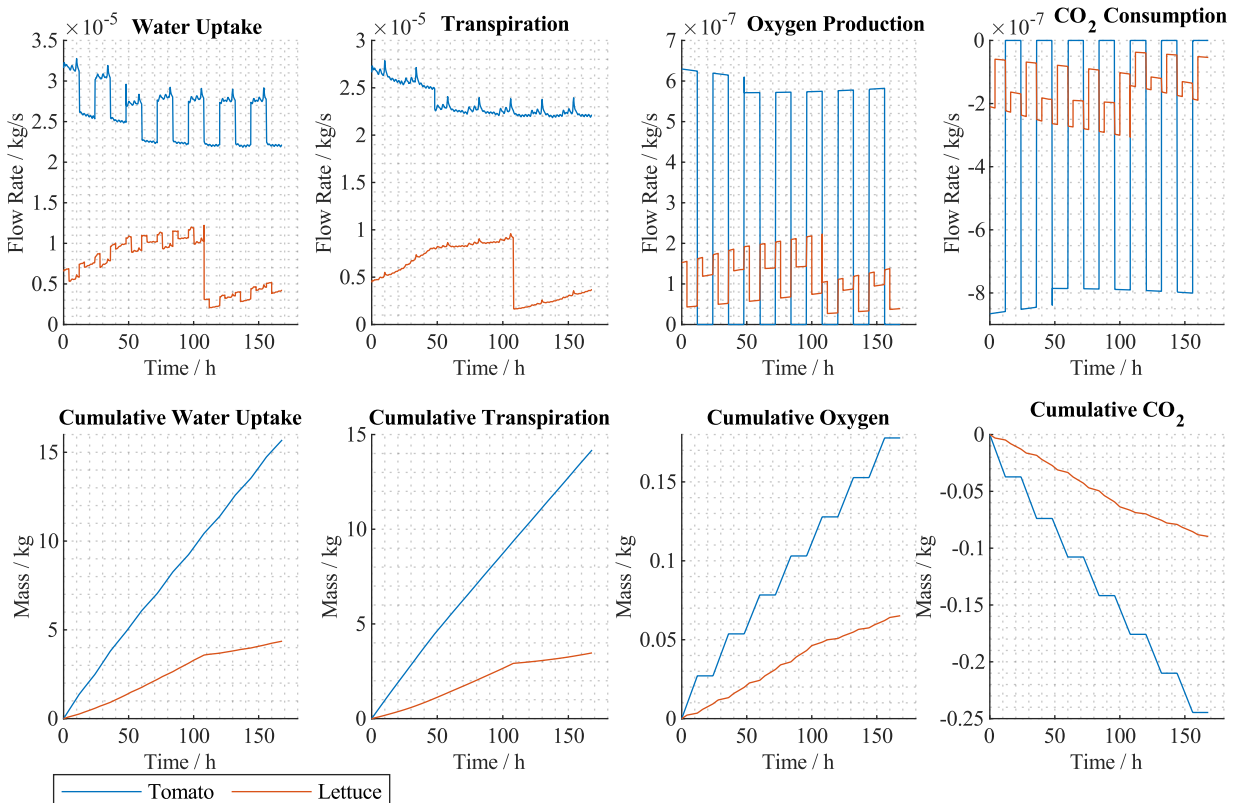


Figure 6.3-8 Overview of the PGC interaction with the environment. Cumulative values represent the integral of the corresponding flowrates.

Figure 6.3-9 shows the nutritional values of the PGC and the nitrate uptake. This figure is only for information and to showcase the nutritional uptake dynamics of the plants, but the implemented control logic will ensure ideal plant growth for the ISS case study.

Figure 6.3-10 shows the recovered condensate masses of the different CCAA for the different locations of the PGC. As Figure 6.3-8 shows the overall transpired water of the PGC is 17.6 kg. For the case where the PGC is located in SM 10.8 kg additional condensate are recovered in SM (or 61% of the transpired water). For the JEM case 11.2 kg of additional condensate are recovered in JEM (or 64% of the transpired water). And for the Columbus case 7.55 kg additional condensate are recovered in Columbus (or 43% of the transpired water). The water recovery in Columbus is the lowest due to the small module volume and the higher coolant water temperature used in the CCAA of Columbus as discussed by (Pütz et al. 2018).

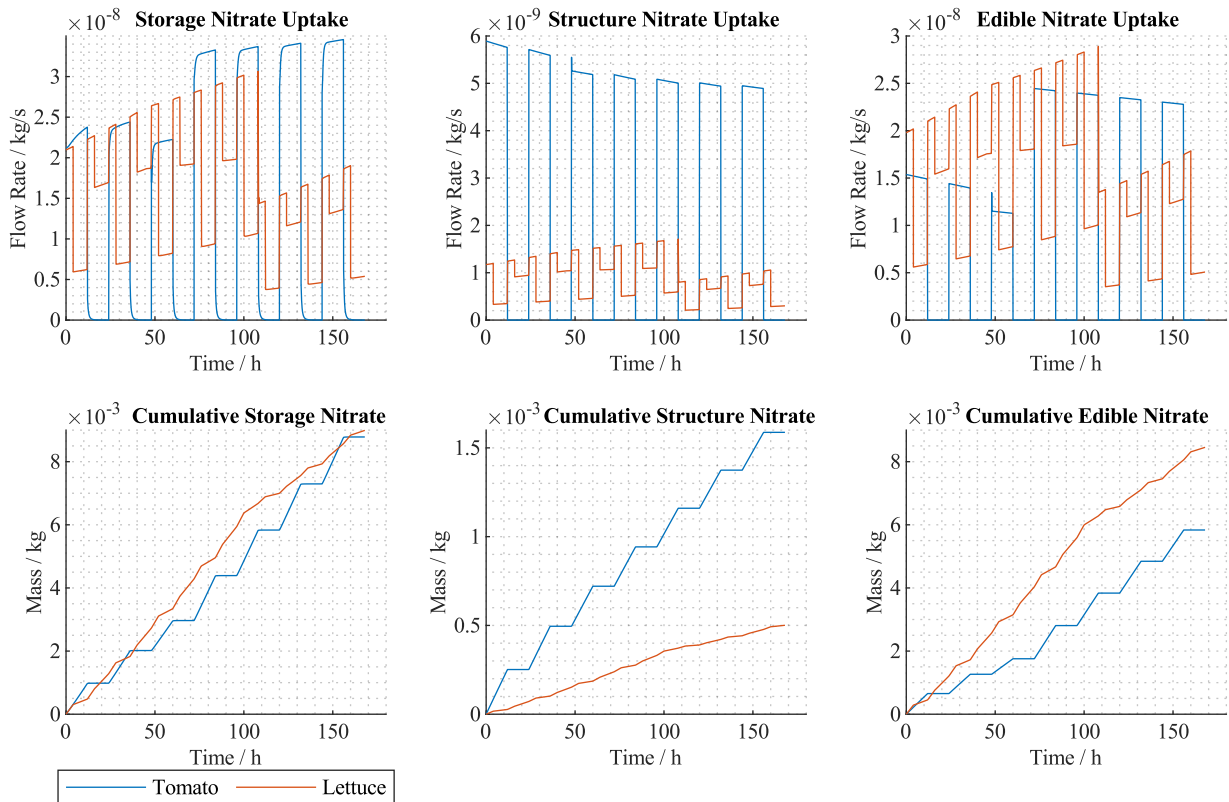


Figure 6.3-9 Overview of the nutritional conditions for the PGC. Cumulative values represent the integral of the corresponding flowrates.

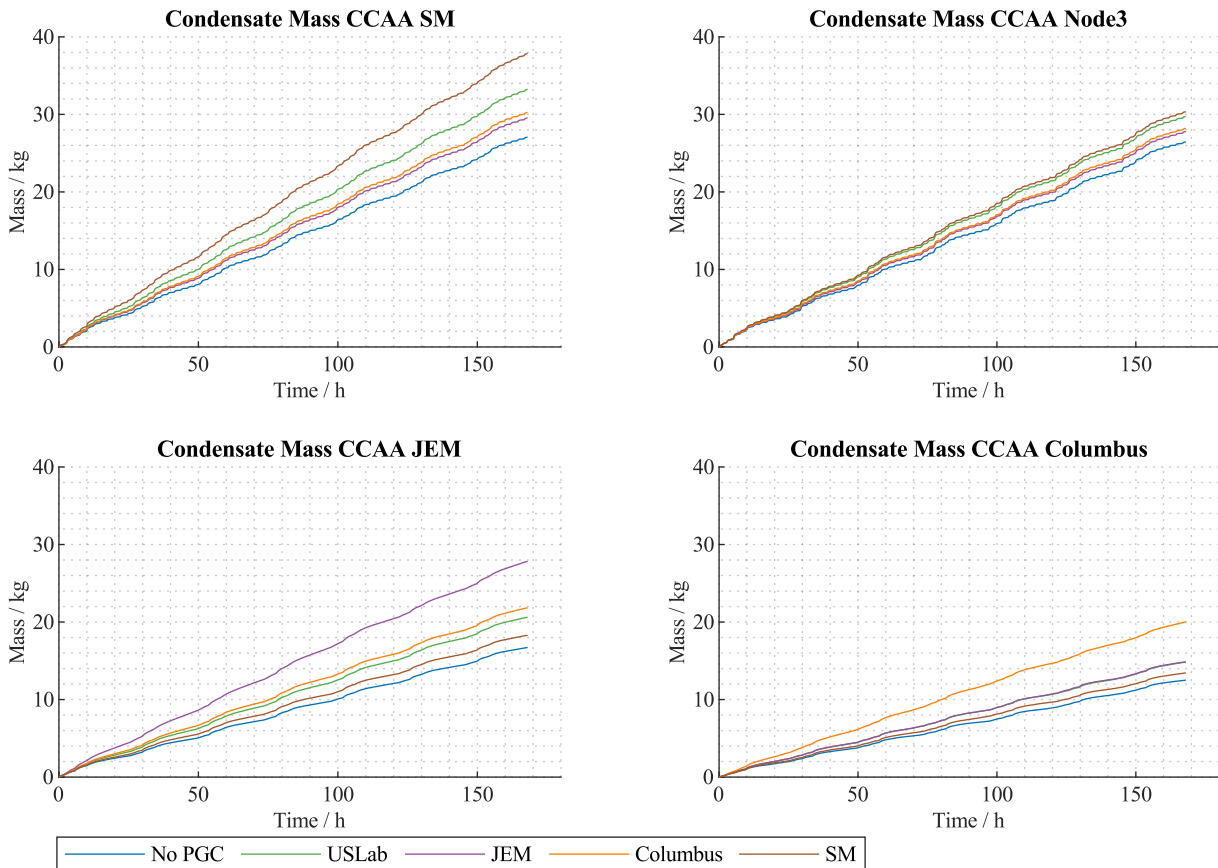


Figure 6.3-10 Condensate mass recovered by the CCAAs for the different locations of the PGC as defined by the legend.

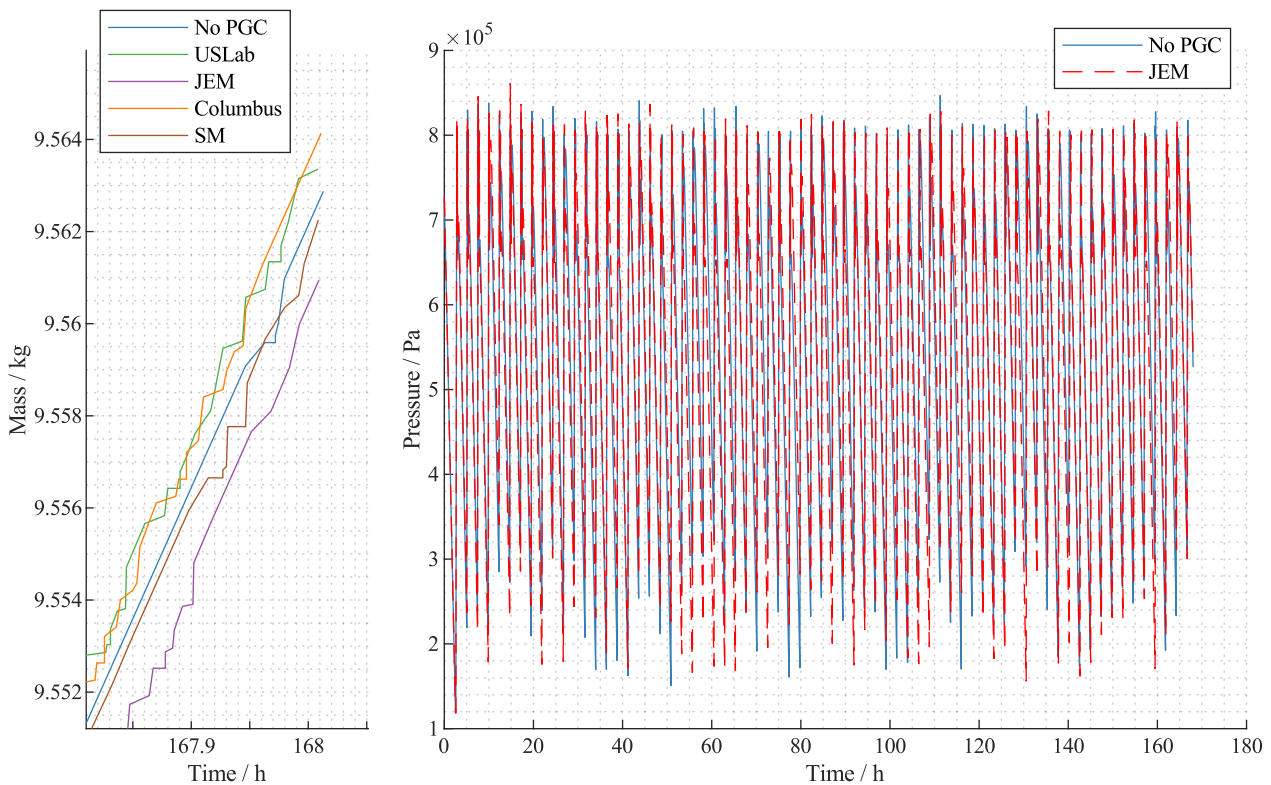


Figure 6.3-11 Produced water by SCRA for the different PGC cases (left). And SCRA accumulator pressure for the case without PGC and with a PGC in JEM.

Figure 6.3-11 shows the final results for the produced water by SCRA, which differs only slightly between the cases and is within the error margin of the simulation. It also shows the pressure within the CO₂ accumulator of SCRA for the case without PGC and the JEM case. The JEM case was selected here because it resulted in the lowest recovered water for SCRA according to the left part of the figure.

6.3.3 Discussion

In this chapter the research questions defined in Table 4.3-1 for mission scenario one are discussed in relation to the results from chapter 6.3.2. The first research question for this mission scenario was:

“Q-1.1 Where is water from a plant system recovered and does this have an impact on required crew time?”

The location of water recovery is spread between the different CCAAs and depends on the location of the PGC. A detailed overview of the location of recovered water is provided in Figure 6.3-10. This does have an impact on crew time as the water balance between the US and Russian ECLSS is affected by more than 10 kg for all cases. This value exceeds the amount of water that can be balanced through e.g. adjustment of OGA production rate. In addition, the location impacts how large this imbalance becomes.

This question is answered by Figure 6.3-10 which shows the difference in water recovery for the CCAAs depending on the PGC location. This can lead to additional required crew time as a water imbalance between the Russian and US segment of the ISS exists (Carter et al. 2016) but no direct water line between the two parts can be placed because of the different biocides used by the Russian systems and the US systems (Li et al. 2018c). This means even without a PGC water must be periodically moved from the US segment to the Russian segment e.g. by transferring condensate water using Contingency Water Containers (Carter et al. 2016). These must be filled manually and therefore require crew time. There are also other options to maintain water balance, like e.g. increasing the oxygen production by OGA to increase the water consumption in the US segment and decrease it in the Russian segment (Carter et al. 2016). However, the 17.6 kg of additional water produced by the PGC (see Figure 6.3-8) would exceed the required water for oxygen production.

Assuming that the PGC cannot be placed in the Russian segment, the second-best location for it according to this analysis would be the US Lab as this has the second highest value of recovered water in the Service Module. However, the Russian CHX is not modelled accurately as it is assumed to be identical to the CCAA, therefore these results can only be considered qualitative results.

The second research question for this mission scenario from Table 4.3-1 was:

“Q-1.2 Is a plant system that is open to the cabin atmosphere feasible or is a dedicated humidity control required?”
Since both the humidity control systems and the water processing systems are capable of handling the additional water load of an ISPR sized PGC, it is feasible to use an open PGC without internal humidity control on the ISS.

See Figure 6.3-4 to Figure 6.3-6 for the required data to support this claim. However, the amount of transpired water can be reduced by a closed PGC if it also has higher humidity for the atmosphere in which the plants are grown. A break-even analysis for open and closed chamber PGC for Gateway was performed in (Pütz et al. 2018). Gateway is planned to use the CO₂ And Moisture Removal Amine Swing-bed (CAMRAS) of Orion, which removes the cabin humidity and vents it into space. Therefore, if an additional CHX is considered, the question arises whether this should be placed in the cabin atmosphere or within the PGC. Figure 6.3-12 shows the break-even analysis for this case.

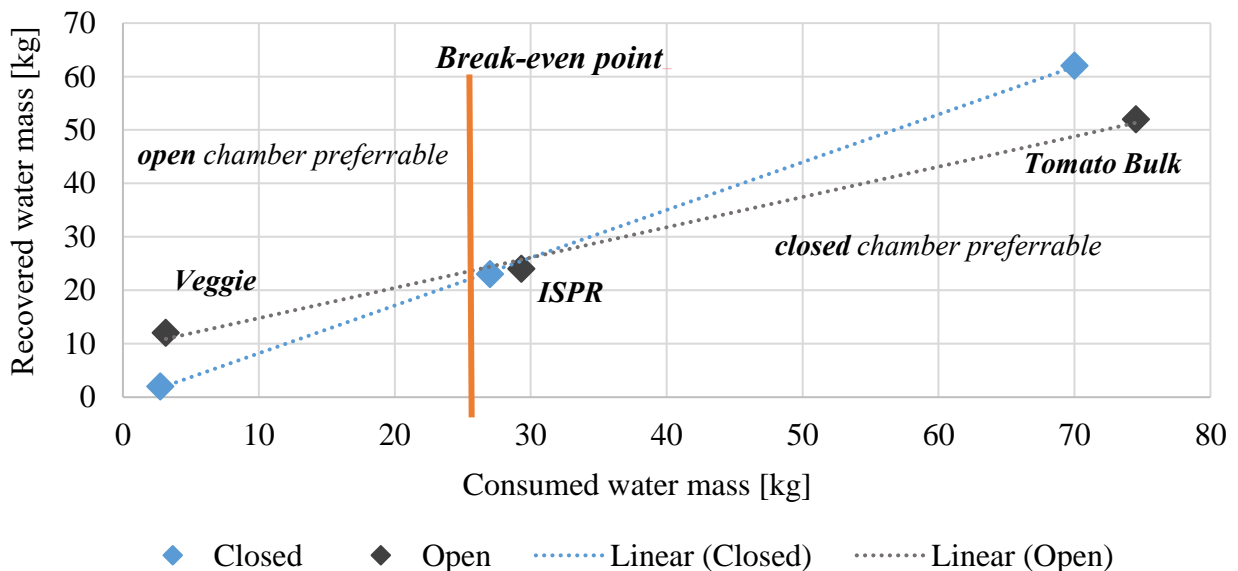


Figure 6.3-12 Recovered water mass over the consumed water mass for an open plant growth chamber with a CCAA in the habitat and for a closed plant growth chamber with a CCAA inside the chamber. In all cases CAMRAS is used as primary air revitalization system. (Pütz et al. 2018)

The third research question for this mission scenario from Table 4.3-1 was:

“Q-1.3 What impact does a plant system have on existing loop closure systems for example the Sabatier reactor?”
All PGC cases have only miniscule effects on the SCRA performance. Therefore, for a PGC on the scale of one ISPR no reduction in performance for SCRA is expected.

Figure 6.3-11 shows the SCRA performance for different PGC locations. No significant reduction in recovered water is observed for any of the considered cases. This is the case because more CO₂ is available than can be consumed by SCRA. The accumulator pressure shown in Figure 6.3-11 shows slightly different behavior, but overall does not reach lower pressure than in the case without PGC. Therefore, an ISPR sized PGC can likely be operated on the ISS without affecting the SCRA.

6.4 Mission Scenario Two: Moon Base

The analysis of the Moon base without bioregenerative subsystems is also discussed in (Kaschubek et al. 2021). Here the results from the paper and two additional cases are discussed. The additional cases include a PBR as well as a PBR and a PGC as biological ECLSS.

Before considering the ECLSS analysis, the boundary conditions must be discussed. For this mission scenario, it was first necessary to identify potential locations for a crewed Moon base. This is discussed in detail in (Kaschubek et al. 2021), the four most promising landing sites are shown in Figure 6.4-1. The landing site selection was performed collaboratively by Matthias Killian and the author of this dissertation. Matthias Killian developed the final implementation for the landing site selection algorithm and derived Figure 6.4-1 from it. The other cited content from (Kaschubek et al. 2021) were primarily contributions of the author of this dissertation with support from the co-authors.

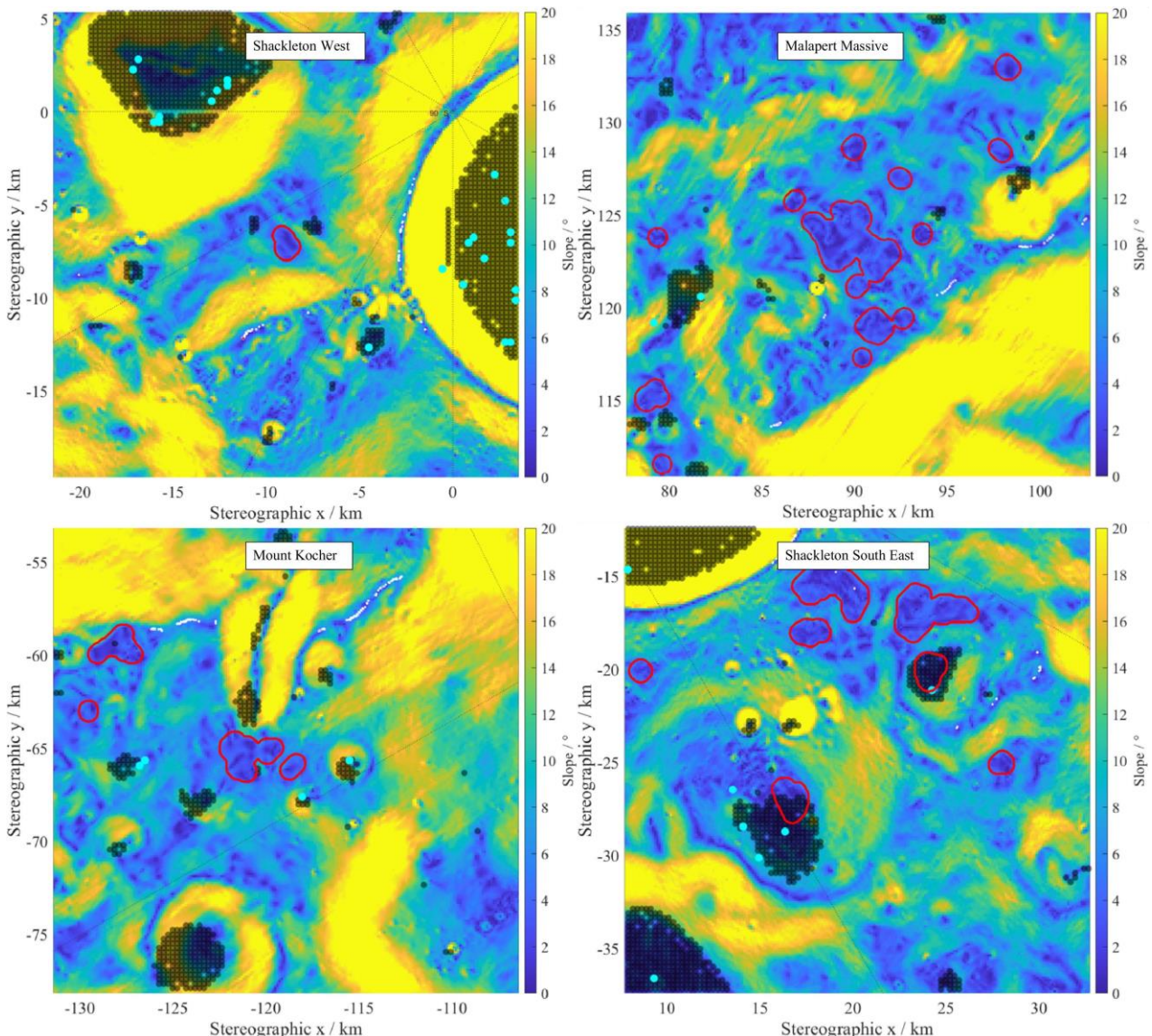


Figure 6.4-1 The four most promising landing sites at the lunar south pole. Areas with low enough slope are marked by red lines. Black points indicate permanently shaded regions, white points are peaks of light, and cyan points water ice from (Li et al. 2018a) as auxiliary information. The figure from (Kaschubek et al. 2021) was created by Matthias Killian.

The illumination at the best available peak of light for each of the four candidate landing sites was analyzed in a preliminary energy storage system analysis shown in Figure 6.4-2. Based on the discussion of landing sites from (Kaschubek et al. 2021) only the Mount Kocher and Shackleton South East sites are further studied.

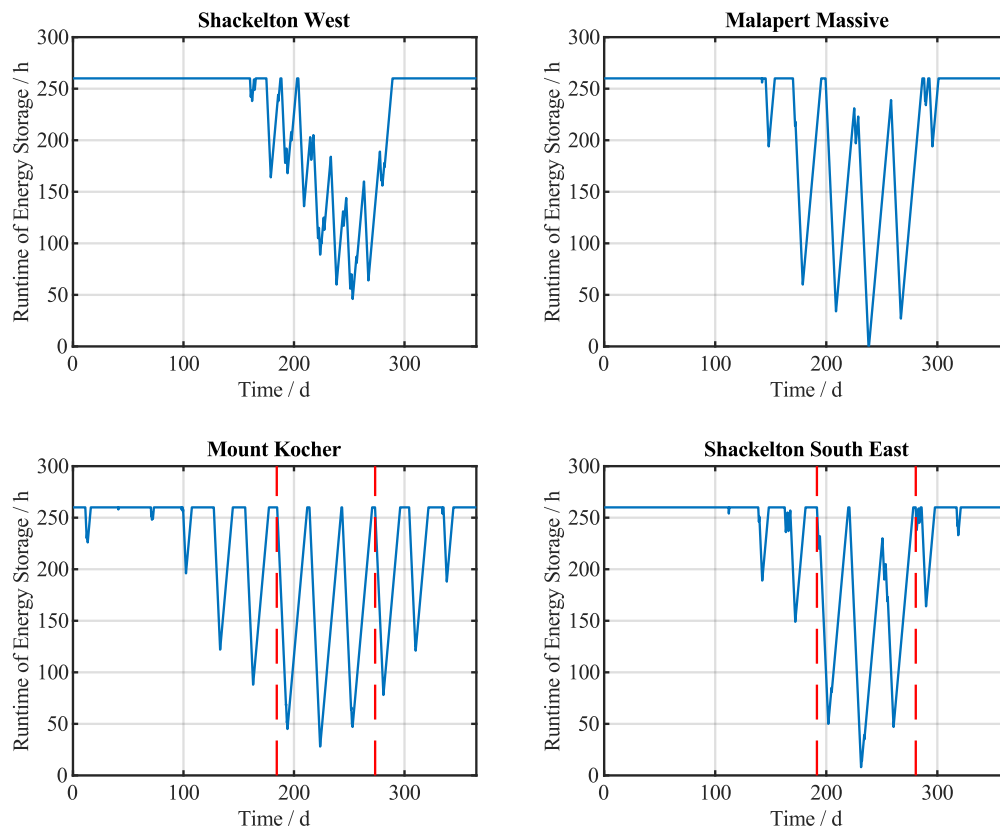


Figure 6.4-2 Estimated remaining energy storage system runtime over one year for the four selected candidate landing sites. The charge to discharge (C/D) ratios are defined to fully recharge the energy storage before the longest continuous shadow duration. The dashed red lines indicate the simulated period for the detailed analysis in the following chapters. Figure from (Kaschubek et al. 2021).

6.4.1 Model Structure

6.4.1.1 ECLSS

“The selected ECLSS is based on the current ISS ECLSS with the adjustment of a Regenerative Fuel Cell System (RFCS) for energy storage and oxygen supply purposes and an ilmenite hydrogen reduction reactor to generate oxygen from lunar regolith. This selection was based on current plans of NASA to use an ISS-based physical/chemical ECLSS with a RFCS as potential energy storage systems for a lunar surface base (Zuniga et al. 2019). RFCS is a broad term covering systems that use a single component for both electrolysis and as fuel cell (so called reversible fuel cells or unitized regenerative fuel cell systems) and systems that use two separate components for the electrolysis and the fuel cell. We decided to use two separate components, because that enables independent scaling of the components to their specific needs and because high pressure electrolysis is assumed which usually requires a separate electrolyzer (Barbir et al. 2005). Figure 6.4-3 provides a schematic overview of the system with the expected nominal daily mass flows without shadow phases. For shadow phase operation, the electrolyzer and ISRU reactor produce more during daytime to cover the required hydrogen and oxygen mass during shadow phases. For an exemplary 14-day, 14-night cycle, the electrolyzer would produce twice the shown amount during daytime to cover oxygen supply and energy needs during nighttime. Remaining flowrates are based on values from Table 5.1-8 and stoichiometric calculations of the system reactions and represent a steady state analysis. For water reprocessing the Urine Processor Assembly (UPA), Brine Processor Assembly (BPA) and Water Processor Assembly (WPA) of the ISS are used. The Common Cabin Air Assembly (CCAA) and the Carbon Dioxide Removal Assembly (CDRA) handle the air revitalization together with oxygen produced by the electrolyzer. The ISRU process generates the required water for oxygen production and receives the recycled hydrogen from the electrolyzer. The Sabatier CO₂ Reprocessing Assembly (SCRA) reprocesses crew CO₂ into CH₄ which can be used as fuel.” (Kaschubek et al. 2021)

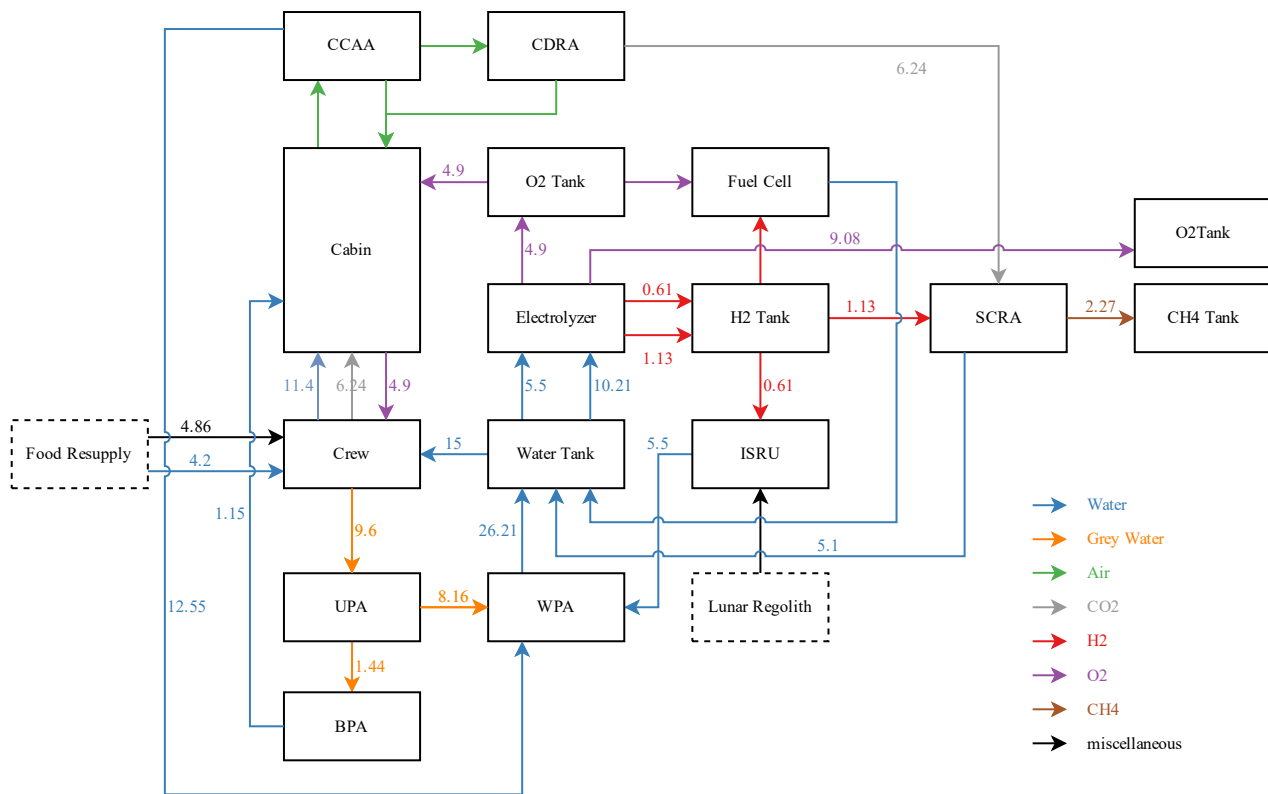


Figure 6.4-3 Schematic of the ECLSS with mass flows in kg/day if no shadow phase is assumed at all. Values are based on a crew of six with metabolic values from (Anderson et al. 2018: 63). Other values assume ideal stoichiometric conversion. Figure from (Kaschubek et al. 2021).

With the assumptions from Table 5.1-8, “a total water recovery rate of 98 % is expected for the ISS (Carter et al. 2019). Furthermore, water is indirectly resupplied to the ECLSS from food resupply (4.2 kg/day for a crew of six (Anderson et al. 2018)) and generated metabolic water (2.07 kg/day to 2.4 kg/day for a crew of six (Anderson et al. 2018)), which leads to a water surplus in the system. In our investigated system, this surplus amounts to 5.71 kg/day and is used to produce fuel from crew CO₂ using the electrolyzer and the SCRA. The SCRA produces water and methane. The produced water is electrolyzed while the methane and corresponding amount of oxygen is stored as rocket fuel. Hydrogen generated in the electrolyzer from the SCRA water is fed back to the SCRA and decreases the required net-water for methane and oxygen production to ~5.1 kg/day. This leaves ~0.6 kg/day of surplus water which can be used to compensate losses in the system or supply payloads. Also, the produced oxygen to methane molar ratio of 2:1 is the correct ratio for rocket fuel. In total, the fuel production amounts to over 4,100 kg per year. Alternatively, it is possible to use surplus water to produce oxygen for the crew and reprocess the produced hydrogen in the SCRA for methane production without the need for an ISRU reactor. However, the produced methane would then lack the required oxygen for combustion. Furthermore, the proposed system has the advantage of dissimilar redundancy, as the oxygen supply for the crew is ensured if either the ISRU reactor or the Sabatier system fails, as long as the electrolyzer works. In addition, this architecture provides the option to demonstrate an ISRU reactor technology for life support without it being a mission critical component of the ECLSS.

The water surplus comes at a cost as the hardware replacement rates in Table 5.1-8 prove. In total, the water recovery system requires a resupply of 2.16 kg/day (0.84 kg for WPA, 1.03 kg for UPA and 0.29 kg for BPA). This amounts to a total of 789 kg/year of resupply for water recovery. However, the considered system in return produces more than five times of this mass as fuel, and therefore we consider it a viable option.

The thermal control subsystem to release heat to the environment is not modelled in detail due to the already large scope of the paper. We consider the full dynamic combination of TherMoS and V-HAB and the inclusion of a thermal control system as future work and we plan to perform such an analysis in the future.” (Kaschubek et al. 2021)



6.4.1.2 Power Subsystem

In order to dimension the power subsystem, it is necessary to first define the power demand of the Moon base. Table 6.4-1 “...summarizes the power consumptions of the considered Moon base subsystems and the sources for the values.

Table 6.4-1 Moon Base subsystem power demand.

Power Consumption	Unit	Value	Source
WPA Operating	W	428	(Carter 2009)
WPA Standby	W	241	(Carter 2009)
WPA Averaged	W	275.1	¹⁴
UPA Operating	W	315	(Carter 2009)
UPA Standby	W	56	(Carter 2009)
UPA Averaged	W	211.4	¹⁵
BPA	W	142	(Carter and Gleich 2016)
SCRA Steady State	W	90	(Junaedi et al. 2014)
SCRA Startup	W	120	(Junaedi et al. 2014)
CCAA	W	470	(Wieland 1998)
CDRA Averaged	W	497	(Wieland 1998)
CDRA Maximum	W	1,351	(Wieland 1998; Coker et al. 2015)
ISRU Reactor Averaged	W	2,000	¹⁶
ISRU Reactor Maximum	W	5,700	¹⁶
Electrolyzer (only for ECLSS)	W	3,210	¹⁷
Average ECLSS Power Demand	W	6,895	¹⁸
Maximum ECLSS Power Demand	W	11,736	¹⁹
Remaining Base	W	32,000	(Anderson et al. 2018)
Overall Average Power Demand	W	38,895	
Overall Maximum Power Demand	W	43,736	

Based on the average power demand and the estimated energy storage capacities from Figure 6.4-2 we calculated the total required energy to survive the shadow phase. We assume that the electrolyzer and ISRU reactor only operate while sunlight is available. Therefore, the average power demand during the shadow phase is

$$P_{shadow} = 32 \text{ kW} + 6.895 \text{ kW} - 3.21 \text{ kW} - 2 \text{ kW} = 33.685 \text{ kW} \quad (6.4-1)$$

Assuming a constant cell voltage of $U_{cell,FC} = 0.75 \text{ V}$ the required hydrogen mass can be calculated using its molar mass of $M_{H_2} = 2 \frac{\text{g}}{\text{mol}}$ and the Faraday constant $F = 96,485 \frac{\text{C}}{\text{mol}}$ with the law of Faraday:

$$\dot{m}_{H_2,FC} = M_{H_2} \cdot \frac{P_{shadow}}{U_{cell,FC} \cdot F \cdot 2} = 0.47 \frac{\text{g}}{\text{s}} \quad (6.4-2)$$

For the Shackleton South East site, the required energy storage time according to Figure 6.4-2 is 252 h and for the Mount Kocher site 232 h. We include a small contingency and assume 260 h and 240 h for further analysis. In the following, we only describe calculations for the Shackleton South East site. Calculations for the Mount Kocher site are analogous.

¹⁴ We assume WPA to operate 18.25 % of the time (based on the required processing capacity from Table 5.1-8 and the nominal processing capacity from Carter et al. (2005)) resulting in an average power demand of 275.11 W.

¹⁵ We assume UPA to alternately operate for 7.5 h and then being in standby for 5 h Tobias et al. (2011) resulting in an average power demand of 211.4 W.

¹⁶ Based on the ISRU reactor model from chapter 5.3.9.

¹⁷ Assuming a cell voltage of $U_{cell,ELY} = 1.65 \text{ V}$ and using the Faraday equation for the required hydrogen from Figure 6.4-3.

¹⁸ Sum of averaged and steady state values of the subsystems

¹⁹ Sum of maximum values of the subsystems

According to equation (6.4-2) the total hydrogen mass required for energy production during the shadow phase is 447.8 kg and the corresponding oxygen mass based on stoichiometric conversion is 3,541 kg. In addition to the hydrogen and oxygen mass required for energy storage, the system shall also store the required oxygen for the crew and the required hydrogen to continue Sabatier operations through the night. For this an additional 12.12 kg of hydrogen and 55.25 kg of oxygen must be stored based on the shadow duration and the values from Figure 6.4-3. The required volumes to store hydrogen and oxygen at 200 bar and 293 K are $\sim 30.8 \text{ m}^3$ for hydrogen and $\sim 12.8 \text{ m}^3$ for oxygen if a residual pressure in the tanks of 2 bar is assumed. For contingency reasons the volume in the final simulation is increased slightly to 32.3 m^3 for hydrogen and 13.5 m^3 for oxygen which is the equivalent to about 420 kWh additional energy storage. This is sufficient to maintain base operations for about half a day.

We estimate the required power for the electrolyzer based on the C/D ratio of 0.5 from Figure 6.4-2. The efficiencies of the electrolyzer and the fuel cell are calculated from the assumed cell voltages $U_{cell,FC} = 0.75 \text{ V}$ and $U_{cell,ELY} = 1.65 \text{ V}$, the ideal cell voltages $U_{ideal,FC} = 1.25 \text{ V}$ and $U_{ideal,ELY} = 1.48 \text{ V}$ (see (Kurzweil 2013) page 19) and the C/D ratio $r_{C/D} = 0.5$ from Figure 6.4-2:

$$P_{ELY} = r_{C/D} \cdot P_{shadow} / \left(\frac{U_{ideal,ELY}}{U_{cell,ELY}} \cdot \frac{U_{cell,FC}}{U_{ideal,FC}} \right) = 35 \text{ kW} \quad (6.4-3)$$

For a conservative design, we slightly increase the electrolyzer power to 36.5 kW. Adding maximum power demand from Table 6.4-1 results in a peak power demand of 80.2 kW and a mean power demand of 75.4 kW. It is not necessary to cover peak power demand as in cases where the solar array power is insufficient the electrolyzer power is reduced accordingly to maintain vital system operations. Therefore, we selected 76.5 kW as design point for the solar cells, again to remain conservative. We calculate the required solar cell area based on the end-of-life efficiency of state-of-the-art solar cells of 26.5 % (Lackner et al. 2019) and the solar constant on the Moon of 1.36 kW/m^2 :

$$A_{SolarCells} = \frac{76.5 \text{ kW}}{0.265 \cdot 1.36 \frac{\text{kW}}{\text{m}^2}} = 212 \text{ m}^2 \quad (6.4-4)$$

“ (Kaschubek et al. 2021)

6.4.1.3 System Mass and Resupply Estimates

“In this chapter, we discuss mass estimates for the RFCS and the required resupply of the moon base. A full ESM analysis of the system is not included here, as it would exceed the scope of his paper. However, the results can support such an analysis in future research and show the viability of the systems considered in this paper.

RFCS achieve energy densities of 500 Wh/kg (Barbir et al. 2005) which would result in a system mass of $17,500 \text{ kg}^{20}$. However, we consider this estimate to be insufficient as it neglects resupply. If we compare the RFCS system to the OGA from the ISS, which produces 9.25 kg/day oxygen at full power (Schaezler and Cook 2015), the required oxygen production is 17.7 times larger. This value is based on the 3,541 kg of required oxygen from chapter 6.4.1.2, which must be produced in 21.67 days²¹ resulting in a daily production of 163.4 kg of oxygen. The initial mass of OGA is 676 kg with a hardware replacement rate of 0.07 kg per kg of oxygen (Bagdigian et al. 2015). Linearly scaling OGA results in 12,000 kg of electrolyzer hardware. Resupply mass is calculated based on the total shadow time, which can be calculated from the data shown in Figure 6.4-2, and the required oxygen per shadow day from chapter 6.4.1.2. The Shackleton South East site for example has 45.1 days of shadow per year, resulting in a total of $14,741 \text{ kg}^{22}$ of oxygen that must be produced. The Mount Kocher site has 63 days of shadow per year. Multiplying the oxygen mass with the hardware replacement rate results in a resupply mass of 1,032 kg per year.

²⁰ $\frac{33,685 \text{ W} \cdot 260 \text{ h}}{500 \text{ Wh/kg}} = 17,516 \text{ kg}$

²¹ $\frac{t_{shadow}}{r_{charge/discharge}} = \frac{260 \text{ h}}{0.5} = 520 \text{ h} = 21.67 \text{ days}$

²² $\frac{3,541 \text{ kg}}{260 \text{ h}} \cdot 45.1 \cdot 24 \text{ h} = 14,741 \text{ kg}$



The fuel cell can be compared e.g. to the shuttle fuel cell which had a mass of 116 kg and provided 12 kW power (Elitzur et al. 2016). The RFCS fuel cell mass is calculated to be 326 kg with linear scaling and based on the power of 33,685 W calculated in chapter 6.4.1.2. The oxygen tank mass is estimated to weigh 1,289 kg using a factor of 0.364 kg tank per kg oxygen (Anderson et al. 2018). The hydrogen tanks of the Space Shuttle had a dry mass of 98 kg and could contain up to 41.8 kg of hydrogen (Elitzur et al. 2016: 581), which results in a factor of 2.34 kg tank per kg hydrogen. This gives a hydrogen tank mass of 1,050 kg for the RFCS.

The required water mass is 4,000 kg and is stored in a tank that weighs 824 kg based on (Jones 2018). A conservative estimate, based on space proven hardware, gives us a total mass of 19,500 kg for the RFCS. While this is slightly larger than the mass if 500 Wh/kg are assumed, this is to be expected as flight proven not state of the art technologies are used. For comparison, a system using lithium-ion batteries with an energy density of 212.9 Wh/kg (Kim et al. 2020) has a system mass of 41,100 kg, which is more than twice the conservative estimate.

The required resupply of food for a six-person crew over one year amounts to 3,307 kg, with an additional 751.2 kg required for clothing. These numbers are based on ISS values from (Anderson et al. 2018: 100). In addition, 1,821 kg of spare parts for the water reprocessing subsystems (WPA, UPA, BPA) and the electrolyzer are expected. One set of spare parts for CDRA (156 kg) and SCRA (219 kg) per year are included based on the spare mass values from (Jones 2017), as well as one replacement fuel cell per year. The total resupply mass for the ECLSS and power system comes to 6,580 kg per year. For the ISRU reactor and the CCAA no information on required spare parts are available, this is why they are neglected in this study. Table 6.4-2 summarizes literature parameters used for this analysis as well as their sources.

Table 6.4-2 Mass estimation literature parameters.

Parameter	Unit	Value	Source
OGA System Mass	kg	676	(Bagdigian et al. 2015)
OGA Resupply Rate	kg/kg	0.07	(Bagdigian et al. 2015)
OGA Oxygen Production Rate	kg/d	9.25	(Schaezler and Cook 2015)
Shuttle Fuel Cell System Mass	kg	116	(Elitzur et al. 2016)
Shuttle Fuel Cell Power	W	12,000	(Elitzur et al. 2016)
Shuttle Hydrogen Tank Mass	kg	98	(Elitzur et al. 2016)
Shuttle Hydrogen Tank Content	kg	41.8	(Elitzur et al. 2016)
Oxygen Tank Mass per Oxygen mass	kg/kg	0.364	(Anderson et al. 2018)
Water Tank Empty Mass	kg	21.2	(Jones 2018)
Water Tank Filled Mass	kg	124.2	(Jones 2017)
CDRA Mass of one Set of Spares	kg	156	(Jones 2017)
SCRA Mass of one Set of Spares	kg	219	(Jones 2017)

” (Kaschubek et al. 2021)

6.4.2 Results

Initially the results for the Moon base ECLSS without bioregenerative components from (Kaschubek et al. 2021) are discussed. As previously mentioned only the candidate sites Mount Kocher and Shackleton South East are studied in detail, see Figure 6.4-2 where the dashed red lines mark the simulated periods shown in this chapter.

“Simulation results including detailed power demand from cycling effects of the subsystems, are depicted in Figure 6.4-4. Results show that solar power is available for longer durations than the electrolyzer requires to recharge the oxygen and hydrogen tanks. This shows that the electrolyzer is over-dimensioned even though the available power for the electrolyzer has to be reduced during peak power demands of the remaining base. For example, at the Mount Kocher site storage tank recharge is finished four days earlier than required in a 29.58-day long recharge cycle. This amounts to a possible electrolyzer power reduction of 15% if the intended contingency of ~5% (see chapter 6.4.1.2) shall remain. Further analysis of electrolyzer power settings could help find the actual possible minimum since full recharge of the hydrogen and oxygen tanks is not necessary for shorter shadow durations.

We assumed pressure tanks for oxygen and hydrogen storage as V-HAB currently lacks a cryogenic tank model. The minimum hydrogen tank pressure is 79.9 bar for the Mount Kocher site and 68.4 bar for the South East Shackleton Site. Therefore, the unused hydrogen mass is 193.5 kg and 170.2 kg respectively. For both simulations, the hydrogen tank volume was set to 32.3 m³, which could therefore be reduced to 16.5 m³ for the Mount Kocher site and to 18.1 m³ for the Shackleton South East Side. The initially planned contingency from chapter 6.4.1.2 was only 1.5 m³ for hydrogen and 0.7 m³ for oxygen. These differences are a result of conservative assumptions (e.g. for the efficiency of the fuel cell and electrolyzer) in the initial sizing, which are depicted more accurately in the dynamic simulation (e.g. base power demand, efficiency calculated dynamically depending on the current densities in fuel cell and electrolyzer).

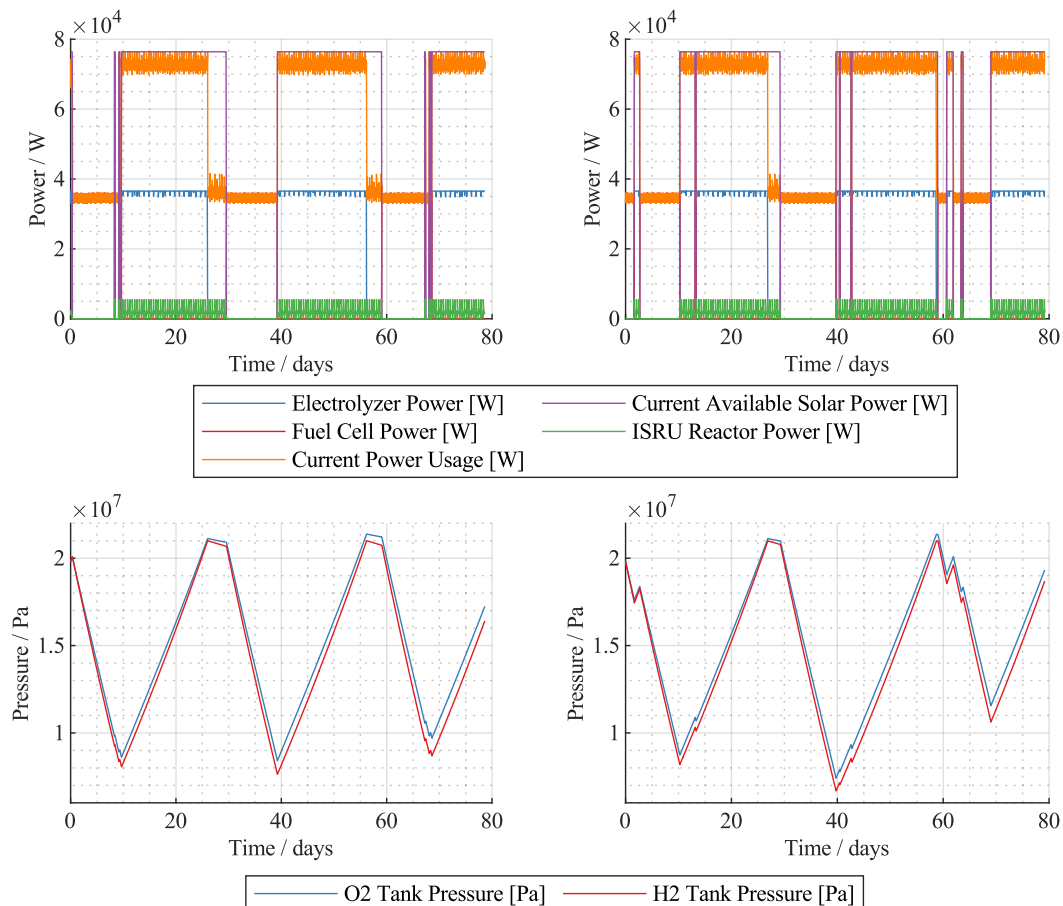


Figure 6.4-4 Power and hydrogen/oxygen tank pressures for the Moon base at Mount Kocher (left) and South East Shackleton (right).

The initial assumption for the potable water tank was an oversized tank filled with 3,000 kg of water even though the oxygen and hydrogen tanks were also filled. From this the required minimum stored water mass is calculated as the difference between maximum and minimum water mass within the tank. Figure 6.4-5 shows the water mass within the water tank. For the Mount Kocher site, the minimum water mass that must be stored is 2,694 kg and for the Shackleton South East site it is 2,890 kg. Figure 6.4-5 shows differences in WPA processing during sun and shadow phases. This is a result of the ISRU reactor operating only during sun phases, which leads to more WPA cycles during this time.

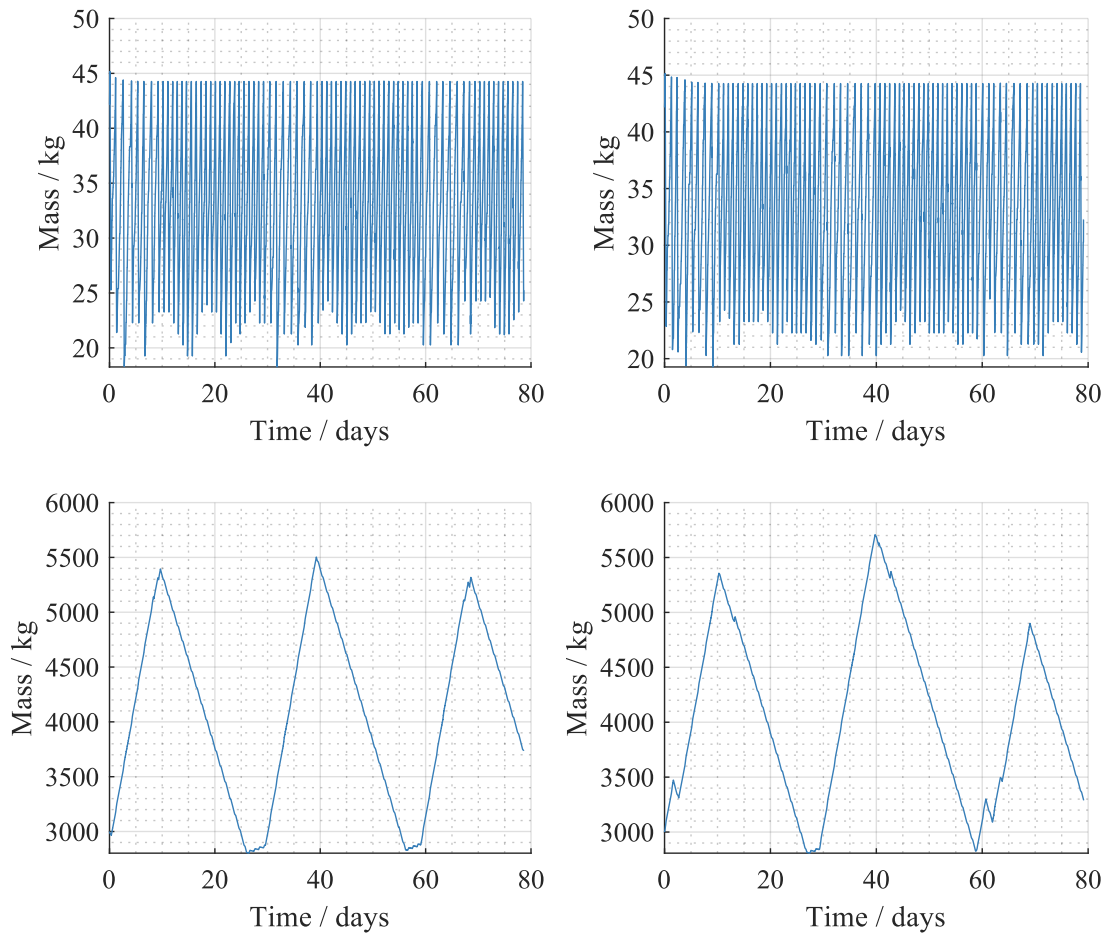


Figure 6.4-5 WPA waste-water tank mass (top) and potable water tank mass (bottom) for the Moon base at Mount Kocher (left) and South East Shackleton (right).

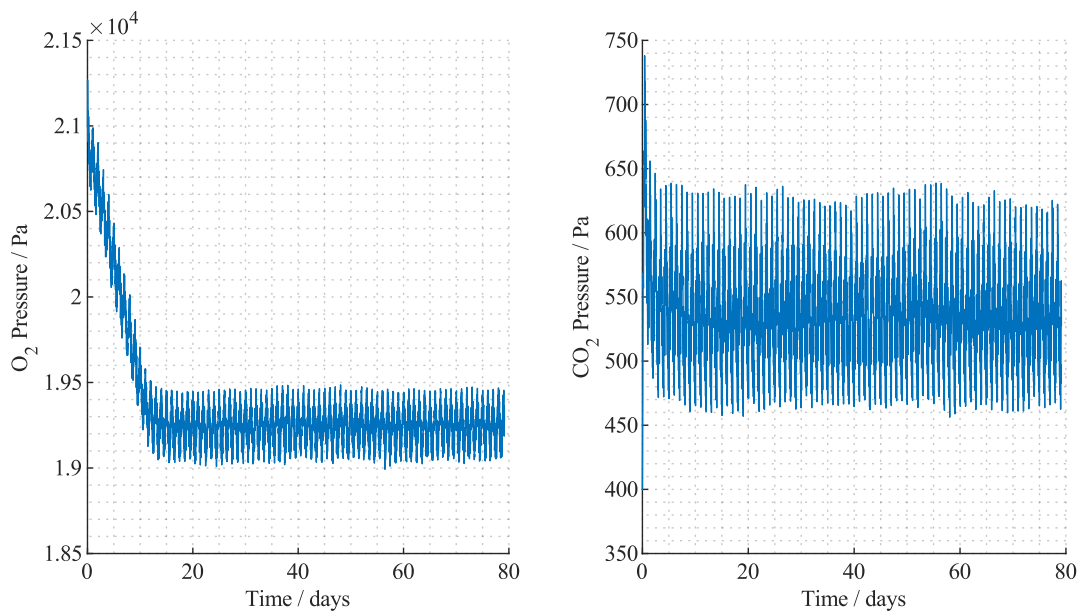


Figure 6.4-6 Oxygen and carbon dioxide partial pressures in the Moon base for the South East Shackleton site.

Crew oxygen demand resulting from the dynamic human model of V-HAB is slightly larger than the values from (Anderson et al. 2018: 50), which results in a decline of oxygen partial pressure as shown in Figure 6.4-6. A simple control logic supplied the expected standard rate of oxygen to the cabin at oxygen partial pressures above 19,500 Pa. If the partial pressure drops below 19,500 Pa additional oxygen is supplied and therefore, the partial pressure remains

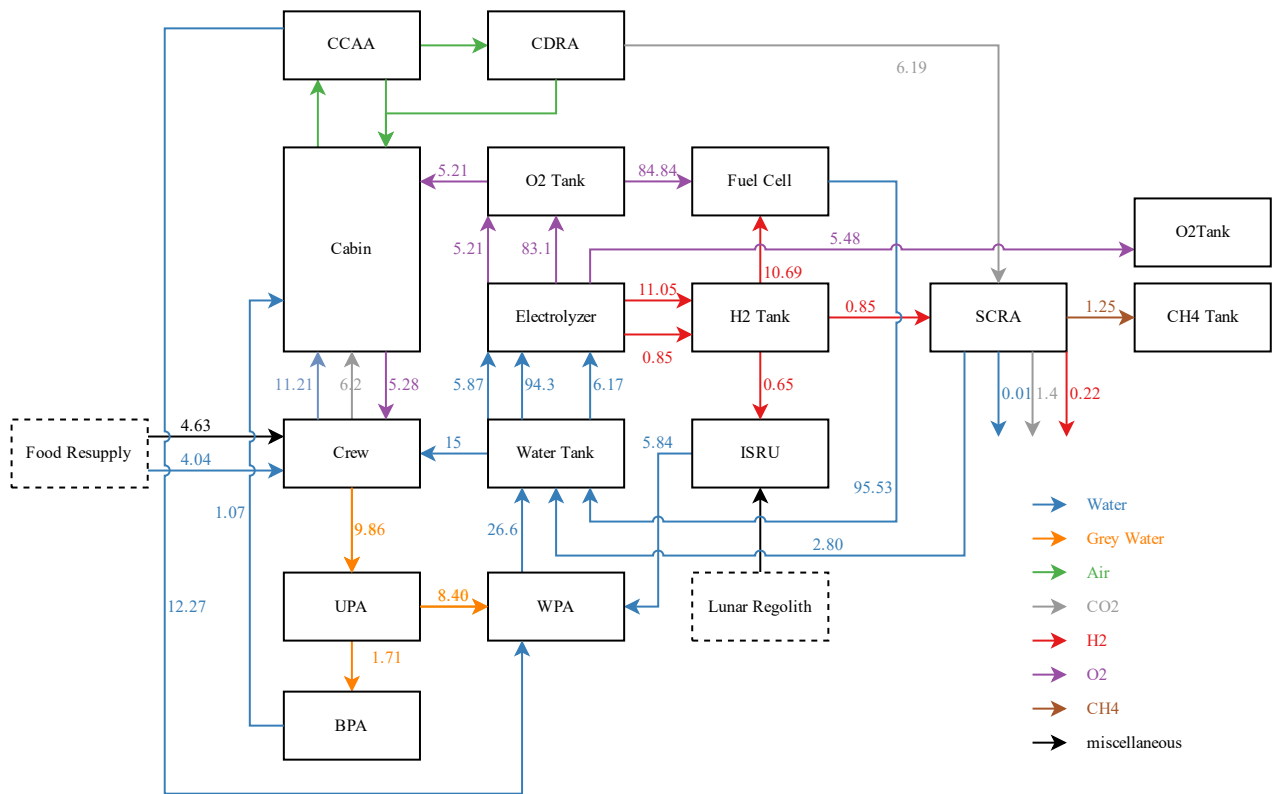


Figure 6.4-8 Average daily mass flow rates for the Shackleton South East site in kg/d.

” (Kaschubek et al. 2021)

In addition to the PC ECLSS analysis from (Kaschubek et al. 2021) an analysis including biological systems was performed for this research. For the PGC an ISPR sized PGC like discussed in chapter 6.3.1 was considered, but as the results in chapter 6.3.2 show a PGC of this size does not have any significant impact on an ISS based PC ECLSS. Therefore, only the PBR case is discussed in this chapter. The PBR is sized as discussed in chapter 5.4.2. Figure 6.4-9 shows the O₂ and CO₂ partial pressures in the Moon base with a PBR. Compared to Figure 6.4-6 the O₂ partial pressure is higher because the PBR produces additional O₂. Since the control logic of the O₂ supply was not adjusted, the upper limit of 23,500 Pa is reached, at which no O₂ from the tank is supplied anymore, and the O₂ partial pressure then oscillates around this value.

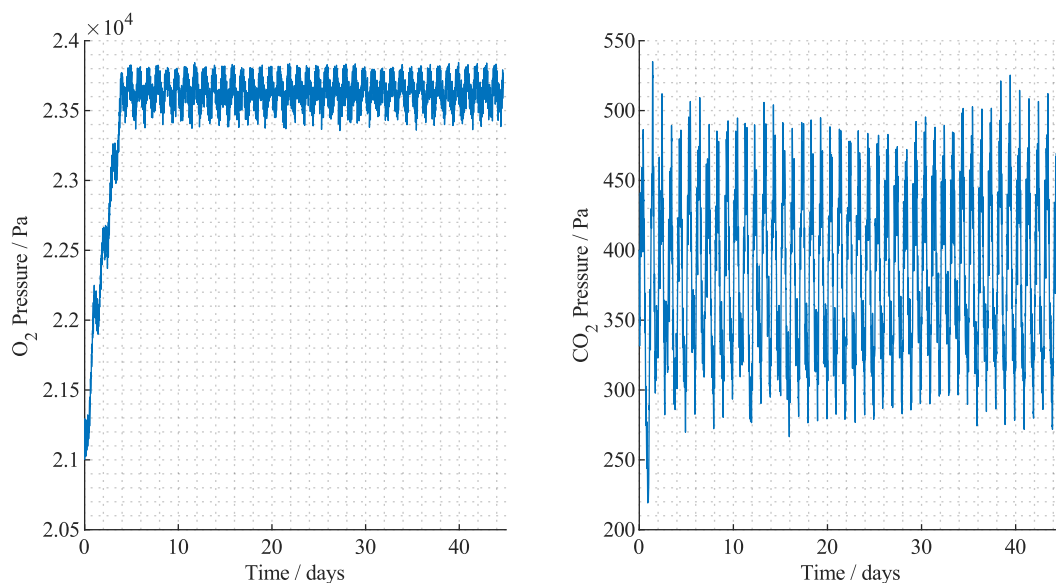


Figure 6.4-9 Oxygen and Carbon Dioxide Partial Pressures in the Moon base for the Mount Koehler Site with PBR.

The CO₂ partial pressure is also lower on average by about 150 Pa when comparing Figure 6.4-6 to Figure 6.4-9. As can be observed from the time axis of Figure 6.4-9 the simulation with PBR was only calculated for 45 days because this is sufficient to analyze the impact of the PBR on the ECLSS.

Figure 6.4-10 shows the average daily mass flow rates within the Moon base ECLSS for the Mount Kocher site with an added PBR for the 45-day simulation.

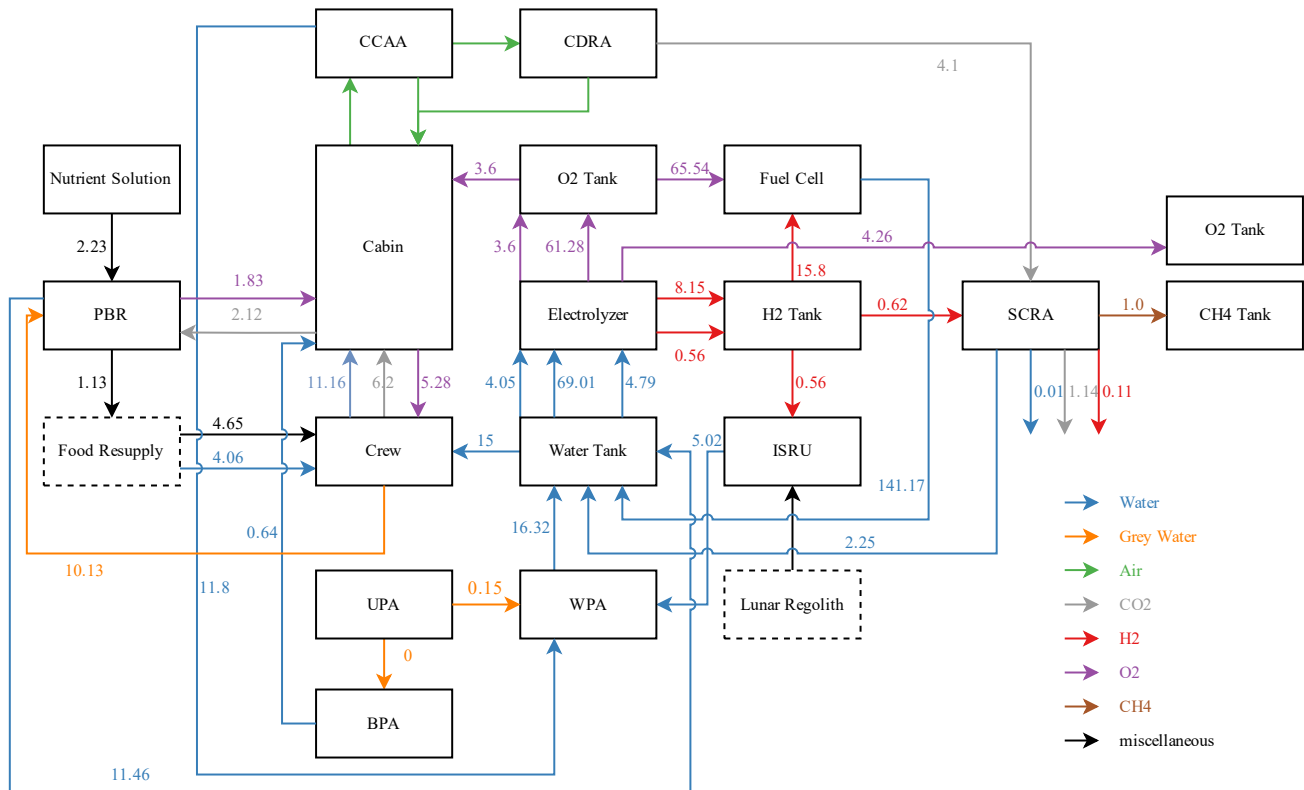


Figure 6.4-10 Average daily mass flow rates for the Mount Kocher site in kg/d with a PBR.

The PBR is now used to handle all urine produced by the crew. The UPA and BPA therefore only process their initially assumed waste masses and then shut down, which explains the lower but still existing processing values. Due to the oxygen produced by the PBR less oxygen supply from the tank is required when compared to the case without PBR from Figure 6.4-7. However, since the PBR also consumes CO₂ less CO₂ for the SCRA is available and therefore the produced methane for fuel is also reduced. In addition, the PBR produces 1.13 kg/d of chlorella mass, which is added to the food store and complements the crew diet. The additional load of the PBR on the energy system was not included in this model, since it would require a complete resizing of this system. This would obviously be necessary for an actual addition of the system to the ECLSS.

Since the nitrogen supply from crew urine is insufficient for the PBR, additional nutrient solution must be supplied to the PBR. The supplied 2.23 kg/d are mostly water with a content of 0.14 g/d of nitrate. Therefore, if the solution is generated on the Moon base, only the nitrate would be considered resupply, while the 2.23 kg/d of water required to generate the nutrient solution could be taken from the water supply of the ECLSS.



6.4.3 Discussion

Here the research questions defined in Table 4.3-1 for mission scenario two are discussed to see if the developed model is capable of answering them.

“Q-2.1 What are the required sizes for energy and consumable storage during shadow phases?”

For the Mount Kocher site, the minimum water mass that must be stored is 2,694 kg and for the Shackleton South East site it is 2,890 kg. The stoichiometric equivalent mass of hydrogen and oxygen is:

Mount Kocher site	hydrogen:	321.1 kg	oxygen: 2,568.9 kg
-------------------	-----------	----------	--------------------

Shackleton South East site	hydrogen:	20.34 m ³	oxygen: 8.56 m ³
----------------------------	-----------	----------------------	-----------------------------

Therefore, the required volumes to store the gases at 200 bar and 293 K are:

Mount Kocher site	hydrogen:	321.1 kg	oxygen: 2,568.9 kg
-------------------	-----------	----------	--------------------

Shackleton South East site	hydrogen:	21.82 m ³	oxygen: 9.18 m ³
----------------------------	-----------	----------------------	-----------------------------

The model includes all aspects of both the energy system and the ECLSS. It therefore provides insight into both the required values for energy storage and the values required for crew consumption while considering the respective dynamics of both systems and the environment. The developed model is therefore capable of answering the defined question as shown above.

“Q-2.2 Is the production of methane as fuel from crew CO₂ feasible for the system?”

Yes, this is feasible without requiring additional resupply if an ilmenite reduction ISRU reactor is used to produce the required water for crew oxygen production. However, the actual producible fuel mass of 2,588 kg/y is lower than the theoretic maximum of 4,100 kg/y.

Whether this is feasible in the real system also depends on the required water for payload supply, which was not included in the analysis. (Tobias et al. 2011) provide values from the ISS program for the required not returned payload water. Including the water required for payload oxygen consumption, 0.45 l of water are required for payloads. Since the other values in the figure are stated per crew member, it is unclear whether this also applies to the payload consumption values. The water surplus in the system is from food water content (4 kg/d) and metabolic water (2.5 kg/d) and therefore amounts to 6.5 kg/d. Of these, 6.17 kg/d are actually consumed for fuel production as shown in Figure 6.4-7. Therefore, even if the payload demand of 0.45 kg/d is subtracted 98% of the considered fuel production is still feasible. If the payload consumption is considered as a value per crewmember and increased to 2.7 kg/d only 61.6% of the considered fuel production would be feasible. This is however still a significant fuel mass of 1594 kg/y. Therefore, even if a high payload water demand is considered, the fuel production from crew CO₂ is feasible.

“Q-2.3 What are the necessary conditions to integrate biological components into the system?”

Adding a PBR that is capable of urine processing results in the UPA and BPA being no longer necessary. However, the nitrogen supply from crew urine is insufficient for the PBR and it requires additional nutrient solution to maintain optimal growth conditions. Ideally, the system is capable of generating this nutrient solution using water and supplied nitrate. Alternatively, the PBR could be sized to utilize crew urine without additional nutrient supply, which would result in slightly lower O₂ production and CO₂ consumption. In addition, the energy system of the base must be rescaled to accommodate the higher energy demand of the PBR (compared to UPA and BPA).

Since the primary content of the supplied nutrient solution is water, only 0.14 g/d of nitrate resupply would be necessary for the considered PBR. The produced chlorella mass represents 24.3% of the total required dry food mass. The dry ISS food has a nutritional energy value of 15.54 MJ/kg (Anderson et al. 2018: 63), while the dried chlorella mass has a nutritional energy value of 20.71 MJ/kg assuming the composition from (Belz et al. 2014). Therefore, from a nutritional perspective 32.4% of the required nutritional energy could be provided by the dry chlorella mass. This is within the



limit of chlorella supply of 20% to 35% for human diet considered by (Belz et al. 2014: 172). However, additional processing of such a high chlorella content in the diet is likely necessary to resolve the palatability issues discussed by (Waslien and Oswald 1975: 141).

From an energy perspective, the UPA and BPA are no longer required, which consume 353.4 W on average according to Table 6.4-1. The PBR in the considered design consumes 5650 W for lighting and other components. The power demand is therefore significantly higher, which would require a corresponding adjustment of the energy subsystems.

“Q-2.4 How does the addition of biological components affect the loop closure of the physical/chemical ECLSS?”

The PBR reduces the available CO₂ for SCRA by 2.12 kg/d, which results in a reduction of methane production from 1.25 kg/d (without PBR) to 1.0 kg/d (with PBR). Thus, the overall fuel production is reduced from 6.73 kg/d to 5.26 kg/d. In return the PBR produces 1.13 kg of edible biomass. It is capable of processing the complete crew urine and therefore replaces the UPA and BPA.

Overall, the addition of the PBR results in the potential reduction of system size for the carbon dioxide removal system CDRA and also for the ISRU reactor because less oxygen from ISRU is required. However, based on the results shown in Figure 6.4-10, and the nutritional energy ratio, the produced chlorella mass can replace 1.5 kg/d of dry stored food mass. This is nearly identical to the reduction in produced fuel mass of 1.47 kg/d.

Using a larger PBR is not favorable, as the produced algae biomass is already at the upper limit for food supply according to (Belz et al. 2014: 172). The produced fuel mass could be enhanced if the efficiency of the Sabatier reactor is improved, which currently vents more than one kg of CO₂. However, increasing this efficiency would also require adjustments in the H₂:CO₂ supply ratio, which would reduce the safety of the reactor. Therefore, the conclusion from the results of this analysis is, that a PBR sized to process the crew urine can improve the overall loop closure and reduce the resupply mass, if it is combined with a highly efficient Sabatier reactor. If the current ISS SCRA is considered, the potential benefit in reduced resupply from produced edible chlorella mass is nearly identical to the reduction in produced fuel. Thus, the system is overall less desirable due to the large size, power consumption and other ESM values as discussed in chapter 5.1.2.5.

6.5 Mission Scenario Three: Permanent Mars Base

This mission scenario assumes a Closed Environmental Life Support System (CELSS), where plants are used to provide the complete diet for a crew of six on the surface of Mars.

6.5.1 Model Structure

Figure 6.5-1 shows the LiSTOT analysis for the proposed exploration plant growth chamber (PGC), which corresponds to the manual case from (Kaschubek 2021). In the LiSTOT analysis, the crop growth area was reduced to maintain carbon balance in the system. The V-HAB analysis includes reprocessing of feces and the human model reacts to the nutritional intake. Therefore, the carbon balance should be closeable in the detailed simulation and the crop growth area is not reduced for the following analyses.

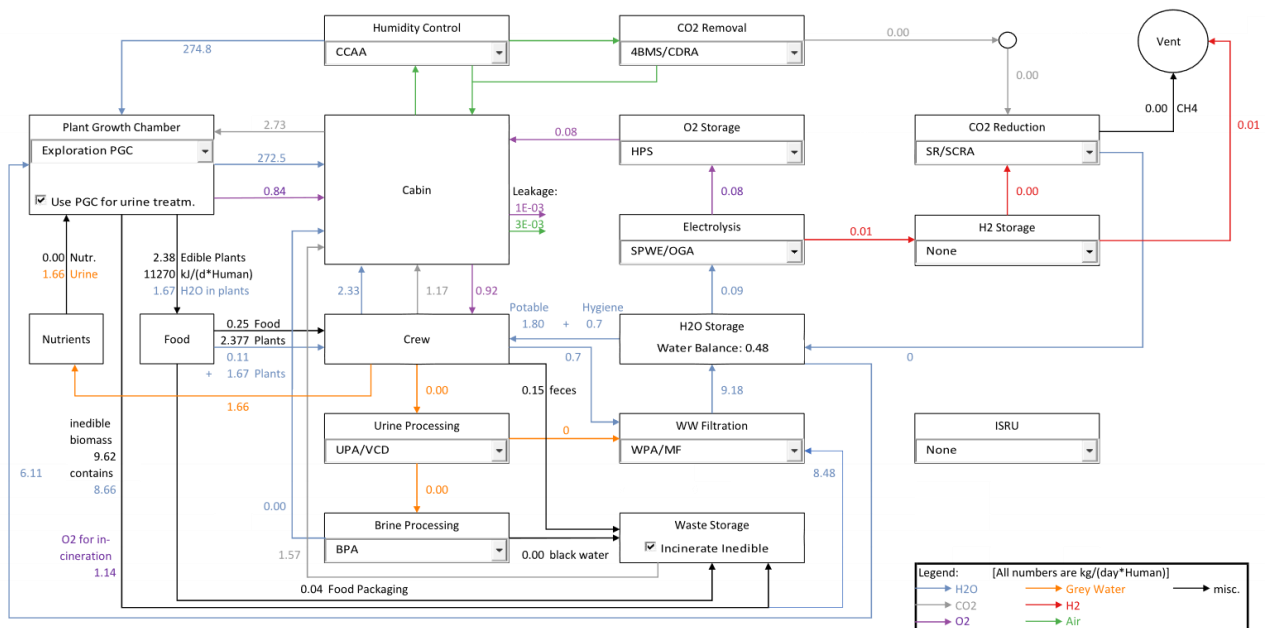


Figure 6.5-1 LiSTOT analysis of the CELSS life support system.

In the V-HAB analysis of this system, the cabin is split into a greenhouse and a normal cabin. The crew is assumed to be in the cabin at all times, while all plants are located in the greenhouse. Between these two areas circulates a ventilation flow of 240 cfm or 0.113 m³/s. The greenhouse contains an upscaled version of the ISS CCAA as the humidity release from plants shown in Figure 6.5-1 is much higher than what the ISS CCAA is expected to handle. The cabin contains an ISS CCAA as the crew size is identical to the ISS. In addition to the SCRA, a PBR is used as potential CO₂ reduction option. Figure 6.5-2 provides an overview of the atmosphere phases, their volume and the location of the different subsystems. The volume of the greenhouse is based on the volume per m² assumed by (Anderson et al. 2018: 176) and differs depending on the used plant growth area.

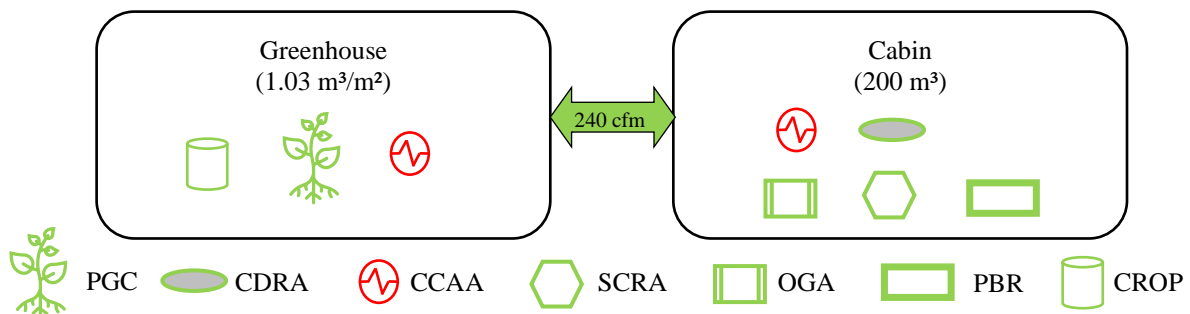


Figure 6.5-2 Location of subsystems in mission scenario three and size of the compartments. Greenhouse volume is in m³ per m² plant growth area.

6.5.1.1 Plant Growth Chamber

The Plant Growth Chamber (PGC) is based on the analysis from (Kaschubek 2021), which was also discussed in chapter 5.1.1.5. The growth areas per crew member (CM) for the manual case derived there are used as the basic case for the following analysis. Table 6.5-1 provides an overview of the plant growth conditions used within this mission scenario. The number of subcultures was chosen to distribute the impact of the plants and create a more continuous water, oxygen and carbon dioxide connection to the ECLSS. Note that the overall plant growth area is divided into the provided number of subcultures. For example, a total growth area of 108 m² is used for wheat, which is divided into six cultures of 18 m² growth area. The culture sow time is distributed evenly across the harvest duration. For example, the six cultures of wheat are each about 13 days apart in growth. In addition, splitting the required growth area into multiple cultures will result in fresh produce being available more often. The emerge time is set to zero days, which basically means the plants are pre-sowed in separate smaller growth racks until they emerge. It is assumed that the time until the plant emerges has no impact on the other systems.

Table 6.5-1: Assumed crop conditions for the Closed Environmental Life Support System.

Unit	Plant Area m ² /CM	Harvest Time d	Subcultures -	Photoperiod h/d	Photonflux μmol/m ² s	Emerge Time d
Sweet Potato	2	85	1	12	650	0
White Potato	8	132	4	12	650	0
Rice	2	85	1	12	764	0
Dry Bean	10	85	4	18	370	0
Soybean	0	97	0	12	650	0
Tomato	5	85	5	12	625	0
Peanut	10	104	5	12	625	0
Lettuce	2	28	4	17	295	0
Wheat	18	79	6	20	1600	0

The crop growth area based on the proposed exploration life support crops from (Anderson et al. 2018: 181) are also analyzed as case studies. The Part ELS case is studied exactly as proposed by (Anderson et al. 2018: 181) while the full ELS case is scaled to provide the full crew diet as discussed by (Kaschubek 2021). For both cases, the growth area of crops which are not available in the MEC model (like carrot, green onion, radish and spinach etc.) is added to the lettuce growth area. In a third case the plant growth areas are not divided into multiple subcultures. Instead, only one culture per crop is modelled for the case shown in Table 6.5-1, while all other conditions, except for the growth areas and subcultures, remain identical. Table 6.5-2 shows the assumed growth areas and subcultures for these cases.

Table 6.5-2: Assumed crop growth areas for the different cases.

Unit	No Subcultures		Full ELS		Part ELS	
	Plant Area m ² /CM	Subcultures -	Plant Area m ² /CM	Subcultures -	Plant Area m ² /CM	Subcultures -
Sweet Potato	2	1	3.73	1	3.48	1
White Potato	8	1	2.5	1	1.614	1
Rice	2	1	5.22	1	0	0
Dry Bean	10	1	4.84	1	1.17	1
Soybean	0	0	116.73	8	0	0
Tomato	5	1	4.13	2	1.209	2
Peanut	10	1	12.15	2	0	0
Lettuce	2	1	4.19	1	2.351	2
Wheat	18	1	10.65	1	9.679	3

In order to prioritize plant growth, the PBR is only activated if the CO₂ level exceeds 250 Pa. Once the CO₂ drops below 150 Pa the PBR is set to minimal operating mode to reduce its CO₂ consumption. This logic was chosen to prevent a quick on/off cycle for the PBR. The CDRA control logic is set to maximize utilization of biological systems. It is only



activated if the CO₂ level is higher than 300 Pa and is then deactivated if the level drops below 250 Pa. Since the target value for the CO₂ level is 300 Pa, this means that CDRA is used if the target is exceeded to prevent further CO₂ buildup.

6.5.1.2 Available Solar Power

Mars has a similar obliquity as earth with about 25° and therefore also experiences seasons. Additionally, the orbit of Mars is elliptical, which results in additional variations for e.g. the solar power (Planetary Science Communications Team 2021). A calculation approach for the solar power on the surface of Mars was presented by (Appelbaum and Flood 1990) and adapted into a MATLAB® algorithm for this research. While the power generation is not a primary research objective for this mission scenario, it was fairly easy to include as long as a RFCS is used together with solar power. Therefore, the Mars base is also assumed to operate using these technologies, although no in-depth trade-off was performed. With the algorithm from (Appelbaum and Flood 1990) the following results for the solar power were calculated. Figure 6.5-3 shows the solar power above the atmosphere, which corresponds to the base value of solar power reaching Mars. This value is 1,360 W/m² for earth and nearly constant over the year, but for Mars the variations over the orbit periods are quite significant. Using this base value and a specific location on Mars, the solar power at the surface can be calculated.

For the analysis the site of Gusev Crater-Columbia Hills (14.6°S, 175.4°E) was chosen, which was identified as one potential region of interest by a NASA Human Exploration of Mars – Sub Analysis Group (HEM-SAG 2008: 62–3). The selection of the Gusev Crater-Columbia Hills landing site from the 58 candidate sites discussed by (HEM-SAG 2008: 62–3) was arbitrary. Figure 6.5-4 shows the surface solar power for more than two Martian years during low dust ($\tau = 0.5$) conditions. The variation in seasonal solar power from the obliquity and the elliptical orbit is also apparent in this figure. The analysis can easily be adjusted to any location and mission time using input values.

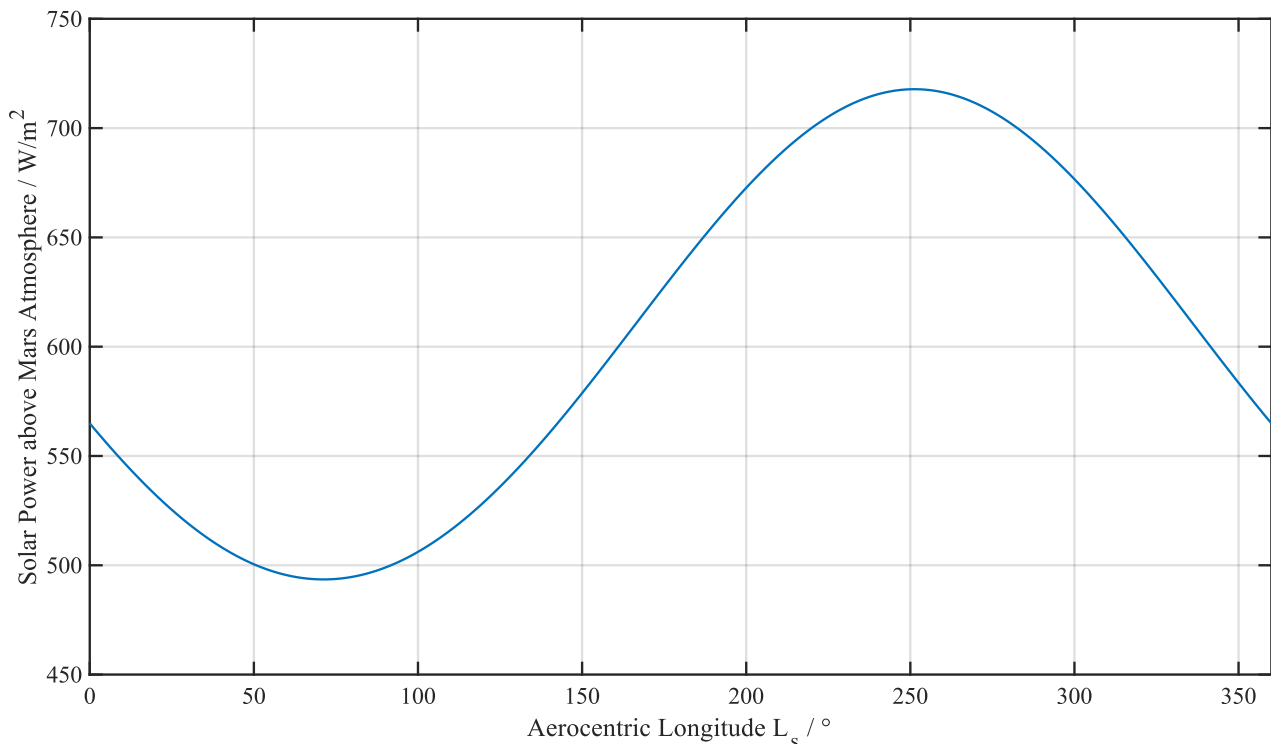


Figure 6.5-3 Solar power above the atmosphere of Mars over the aerocentric longitude of Mars.

The start date for Figure 6.5-4 was chosen to coincide with a potential long stay conjunction class mission (Mars Architecture Steering Group 2009: 62). The overall lowest solar power for the selected landing site is e.g. on June 21st 2039 or on May 10th 2041 with similar low values at June 21st 2038 and May 10th 2040. Therefore, these are the dates for which the energy system must be dimensioned. Figure 6.5-4 also shows the potential benefit from tracking solar cells (which assumes a perpendicular incidence angle). Since the worst case is still similar to the overall worst case, tracking is not further considered in the analysis.

Polar landing sites are not feasible if solar power is considered as power source. Due to the obliquity, the polar regions experience a cycle of day and night on the scale of multiple months. For example, the candidate landing site Chasma Boreale (82.6°N, 47.3°W) would be of high interest due to the potential of water ice in the polar regions (HEM-SAG 2008: 62–3). However, as Figure 6.5-5 shows, the polar nights are multiple months long and therefore would require large energy storage systems if solar power is used.

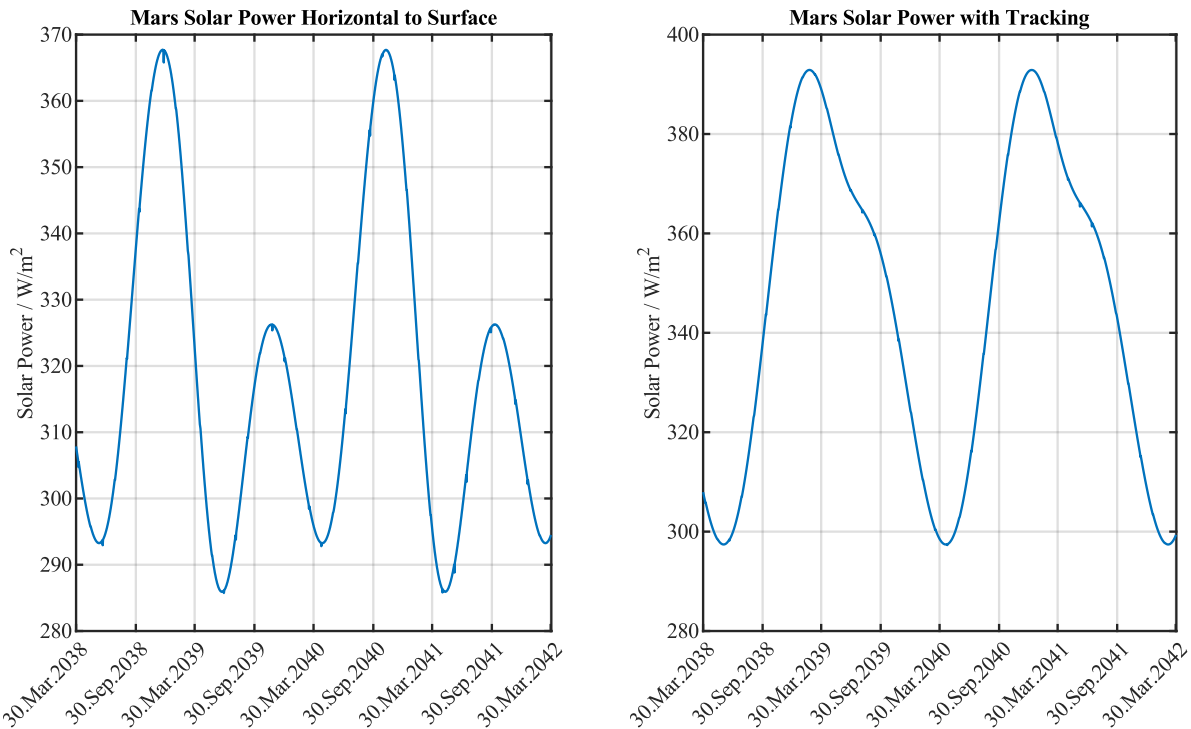


Figure 6.5-4 Solar power with and without tracking at Martian surface assuming an average atmospheric opacity of $\tau = 0.5$ at the selected landing site of Gusev Crater-Columbia Hills: (14.6°S, 175.4°E)

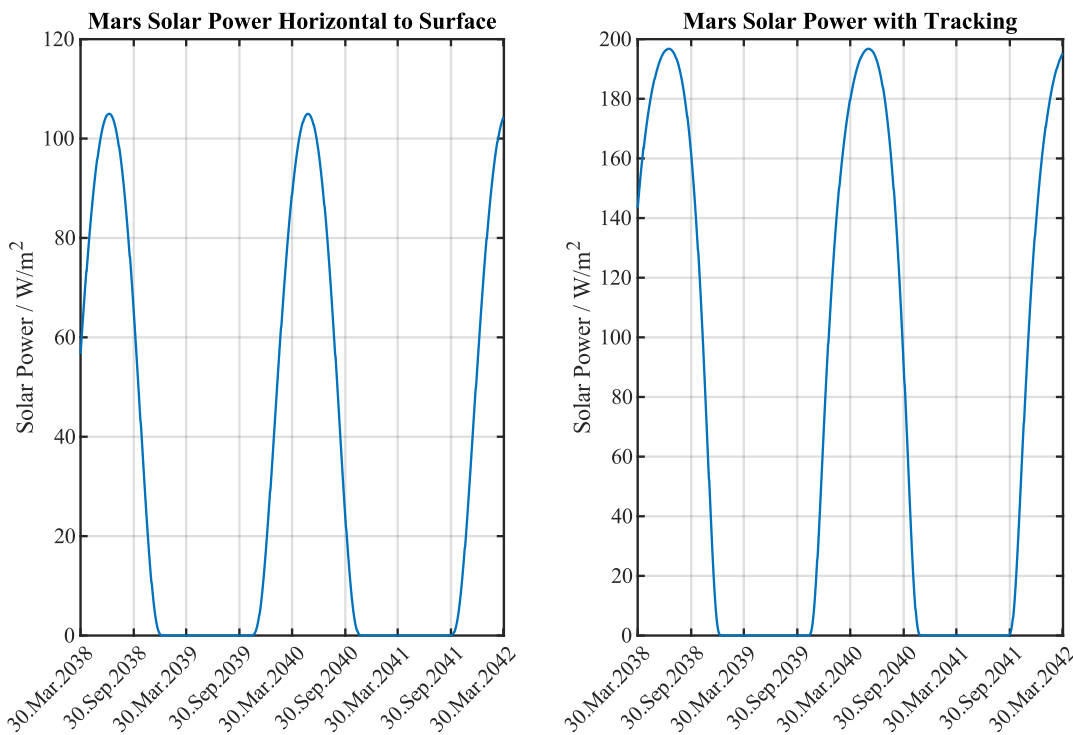


Figure 6.5-5 Solar power with and without tracking at Martian surface assuming an average atmospheric opacity of $\tau = 0.5$ at the candidate landing site of Chasma Boreale: (82.6°N, 47.3°W)



6.5.2 Results

6.5.2.1 Greenhouse CCAA Control Logic

Initially the control logic of the new upscaled CCAA for the greenhouse is studied. For this purpose, the case is analyzed without previous plant growth, so the plants just start growing at the beginning of the simulation. This results in high thermal loads from the LEDs without the respective humidity loads from the plants and is therefore a fundamentally different case from the one the original CCAA control logic is supposed to handle. Therefore, a new control logic with a Proportional–Integral–Derivative (PID) controller was derived, while the original logic only used a proportional and integral part. The general equation for a PID controller is:

$$u(t) = K_{proportional} \cdot e(t) + K_{integral} \cdot \int_0^t e(\tau) d\tau + K_{differential} \cdot \frac{de(t)}{dt} \quad (6.5-1)$$

The change for the control parameter $u(t)$ is derived from the error $e(t)$. The parameters of the PID controller are the proportional K_p , integral K_i and differential K_d constants, which are system specific. The parameters for the PID controller were derived through the empirical control design approaches described in (Heinrich and Schneider 2019). Basically, multiple simulations with various control parameters were tested to derive a stable PID control logic. This simplistic approach is sufficient to show the applicability of the derived models to support controller design. A more sophisticated control logic can be derived if that is the primary goal. For example, by using an internal model controller, which uses the derived simulation tool as internal model. For this thesis, only a working stable controller was required without further optimization. For the CCAA the control parameter is the angle of the TCCV, which controls the ratio of air flow passing through the CHX. The error is the difference between the current temperature and the setpoint temperature. The original CCAA control logic limited the angle between 9° and 84° . This limits the ratio of the air flow passing through the CHX to a value between 93.4% for 9° and 8.4% for 84° . For the ISS this range was sufficient because the heat loads do not drop below a certain value. However, in the greenhouse with small plants, the heat and humidity loads are almost zero once the LEDs are turned off. Therefore, the air flow through the CHX must be controllable to even smaller values. In addition, the overall air flow used in the upscaled CCAA is larger, which means a smaller percentage still results in the CHX removing more heat than the ISS CHX. Therefore, the range for the TCCV angle was increased to allow a value between 1° (105°) and 100° (-12°). In addition, the deadband of the solver in which it does not react was set to 0 K instead of 0.5 K. Table 6.5-3 summarizes the parameters of the new PID controller.

Table 6.5-3: Parameters for the PID control logic of the greenhouse CCAA.

Set Point Conditions	Unit	Value
Proportional Parameter $K_{proportional}$	-	0.01
Integral Parameter $K_{integral}$	-	0.00005
Differential Parameter $K_{differential}$	-	10
Maximum TCCV Angle	$^\circ$	105
Minimum TCCV Angle	$^\circ$	-12
Maximum TCCV Angle change	$^\circ$	1

Figure 6.5-6 shows the greenhouse atmosphere temperature and relative humidity with the original CCAA control logic and the new control logic for the first day without any plant growth but active LED growth lights. Figure 6.5-7 shows the corresponding heat flows within the greenhouse CCAA and the TCCV angle. Notably the temperature with the old control logic cannot be sufficiently controlled at the beginning due to the limits on the air flow through the CHX. During the dark period of the plants at the end of the day, the temperature can be controlled by both controllers. However, due to the larger size and therefore quicker reaction of the upscaled CCAA the old control logic oscillates and has large and quick changes of the TCCV angle. The new logic is more stable and does not result in such fast change rates for the TCCV angle. The heat flow in the CCAA is therefore better controlled with the new control logic. There are some notable sudden changes in the heat flow which result in the control logic oscillating around 295 K. This behavior seems counterintuitive, as the control parameter is well controlled and does not show quick changes. However, the behavior is realistic as it marks the transition from laminar flow in the CHX to turbulent flow in the CHX at a Reynolds number of around 3200. Each time the CHX transitions into laminar flow, the heat flow is reduced suddenly while it increases

suddenly once turbulent flow conditions are reached. This is a realistic behavior, as heat exchange is much more efficient in turbulent flows. Further optimization could be feasible by using separate CHX for the individual plant growth areas. But this would also increase the computational demand of the simulation, which was therefore not analyzed here. The objective was not to derive the optimal configuration for the temperature and humidity control but one that is working sufficiently well to maintain suitable growth conditions for the plants. This objective was achieved.

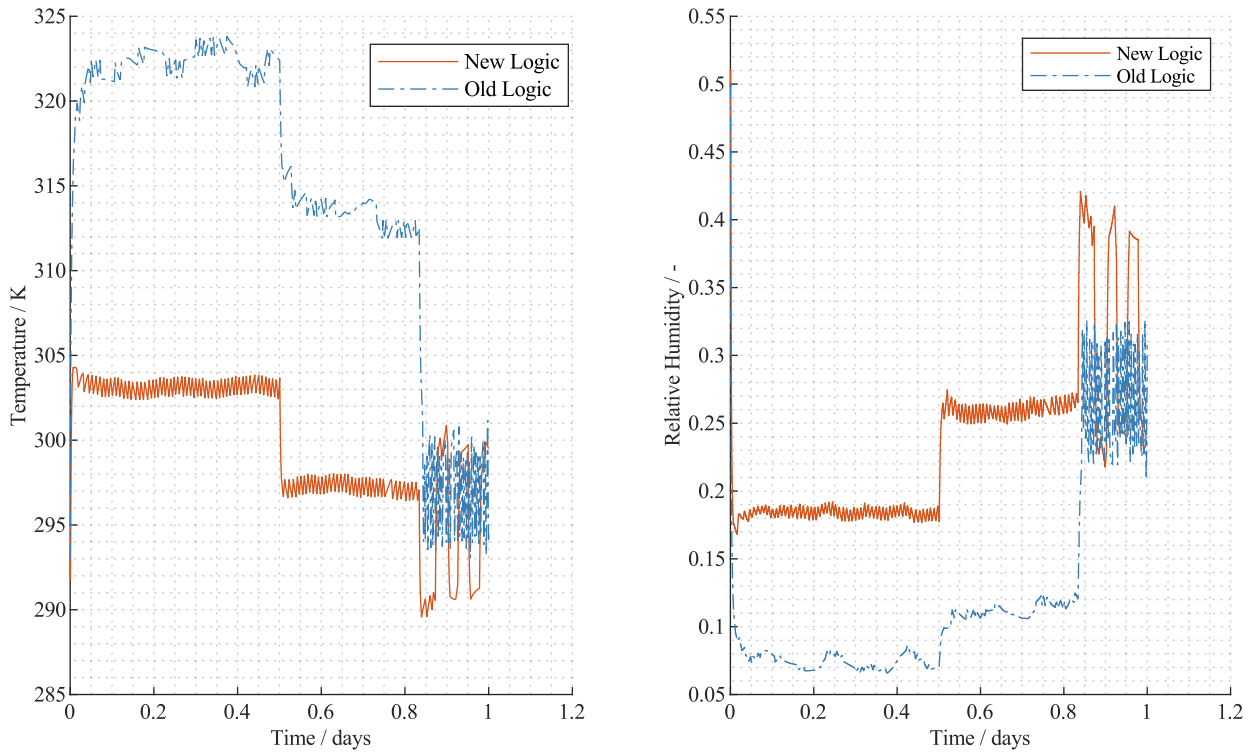


Figure 6.5-6 Greenhouse temperature and relative humidity for the first day of plant growth with the normal CCAA control logic (old logic) and a newly derived PID control logic (new logic).

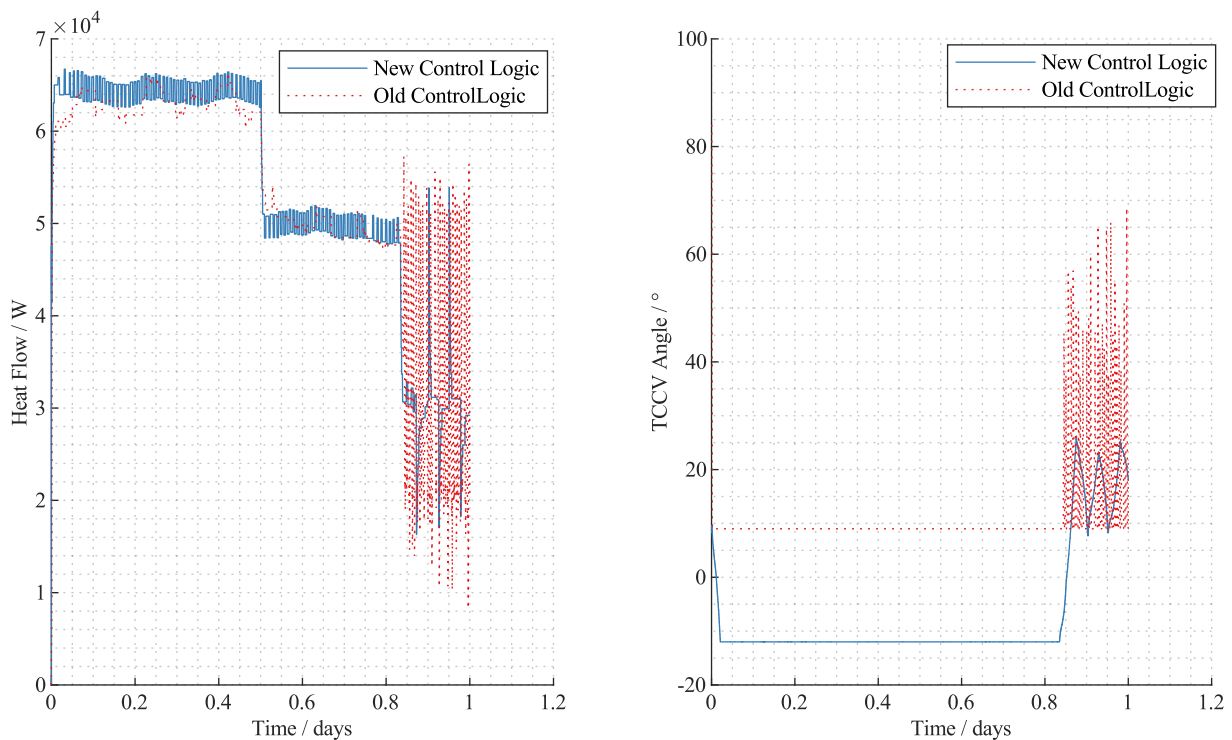


Figure 6.5-7 Total heat flow of the CCAA and angle of the TCCV in the greenhouse for the first day of plant growth with the normal CCAA control logic (old logic) and a newly derived PID control logic (new logic).

Notably the water uptake from food is significantly higher than for the Moon base scenario of Figure 6.4-7 due to the high water content of the produced vegetables instead of the pre-stored food. The average respiratory coefficient is 0.917, which is quite similar to the 0.92 stated by (Anderson et al. 2018: 63). This is not surprising, as the vegetable composition is designed to produce a similar composition of proteins, fats and carbohydrates. Figure 6.3-9 shows the content of the food store over the simulation. The increases at day two are harvest events for sweet potato and lettuce as well as at day six for wheat. The food consumption of the crew depends on the available food. If for example, a lot of sweet potato is currently available, the crew will consume more sweet potato and less of the other available food.

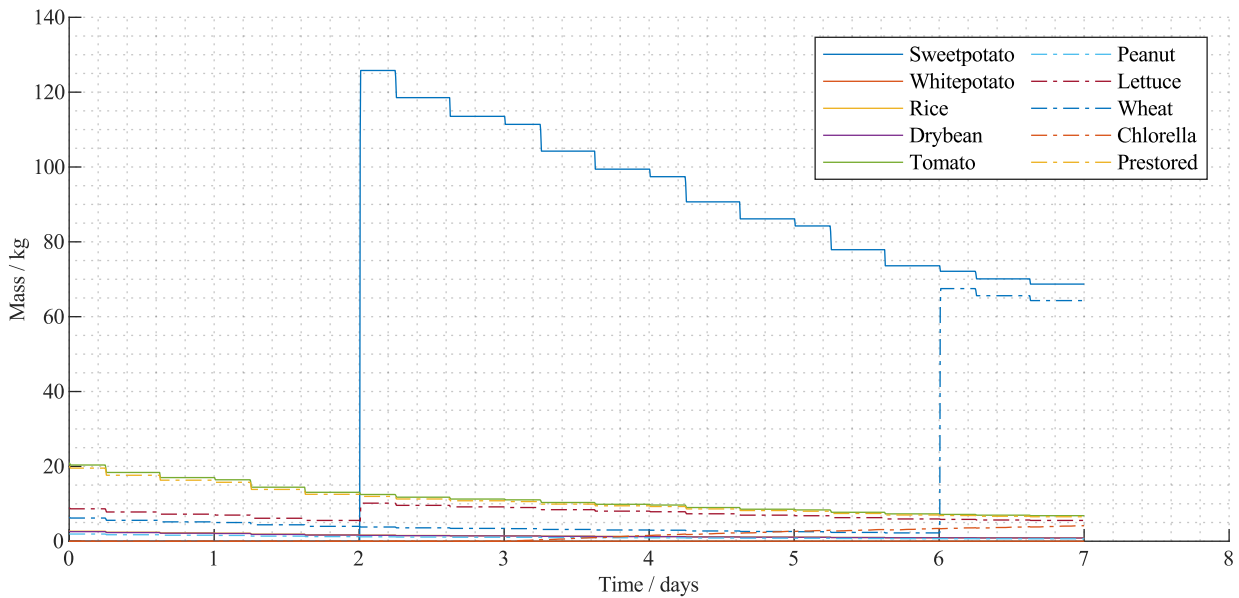


Figure 6.5-9 Available food masses in the base CELSS.

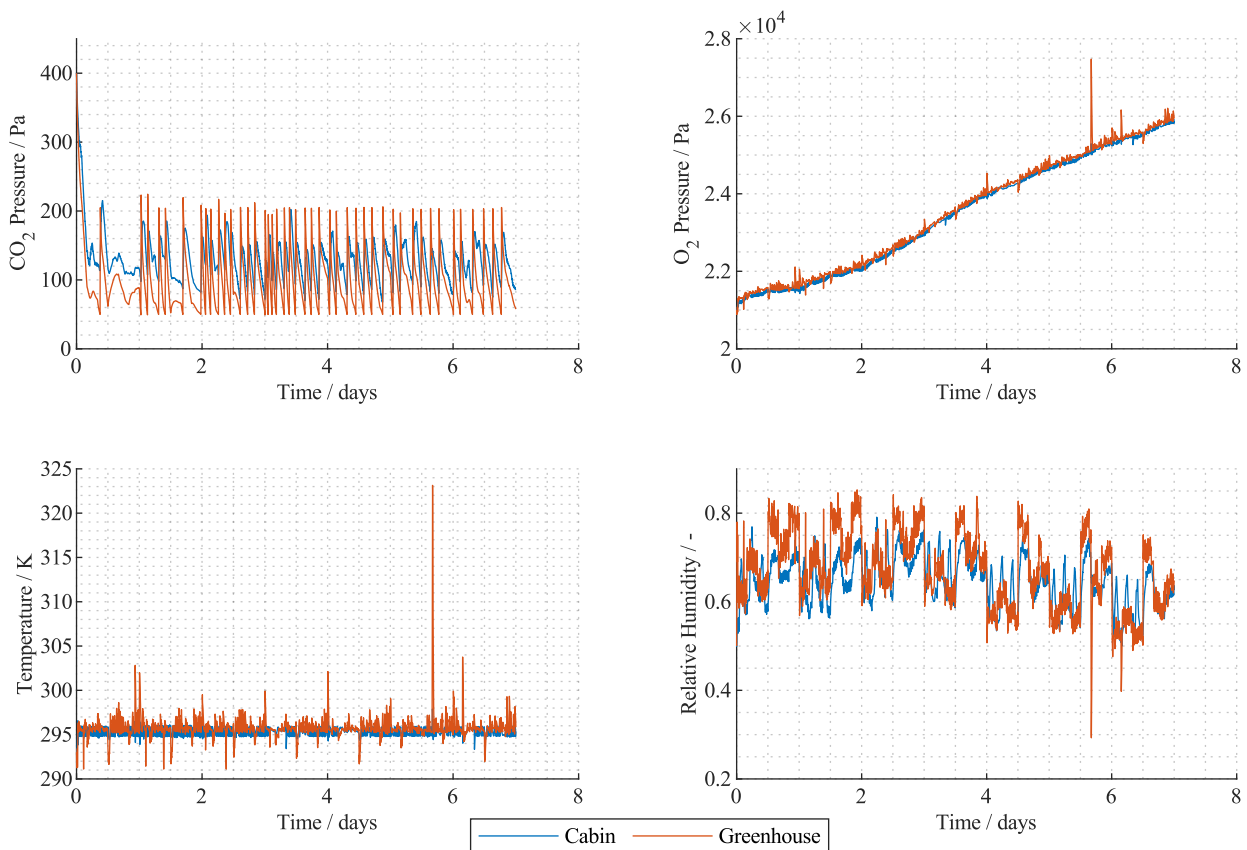


Figure 6.5-10 Atmosphere values for the cabin and greenhouse in the base CELSS.



Figure 6.5-10 shows the atmosphere parameters for CO₂, O₂, temperature and humidity in the habitat. As shown in Figure 6.5-8 the plants consume more CO₂ than is produced by CROP. Therefore, CO₂ from storage is added to the atmosphere whenever the partial pressure drops below 50 Pa, causing the oscillation shown in Figure 6.5-10. This can be a result of the assumption used to initialize the system, but due to the different time scales for plant growth and waste management, this behavior is likely realistic.

The O₂ partial pressure also increases, because the production from plants and the consumption by CROP does not match. While this is an issue for the ECLSS it is not considered a problem of the simulation, as these results are realistic and show that the plants and waste management in the hybrid LSS must be better balanced. The simulation shows the required influences and impacts between the different systems and can therefore be used to support such analyses in the future. The temperature is overall better controlled as in the case without previous plant growth shown in Figure 6.5-6. There is one short period where the temperature reaches 323 K in the greenhouse, but this is quickly counteracted by the control logic. While the humidity in Figure 6.5-6 was extremely low within the greenhouse, the humidity in Figure 6.5-10 is now around the maximum desired humidity value of 75%. The control logic cannot perform better here, because humidity is only controlled passively through the temperature. The relation between temperature control and humidity control depends on the design of CHX and the coolant temperature. Therefore, to improve the performance the CHX design must be adapted because the CCAA CHX is optimized for a different ratio of heat removal compared to humidity removal.

The spike in relative humidity and oxygen partial pressure shortly before day six are a result of the increased temperature which can be observed at the same time. The spike in the temperature shows that the control logic is not always able to maintain the temperature within the desired area, but as the difference is short and quickly counteracted by the control logic this is not considered an issue. As stated in chapter 6.5.2.1 further work with respect to the control logic would be necessary for a real system.

Figure 6.5-11 shows the pressure in the O₂ and H₂ tanks and the overview of the power subsystem. The solar cell area is not sized sufficiently to regenerate the O₂ and H₂ masses during the Martian day. The assumed area for solar cells was 40,000 m² with an efficiency of 29%. However, the plant growth chamber consumes a significant amount of energy (>300 kW) and the solar power reaching the surface during this period is fairly low with about 285 W (see Figure 6.5-4). Therefore, further dimensioning of the solar cells would be required for a finalized ECLSS design.

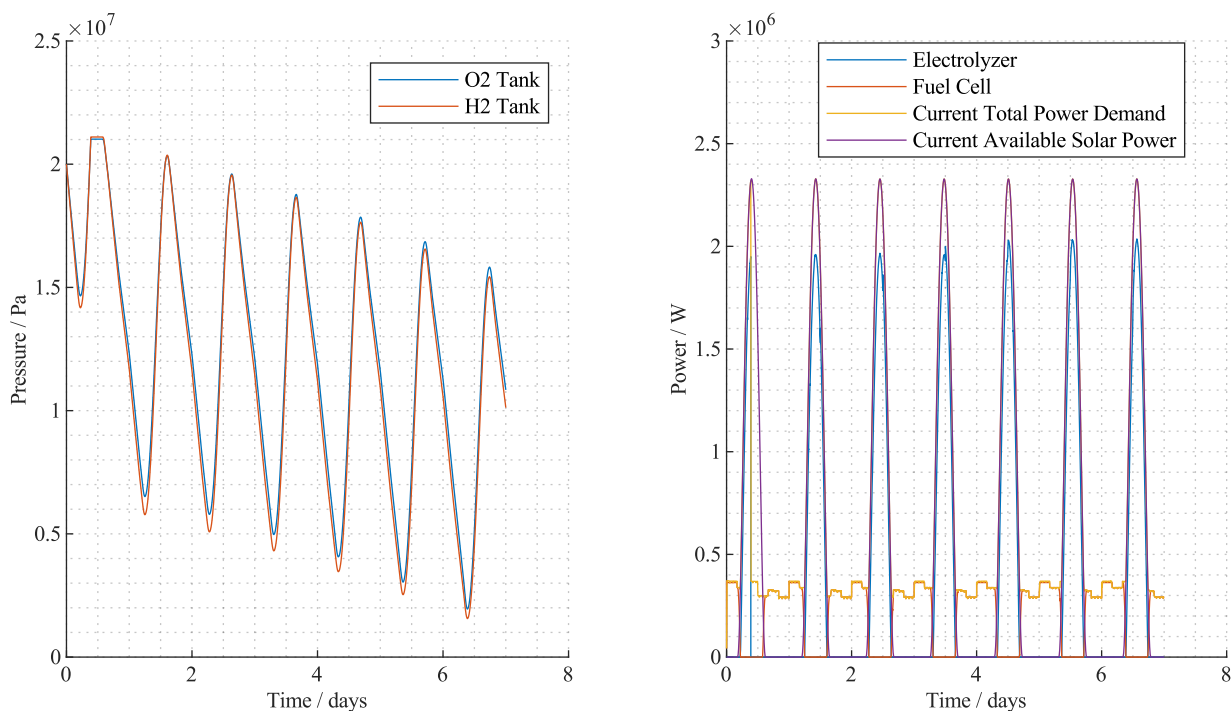


Figure 6.5-11 Energy system parameters for the base CELSS.

Figure 6.5-12 shows the adsorbed water masses within CDRA for this case. Notably, CDRA is only operated for one half-cycle before being turned off due to the low partial pressure of CO_2 . During this half-cycle, the second zeolite 5A bed, which should only adsorb CO_2 , became saturated with water. This is likely due to the high humidity in the cabin and the low partial pressure of CO_2 . Since water is adsorbed first in the competitive adsorption between water and CO_2 this could impair the functionality of CDRA in case it is required to remove CO_2 later on.

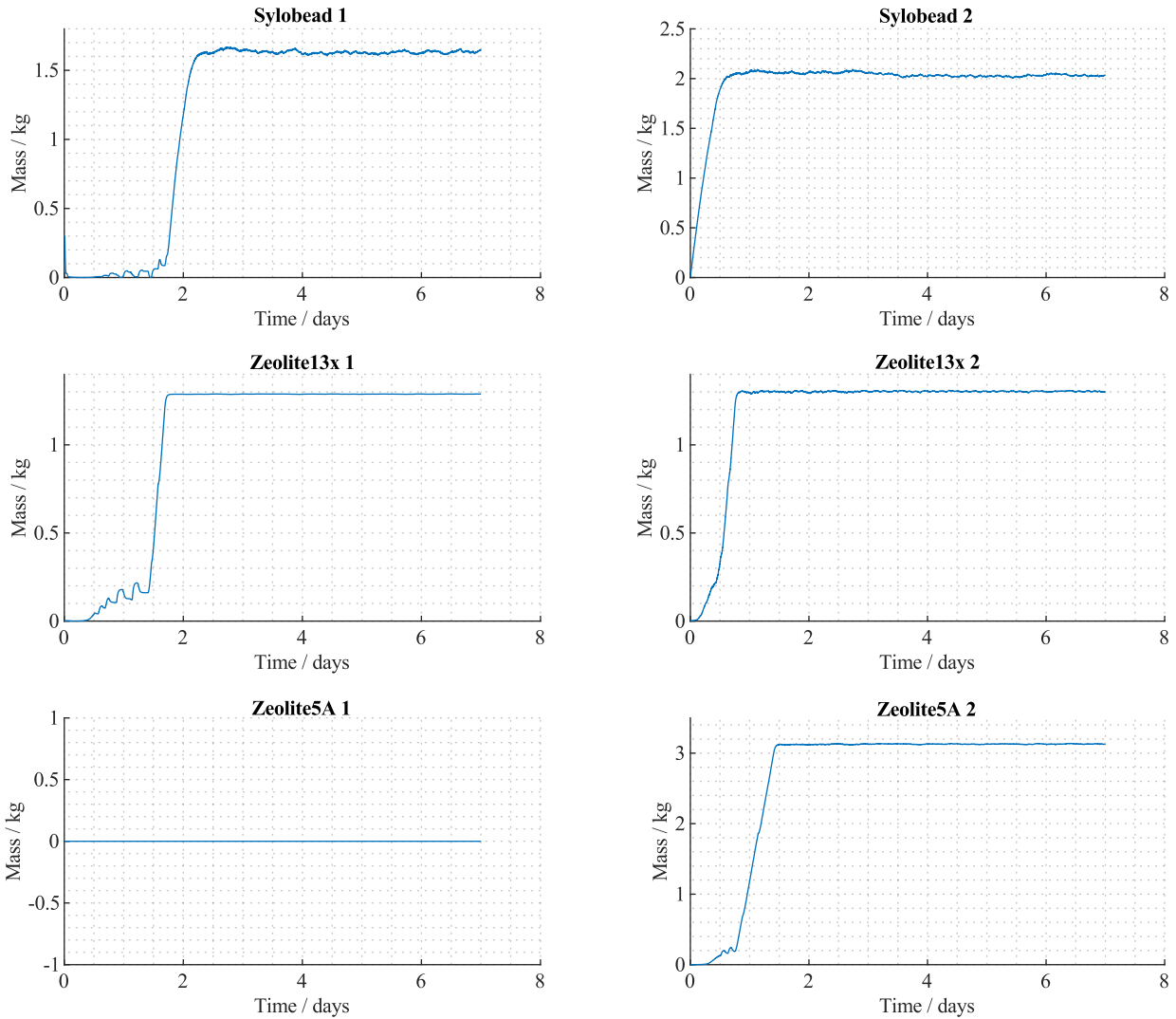


Figure 6.5-12 Adsorbed water masses in CDRA for the base CELSS case.



6.5.2.3 Single Plant Cultures

The first alternative case from Table 6.5-2 uses the same plant growth areas as the base CELSS but does not separate it into multiple subcultures to spread the impact of plants. The other parameters are initialized as discussed in chapter 6.5.2.2 for the base CELSS. Figure 6.5-13 shows the results for the atmosphere in this case.

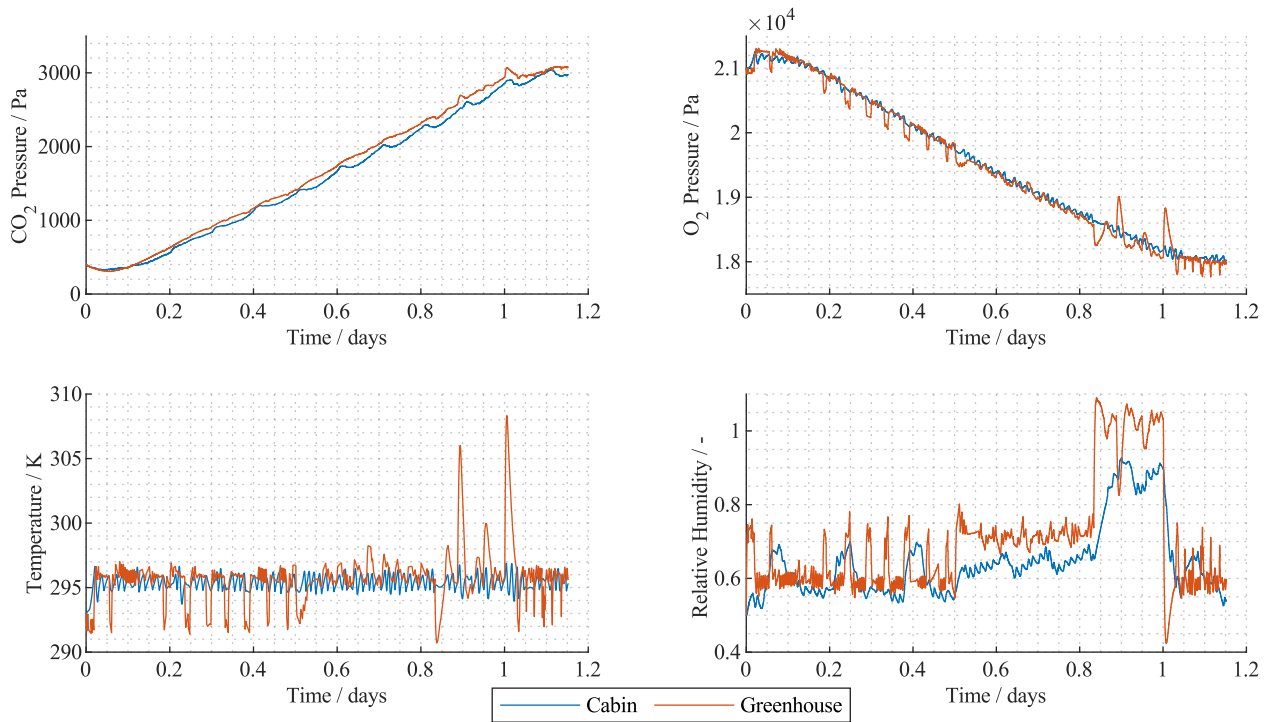


Figure 6.5-13 Atmosphere values for the cabin and greenhouse in the single cultures CELSS.

Only slightly more than one day could be simulated for this case, because the CO₂ partial pressure rose above values that the human model can handle. Figure 6.5-14 shows that CROP is the reason for this large increase in CO₂. Since only one culture is used per plant, a much larger quantity of inedible biomass is supplied to CROP at each harvest.

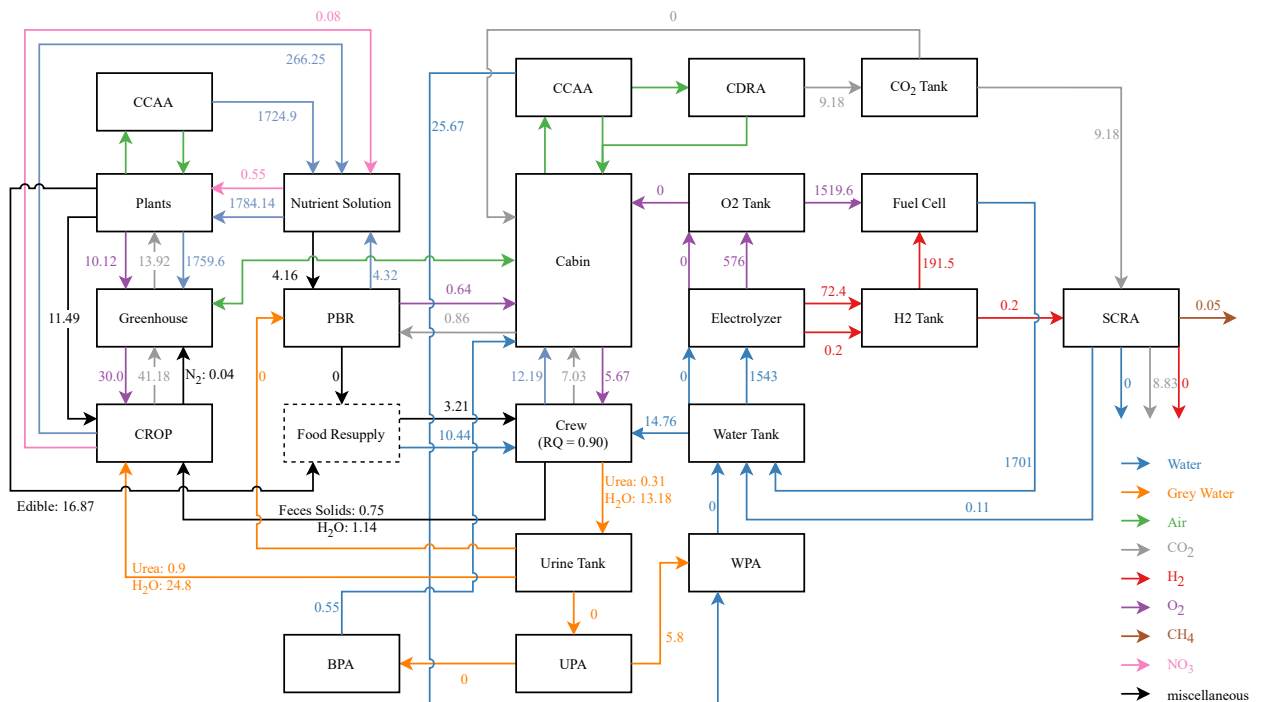


Figure 6.5-14 Averaged daily flowrates for the single culture case with 118 days of prior plant growth.

The current CO₂ production of CROP depends on the current inedible biomass supplied to it. After a delay, in which the system adjusts to the additional mass input, it will process the available biomass within the system in a specific amount of time. Therefore, if more mass is supplied to CROP the CO₂ production will increase accordingly. In the case of multiple cultures per plant species the CO₂ production from CROP is also spread out more evenly over the mission duration. However with single cultures the CO₂ imbalance becomes more pronounced as the plants will consume CO₂ during growth and once they are harvested a significant production of CO₂ will occur.

6.5.2.4 Full Exploration Life Support Plant Growth Chamber

For the Full ELS PGC 164 m² per crew member of plant growth area are used with the majority of it being soybean. This results in a much larger ratio of inedible biomass, which is converted in CROP. Figure 6.5-15 shows the atmosphere values for this case. Due to the higher amount of inedible biomass, CROP can produce sufficient CO₂ and the CO₂ partial pressure does not drop below 50 Pa. However, the higher plant growth area results in an undersized CHX for the greenhouse, which therefore has temperatures constantly above 305 K. Only less than a day could be modelled for this case, due to the high temperature in the greenhouse and resulting errors in the subsystem models. Since the CHX is the root cause for this, the system is not considered stable without further adjustments to the CHX.

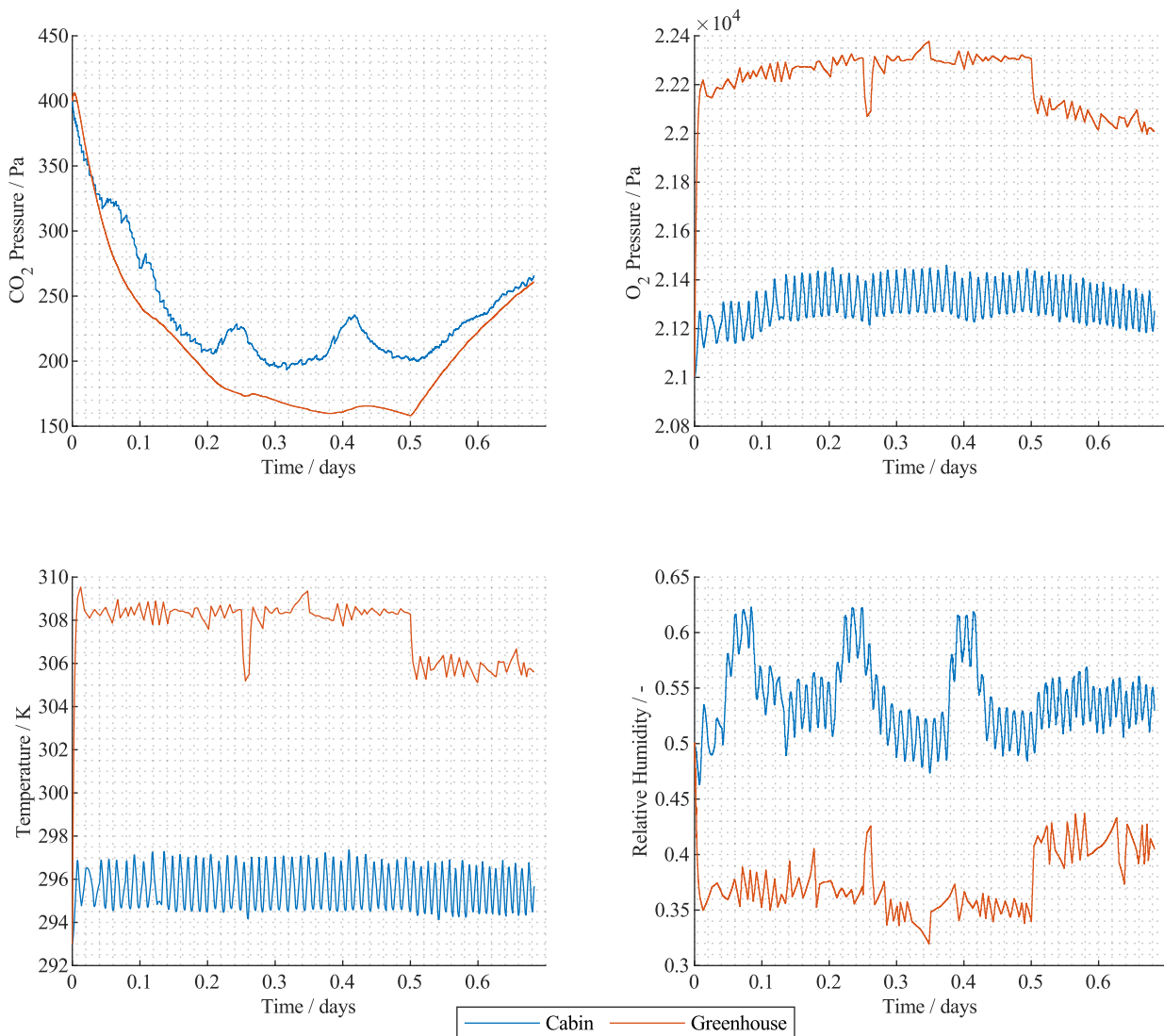


Figure 6.5-15 Atmosphere values for the cabin and greenhouse in the full ELS CELSS.



6.5.2.5 Part Exploration Life Support Plant Growth Chamber

This case uses the 19.5 m² per crew member crop composition from (Anderson et al. 2018: 134) to analyze a smaller plant growth chamber. The subcultures are similarly sized than the base case with a slightly larger wheat growth area per subculture of 19.36 m² (see Table 6.5-2). In this case, the harvests are on day two for sweet potato and lettuce as well as on day four for wheat. Figure 6.5-16 shows the atmosphere parameters for the Part ELS case.

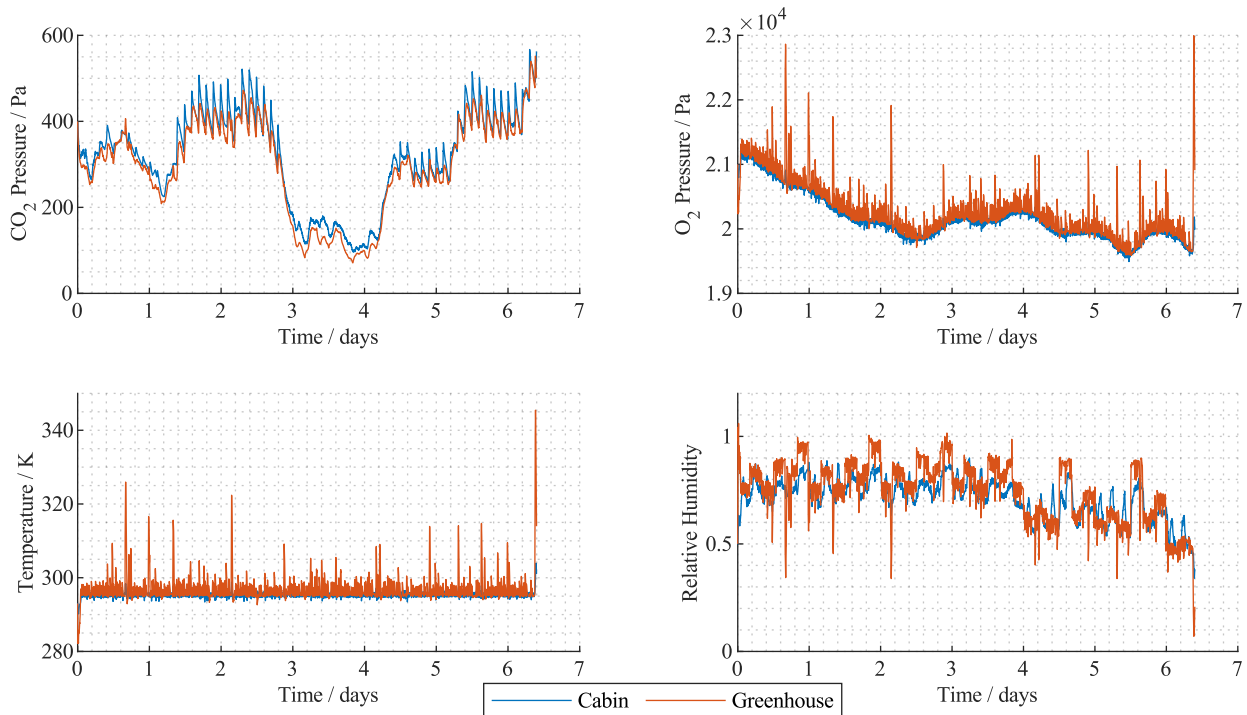


Figure 6.5-16 Atmosphere values for the cabin and greenhouse in the part ELS CELSS.

After the first harvest the CO₂ pressure increases slightly, but then drops to values below 200 Pa before the wheat is harvested. After the wheat harvest, the CO₂ pressure increases sharply because new inedible biomass is supplied to CROP to produce CO₂ and additionally a primary CO₂ sink was just removed. On day six at the beginning of daytime the temperature in the greenhouse exceeds 340 K for a short duration. This also resulted in the simulation stopping shortly after, as two-phasic flow conditions occurred in some subsystems due to these high temperatures. Since this case is more pronounced than the base case in Figure 6.5-10 a closer look into the CCAA is taken in Figure 6.5-17.

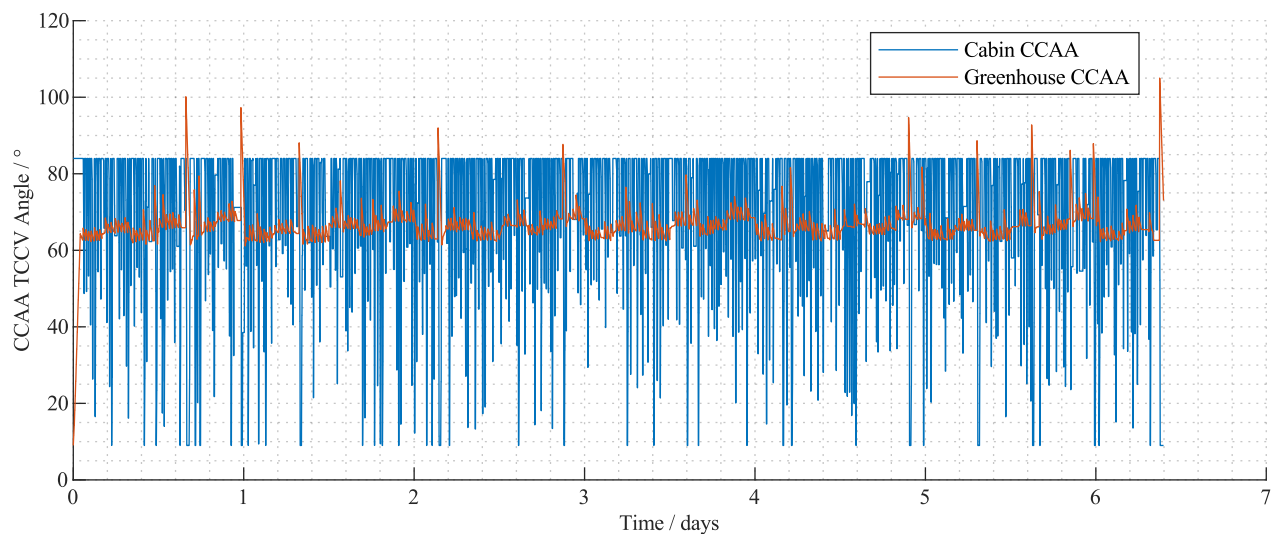


Figure 6.5-17 TCCV Angle for the CCAAs in the part ELS CELSS.

Overall, the high TCCV angle for the greenhouse, which results in small flowrates through the CHX, shows that the CHX is oversized for this case. At the end of the simulation, where the highest temperature occurs, the TCCV angle reaches the maximum value of 105° . At this value no air passes through the CHX at all, which causes the increased temperature. This is an overreaction of the control logic after the humidity production became smaller. A redesign of the CHX to better fit the loads of this case could likely solve this issue.

The CO_2 partial pressure in Figure 6.5-16 is also of interest, because it varies between the values where CDRA is active at the beginning and the end of the simulation and also includes a period where CDRA is inactive in the middle. In Figure 6.5-12 the CDRA for the base case had adsorbed water and it was unclear how it would react to higher CO_2 partial pressures after this. As Figure 6.5-18 shows this is also the case for CDRA here, but after the humidity and CO_2 levels normalize, CDRA is able to recover and return to normal operations.

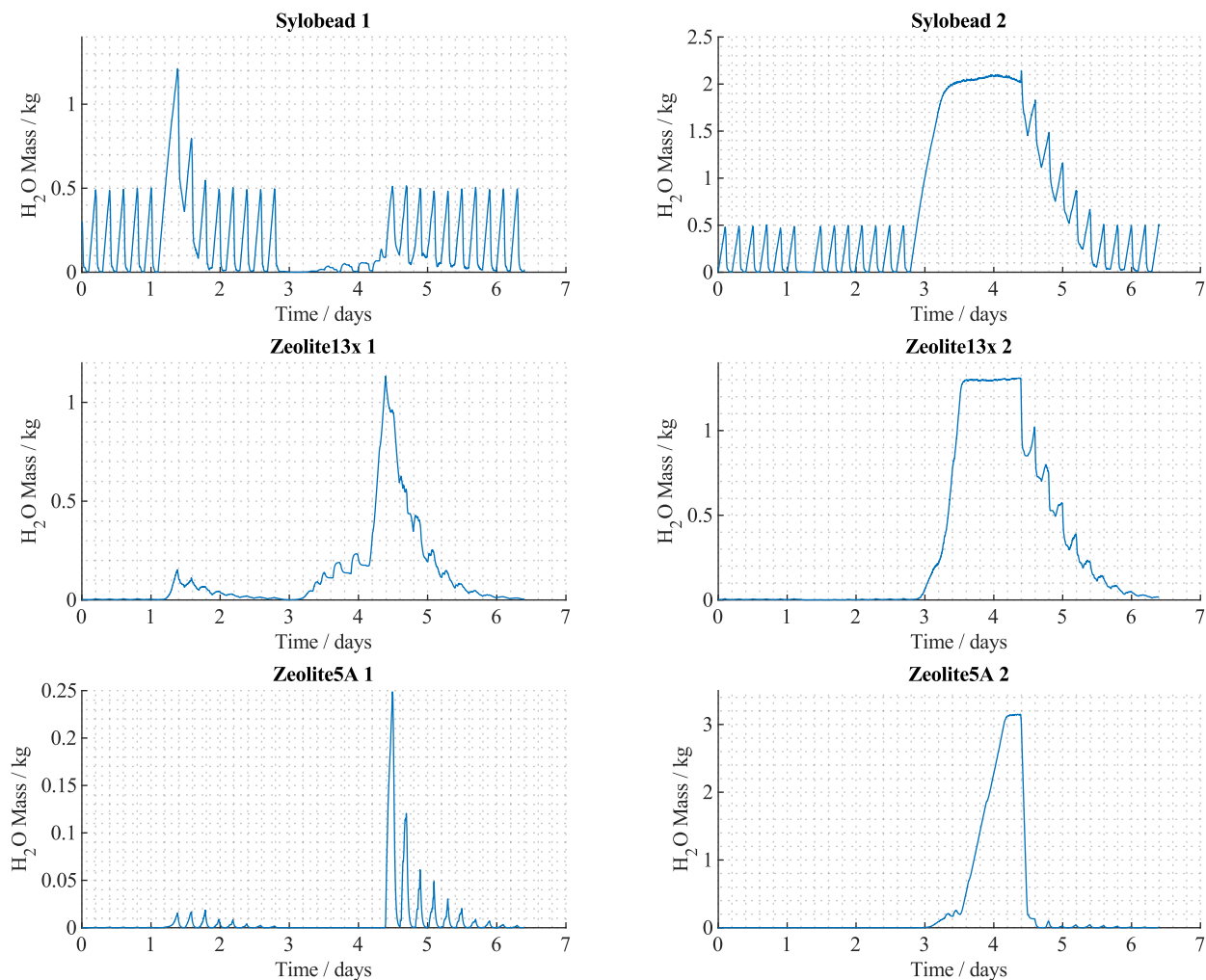


Figure 6.5-18 Adsorbed water masses in CDRA for the Part ELS case.

However, as Figure 6.5-19 shows the CO_2 adsorption on day three and four is affected by this water carry over. It normalizes at the end of day four, where the CO_2 and humidity levels in the cabin are again close to the nominal operating conditions for CDRA. This answers the question whether the adsorption of water into CDRA would hamper its usage as a backup system. Since CDRA is able to recover from this condition and again control the CO_2 level in the cabin, this is not the case. The higher CO_2 levels in Figure 6.5-16 at the end of the simulation are a result of the increased temperature, as a higher temperature also causes a higher pressure.

Figure 6.5-20 shows the averaged daily flowrates for this case. Overall, the O_2 balance is better maintained. Some O_2 supply from storage is necessary at the end of the simulation, where low partial pressures for O_2 occurred as Figure 6.5-16 shows. The water content in the consumed biomass for this case is also higher than for the other cases, as less plants with low water content, like rice and peanuts, are used in this case.

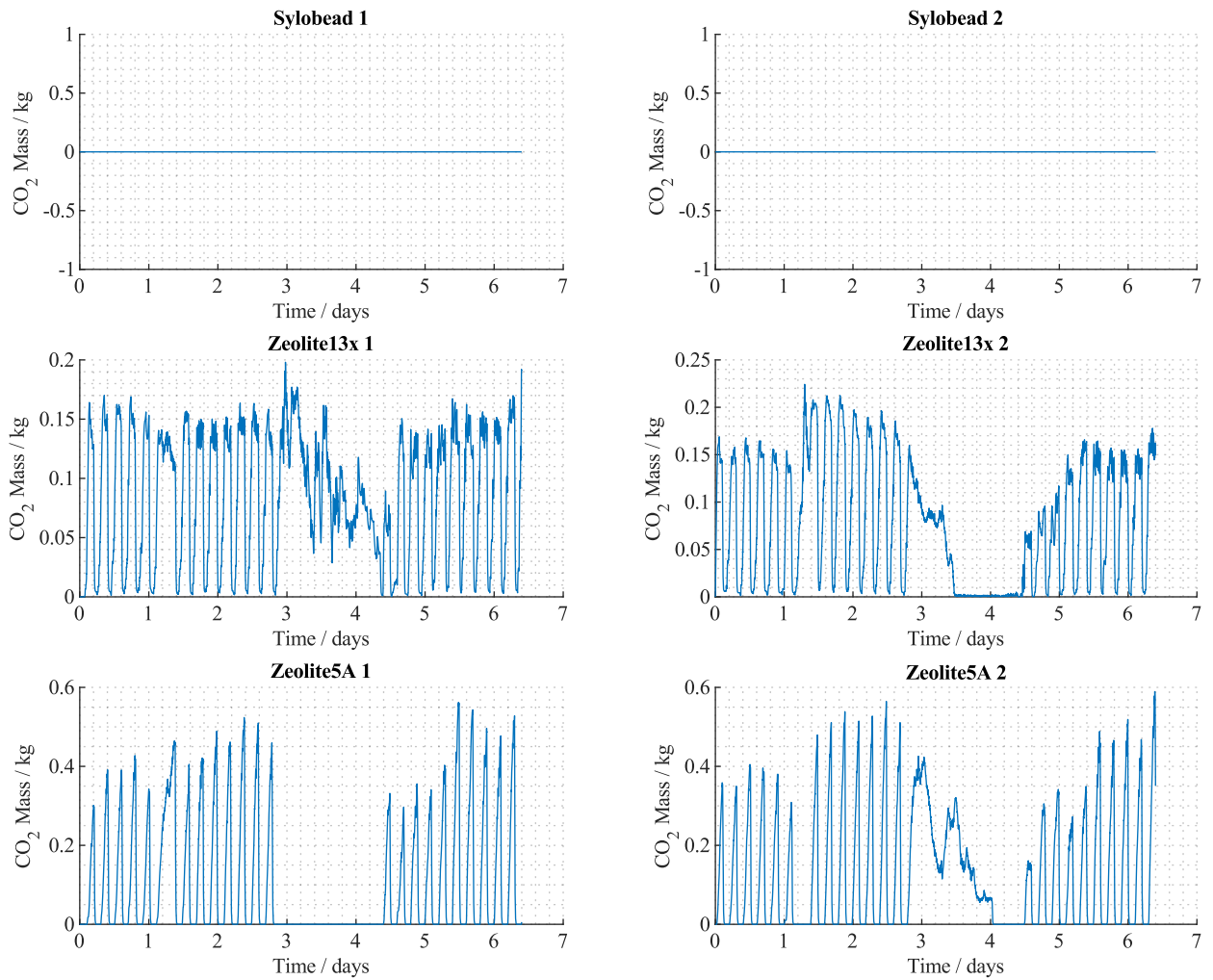


Figure 6.5-19 Adsorbed CO₂ masses in CDRA for the Part ELS case.

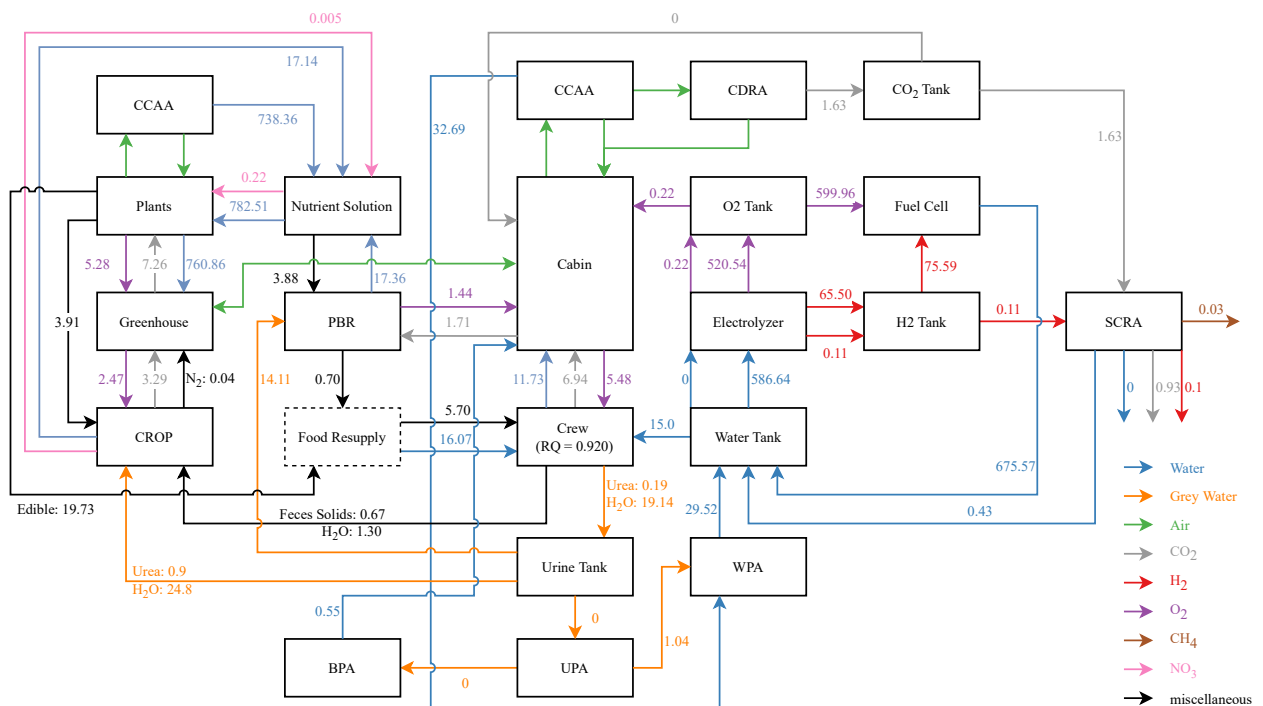


Figure 6.5-20 Averaged daily flowrates for the Part ELS case with 118 days of prior plant growth.

6.5.2.6 Base CELSS Startup

For the following results, the mission is assumed to land on March 30th 2038 at Gusev Crater-Columbia Hills (14.6°S, 175.4°E). Crewed operations as well as plant growth start on March 30th as well. The simulation also starts at this date and therefore shows a startup case for the operation of the ECLSS. For the plants the cultures are initialized to start with the delay between each culture, as discussed for the base CELSS in chapter 6.5.2.2. Therefore, during the simulated period only one culture of each plant is currently active. For this reason, the relative humidity in Figure 6.5-21 is quite low because only little transpiration occurs.

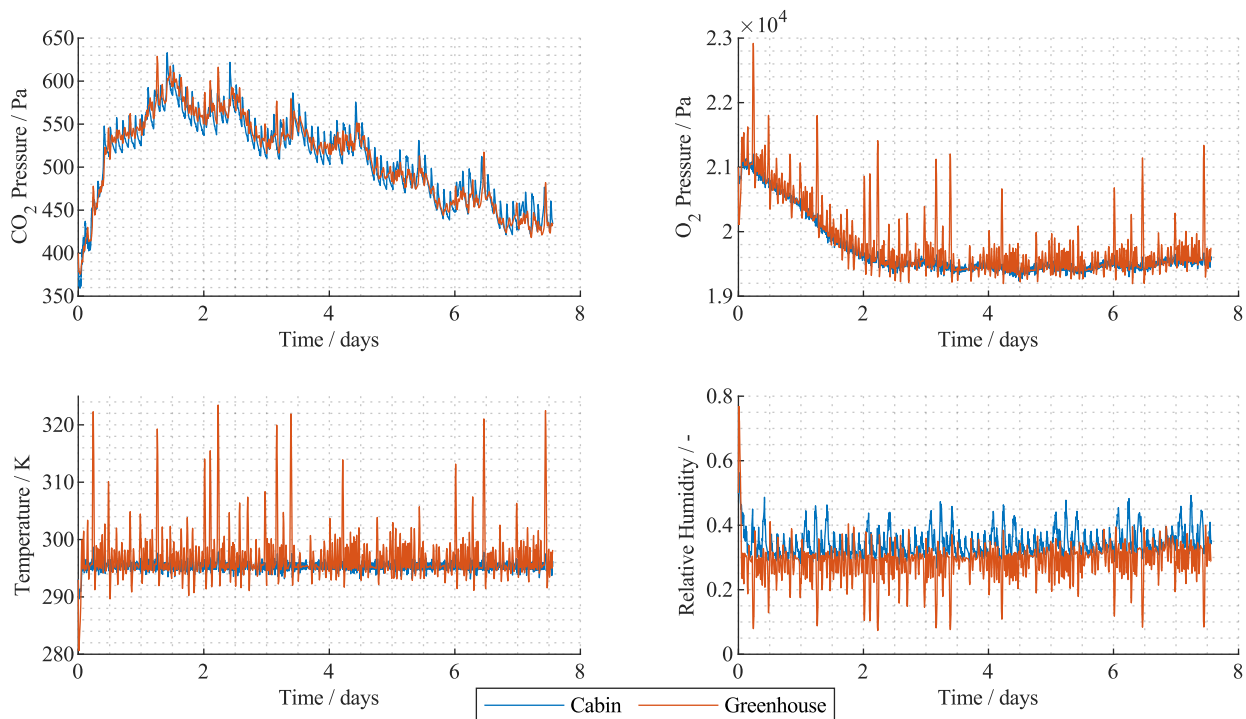


Figure 6.5-21 Atmosphere values for the cabin and greenhouse in the base CELSS during the startup phase.

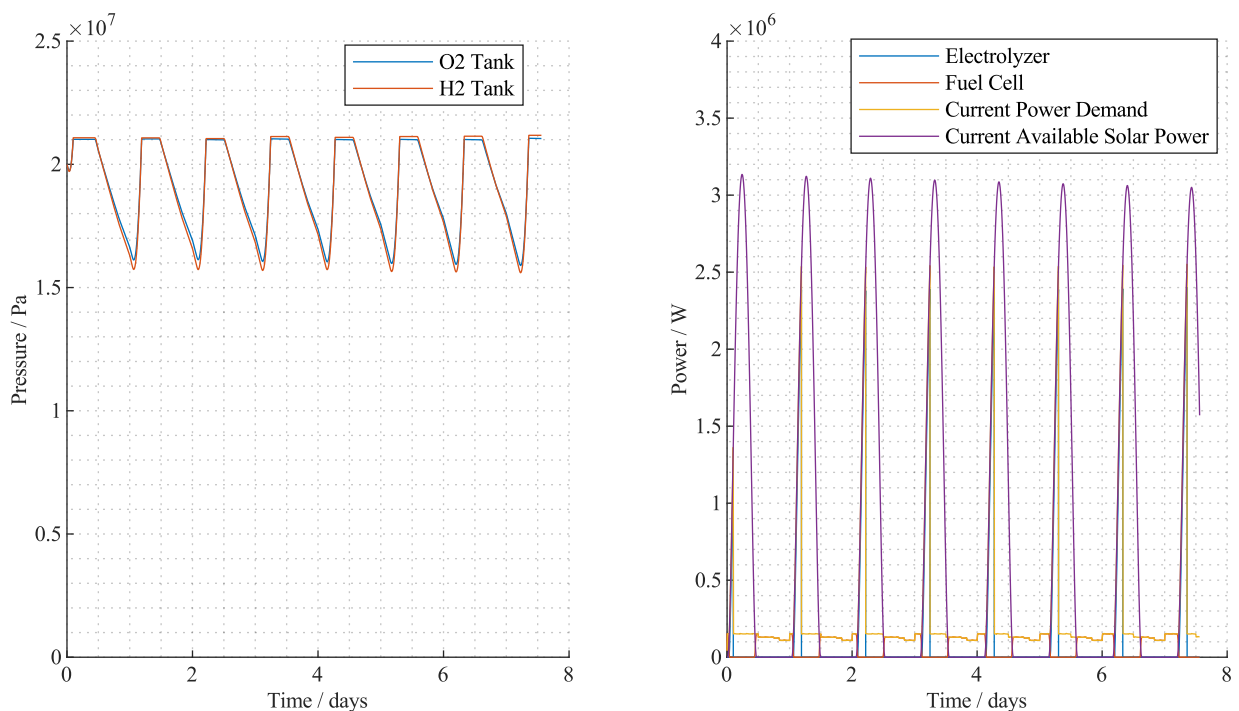


Figure 6.5-22 Energy system parameters for the base CELSS during the startup phase.



In Figure 6.5-21 the O₂ pressure drops until O₂ from the tank is used to maintain a habitable atmosphere. The CO₂ level initially rises until the plants are sufficiently grown to support the air revitalization. The fewer illuminated plants (as only the LEDs of the currently growing cultures are active) and the higher seasonal illumination on Mars result in an oversized energy storage system, as shown in Figure 6.5-22. Not even half a day is required to fully recharge the RFCS during this operating phase and less than 25% of the stored H₂ and O₂ is consumed during the night.

Figure 6.5-23 shows the averaged daily flowrates for this case. The flowrates of the plants are lower than in Figure 6.5-8 due to the plant growth just starting for only a single culture per plant. The primary CO₂ removal during this phase is handled by CDRA because the PBR is also currently in startup operations. The CROP only handles the produced feces and urine because no inedible biomass has been harvested yet. Therefore, the flowrates of CROP are also lower. The CO₂ level rises up to 600 Pa for a short time because the CDRA is not sized to handle the load from CROP in addition to a crew of six with one hour of exercise per day and crew member. This case shows, that CDRA is sufficient to keep the CO₂ level below the seven-day limit of 700 Pa (James et al. 2008) for the period before the plants and PBR consume CO₂.

Since only a single culture is currently growing for each plant, the nutrient demand of the plant growth system is also smaller during this operating phase. The buffer derived in chapter 6.5.2.2 for nitrate with 33.3 kg would suffice for more than 1,000 days at the shown nutrient consumption during startup. The derived buffer therefore is also sufficiently sized to support the plant growth during the startup phase, as the limiting case is indeed chapter 6.5.2.2.

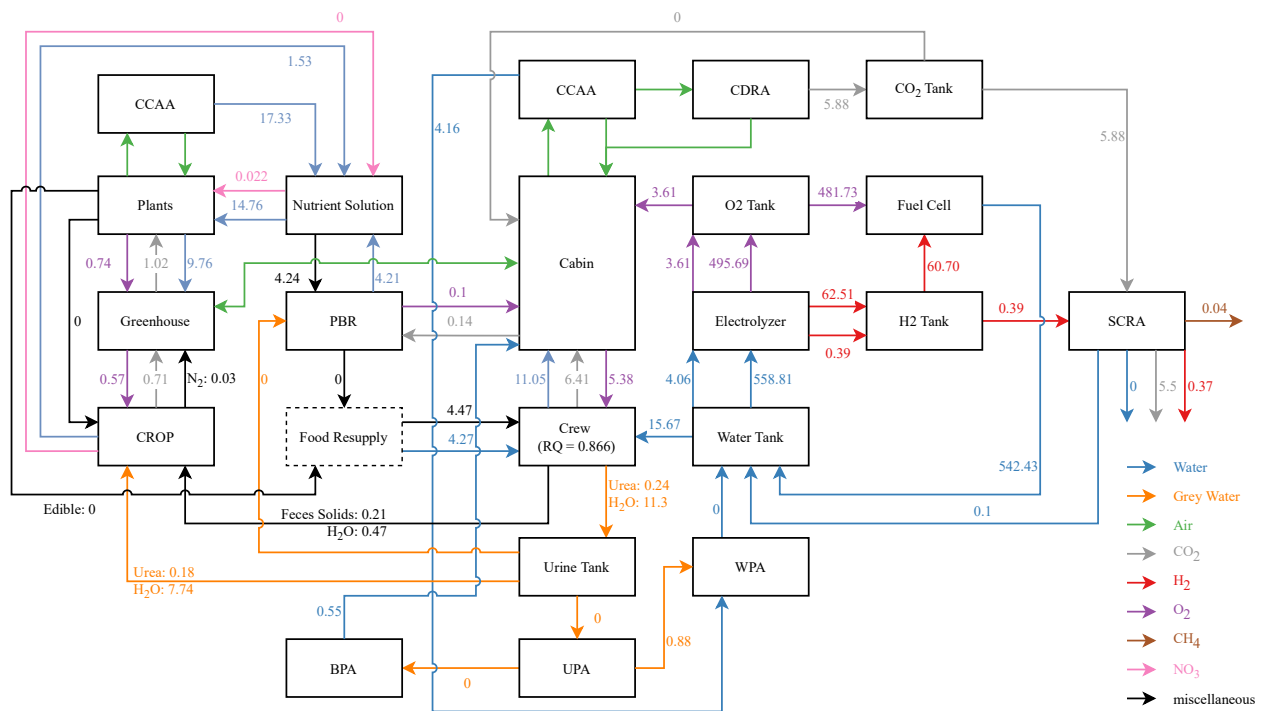


Figure 6.5-23 Averaged daily flowrates over a seven-day period for the base CELSS case during the startup phase.

6.5.3 Discussion

Here the research questions defined in Table 4.3-1 for mission scenario three are discussed. The first research question for the permanent Mars base is answered on the basis of chapter 5.1.2 since it requires LiSTOT instead of V-HAB.

“Q-3.1: Where are the breakeven points between different life support technologies?”

The earliest break-even point between the ISS ECLSS and a hybrid ECLSS with urine treatment is after 15.6 years. Without nutrient recycling from human waste, the break-even occurs after more than 86 years. Other PC subsystem options like a Bosch reactor or other biological options like a PBR do not trade favorably compared to the ISS ECLSS and require long break-even times (PBR 87.4 years) or do not result in improvements (Bosch reactor).

Figure 5.1-11 shows the different ESM values of these systems over time and provides an overview of the time required for each system to outperform the ISS ECLSS. One general conclusion drawn from this was the requirement of nutrient cycling for a plant growth system to be a viable alternative.

“Q-3.2: Can the developed tool be used to identify stability conditions for the ECLSS?”

The initially stability issue encountered for this case was the control logic for the upscaled CCAA. The model proved capable to support the redefinition of this control logic to a stable one for the base case. Then different sized plant growth chambers were analyzed, which showed the limits of this new control logic. This example shows that the tool is capable of identifying required conditions for stability (here the control parameters of CCAA) and also to identify the limits of these conditions with regard to differently sized plant growth areas. In addition, the stability with regard to other aspects, like O₂ and CO₂ levels can be analyzed with the developed tool. Another example, where the stability of the system was proven, is a water carry over event in CDRA from which the system could recover.

The control logic of the CCAA serves as one example for the ability to identify stability conditions of the ECLSS. Since transpiration is one of the primary impacts of plants on the cabin atmosphere, the temperature and humidity control is the most affected PC system. Additional stability conditions that were studied include the separation of the growth area into subcultures to better distribute the impact of plants over time. The case without subcultures from chapter 6.5.2.3 proved unstable as the CO₂ could not be controlled. On the other hand, the case from chapter 6.5.2.2, with sufficient subcultures to achieve similar average values per day as stated by (Anderson et al. 2018: 180), resulted in rising oxygen levels because the processing of waste biomass to consume the oxygen is only possible after harvest. This suggests that more subcultures are required to not only spread the dynamic effects of the plants themselves but also of the waste management systems. These examples show that the developed tool is capable of identifying stability conditions. However, the objective of this thesis was not to derive a final functional design for the ECLSS as that would require further work and more analyses. The objective to develop a tool that can identify whether a ECLSS design is stable or not was achieved.

“Q3-3: Can the model detect failure cases and adjust control logics of the LSS to improve fail-safe capabilities of the LSS?”

Yes, as can be seen from the example of the CCAA control logic. The system also shows potential failure cases where the new control logic is not sufficient to remain in the desired operation envelope and thus e.g. the temperature is exceeded. A real system could utilize the developed tool for an internal model control to react quicker to the large changes occurring in the hybrid LSS where the classic PID controller proved insufficient. As the developed tool is also able to predict failure cases where the O₂ or CO₂ pressures exceed the desired values, internal model control could also be used to react to these changes before they occur and therefore improve the fail-safe.

To improve fail-safe capabilities of a real system, the developed tool could e.g. be operated in parallel. In the model different failure cases, like the loss of a plant culture, and their impact on the system can be predicted to inform the control logic of the required values to maintain stable operations. Through this information the control logic is no longer limited to hard coded values of e.g. partial pressures, as the future CO₂ level in case of a failure could impact the control logic to ensure stable operations.



“Q3.4 How large are the required nutrient, water and energy buffers to ensure that the ECLSS does not run out of consumables during nominal operation?”

The required buffer size for nitrate, H₂, O₂ and H₂O depends on the plant system used. For the base case the required nutrient buffer size for nitrate was estimated to 33.3 kg based on the presented dynamic results. The required buffers for the longest night in 2038 result in the following required buffer masses:

A long simulation over multiple months was not finished in time for this thesis, due to the length of the simulation (~90 days real time to simulate 180 days) and the iterative process required to optimize the ECLSS design. Therefore, the nutrient buffer was estimated based on the presented dynamic results. However, the presented simulation tool allows the derivation of an optimized ECLSS design based on the results presented in this thesis, which is currently studied as future work. The objective of this thesis was not to finalize the ECLSS design. The objective to develop a tool, which can help optimize the design, was achieved. Further improving the ECLSS design with the help of the developed tool, including a full nitrate cycle analysis, is considered future work and will be presented in future publications.

While the buffer stores for H₂, O₂ and H₂O were over dimensioned in the simulation, the required masses for each buffer can be calculated from the difference between the maximum and minimum mass. The simulation case was chosen to be the worst-case with regard to the required buffer sizes. Therefore, these values represent the overall required buffer sizes for the ECLSS even though the simulation only covers seven days. The sum of O₂ and H₂ mass is larger than the required H₂O buffer mass due to the system dynamic for the water recovery. The current results suggests that CO₂ and O₂ buffers are required, even though the impact of the plants is close to the averaged values from (Anderson et al. 2018: 180) and for the averaged values shown in Figure 6.5-1 no buffers would be required. However, due to the dynamics of the waste management system, addition of CO₂ from a buffer is required and the rising O₂ level could only be handled by removing it from the atmosphere and storing it for later use. Finally, further study is required to optimize the number of subcultures, which could potentially result in a stable ECLSS design without the necessity of CO₂ and O₂ buffers.

7 Discussion

7.1 Summary

In this thesis a modular simulation architecture for hybrid ECLSS was derived. In order to more efficiently perform a trade-off for different ECLSS options, a new trade-off tool called the Life Support Trade Off Tool or short LiSTOT was developed. This tool was created in cooperation with two master theses (Schreck 2017; Feigel 2019) as a precursor to the more in-depth dynamic analysis of V-HAB. LiSTOT addresses the lack of an ESM calculation in V-HAB that was stated as future work by (Czupalla 2011: 333). It enabled the analysis of a photo bio-reactor (PBR) and various plant growth chambers (PGC) compared to physical/chemical ECLSS options, foremost to the ISS ECLSS. In this analysis, the current crop compositions for PGC assumed in (Anderson et al. 2018: 181) proved unfavorable compared to the current ISS ECLSS. Unfavorable in this context means, that with the assumptions from (Anderson et al. 2018: 176) a PGC would require more resupply than the ISS ECLSS even if spare parts for the ISS ECLSS are considered. Therefore, an optimization approach considering the required crop growth area and the nutritional content was developed and used to derive an optimized PGC with 57 m² growth area that provides the full diet of the crew. This optimized PGC can reach break-even with the ISS ECLSS after 15.6 years if full nutrient recycling and favorable assumptions regarding the growth lights are used. This part of the research is also presented in (Kaschubek 2021). The alternatives for the PC ECLSS (e.g. a Bosch Reactor) did not improve the ESM significantly because of the already high degree of water closure (98%) in the ISS ECLSS. With this high water loop closure no water resupply is required even for the currently used Sabatier reactor, thus making food the largest resupply mass. Therefore, biological options which also produce food are the only viable alternatives to further reduce the ESM for missions longer than 15 years.

While this steady state analysis is well suited for overall architecture trade-offs it is insufficient to answer questions regarding required buffer sizes and nutrient cycling. Especially the nutrient cycle is of interest in the analysis of bioregenerative ECLSS because nutrient resupply is one of the primary resupply masses if it cannot be closed. For example, in the analysis performed with LiSTOT the carbon balance in the system could not be completely closed, which resulted in slightly reduced crop growth areas. This is likely due to the fact that feces are currently not part of the cycling analysis in LiSTOT, but it could also be caused by the fixed values used for the human model. Therefore, subsystems capable of modelling the nutrient and element cycling in the ECLSS were developed. However, the objective of this thesis is not to model a purely bioregenerative ECLSS but to include the interactions between the bioregenerative subsystems and the required PC subsystems. The PC subsystems still required in bioregenerative ECLSS are the CCAA and the WPA. The CCAA is necessary to control the humidity and recover the transpired water from the plants, as no biological options exist for this. The WPA is necessary to ensure the production of water with potable quality. In addition to these two subsystems the CDRA is also important as backup CO₂ removal system because the plants do not remove CO₂ continuously. Therefore, the primary modelling effort with regard to the PC subsystems was focused on these three systems. The currently available subsystem models of these systems were analyzed and transformed into V-HAB subsystems. To achieve fast enough simulation speeds for system-level analysis some simplifications were required compared to the models identified in the literature survey. For example, the CDRA model was a CFD model implemented in COMSOL (Coker and Knox 2016a), which is not directly compatible to any of the existing system-level ECLSS analysis tools. Therefore, a derivate model of it was created in V-HAB. A 1D model of WPA developed by (Hokanson 2004) was adapted to a 1D V-HAB model. To increase simulation speed, the cell masses in the 1D V-HAB model had to be neglected. For the CCAA only a MCL 4 model based on tabulated values existed previously. Since the CCAA must be upscaled to handle the humidity loads from plants a new 2D discretized model was developed.

With regard to the biological subsystem, the MEC plant growth model was implemented in V-HAB at the beginning of this thesis. However, the existing MEC model was incapable of modelling nutrient cycling as neither the nutrient uptake of the different substances was modelled, nor the composition of the biomass. Therefore, the MEC model had to be adjusted to include a nutrient uptake algorithm based on the Michaelis Menten kinetic. The overall nitrogen demand of the plants was calculated based on two factors: The aforementioned kinetic and the average values of nutrient content



for the edible and inedible plant. For the edible biomass, the data from (U.S. Department of Agriculture 2021) is used to derive the composition for the different plants.

The bioregenerative waste recycling system CROP, which converts the urea content of urine into nitrate for the plants, is modelled with enzymatic kinetics that were fitted to test data. While it is no longer planned to utilize this system for waste biomass handling and feces handling, the assumption for this thesis was that this is the case, and the system is also capable of performing these roles (Hauslage et al. 2014; Bornemann et al. 2018).

The final part required to model the nutrient and substance cycling is a human model. During literature review, two candidate models were identified, HumMod (Hester et al. 2019; HC Simulation 2020) and the V-HAB 1 human model (Czupalla 2011). The V-HAB 1 human model was a Simulink model, which was not compatible to the new V-HAB 2 structure. Therefore, this model had to be reworked into an object-based V-HAB 2 model using the new class architecture. In addition, the metabolism layer of the human model was completely reworked, as the previous implementation was outdated and lacked the protein metabolism, which is mandatory to calculate the urea production and nitrogen cycling. The new version of the V-HAB human model developed in this thesis was compared to HumMod to select the best suited human model. During this comparison, HumMod showed severe differences in the respiratory values for O₂ and CO₂ compared to NASA values (Anderson et al. 2018: 63). Furthermore, in HumMod the human enters a state of cardiac arrest if the human exercises at elevated CO₂ levels. Overall, the new V-HAB human model proved more reliable and better suited to ECLSS analysis than HumMod.

All tools and models developed in this thesis are modular and can be easily adapted and expanded. This was an inherent focus of this research, as the models are not used for one specific analysis but instead for different mission scenarios and case studies. This also means the individual subsystem models can be used for other ECLSS analysis and a new drag and drop GUI supports the easy definition of alternative ECLSS compositions.

Regarding V-HAB itself multiple future work tasks from previous theses were addressed. The primary future work task from (Olthoff 2017: 249) to develop a better and more stable solver was addressed for both the matter and the thermal domain. The thermal domain was also further developed to provide clear interfaces and a common class architecture with the matter domain. The common architecture makes it easier to maintain the code as many basic functionalities are identical between the two layers. These enhancements were necessary to achieve simulation speeds that are faster than real time for the complex models. The new approach solves a network of branches by creating a connectivity matrix between the different phases and then using vector matrix operations to solve the branch flowrates. A combination of the thermal and matter domain allows the detailed modelling of all relevant effects in the subsystem models. For example, in the CDRA model the heat of adsorption has a large impact on the overall system behavior and at the same time depends on the adsorbed mass flows. This can only be captured in a multi-physics simulation.

The position of the crew, which was previously static within the habitat (Czupalla 2011: 332), is now variable and the crew can move between the different modules. The required simplified CFD analysis to enable this movement through the different modules was derived for the ISS in earlier research by the author of this thesis (Pütz et al. 2016). In addition, the temperature was considered constant in previous V-HAB 1 analyses of habitat ECLSS (Czupalla 2011: 332). Through the new thermal domain and the CCAA model the temperature in the habitat is now dynamic and changes depending on the various heat loads from the crew and the various systems. The impact on the other parameters, like relative humidity and partial pressures, is also included in the new analyses.

In addition to the future work tasks defined by previous research, further improvements were made to V-HAB to enable the desired analyses. The representation of matter was adjusted to correctly depict the composition of different masses. For example, the inedible biomass of plants is represented as a compound mass, which consists of the plant biomass and the nitrate mass. The edible biomass of plants is modelled as a compound mass, which consists of the various nutrients as defined by (U.S. Department of Agriculture 2021). Other enhancements to V-HAB include the rework of the timer and the execution order to provide a well-documented and comprehensible framework to future users of V-HAB. The component library of V-HAB was also enhanced significantly. The previously not migrated detailed human model is now available and many current or future detailed ECLSS subsystem models and general calculations (like for the pH-value) were added. In addition, test cases for all of these models were defined that include validation data to quickly check if the models represent the real system behavior after future changes to V-HAB. Thanks to a growing Wiki that is openly accessible at <https://wiki.tum.de/display/vhab> the documentation of V-HAB also improved

significantly. Overall, the current version of V-HAB is better documented, easier to maintain and more accessible to new users than previous versions. An open-source release for V-HAB is planned as well, which will allow anyone to use V-HAB as long as access to MATLAB is available.

The developed tool was then used to analyze three different mission scenarios with varying biological components to study the interaction between the systems. The first scenario studies the addition of an ISPR sized plant growth chamber into the ISS ECLSS. The results show the impact on the water imbalance between the Russian and US segment, which changes by up to 10.8 kg. In addition, the reduction of produced water by the Sabatier reactor was analyzed and deemed negligible. The second mission scenario is a Moon base at the lunar south pole and includes lighting conditions and a regenerative fuel cell system for energy storage. Here the addition of the ISPR sized growth chamber and a larger photo bio reactor were analyzed, as well the potential usage of a Sabatier reactor to create methane and oxygen as rocket fuel. The production of fuel is feasible with a potential production of 6.73 kg/d from a crew of six. The photo bioreactor only improves the system if it is sized to process the urine of the crew and supplies part of the diet and would reduce the required food supply by 1.5 kg/d. However, the potential improvements are counteracted by reducing the fuel production by 1.47 kg/d to 5.26 kg/d potentially produced fuel. The third mission scenario analyses a permanent Mars base with full food provision from plants. To accommodate the large plant growth areas an upscaled version of the ISS condensing heat exchanger and an adjusted control logic were derived to maintain temperature and humidity values within the desired area. The nutrient dynamics of the system were also analyzed and overall showed the difficulty in maintaining a balance for all involved substances due to the different time frames for each process. The tool can calculate the nitrogen nutrient cycle for all involved subsystems and can support the sizing of nutrient buffers. For the considered case about 33.3 kg of nitrate are required as buffer. The tool also supports the addition of further nutrients to the cycling analysis.

7.2 Conclusion

This chapter discusses whether the objective of the thesis was achieved and whether the requirements defined in Table 4.3-2 were met. It will not include a discussion of the individual results for each mission scenario, as these are summarized in the respective discussions of chapter 6. The primary objective for this thesis was stated in chapter 1.2:

To develop a simulation tool for hybrid life support systems that can perform dynamic, holistic, system-level simulations and predict the dynamic exchange rates of energy and mass between the subsystems.

To specify whether this objective was achieved, three mission scenarios for different hybrid LSS were defined. These ranged from an early implementation of a small PGC on the ISS over a Moon base with plants and algae to a permanent Martian base with full food closure. Specific research questions the tool shall answer for each scenario were stated in Table 4.3-1, and a tool capable of answering these questions is considered to achieve the primary objective. As discussed in detail in chapter 6 the individual questions were answered with the tool, therefore achieving the primary objective of this thesis. The developed tool is the first hybrid LSS model capable of performing nutrient cycle analysis for the primary nutrient cycle of nitrogen at system-level in a dynamic context. In addition, the subsystem models used in the tool are derived from first principles. They are therefore considered capable of predicting the subsystem behavior for off-nominal conditions outside the design envelope of the respective subsystem. However, this capability could not be proven because it would require hardware tests for such off-nominal conditions to check the predictive capabilities of the models. The dynamic flowrates for all major substances, consisting of the elements N, O, H, C, and the primary energy flows of electricity and heat are depicted in detail in the model. This corresponds to the desired MCL of 8 for the developed tool, as all subsystem models are correlated to the extent feasible with available data and able to model realistic interconnected system behavior. Overall, a holistic and modular simulation tool for hybrid LSS including the energy subsystems was developed in this thesis.

In addition to the primary objective and research questions, requirements for the model were defined in Table 4.3-2, which are summarized below:

- R-1: A single analysis shall require a maximum of 2-4 weeks of computation time on a personal computer.
- R-2: Dynamic models shall be used for all subsystems.



- R-3: Validated models shall be used for all subsystems.
- R-4: A Graphical User Interface (GUI) shall be developed.
- R-5: Maintain a closed mass balance and check the impact of the remaining error on the simulation.

The first requirement depends on the utilized computer for the simulation. In the context of this thesis, a personal workstation with 32 gigabytes of working memory and an Intel Core i7-6700 processor was used for mission scenarios one and two. For mission scenario three the individual cases were analyzed as batch jobs on nodes of a high-performance computer. Each node utilized 16 gigabyte working memory and four cores of an AMD EPYC 7662 processor. The simulation of one week for the ISS required about 1.7 days on the personal workstation, while for the Moon base, a simulation of 89 days required 15 days. The simulation of one week for the Mars base required about 2.5 days on a node of the high-performance computer. The exact simulation times depend on the specific case but are similar for all considered cases of the individual scenarios. Therefore, requirement R-1 is met for all mission scenarios. It would have been favorable to achieve simulation speeds where several months can be simulated for the Mars base in the considered timeframe, which was not feasible while using the detailed subsystem models. However, with the help of initialization logics for the plants and other subsystems of the Mars base scenario, the most relevant times of its operation can be simulated. This includes the times where large plant cultures are harvested and other plant cultures currently have the highest dynamic exchange rates with the hybrid LSS. Therefore, this requirement is considered partially met, as not the full duration simulations were feasible but instead initializations to model the most critical periods were used.

The second requirement (R-2) states that all subsystem models shall be dynamic, while the third requirement (R-3) states that they shall also be validated. This was achieved by adapting existing dynamic models for the subsystems or developing new models and then validating the behavior of the subsystem with reported test data in chapter 5. The only limitations concern CROP and the plant nutrient dynamics. CROP could not be validated due to lacking data for the desired operating conditions. Still, the model is developed and validated based on the available data at lower urine concentrations. The nutrient dynamics of the plant model could also not be validated generally. However, the basic behavior matches reported literature values and the general plant behavior was validated. Therefore, requirements R-2 and R-3 are also considered met.

The fourth requirement (R-4) states the necessity for a graphical user interface. This was introduced as a requirement to support a planned future open-source release of V-HAB. By supervising different students working with V-HAB the initial complexity when learning V-HAB became apparent. In order to reduce the initial learning curve a GUI was developed. As discussed in chapter 5.2.6, the GUI allows the definition of ECLSS compositions via drag and drop in draw.io. This reduces the complexity for the primary use cases of V-HAB to analyze different ECLSS compositions.

The fifth requirement (R-5) states the necessity to maintain a closed mass balance in the analyses. The remaining mass balance errors are calculated by V-HAB and shown at the end of a simulation. For the different scenarios the mass balance errors are on the same order of magnitude but differ slightly between each specific case. For mission scenario one, the ISS, the error is around 0.1 g, which is negligible compared to the total modelled mass of more than $1.5 \cdot 10^4$ kg. For mission scenarios two and three (the Moon and Mars base) the errors are larger with -29 g and -65 g respectively, because the considered masses are also larger with $1 \cdot 10^6$ kg and $1.28 \cdot 10^6$ kg. This is also evident in the derived buffer sizes. However, even if the complete mass balance error only affected the smallest derived buffer, the nitrate buffer of 33.3 kg, the impact would still be in the range of 0.2% and therefore be negligible. The mass balance errors are however usually spread over the system, as they are e.g. a result of floating point precision for each calculation. Therefore, it is unlikely that the complete mass balance error would affect a single value. For this reason, the errors, which are below 0.1 kg for all cases, are deemed small enough to be negligible. For comparison, the previous V-HAB human model produced a mass balance error of about 0.1 kg for a simulation of one day in just the glycogen storage (Matthias Pfeiffer 2007: 170–1). The overall mass balance error was not calculated in V-HAB 1 but simply by assuming a crew of six, the mass balance error for a one-day simulation would already exceed 0.5 kg. In comparison having a total mass balance error of less than 0.1 kg for a simulation of 89 days or 7 days respectively can be considered small.



7.3 Future Work

This chapter discusses different areas for potential future improvements. The first subchapter covers the developed subsystem models and specific improvements for each of them. The second subchapter considers the overall hybrid ECLSS analyses and potential future studies and improvements. The last subchapter discusses potential areas for improvement to V-HAB in general.

7.3.1 Subsystem Models

7.3.1.1 Physical/Chemical Models

As future work further approaches to improve the WPA model while maintaining the performance for system-level simulations shall be studied. As an initial step, the subsystem model that provided a better overlap can be compared to the current model to identify specific differences in the adsorption flows. This could help identify the specific reason for the difference in system behavior between the two models.

The Sabatier reactor model in this work was simplified because the outlet of the Sabatier reactor does not interact with other parts of the ECLSS. If this becomes necessary for future analyses a detailed subsystem model for the Sabatier reactor should be derived to ensure the validity of the resulting dynamics.

Similarly, the models for the UPA and BPA are only developed to a point where they mimic the external dynamic impacts on the ECLSS correctly, but the internal processes are not modelled sufficiently to analyze these systems in detail. Depending on future use-cases for V-HAB these models must also be improved.

7.3.1.2 Plant Model

The MEC plant model in V-HAB was further improved to include nutrients. The edible biomass nutrient composition is currently not variable but fixed, which could be improved in future models. In addition, the nutrient dynamics are currently limited to nitrogen. However, the basic calculations are identical for other nutrients, like potassium and phosphor, and the addition of these to the plant model from a programming perspective is not difficult. The larger difficulty is the availability of reliable data regarding the nutrient uptake for multiple nutrients (multivariable dynamics) with varying concentrations for different plants. During the development of a nutrient dependent plant model the limitation of the MEC model became apparent. Since the MEC model does not differentiate between different plant parts like roots, stem and leaves the nutrient dynamics cannot be captured without extensive hardware tests to define the required parameters (Nikic 2017: 80). Therefore, a better way to further improve the plant model may be to study the mechanistic plant model developed by (Hezard 2012; Poulet 2018) and check whether it is applicable to the desired system-level analyses. If it is not applicable directly, a better implementation for the nutrient dynamics into the MEC model could potentially be derived from this model.

7.3.1.3 CROP Model

During the work on this thesis, the use-case for the CROP system was narrowed down to urine treatment. While this is still one of the major functions required for the ECLSS, the treatment of feces and inedible plant biomass is also important to close the nutrient cycle. Since CROP is no longer planned to perform these functions, a simplified representation based on early tests was implemented for these processes. Further improvement of this area for CROP is not productive as other systems will be used in the future for these functions. Therefore, the focus on improvement with regard to CROP should be on further parameter fitting of the enzymatic kinetics to high urine concentration data. This data did not become available in time for this thesis but will be available in the near future.

7.3.1.4 Human Model

The human model currently is a generic androgynous human who most closely resembles the average steady state values from NASA (Anderson et al. 2018: 63). In the future, different ages, genders and body masses should be included in the human model to further provide variability to the analysis. This is important because the composition of the crew has an impact on the loop closure as the Lunar Palace experiment showed (Fu et al. 2016: 934).



Additionally, while the new metabolic model does include all relevant major pathways, it does not differentiate between the different types of proteins, carbohydrates and fatty acids. Based on the discussed metabolic pathways from Appendix D it is feasible to derive a more generic metabolism model that handles all different substances individually. The required information for their inclusion in the food model is already implemented in V-HAB and can easily be added to the food and edible plant biomass.

7.3.2 Hybrid Life Support Analyses

The various errors that can occur in the system are the current limitation in quickly and efficiently running and evaluating multiple hybrid LSS analyses. Basically, the errors can be separated into two categories: programming errors that only occur in the model and design errors that would also affect a real system. The first errors should be eliminated before evaluating multiple ECLSS. While it is not possible to be completely sure that all programmatical errors are eliminated, the remaining programming errors in the presented tool should be minimal since the presented research was able to run the hybrid LSS analyses for different missions scenarios with a variety of cases. Of the design errors some are fairly simple ones, like a too small solar cell area to provide the required electricity, or an undersized water storage tank, while others are more intricate and a result of the interaction between the various subsystems. Currently a large-scale analysis with multiple hundred simulations to identify sensitivities is feasible through parallelization, but the various errors that occur are difficult to interpret. If this could be automated to e.g. result in outputs that directly show the cause of failure (e.g. too small water storage) and then provide a comprehensive figure showing these results, quick parameterized analyses would be feasible with the developed model.

Another potential area for improvement is the addition of alternative biological subsystems to consume inedible biomass and produce CO₂ and food. Candidate technologies that were not considered in this thesis are for example snails (Kovalev et al. 2015) or mealworms (Fu et al. 2019). The animals would consume the inedible biomass and provide a valuable protein source. This would allow the plant system to focus on the provision of carbohydrates and fats, which have high harvest indexes and require smaller growth areas compared to protein-rich crops like soybean. Thus, the required plant growth areas could be further minimized, while at the same time increasing loop closure.

Regarding the cycling analysis, other nutrients and waste stream substances should be included in future research. For example, phosphorus and potassium would be the next steps regarding the nutrient cycling. Many subsystem models already include these substances and do not have to be adjusted but the human model currently does not consider them. Any substance, aside from the macro nutrients and NaCl, that the human consumes, is just excreted after passing through the digestive tract. Including these additional substances in the human model is therefore likely the largest challenge. In addition, the nutrient cycle over longer time frames including the initial startup of the plant growth system should be studied.

Another area for improvement is the logic controlling the diet for the crew. Currently the human just demands a specific nutritional energy and is provided an according amount of food based on the currently stored masses. For example, if 50% of the currently available food mass is wheat, then the food consumed by the human will also consist of 50% wheat. While this logic ensures the produced masses are consumed according to their availability, it neglects the other nutritional demands of a human. Including these demands and adding priority to foods that are quickly perishable would improve this logic significantly.

7.3.3 V-HAB

Regarding V-HAB itself the primary areas of improvement are in the area of usability. The documentation in the wiki is an ongoing effort and must be completed in the future. In addition, the GUI should be enhanced to enable the definition of more complex analyses with it. For example, a better interface to the plant module could allow the addition of multiple different plants with multiple subcultures through a single plant block in the GUI. Currently the definition of plotting is also limited in the GUI. This could be improved by defining a basic set for logging and plotting variables for each subsystem model in the GUI, which can be toggled on and off. Another potential usability improvement would be a direct link between LiSTOT and either the developed GUI or V-HAB itself. This should allow a user of LiSTOT to directly model the defined ECLSS from LiSTOT in V-HAB without requiring manual work in between. Especially the sizing of the different subsystems from LiSTOT could improve the usability of V-HAB for different ECLSS analyses, by providing a better initial estimation of the required system sizes.

Another area that may be considered in the future are further improvements regarding simulation speed. This was already enhanced compared to the state at the beginning of this thesis. A simulation of the ISS with much simpler subsystem models was slower than real time in (Pütz et al. 2016). Now even a large-scale analysis with the detailed human model and a large number of plants etc. is faster than real time. However, compared to the previous simulation speed of V-HAB 1, which required 14 days to simulate a 600 day Mars mission (Czupalla 2011: 333), the current simulations are slow. Of course, this is in part a trade-off and the price to pay for the detailed subsystem models. Therefore, it may not be feasible to further improve the calculation speed without decreasing the level of detail for the subsystems. However, one potential approach could be to store previously calculated conditions. For example, the conditions in an ECLSS are often repetitive on a small scale with small changes over a longer duration, e.g. in the cabin temperature and humidity levels. If the CHX remembers the resulting heat flows and condensate flows for conditions it encountered previously, it could simply reuse these values without requiring the 2D iterative calculation to be executed. The various parameters influencing the CHX behavior are a challenge for such an approach. For example, not only the temperatures and humidity levels are relevant, the flowrates within the CHX, the pressure and composition of the gas stream as well as various other parameters influence the system behavior as well.



8 References

- Abdin, Z., Webb, C. J., and Gray, E. (2015), 'Modelling and simulation of a proton exchange membrane (PEM) electrolyser cell', *International Journal of Hydrogen Energy*, 40/39: 13243–13257.
- Abney, M. B., Schneider, W., Brown, B. et al. (2020), 'Comparison of Exploration Oxygen Recovery Technology Options Using ESM and LSMAC', in , *50th International Conference on Environmental Systems 2020* <<https://hdl.handle.net/2346/86428>>, accessed 13 Nov 2020.
- Agren, G. I., and Franklin, O. (2003), 'Root. Shoot ratios, optimization and nitrogen productivity', *Annals of botany*, 92/6: 795–800.
- Aleman, L., Peiro, E., Arnau, C. et al. (2019), 'Continuous controlled long-term operation and modeling of a closed loop connecting an air-lift photobioreactor and an animal compartment for the development of a life support system', *Biochemical Engineering Journal*, 151: 107323.
- Alexander Schmid (2018), 'Development of a Dynamic Condensing Heat Exchanger Simulation Model for Virtual Habitat', Term Paper (Munich, Technical University of Munich).
- Allen, R., Peirera, L. S., Raes, D. et al. (2015), *Crop evapotranspiration. FAO irrigation and drainage paper no. 56*, FAO, Rome.
- Allen, R. G., Pereira, L. S., Raes, D. et al. (1998), 'FAO Irrigation and drainage paper No. 56', *Rome: Food and Agriculture Organization of the United Nations*, 56/97: e156.
- Amitrano, C., Chirico, G. B., Pascale, S. D. et al. (2019), 'Application of a MEC model for the irrigation control in green and red-leaved lettuce in precision indoor cultivation', in , *2019 IEEE International Workshop on Metrology for Agriculture and Forestry (MetroAgriFor)* (IEEE), 196–201 <<https://ieeexplore.ieee.org/stamp/stamp.jsp?tp=&arnumber=8909235>>, accessed 18 Nov 2020.
- Anderson, M. S., Barta, D. J., Douglas, G. et al. (2017a), 'Key Gaps for Enabling Plant Growth in Future Missions', in , *Annual AIAA Space and Astronautics Forum an Exposition 2017* <<https://ntrs.nasa.gov/search.jsp?R=20170009945>>, accessed 9 Feb 2018.
- Anderson, M. S., Broyan, J., Macatangay, A. et al. (2017b), 'NASA Environmental Control and Life Support Technology Development and Maturation for Exploration: 2016 to 2017 Overview', in , *47th International Conference on Environmental Systems*.
- Anderson, M. S., Ewert, M. K., and Keener, J. F. (2018), *Life Support Baseline Values and Assumptions Document*, NASA/TP-2015-218570/REV1.
- Anthony, S. M., and Hintze, P. E. (2014), 'Trash-to-Gas: Determining the ideal technology for converting space trash into useful products', in , *44th International Conference on Environmental Systems*.
- Appelbaum, J., and Flood, D. J. (1990), 'Solar radiation on Mars', *Solar Energy*, 45/6: 353–363.
- Awasthi, A., Scott, K., and Basu, S. (2011), 'Dynamic modeling and simulation of a proton exchange membrane electrolyzer for hydrogen production', *International Journal of Hydrogen Energy*, 36/22: 14779–14786.
- Babcock, P. S., Auslander, D. M., and Spear, R. C. (1984), 'Dynamic considerations for control of closed life support systems', *Advances in Space Research*, 4/12: 263–270.
- Bagdigian, R. M., Dake, J., Gentry, G. et al. (2015), 'International Space Station Environmental Control and Life Support System Mass and Crewtime Utilization In Comparison to a Long Duration Human Space Exploration Mission', in , *45th International Conference on Environmental Systems*.
- Barbir, F., Molter, T., and Dalton, L. (2005), 'Efficiency and weight trade-off analysis of regenerative fuel cells as energy storage for aerospace applications', *International Journal of Hydrogen Energy*, 30/4: 351–357.
- Béchet, Q., Shilton, A., and Guieysse, B. (2013), 'Modeling the effects of light and temperature on algae growth: State of the art and critical assessment for productivity prediction during outdoor cultivation', *Biotechnology Advances*, 31/8: 1648–1663 <<http://www.sciencedirect.com/science/article/pii/S0734975013001481>>.
- Belz, S., Buchert, M., Bretschneider, J. et al. (2014), 'Physicochemical and biological technologies for future exploration missions', *Acta Astronautica*, 101: 170–179.
- Berg, J. M., Tymoczko, J. L., Stryer, L. et al. (2013), *Biochemie* (7. Auflage, Berlin: Springer Spektrum) <<http://dx.doi.org/10.1007/978-3-8274-2989-6>>.

- Binnewies, M., Finze, M., Jäckel, M. et al. (2016), *Allgemeine und Anorganische Chemie* (3., vollständig überarbeitete Auflage, Berlin: Springer Spektrum) <<http://dx.doi.org/10.1007/978-3-662-45067-3>>.
- Bitog, J. P., Lee, I.-B., Lee, C.-G. et al. (2011), ‘Application of computational fluid dynamics for modeling and designing photobioreactors for microalgae production: A review’, *Computers and Electronics in Agriculture*, 76/2: 131–147.
- Blank, T. (2019a), ‘Automatisierung und Funktionsüberprüfung der V-Hab Pflanzenkammer’, Term Paper (Munich, Technical University of Munich).
- (2019b), ‘Verifikation des V-HAB Pflanzenmodells mit experimentellen Daten’, Master Thesis (Munich, Technical University of Munich).
- Bockstahler, K., Hartwich, R., Matthias, C. et al. (2017), ‘Status of the Advanced Closed Loop System ACLS for Accommodation on the ISS’, in , *47th International Conference on Environmental Systems*.
- Bockstahler, K., Matthias, C., and Lucas, J. (2015), ‘Development Status of the Advanced Closed Loop System ACLS’, in , *45th International Conference on Environmental Systems*.
- Bornemann, G., Waßer, K., and Hauslage, J. (2018), ‘The influence of nitrogen concentration and precipitation on fertilizer production from urine using a trickling filter’, *Life Sciences in Space Research*, 18: 12–20.
- Bornemann, G., Waßer, K., Tonat, T. et al. (2015), ‘Natural microbial populations in a water-based biowaste management system for space life support’, *Life Sciences in Space Research*, 7: 39–52 <<http://www.sciencedirect.com/science/article/pii/S2214552415000802>>.
- Bosch, C. (2018), ‘Entwicklung einer hydroponischen Pflanzenwachstumschamber zur Verifikation des V-HAB Pflanzenmodells’, Masterarbeit (München, Technische Universität München).
- Boscheri, G., Kacira, M., Patterson, L. et al. (2012), ‘Modified energy cascade model adapted for a multicrop Lunar greenhouse prototype’, *Advances in Space Research*, 50/7: 941–951.
- Boscheri, G., Volponi, M., Lamantea, M. et al. (2017), ‘Main performance results of the EDEN ISS Rack-Like Plant Growth Facility’, in , *47th International Conference on Environmental Systems*.
- Burgner, S. E., Mitchell, C., Massa, G. et al. (2019), ‘Troubleshooting Performance Failures of Chinese Cabbage for Veggie on the ISS’, in , *49th International Conference on Environmental Systems* (Boston) <<https://hdl.handle.net/2346/84553>>, accessed 16 Nov 2020.
- Burns, R. A., and Ignatonis, A. J. (1974), ‘Spacelab Phase B study environmental control system component handbook’, 1974.
- Busch, T. (2019), ‘Accuracy verification of V-HAB solver by the help of Ansys CFX’, Term Paper (Munich, Technical University of Munich).
- Button, A. B., and Sweterlitsch, J. (2013), ‘Reduced Pressure Cabin Testing of the Orion Atmosphere Revitalization Technology’, in , *43rd International Conference on Environmental Systems*, 3491 <<https://ntrs.nasa.gov/archive/nasa/casi.ntrs.nasa.gov/20130011191.pdf>>, accessed 9 Feb 2018.
- Carter, D., Brown, C., Bazley, J. et al. (2017a), ‘Status of ISS Water Management and Recovery’, in , *47th International Conference on Environmental Systems* <<http://hdl.handle.net/2346/72880>>, accessed 26 Jun 2020.
- Carter, D., and Gleich, A. (2016), ‘Selection of a Brine Processor Technology for NASA Manned Missions’, in , *46th International Conference on Environmental Systems*.
- Carter, D., Schaezler, R., Bankers, L. et al. (2016), ‘Status of ISS Water Management and Recovery’, in , *46th International Conference on Environmental Systems* <<http://hdl.handle.net/2346/67461>>, accessed 15 Jun 2021.
- Carter, D. L. (2009), ‘Status of the Regenerative ECLSS Water Recovery System’, in , *SAE Technical Paper Series* (SAE Technical Paper Series: SAE International400 Commonwealth Drive, Warrendale, PA, United States).
- Carter, D. L., Williamson, J., Brown, C. A. et al. (2019), ‘Status of ISS Water Management and Recovery’, in , *49th International Conference on Environmental Systems* <<https://hdl.handle.net/2346/84720>>.
- Carter, L., Tabb, D., Tatara, J. D. et al. (2005), ‘Performance Qualification Test of the ISS Water Processor Assembly (WPA) Expendables’, in , *SAE Technical Paper Series* (SAE Technical Paper Series: SAE International400 Commonwealth Drive, Warrendale, PA, United States).
- Carter, L., Takada, K., Brown, C. et al. (2017b), ‘Status of ISS Water Management and Recovery’, in , *47th International Conference on Environmental Systems*.
- Cavazzoni, J. (2004), ‘Using explanatory crop models to develop simple tools for Advanced Life Support system studies’, *Advances in Space Research*, 34/7: 1528–1538.



- Chambliss, J., Stambaugh, I., and Moore, M. (2016), 'Resource Tracking Model Updates and Trade Studies', in , *46th International Conference on Environmental Systems* <<http://hdl.handle.net/2346/67731>>, accessed 17 Nov 2020.
- Chambliss, J., Stambaugh, I., Sargusingh, M. et al. (2015), 'Development of a Water Recovery System Resource Tracking Model', in , *45th International Conference on Environmental Systems*.
- Christenson, D., Sevanthi, R., Morse, A. et al. (2020), 'Assessment of Membrane-Aerated Biological Reactors (MABRs) for Integration into Space-Based Water Recycling System Architectures', *Gravitational and Space Research*, 6/2: 12–27.
- Coker, R., and Knox, J. (2016a), 'Predictive Modeling of the CDRA 4BMS', in , *46th International Conference on Environmental Systems* <<http://hdl.handle.net/2346/67523>>, accessed 13 Nov 2020.
- Coker, R., Knox, J., Cummings, R. et al. (2013), 'Additional Developments in Atmosphere Revitalization Modeling and Simulation', in , *43rd International Conference on Environmental Systems* (Reston, Virginia: American Institute of Aeronautics and Astronautics).
- Coker, R. F., and Knox, J. (2016b), 'Predictive Modeling of the CDRA Four Bed Molecular Sieve', in , *46th International Conference on Environmental Systems*.
- Coker, R. F., Knox, J., Schunk, G. et al. (2015), 'Computer Simulation and Modeling of CO₂ Removal Systems for Exploration', in , *45th International Conference on Environmental Systems*.
- Coker, R. F., Knox, J. C., Gauto, H. et al. (2014), 'Full System Modeling and Validation of the Carbon Dioxide Removal Assembly', in , *44th International Conference on Environmental Systems*.
- Constantin, J., Le Bas, C., and Justes, E. (2015), 'Large-scale assessment of optimal emergence and destruction dates for cover crops to reduce nitrate leaching in temperate conditions using the STICS soil–crop model', *European Journal of Agronomy*, 69: 75–87 <<http://www.sciencedirect.com/science/article/pii/S1161030115000726>>.
- Crusan, J., and Gatens, R. (2017), *Cislunar Habitation & Environmental Control & Life Support Systems* <https://www.nasa.gov/sites/default/files/atoms/files/20170329-nacheoc-crusan-gatens-hab-eclss-v5b_tagged.pdf>, accessed 13 Nov 2021.
- Czupalla, M. (2011), 'Integral Modeling and Dynamic Simulation of Life Support Systems', Dissertation (Munich, Technical University of Munich).
- Czupalla, M., Hager, P., Hein, A. et al. (2009), 'Model Confidence Level - A Systematic Metric for Development of a Virtual Space Habitat', in , *SAE Technical Paper Series* (SAE Technical Paper Series: SAE International400 Commonwealth Drive, Warrendale, PA, United States).
- Darnell, A., Azad, A., Borlaug, B. et al. (2015), 'MarsOASIS. A predeployable miniature Martian greenhouse for crop production research', in , *45th International Conference on Environmental Systems*.
- Deng, S., Xie, B., and Liu, H. (2016), 'The recycle of water and nitrogen from urine in bioregenerative life support system', *Acta Astronautica*, 123: 86–90.
- Detrell, G., and Belz, S. (2017), 'ELISSA – a comprehensive software package for ECLSS technology selection, modelling and simulation for human spaceflight missions', in , *47th International Conference on Environmental Systems*.
- Detrell, G., and Ewald, R. (2019), 'LSS design tool for the Space Station Design Workshop at the Institute of Space Systems-University of Stuttgart', in , *49th International Conference on Environmental Systems* (Boston) <<https://hdl.handle.net/2346/84420>>, accessed 17 Nov 2020.
- Detrell, G., Helisch, H., Keppler, J. et al. (2020), 'PBR@LSR: the Algae-based Photobioreactor Experiment at the ISS – Operations and Results', ICES-2020-25, in , *50th International Conference on Environmental Systems 2020* <<https://hdl.handle.net/2346/86331>>, accessed 29 Sep 2020.
- DIN ISO 16290 (2016), *DIN ISO 16290:2016-09, Raumfahrtsysteme_- Definition des Technologie-Reifegrades_(TRL) und der Beurteilungskriterien (ISO_16290:2013)* (Berlin: Beuth Verlag GmbH), updated 09.2016.
- Do, S., Owens, A., and Weck, O. d. (2015), 'HabNet-An Integrated Habitation and Supportability Architecting and Analysis Environment', in , *45th International Conference on Environmental Systems*.
- Dong, C., Fu, Y., Xie, B. et al. (2017), 'Element Cycling and Energy Flux Responses in Ecosystem Simulations Conducted at the Chinese Lunar Palace-1', *Astrobiology*, 17/1: 78–86.
- Duffield, B. E. (2001), 'Advanced life support (ALS) technologies list version 4', *Lockheed Martin Space Mission Systems & Services*, 2001.

- EcoSimPro (2018), *Fact Sheet* <https://www.ecosimpro.com/wp-content/uploads/2018/10/ecosimpro_proosis_platform_fact_sheet.pdf>, accessed 18 Nov 2020.
- Ehrlich, J. W., Massa, G. D., Wheeler, R. M. et al. (2017), ‘Plant Growth Optimization by Vegetable Production System in HI-SEAS Analog Habitat’, 2017.
- Elitzur, S., Rosenband, V., and Gany, A. (2016), ‘Combined energy production and waste management in manned spacecraft utilizing on-demand hydrogen production and fuel cells’, *Acta Astronautica*, 128: 580–583.
- Eshima, S. P., Nabity, J., and Moroshima, R. (2020), ‘Analysis of Fault Propagation of Environmental Control and Life Support System for Self-Awareness’, in , *ASCEND 2020* (Reston, Virginia: American Institute of Aeronautics and Astronautics).
- Eshima, S. P., and Nabity, J. A. (2020), ‘Failure Mode and Effects Analysis for Environmental Control and Life Support System Self-Awareness’, in , *50th International Conference on Environmental Systems 2020* <<https://ttu-ir.tdl.org/bitstream/handle/2346/86311/ICES-2020-488.pdf?sequence=1>>, accessed 29 Sep 2020.
- Ewert, M. K., and Broyan, J. L. (2013), ‘Mission Benefits Analysis of Logistics Reduction Technologies’, in , *43rd International Conference on Environmental Systems*, 3383.
- Fabian Lübbert (2018), ‘Modelling and Validation of the ISS Common Cabin Air Assembly in V-HAB’, Master Thesis (Munich, Technical University of Munich).
- Falcão, D. S., and Pinto, A. (2020), ‘A review on PEM electrolyzer modelling: Guidelines for beginners’, *Journal of Cleaner Production*, 261: 121184.
- Feigel, A. (2019), ‘Advancement of a Trade-off Tool for Life Support Technologies and its Application in Proposing a Life Support Architecture for the Gateway’, Master Thesis (Munich, Technical University of Munich).
- Fu, Y., Guo, R., and Liu, H. (2019), ‘An optimized 4-day diet meal plan for 'Lunar Palace 1'', *Journal of the science of food and agriculture*, 99/2: 696–702.
- Fu, Y., Li, L., Xie, B. et al. (2016), ‘How to Establish a Bioregenerative Life Support System for Long-Term Crewed Missions to the Moon or Mars’, *Astrobiology*, 16/12: 925–936.
- Fu, Y., Yi, Z., Du, Y. et al. (2021), *Establishment of a closed artificial ecosystem to ensure human long-term survival on the moon* (41).
- Furfaro, R., Gellenbeck, S., Giacomelli, G. et al. (2017), ‘Mars-Lunar Greenhouse (MLGH) Prototype for Bioregenerative Life Support Systems: Current Status and Future Efforts’, in , *47th International Conference on Environmental Systems*.
- Gesellschaft Verfahrenstechnik und Chemieingenieurwesen (2013), *VDI-Wärmeatlas: Mit 320 Tabellen* (VDI-Buch; 11., bearb. und erw. Aufl., Berlin: Springer Vieweg) <<http://dx.doi.org/10.1007/978-3-642-19981-3>>.
- Godin, C., and Sinoquet, H. (2005), ‘Functional-structural plant modelling’, *The New phytologist*, 166/3: 705–708.
- Goudarzi, S., and Ting, K. C. (1999), *Top level modeling of crew component of ALSS*.
- Greenception (2021), ‘GC 16 plus’ <<https://greenception.com/de/produkt/gc-16-plus/>>, accessed 16 Mar 2021.
- Greenwood, Z. W., Abney, M. B., Brown, B. R. et al. (2018), ‘State of NASA Oxygen Recovery’, in , *48th International Conference on Environmental Systems* <<http://hdl.handle.net/2346/74060>>, accessed 13 Nov 2020.
- Guo, B., Holder, D. W., and Tester, J. T. (2005), ‘Two-Phase Oxidizing Flow in a Volatile Removal Assembly Reactor under Microgravity Conditions’, *AIAA Journal*, 43/12: 2586–2592.
- Häder, D.-P. (2019), ‘On the Way to Mars-Flagellated Algae in Bioregenerative Life Support Systems Under Microgravity Conditions’, *Frontiers in plant science*, 10: 1621.
- Han, B., Mo, J., Kang, Z. et al. (2016), ‘Effects of membrane electrode assembly properties on two-phase transport and performance in proton exchange membrane electrolyzer cells’, *Electrochimica Acta*, 188/3: 317–326.
- Hanford, A. J. (2004), *Advanced Life Support Baseline Values and Assumptions Document*, NASA/CR—2004—208941 <<https://core.ac.uk/download/pdf/4947189.pdf>>, accessed 28 Mar 2021.
- Hansen, S., Wright, S., Wallace, S. et al. (2017), ‘Laser Processed Condensing Heat Exchanger Technology Development’, in , *47th International Conference on Environmental Systems*.
- Harper, L. D., Neal, C. R., Poynter, J. et al. (2016), ‘Life Support for a Low-Cost Lunar Settlement. No Showstoppers’, *New Space*, 4/1: 40–49.
- Hauslage, J., Bornemann, G., Winzer, F. et al. (2014), *C.R.O.P. - Combined Regenerative Organic food Production: Using trickling filters for wet composting of organic waste in hydroponic greenhouse cultures* <https://elib.dlr.de/94910/1/Pres_ASC_2014_Hauslage_s7.pdf>, accessed 27 Nov 2020.
- HC Simulation, L. L. (2020), ‘HumMod’ <<http://hummod.org/>>, updated 14 Aug 2020.



- Heinrich, B., and Schneider, W. (2019), *Grundlagen Regelungstechnik* (Wiesbaden: Springer Fachmedien Wiesbaden).
- Helisch, H., Keppler, J., Detrell, G. et al. (2020), 'High density long-term cultivation of *Chlorella vulgaris* SAG 211-12 in a novel microgravity-capable membrane raceway photobioreactor for future bioregenerative life support in SPACE', *Life Sciences in Space Research*, 24: 91–107.
- HEM-SAG, M. (2008), 'Planning for the Scientific Exploration of Mars by Humans', *Unpublished white paper, TBD p, posted March, 2008* <https://mepag.jpl.nasa.gov/reports/HEM-SAG_final_draft_4_v2-2.doc>, accessed 14 Jun 2021.
- Hester, R., Brown, A., Husband, L. et al. (2011), 'HumMod. A Modeling Environment for the Simulation of Integrative Human Physiology', *Frontiers in Physiology*, 2: 12 <<https://www.frontiersin.org/article/10.3389/fphys.2011.00012>>.
- Hester, R. L., Pruett, W., Clemmer, J. et al. (2019), 'Simulation of integrative physiology for medical education', *Morphologie*, 103/343: 187–193 <<http://www.sciencedirect.com/science/article/pii/S1286011519300554>>.
- Hezard, P. (2012), 'Higher plant growth modelling for life support systems. Global model design and simulation of mass and energy transfers at the plant level', Theses (Université Blaise Pascal - Clermont-Ferrand II).
- Hofmann, E. (1979), *Funktionelle Biochemie des Menschen: Band 1 und Band 2* (Reihe Wissenschaft, Wiesbaden, s.l.: Vieweg+Teubner Verlag) <<http://dx.doi.org/10.1007/978-3-322-90099-9>>.
- Hokanson, D. R. (2004), 'DEVELOPMENT OF ION EXCHANGE MODELS FOR WATER TREATMENT AND APPLICATION TO THE INTERNATIONAL SPACE STATION WATER PROCESSOR', Dissertation (Michigan Technological University).
- Honari, G., and Maibach, H. (2014), 'Skin Structure and Function', in , *Applied Dermatotoxicology* (Elsevier), 1–10.
- Horiike, K., Miura, R., Ishida, T. et al. (1996), 'Stoichiometry of the water molecules in glucose oxidation revisited: inorganic phosphate plays a unique role as water in substrate-level phosphorylation', *Biochemical Education*, 24/1: 17–20.
- Horizon (2021), 'Horizon Product Overview' <<https://www.horizon-growlight.com/produkte>>, updated 16 Mar 2021.
- Hou, B., Huang, Y., Wang, X. et al. (2016), 'Optimization and simulation of the Sabatier reaction process in a packed bed', *AIChE J.*, 62/8: 2879–2892.
- Institute of Medicine (1997), *Dietary reference intakes: Calcium, phosphorus, magnesium, vitamin D, and fluoride* (Washington, D.C: National Academy Press) <<http://dx.doi.org/10.17226/5776>>.
- (2005), *Dietary reference intakes for energy, carbohydrate, fiber, fat, fatty acids, cholesterol, protein, and amino acids* (Washington, D.C: National Academy Press) <<http://dx.doi.org/10.17226/10490>>.
- International Space Exploration Coordination Group (2018), 'Global Exploration Roadmap' <https://www.globalspaceexploration.org/wordpress/wp-content/isecg/GER_2018_small_mobile.pdf>, accessed 29 Sep 2020.
- James, J. T., Haddock, C., Duncan, M. et al. (2008), *Spacecraft Maximum Allowable Concentrations for Airborne Contaminants*, JSC-20584 <<https://standards.nasa.gov/standard/jsc/jsc-20584>>, accessed 30 Jun 2021.
- Jeong, K., Kessen, M. J., Bilirgen, H. et al. (2010), 'Analytical modeling of water condensation in condensing heat exchanger', *International Journal of Heat and Mass Transfer*, 53/11-12: 2361–2368.
- Jones, H. (2003), 'Dynamic Modeling of ALS Systems', in Society of Automotive Engineers (ed.), *33th International Conference on Environmental Systems*.
- (2009), 'Planning Dynamic Simulation of Space Life Support', in , *International Conference On Environmental Systems* (SAE Technical Paper Series: SAE International 400 Commonwealth Drive, Warrendale, PA, United States).
- (2017), 'Would Current International Space Station (ISS) Recycling Life Support Systems Save Mass on a Mars Transit?', in , *International Conference on Environmental Systems* <<http://hdl.handle.net/2346/72911>>, accessed 19 Jan 2021.
- Jones, H. W. (2018), 'Impact of Lower Launch Cost on Space Life Support', in , *2018 AIAA SPACE and Astronautics Forum and Exposition* (Reston, Virginia: American Institute of Aeronautics and Astronautics), 1969.
- Junaedi, C., Hawley, K., Walsh, D. et al. (2014), 'Co2 reduction assembly prototype using microlith-based sabatier reactor for ground demonstration', in , *44th International Conference on Environmental Systems*.
- Kang, M. Z., Cournède, P. H., Reffye, P. de et al. (2008), 'Analytical study of a stochastic plant growth model: Application to the GreenLab model', *Mathematics and Computers in Simulation*, 78/1: 57–75.

- Kaschubek, D. (2021), ‘Optimized Crop Growth Area Composition for Long Duration Spaceflight’, *Life Sciences in Space Research*, 2021.
- Kaschubek, D., Killian, M., and Grill, L. (2021), ‘System analysis of a Moon base at the south pole: Considering landing sites, ECLSS and ISRU’, *Acta Astronautica*, 180: 104750.
- Keith Sharp, M., Batzel, J. J., and Montani, J.-P. (2013), ‘Space physiology IV: mathematical modeling of the cardiovascular system in space exploration’, *European journal of applied physiology*, 113/8: 1919–1937.
- Kelsey, L., Pasadilla, P., and Cognata, T. (2018), ‘Closing the Water Loop for Exploration: 2018 Status of the Brine Processor Assembly’, in , *48th International Conference on Environmental Systems* <<http://hdl.handle.net/2346/74218>>.
- Kim, J.-S., Lee, D.-C., Lee, J.-J. et al. (2020), ‘Optimization for maximum specific energy density of a lithium-ion battery using progressive quadratic response surface method and design of experiments’, *Scientific reports*, 10/1: 15586.
- Kniemeyer, O. (2008), ‘Design and Implementation of a Graph Grammar Based Language for Functional-Structural Plant Modelling’ (Cottbus, Germany, Brandenburgische Technische Universität Cottbus).
- Knox, J. C. (2000), ‘International Space Station Carbon Dioxide Removal Assembly Testing’, in (SAE Technical Paper Series: SAE International400 Commonwealth Drive, Warrendale, PA, United States).
- Knox, J. C., Campbell, M., Murdoch, K. et al. (2005), ‘Integrated Test and Evaluation of a 4-Bed Molecular Sieve (4BMS) Carbon Dioxide Removal System (CDRA), Mechanical Compressor Engineering Development Unit (EDU), and Sabatier Engineering Development Unit (EDU)’, in , *SAE Technical Paper Series* (SAE Technical Paper Series: SAE International400 Commonwealth Drive, Warrendale, PA, United States).
- Kortenkamp, D., and Bell, S. (2003), ‘BioSim. An integrated simulation of an advanced life support system for intelligent control research’, in , *Proc. of the 7th Intl. Symposium on Artificial Intelligence, Robotics and Automation in Space*.
- Kovalev, V. S., Manukovsky, N. S., Tikhomirov, A. A. et al. (2015), ‘Modeling snail breeding in a bioregenerative life support system’, *Life Sciences in Space Research*, 6: 44–50.
- Kurzweil, P. (2013), *Brennstoffzellentechnik* (Wiesbaden: Springer Fachmedien Wiesbaden).
- Kusuma, P., Pattison, P. M., and Bugbee, B. (2020), ‘From physics to fixtures to food: current and potential LED efficacy’, *Horticulture research*, 7: 56.
- Lackner, D., Schwar, J., Dimroth, F. et al. (2019), ‘Radiation hard four-junction space solar cell based on GaInAsP alloys’, in , *2019 European Space Power Conference (ESPC)* (IEEE), 1–3.
- Levri, J. A., Drysdale, A. E., Ewert, M. K. et al. (2003), *Advanced life support equivalent system mass guidelines document*, NASA/TM-2003-212278 (California) <<https://ntrs.nasa.gov/api/citations/20040021355/downloads/20040021355.pdf>>, accessed 11 Mar 2021.
- Li, S., Lucey, P. G., Milliken, R. E. et al. (2018a), ‘Direct evidence of surface exposed water ice in the lunar polar regions’, *Proceedings of the National Academy of Sciences of the United States of America*, 115/36: 8907–8912.
- Li, T., Zhang, L., Ai, W. et al. (2018b), ‘A modified MBR system with post advanced purification for domestic water supply system in 180-day CELSS. Construction, pollutant removal and water allocation’, *Journal of environmental management*, 222: 37–43.
- Li, W., Calle, L., Hanford, A. et al. (2018c), ‘Investigation of Silver Biocide as a Disinfection Tehcnology for Spacecraft-An Early Literature Review’, in , *48th International Conference on Environmental Systems* <<http://hdl.handle.net/2346/74083>>, accessed 15 Jun 2021.
- Linstrom, P. (1997), *NIST Chemistry WebBook, NIST Standard Reference Database 69*.
- Liskowsky, D. R., and Seitz, W. W. (2014), *Human Intergration Design Handbook*, NASA/SP-2010-3407/REV1 (Washington DC) <https://www.nasa.gov/sites/default/files/atoms/files/human_integration_design_handbook_revision_1.pdf>, accessed 12 Feb 2019.
- Lodish, H. (op. 2016), *Molecular Cell Biology* (8th ed., New York: W. H. Freeman and Co).
- Losa, J. P., Santos, F. M., Alvim-Ferraz, M. C. et al. (2020), ‘Dynamic Modeling of Microalgal Growth’, in S.-K. Kim (ed.), *Encyclopedia of marine biotechnology* (Hoboken: Wiley-Blackwell), 547–67.
- Malone, R. W., Kersebaum, K. C., Kaspar, T. C. et al. (2017), ‘Winter rye as a cover crop reduces nitrate loss to subsurface drainage as simulated by HERMES’, *Agricultural Water Management*, 184: 156–169.
- Mars Architecture Steering Group (2009), *Human Exploration of Mars Design Reference Architecture 5.0*, NASA-SP-2009-566 <https://www.nasa.gov/pdf/373665main_NASA-SP-2009-566.pdf>, accessed 30 Nov 2020.



- Martin, K., Sathyamoorthy, S., Houweling, D. et al. (2017), 'A sensitivity analysis of model parameters influencing the biofilm nitrification rate: Comparison between the aerated biofilm reactor (MABR) and Integrated fixed film activated sludge (IFAS) process', *Proceedings of the Water Environment Federation*, 2017/16: 257–265.
- Massa, G. D., Wheeler, R. M., Morrow, R. C. et al. (2016) (eds.), *Growth chambers on the International Space Station for large plants* (International Society for Horticultural Science (ISHS), Leuven, Belgium).
- Masuda, T., Arai, R., Komatsubara, O. et al. (2005), 'Development of a 1-week cycle menu for an Advanced Life Support System (ALSS) utilizing practical biomass production data from the Closed Ecology Experiment Facilities (CEEFF)', *Habitation (Elmsford, N.Y.)*, 10/2: 87–97.
- MathWorks® (2021), 'linprog Documentation' <<https://de.mathworks.com/help/optim/ug/linprog.html>>, accessed 30 Mar 2021.
- Matthias Pfeiffer (2007), 'Design of a human metabolic model for integrated ECLSS robustness analysis', Diplomarbeit (Munich, Technical University of Munich).
- McArdle, W. D. (2015), *Exercise physiology: Nutrition, energy and human performance* (8. ed., internat. ed., Baltimore, Md.[u.a.]: Wolters Kluwer).
- McKellar, M., Stoots, C., Sohal, M. et al. (2010), 'The Concept and Analytical Investigation of CO₂ and Steam Co-Electrolysis for Resource Utilization in Space Exploration', in , *40th International Conference on Environmental Systems* (Reston, Virginia: American Institute of Aeronautics and Astronautics).
- MELiSSA Foundation PS (2021), 'MELiSSA FAQ' <<https://www.melissafoundation.org/page/faq>>, accessed 23 Jun 2021.
- Mohamed, B., Alli, B., and Ahmed, B. (2016), 'Using the hydrogen for sustainable energy storage: Designs, modeling, identification and simulation membrane behavior in PEM system electrolyser', *Journal of Energy Storage*, 7: 270–285.
- Monje, O., Richards, J. T., Carver, J. A. et al. (2020), 'Hardware Validation of the Advanced Plant Habitat on ISS: Canopy Photosynthesis in Reduced Gravity', *Frontiers in plant science*, 11: 673.
- Moradi Nafchi, F., Afshari, E., Baniasadi, E. et al. (2019), 'A parametric study of polymer membrane electrolyser performance, energy and exergy analyses', *International Journal of Hydrogen Energy*, 44/34: 18662–18670.
- Moriyama, E., Moroshima, R., Ohura, S. et al. (2015), 'New ECLSS Simulation Software and Its Demonstration by Manned Mars Missions', in , *45th International Conference on Environmental Systems*.
- Mühlhaus, M. (2017), 'Dynamic modeling of the Water Processor Assembly of the International Space Station', Bachelor Thesis (Technische Universität München).
- Niederwieser, T., and Klaus, D. (2018), 'Feasibility Study of an Algal-Based Life Support System', in , *69th International Astronautical Congress*.
- Nikic, A. (2017), 'Modelling Nutrient Dependency of Plants in Life Support Systems in the Virtual Habitat', Master Thesis (Munich, Technical University of Munich).
- Olthoff, C. (2017), 'Dynamic Simulation of Extravehicular Activities', Dissertation (Verlag Dr. Hut).
- Ordóñez, L., Lasseur, C., Poughon, L. et al. (2004), *MELiSSA higher plants compartment modeling using ecosimpro*.
- Oria, M., Harrison, M., and Stallings, V. A. (2019) (eds.), *Dietary Reference Intakes for Sodium and Potassium* (Washington (DC)).
- Perry, J. L. (2017), *Trace Contaminant Control for the International Space Station's Node 1 - Analysis, Design, and Verification*, No. 20170005170 <<https://ntrs.nasa.gov/api/citations/20170005170/downloads/20170005170.pdf>>, accessed 16 Nov 2020.
- Pickett, M. T., Roberson, L. B., Calabria, J. L. et al. (2020), 'Regenerative water purification for space applications: Needs, challenges, and technologies towards 'closing the loop'', *Life Sciences in Space Research*, 24: 64–82.
- Pires, J. C., Alvim-Ferraz, M. C., and Martins, F. G. (2017), 'Photobioreactor design for microalgae production through computational fluid dynamics: A review', *Renewable and Sustainable Energy Reviews*, 79: 248–254.
- Planetary Science Communications Team (2021), 'Mars - The Red Planet' <<https://solarsystem.nasa.gov/planets/mars/in-depth/>>, updated 14 Jun 2021.
- Polifke, W., and Kopitz, J. (2009), *Wärmeübertragung: Grundlagen, analytische und numerische Methoden* (Always learning; 2. aktual. Aufl., München u.a: Pearson Studium) <<http://lib.mylibrary.com/detail.asp?id=505990>>.
- Portner, B. (2013), 'Numerical Modeling of a Fixed Bed Adsorber Numerical Modeling of a Fixed Bed Adsorber for Carbon Dioxide Removal in Human Space Flight', Bachelor Thesis (Munich, Technical University of Munich).

- Poughon, L., Laroche, C., Creuly, C. et al. (2020), 'Limnospira indica PCC8005 growth in photobioreactor: model and simulation of the ISS and ground experiments', *Life Sciences in Space Research*, 25: 53–65 <<http://www.sciencedirect.com/science/article/pii/S2214552420300158>>.
- Poulet, L. (2018), 'Developing physical models to understand the growth of plants in reduced gravity environments for applications in life-support systems', Theses (Université Clermont Auvergne).
- Poulet, L., Dussap, C.-G., and Fontaine, J.-P. (2020), 'Development of a mechanistic model of leaf surface gas exchange coupling mass and energy balances for life-support systems applications', *Acta Astronautica*, 175: 517–530.
- Pradal, C., Boudon, F., Nouguier, C. et al. (2009), 'PlantGL. A Python-based geometric library for 3D plant modelling at different scales', *Graphical Models*, 71/1: 1–21.
- Pruitt, J. M., Carter, L., Bagdigian, R. M. et al. (2015), 'Upgrades to the ISS Water Recovery System', in , *45th International Conference on Environmental Systems*.
- Pütz, D. (2017), 'Analysis of the Impacts the Humidity released by ACLS has on other Systems and Crew Time using V-HAB', in , *47th International Conference on Environmental Systems*.
- Pütz, D., Olthoff, C., Ewert, M. K. et al. (2016), 'Assessment of the Impacts of ACLS on the ISS Life Support System using Dynamic Simulations in V-HAB', in , *46th International Conference on Environmental Systems* <<http://hdl.handle.net/2346/67574>>.
- Pütz, D., Olthoff, C., Schnaitmann, J. et al. (2019), 'Development Status of the Virtual Habitat (V-HAB) Simulation System', in , *49th International Conference on Environmental Systems (Boston)* <<https://hdl.handle.net/2346/84930>>.
- Pütz, D., Traub, C., Ewert, M. et al. (2018), 'Impacts of 'Pick-and-Eat' Plant Growth Systems on the ISS and Gateway', in , *48th International Conference on Environmental Systems* <<https://ttu-ir.tdl.org/handle/2346/74050>>, accessed 29 Apr 2019.
- Ranz, H., Dionne, S., and Garr, J. (2019), 'A Thermally-Regenerated Solid Amine CO₂Removal System Incorporating Water Vapor Recovery and Ullage Air Recovery', in , *49th International Conference on Environmental Systems (Boston)* <<https://hdl.handle.net/2346/84942>>, accessed 10 Nov 2020.
- Rines, M. R., Balchanos, M. G., and Mavris, D. N. (2019), 'Dynamic Implementation of Resource Management Strategies for a Resilient Advanced Life Support System', in , *AIAA Scitech 2019 Forum 01.07.2019*, 966.
- Rodríguez, L. F., Bell, S., and Kortenkamp, D. (2006), 'Use of genetic algorithms and transient models for life-support systems analysis', *Journal of spacecraft and rockets*, 43/6: 1395–1403.
- Rodríguez, L. F., Jiang, H., Stark, K. et al. (2007), 'Validation of heuristic techniques for design of life support systems', 2007.
- Rodríguez, R. A., Funke, H., and Witt, J. (2005), 'Simulation Model of the Air Revitalization System for ISS', in , *SAE Technical Paper Series* (SAE Technical Paper Series: SAE International 400 Commonwealth Drive, Warrendale, PA, United States).
- Rohatgi, A. (2020), 'Webplotdigitizer: Version 4.4' <<https://automeris.io/WebPlotDigitizer>>, accessed 12 Apr 2021.
- Roth, C. (2012), 'ISS Active Thermal Control System Dynamic Modeling', Diploma Thesis (Munich, Technical University of Munich).
- Ruck, T. (2018), 'Development of a Dynamic Simulation Model for Performance Prediction of Photobioreactors in Biological Life Support Systems for Human Spaceflight', Masterarbeit (Munich, Technische Universität München).
- Ruck, T., Niederwieser, T., and Pütz, D. (2019), 'Dynamic Simulation of Performance and Mass, Power, and Volume prediction of an Algal Life Support System', in , *49th International Conference on Environmental Systems (Boston)* <<https://ttu-ir.tdl.org/bitstream/handle/2346/84436/ICES-2019-207.pdf?sequence=1&isAllowed=y>>, accessed 3 Dec 2019.
- Rummel, J. D., and Volk, T. (1987), 'A modular BLSS simulation model', *Advances in Space Research*, 7/4: 59–67.
- Ruuskanen, V., Koponen, J., Huoman, K. et al. (2017), 'PEM water electrolyzer model for a power-hardware-in-loop simulator', *International Journal of Hydrogen Energy*, 42/16: 10775–10784.
- Saad, D. (2015), 'Dynamic Modelling and Simulation of a Greenhouse at a South Polar Station', Bachelor Thesis (Munich, Technical University of Munich).
- Salisbury, F. B., Gitelson, J. I., and Lisovsky, G. M. (1997), 'Bios-3. Siberian experiments in bioregenerative life support', *BioScience*, 47/9: 575–585.



- Schaezler, R. N., and Cook, A. J. (2015), 'Report on ISS O₂ Production, Gas Supply & Partial Pressure Management', in , *45th International Conference on Environmental Systems* <<http://hdl.handle.net/2346/64417>>, accessed 13 Nov 2020.
- Schalz, P. (2019), 'Experimentelle Verifikation eines Enzymkinetik Modells für Biologische Rieselfilter', Masterarbeit (Technische Universität München).
- Schreck, B. (2017), 'Feasibility Analysis of a Life Support Architecture for an Interplanetary Transport Ship', Master Thesis (Technische Universität München).
- Scott M. Smith, Sara R. Zwart, and Martina Heer (2014), *HUMAN ADAPTATION TO SPACE FLIGHT: THE ROLE OF NUTRITION*, NP-2014-10-018-JSC (Houston, Texas) <<https://www.nasa.gov/sites/default/files/human-adaptation-to-spaceflight-the-role-of-nutrition.pdf>>, accessed 25 Mar 2021.
- Seedhouse, E. (2020), *Life Support Systems for Humans in Space* (Cham: Springer International Publishing).
- Shaw, L. A., Garr, J. D., Gavin, L. L. et al. (2020), 'International Space Station as a Testbed for Exploration Environmental Control and Life Support Systems-2020 Status', in , *50th International Conference on Environmental Systems 2020*.
- Shull, S. A., and Schneider, W. (2016), 'NASA Advanced Explorations Systems: Advancements in Life Support Systems', in , *AIAA SPACE 2016* (Reston, Virginia: American Institute of Aeronautics and Astronautics).
- Son, C. (2015), *Inter Modular Ventilation THC_post_relocation 2015_v2*.
- Springer, T. E., Zawodzinski, T. A., and Gottesfeld, S. (1991), 'Polymer Electrolyte Fuel Cell Model', *J. Electrochem. Soc.*, 138/8: 2334–2342.
- Stolwijk, J. (1971), *A MATHEMATICAL MODEL OF PHYSIOLOGICAL TEMPERATURE REGULATION IN MAN*, NASA CR-1855 <<https://ntrs.nasa.gov/api/citations/19710023925/downloads/19710023925.pdf>>, accessed 13 Nov 2021.
- Stölzle, A. (2013), 'veCROP - Development of a Dynamic Plant Model for the Use in Biological Life Support Simulations', Diploma Thesis (Munich, Technical University of Munich).
- Stouch Lighting (2021), 'Lighting Comparison: LED vs High Pressure Sodium/Low Pressure Sodium' <<https://www.stouchlighting.com/blog/led-vs-hps-lps-high-and-low-pressure-sodium>>, updated 16 Mar 2021.
- Suermann, M., Schmidt, T. J., and Büchi, F. N. (2016), 'Cell Performance Determining Parameters in High Pressure Water Electrolysis', *Electrochimica Acta*, 211: 989–997.
- Summers, R., Coleman, T., and Meck, J. (2008), 'Development of the Digital Astronaut Project for the analysis of the mechanisms of physiologic adaptation to microgravity: Validation of the cardiovascular system module', *Acta Astronautica*, 63/7: 758–762 <<http://www.sciencedirect.com/science/article/pii/S0094576508000064>>.
- Sun, Y. (2016), 'Dynamic simulation of enzyme kinetic processes in C.R.O.P. system', Master Thesis (Munich, Technical University of Munich).
- Swickrath, M. J., Anderson, M. S., and Bagdigian, R. M. (2011), 'Parametric analysis of life support systems for future space exploration missions', in , *Proceedings of 41th International Conference on Environmental Systems*.
- Takada, K., Velasquez, L. E., van Keuren, S. et al. (2019), 'Advanced Oxygen Generation Assembly for Exploration Missions', in , *49th International Conference on Environmental Systems* (Boston) <<https://hdl.handle.net/2346/84610>>, accessed 13 Nov 2020.
- Tako, Y., Arai, R., Tsuga, S. et al. (2010), 'CEEf: CLOSED ECOLOGY EXPERIMENT FACILITIES', *Gravitational and Space Research*, 2010 <<http://gravitationalandspaceresearch.org/index.php/journal/article/download/489/483>>, accessed 18 Nov 2020.
- Tako, Y., Masuda, T., Tsuga, S. et al. (2017), 'Major achievements of material circulation-closed habitation experiments using Closed Ecology Experiment Facilities', *title 宇宙環境利用シンポジウム 第31回: 平成28年度 Space Utilization Research*, 2017 <https://jaxa.repo.nii.ac.jp/?action=repository_action_common_download&item_id=12847&item_no=1&attribute_id=31&file_no=1>, accessed 18 Nov 2020.
- Tao, R., Bair, R., Pickett, M. et al. (2020), 'Low concentration of zeolite to enhance microalgal growth and ammonium removal efficiency in a membrane photobioreactor', *Environmental Technology*, 2020: 1–14.
- Tertilt, G. (2013), 'Development of a model of a microbiological trickle filter for bioregenerative life support systems', Diploma Thesis (Munich, Technical University of Munich).
- Thomson, S. C., and Blantz, R. C. (2008), 'Glomerulotubular balance, tubuloglomerular feedback, and salt homeostasis', *Journal of the American Society of Nephrology : JASN*, 19/12: 2272–2275.

- Tikhomirov, A. A., Ushakova, S. A., Velichko, V. V. et al. (2011), ‘Assessment of the possibility of establishing material cycling in an experimental model of the bio-technical life support system with plant and human wastes included in mass exchange’, *Acta Astronautica*, 68/9-10: 1548–1554.
- Tikhomirov, A. A., Ushakova, S. A., Velichko, V. V. et al. (2018), ‘A small closed ecosystem with an estimated portion of human metabolism’, *Life Sciences in Space Research*, 19: 63–67.
- Tischner, R. (2000), ‘Nitrate uptake and reduction in higher and lower plants’, *Plant, Cell & Environment*, 23/10: 1005–1024.
- Tobias, B., Garr, J., and Erne, M. (2011), ‘International Space Station Water Balance Operations’, in , *41st International Conference on Environmental Systems* ([Reston, Va.]: [American Institute of Aeronautics and Astronautics]).
- Trifonov, S. V., Ushakova, S. A., Kudenko, Y. A. et al. (2016), ‘Physicochemical control of the composition of the atmosphere in the physical model of the closed ecosystem’, *Proceedings of the International Astronautical Congress, IAC, 2016* <<https://www.scopus.com/inward/record.uri?eid=2-s2.0-85016451075&partnerID=40&md5=685194371765d8809e33c3a6f384854d>>.
- U.S. Department of Agriculture (2021), ‘Food Data Central’ <<https://fdc.nal.usda.gov/index.html>>, updated 25 Mar 2021.
- United States Department of Agriculture (2019), ‘USDA Food Composition Databases’ <<https://ndb.nal.usda.gov/ndb/>>, updated 27 Feb 2019.
- US Food and Drug Administration (2020), ‘Nutrition Fact Sheets for Total Fat, Total Carbohydrates and Proteins’ <<https://www.accessdata.fda.gov/scripts/InteractiveNutritionFactsLabel/factsheets.cfm>>, accessed 26 Mar 2021.
- Volk, T., and Rummel, J. D. (1987), ‘Mass balances for a biological life support system simulation model’, *Advances in Space Research*, 7/4: 141–148.
- Volponi, M., and Lasseur, C. (2020), ‘Considerations on Life Support Systems for Interstellar Travel: a Regenerative Story’, *Acta Futura*, 2020: 133–149 <<https://zenodo.org/record/3747356>>, accessed 23 Jun 2021.
- Vos, J., Evers, J. B., Buck-Sorlin, G. H. et al. (2010), ‘Functional-structural plant modelling. A new versatile tool in crop science’, *Journal of experimental botany*, 61/8: 2101–2115.
- Vos, J., Marcelis, L., Visser, P. de et al. (2007) (eds.), *Functional-Structural Plant Modelling in Crop Production* (Dordrecht: Springer Netherlands).
- Walker, J., and Granjou, C. (2017), ‘MELiSSA. The minimal Biosphere: human life and human waste in deep space’, *Futures*, 2017 <<https://halshs.archives-ouvertes.fr/halshs-01476294>>.
- Waslien, C. I., and Oswald, W. (1975), ‘Unusual sources of proteins for man’, *C R C Critical Reviews in Food Science and Nutrition*, 6/1: 77–151.
- Weber, J., and Schnaitmann, J. (2016), ‘A New Human Thermal Model for the Dynamic Life Support System Simulation V-HAB’, in , *46th International Conference on Environmental Systems* <<http://hdl.handle.net/2346/67726>>, accessed 2 Jun 2021.
- Wheeler, R. M. (2003), ‘Carbon balance in bioregenerative life support systems. Some effects of system closure, waste management, and crop harvest index’, *Advances in Space Research*, 31/1: 169–175.
- (2006), ‘Potato and Human Exploration of Space: Some Observations from NASA-Sponsored Controlled Environment Studies’, *Potato Research*, 49/1: 67–90.
- Wheeler, R. M., Berry, W. L., Mackowiak, C. et al. (1993), ‘A data base of crop nutrient use, water use, and carbon dioxide exchange in a 20 square meter growth chamber: I. Wheat as a case study’, *Journal of Plant Nutrition*, 16/10: 1881–1915.
- Wheeler, R. M., Mackowiak, C. L., Peterson, B. V. et al. (1998), *A Data Base of Nutrient Use, Water Use, CO₂ Exchange, and Ethylene Production by Soybeans in a Controlled Environment*, NASA/TM-1998-270903 <<https://ntrs.nasa.gov/api/citations/19980137405/downloads/19980137405.pdf>>.
- Wieland, P. O. (1998), *Living together in space: the design and operation of the life support systems on the International Space Station* (National Aeronautics and Space Administration, Marshall Space Flight Center ...).
- WISSLER, E. H. (1964), ‘A Mathematical Model of the Human Thermal System’, *The Bulletin of mathematical biophysics*, 26: 147–166.
- Witt, J., Hovland, S., Laurini, D. et al. (2020), ‘On-orbit Testing of the Advanced Closed Loop System ACLS’, in , *50th International Conference on Environmental Systems 2020* <<https://hdl.handle.net/2346/86479>>, accessed 10 Nov 2020.



- Wójtowicz, M. A., Cosgrove, J. E., Serio, M. A. et al. (2019), 'Monolithic Trace-Contaminant Sorbents Fabricated from 3D-printed Polymer Precursors', in , *49th International Conference on Environmental Systems* (Boston) <<https://hdl.handle.net/2346/84489>>, accessed 16 Nov 2020.
- Zabel, P. (2020), 'Influence of crop cultivation conditions on space greenhouse equivalent system mass', *CEAS Space J*, 10: 1.
- Zabel, P., Bamsey, M., Schubert, D. et al. (2016), 'Review and analysis of over 40 years of space plant growth systems', *Life Sciences in Space Research*, 10: 1–16.
- Zabel, P., Bornemann, G., Tajmar, M. et al. (2019), 'Yield of dwarf tomatoes grown with a nutrient solution based on recycled synthetic urine', *Life Sciences in Space Research*, 20: 62–71.
- Zabel, P., Zeidler, C., Vrakking, V. et al. (2017), 'Future Exploration Greenhouse Design of the EDEN ISS Project', in , *47th International Conference on Environmental Systems*.
- Zabel, P., Zeidler, C., Vrakking, V. et al. (2020), 'Biomass Production of the EDEN ISS Space Greenhouse in Antarctica During the 2018 Experiment Phase', *Frontiers in plant science*, 11: 656.
- Zhang, H., Su, S., Lin, G. et al. (2012), 'Efficiency calculation and configuration design of a PEM electrolyzer system for hydrogen production', *International journal of electrochemical science*, 7/4: 4143–4157.
- Zhang, Y., Kirriwa, Y., and Nukaya, A. (2015), 'Influence of Nutrient Concentration and Composition on the Growth, Uptake Patterns of Nutrient Elements and Fruit Coloring Disorder for Tomatoes Grown in Extremely Low-volume Substrate', *The Horticulture J*, 84/1: 37–45.
- Zhu, J., Dai, Z., Vivin, P. et al. (2018), 'A 3-D functional-structural grapevine model that couples the dynamics of water transport with leaf gas exchange', *Annals of botany*, 121/5: 833–848.
- Zolotukhin, I. G., Tikhomirov, A. A., Kudenko, Y. A. et al. (2005a), 'Biological and physicochemical methods for utilization of plant wastes and human exometabolites for increasing internal cycling and closure of life support systems', *Advances in Space Research*, 35/9: 1559–1562.
- Zolotukhin, I. G., Tikhomirov, A. A., Kudenko, Y. A. et al. (2005b), 'Biological and physicochemical methods for utilization of plant wastes and human exometabolites for increasing internal cycling and closure of life support systems', *Advances in Space Research*, 35/9: 1559–1562.
- Zuniga, A., Modi, H., Kaluthantrige, A. et al. (2019), 'Building an Economical and Sustainable Lunar Infrastructure to Enable Human Missions', in , *70th International Astronautical Congress* <https://www.nasa.gov/sites/default/files/atoms/files/building_an_economical_and_sustainable_lunar_infrastructure_to_enable_human_lunar_missions.pdf>, accessed 8 Oct 2020.

This page intentionally left blank.



Appendix A Figures and Tables

A.1 List of Figures

Figure 1.1-1 Simplified representation of a hybrid LSS.	1
Figure 1.2-1 Mission Scenario One: The life support system of the International Space Station (Seedhouse 2020: 82).	3
Figure 1.2-2 Mission Scenario Two: south pole Moon base system overview. Dashed systems are optional.	3
Figure 1.2-3 Mission Scenario Three: Permanent Martian base system overview. Dashed systems are optional.	4
Figure 1.3-1 Dissertation overview.	5
Figure 2.3-1 A schematic representation of the MELiSSA loop, with the five compartments and their relations highlighted (Volponi and Lasseur 2020).	11
Figure 2.3-2 Flow chart of the SCE when a human is connected to the system (Tikhomirov et al. 2018).	12
Figure 2.3-3 Material flows in CEEF (Tako et al. 2017).	13
Figure 2.3-4 Material cycling in the Lunar Palace experiment (Dong et al. 2017).	14
Figure 4.1-1 Simplified representation of a hybrid LSS with additional influences on the components.	21
Figure 5.1-1 User form to define schedules in LiSTOT.	30
Figure 5.1-2 Flow chart for the criticality analysis.	32
Figure 5.1-3 Crew schedule used for the trade-off.	42
Figure 5.1-4 Daily CO ₂ partial pressure and production in LiSTOT. Since all systems are scaled to achieve the same average CO ₂ removal, these results are independent of the selected subsystems.	43
Figure 5.1-5 Daily humidity, waste-water and urine production in LiSTOT.	43
Figure 5.1-6 ISS ECLSS composition.	45
Figure 5.1-7 ISS based Open-Loop ECLSS composition.	45
Figure 5.1-8 Alternative CO ₂ reduction options. Left Bosch reactor with higher oxygen recovery than SCRA. Right PBR which directly produces oxygen without requiring hydrogen.	46
Figure 5.1-9 PGC options for ECLSS composition.	46
Figure 5.1-10 Exploration PGC with urine treatment composition analysis.	47
Figure 5.1-11 ESM results over time for the different ECLSS compositions including the break-even times.	48
Figure 5.1-12 ECLSS subsystem ESM allocation for the different considered options excluding spares.	49
Figure 5.2-1 Basic structure of V-HAB (Pütz et al. 2019).	51
Figure 5.2-2 V-HAB modelling philosophy.	52
Figure 5.2-3 Overview of execution order in V-HAB.	53
Figure 5.2-4 Basic V-HAB model. <i>Branches are represented as arrows with the arrow indicating the positive flow direction of the branch.</i>	55
Figure 5.2-5 Example system for the matter network solver.	56
Figure 5.2-6: Mass flow for a roughness of 0.001 mm ($\Delta p = 1$ bar) (Busch 2019).	57
Figure 5.2-7: Mass flow for a roughness of 0.01 mm ($\Delta p = 1$ bar) (Busch 2019).	57
Figure 5.2-8: Mass flow for a roughness of 0.1 mm ($\Delta p = 1$ bar) (Busch 2019).	58
Figure 5.2-9: Mass flow for a roughness of 1 mm ($\Delta p = 1$ bar) (Busch 2019).	58
Figure 5.2-10 Example system for the thermal network solver.	58
Figure 5.2-11 Comparison of V-HAB pH calculation for a titration curve of H ₃ PO ₄ with NaOH.	60
Figure 5.2-12 V-HAB draw.io library.	61
Figure 5.2-13 Example ECLSS model created with draw.io (Pütz et al. 2019).	62
Figure 5.3-1: Comparison of LDF calculation at different step sizes with the exponential approach.	64
Figure 5.3-2 CDRA model structure.	65
Figure 5.3-3: CDRA model comparison to test data from (Knox 2000).	66

Figure 5.3-4 Convergence analysis of the CDRA model showing the mean difference in CO ₂ partial pressure. Since the difference between model and test data is generally positive, the mean squared error shows the same basic behavior.	66
Figure 5.3-5 SCRA model structure.	67
Figure 5.3-6 SCRA accumulator pressure and cumulative produced (H ₂ O) and vented (all other) masses for the simulation.	68
Figure 5.3-7 Flowrates within the SCRA during the validation case.	68
Figure 5.3-8 Cell temperatures inside the CCAA condensing heat exchanger for the water and air flow.	69
Figure 5.3-9 CCAA simulation results compared to proto-flight test data.	70
Figure 5.3-10 CCAA parameter fitting for the average air outlet temperature difference over the six proto-flight tests.	70
Figure 5.3-11 WPA model structure showing only two cells per resin. Resins are manufacturer names from (Hokanson 2004).	71
Figure 5.3-12 Comparison of sodium breakthrough from (Hokanson 2004: 287) (dashed lines) with the V-HAB model.	74
Figure 5.3-13 Comparison of sodium breakthrough from (Mühlhaus 2017: 30).	74
Figure 5.3-14 Comparison of acetate breakthrough from (Hokanson 2004: 289) (dashed lines) with the V-HAB model.	75
Figure 5.3-15 UPA model structure.	75
Figure 5.3-16 UPA validation simulation over 60 days.	76
Figure 5.3-17 BPA model structure.	77
Figure 5.3-18 BPA validation simulation over 60 days.	77
Figure 5.3-19 V-HAB model structure of electrolyzer.	81
Figure 5.3-20 Overpotentials in the electrolyzer model at different pressures compared to data (squares, triangles and circles for the respective overpotentials) from (Suermann et al. 2016).	81
Figure 5.3-21 Overpotentials in the electrolyzer model at different temperatures compared to data (squares, triangles and circles for the respective overpotentials) from (Suermann et al. 2016).	82
Figure 5.3-22 Overview of the ISRU reactor model. The number of cells is reduced to three compared to 10 in the model. (Kaschubek et al. 2021)	84
Figure 5.3-23 Results of ISRU reactor optimization in produced water per day per ESM with different equivalency factors for power and cooling. (Kaschubek et al. 2021)	86
Figure 5.3-24 Outer temperature of the ISRU reactor. The warmer front side points towards the sun. (Kaschubek et al. 2021).	87
Figure 5.3-25 Temperature of the lunar surface below the reactor. The shadow of the reactor is not considered. (Kaschubek et al. 2021)	87
Figure 5.3-26 ISRU reactor values. Top left corner shows the current conversion ratio of ilmenite in blue and the desired conversion ratio of 0.9 in red. The top right corner shows the total heat flow between the regolith and the reactor shell. Bottom left corner shows the temperatures of the cells in the reactor and bottom right corner shows the heat flow of the electrical heaters within the reactor cells. (Kaschubek et al. 2021)	88
Figure 5.4-1 Exemplary daytime CO ₂ exchange for the MEC model.	89
Figure 5.4-2 Overview of plant model in V-HAB.	91
Figure 5.4-3 Average daily flowrate validation for oxygen production (O ₂), carbon dioxide consumption (CO ₂), transpiration (H ₂ O) and biomass growth (edible and inedible) of plant model (simulation) compared to test data from (Anderson et al. 2018: 179). Transpiration is in hecto-gram per m ² and day while all other values are in gram per m ² and day.	92
Figure 5.4-4 Dynamic validation of carbon dioxide exchange and transpiration compared to test data from the following sources: Soybean (Wheeler et al. 1998), Wheat (Wheeler et al. 1993) and Potato (Wheeler 2006).	93
Figure 5.4-5 Nitrate mass in the storage compartment of the plant model with nutrient supply turned off after 80 days.	94
Figure 5.4-6 Nitrate Mass in the different compartments of a tomato plant without nutrient deficiency. Total mass includes nitrogen required for edible biomass and the storage and structural mass contained in the inedible biomass.	94



Figure 5.4-7 Picture of the plant growth chamber with an overview of the ventilators and airflows translated from (Blank 2019b: 36). 95

Figure 5.4-8 Biomass from experiment in plant growth chamber compared to simulation. (Blank 2019b: 96) 96

Figure 5.4-9 β corrected CO₂ draw down tests comparison between experiment and simulation. (Blank 2019b: 99). 97

Figure 5.4-10 Model overview of the V-HAB photo bio reactor and algae models. 98

Figure 5.4-11 Reference Gompertz model biomass concentration and concentration increase. 99

Figure 5.4-12 Partial pressure of oxygen and carbon dioxide in 65m³ cabin with PBR. 100

Figure 5.4-13 Factors impacting algae growth for the modelled PBR test case. 101

Figure 5.4-14 Consumed masses (CO₂ and Urine) and produced masses of the PBR. 101

Figure 5.4-15 Overview of CROP V-HAB model structure. 104

Figure 5.4-16 pH Value and masses in the CROP solution during a simulation. 105

Figure 5.4-17 Enzymatic kinetic flowrates of the different substances within CROP. 106

Figure 5.4-18 Cumulative exchanged masses of CROP, positive values represent an uptake of CROP while negative values represent a production of that mass by CROP. Dissolved masses represent the uptake from the calcite mass within the system while consumed calcite is the cumulative supply via the calcite interface. 106

Figure 5.5-1 Connections in the V-HAB human model. (Czupalla 2011: 164) 107

Figure 5.5-2 V-HAB model structure of the respiration and cardiovascular layer. 108

Figure 5.5-3 V-HAB model structure of the metabolic layer. 109

Figure 5.5-4 V-HAB model structure of the water balance layer. 112

Figure 5.5-5 V-HAB model structure of the digestion layer. 113

Figure 5.5-6 Overview of the new V-HAB human model with all connections between the different layers. The thermal layer is not shown here, as it does not have mass flow interfaces with the other layers and only controls thermal heat flows and sweat production. Sweat production is shown here as the water branch connected to respiration, as all sweat is assumed to evaporate. 114

Figure 6.3-1 ISS Configuration used for the simulation (dashed symbols indicate inactive systems). IMV flows are provided in cubic feet per minute (cfm) as these are the values used by NASA. Adapted from (Pütz et al. 2018) 118

Figure 6.3-2 Top view (left) and front view(right) of an ISPR based plant growth chamber with lettuce (green) and tomato (red) compartments. The area size in grey is used for all crop growth compartments. (Pütz et al. 2018) 119

Figure 6.3-3 Partial pressure of CO₂ on the ISS without a plant growth chamber. 120

Figure 6.3-4 Relative humidity on the ISS without a plant growth chamber. 121

Figure 6.3-5 Dew Point on the ISS without a plant growth chamber. 122

Figure 6.3-6 Overview of different masses in the ISS ECLSS. Top left: Water Storage System (WSS) potable water mass. Top right: WPA waste-water tank mass. Bottom left: food storage mass. Bottom right: waste processing system masses. For the bottom right figure, dash-dotted lines represent the Columbus case, while solid lines are the case without PGC. 123

Figure 6.3-7 Overview of PGC biomass values. The values are the summation over the four cultures for each crop. Cumulative values represent the integral of the corresponding flowrates. 123

Figure 6.3-8 Overview of the PGC interaction with the environment. Cumulative values represent the integral of the corresponding flowrates. 124

Figure 6.3-9 Overview of the nutritional conditions for the PGC. Cumulative values represent the integral of the corresponding flowrates. 125

Figure 6.3-10 Condensate mass recovered by the CCAAs for the different locations of the PGC as defined by the legend. 125

Figure 6.3-11 Produced water by SCRA for the different PGC cases (left). And SCRA accumulator pressure for the case without PGC and with a PGC in JEM. 126

Figure 6.3-12 Recovered water mass over the consumed water mass for an open plant growth chamber with a CCAA in the habitat and for a closed plant growth chamber with a CCAA inside the chamber. In all cases CAMRAS is used as primary air revitalization system. (Pütz et al. 2018) 127

Figure 6.4-1 The four most promising landing sites at the lunar south pole. Ares with low enough slope are marked by red lines. Black points indicate permanently shaded regions, white points are peaks of light, and cyan points water ice

from (Li et al. 2018a) as auxiliary information. The figure from (Kaschubek et al. 2021) was created by Matthias Killian.
.....128

Figure 6.4-2 Estimated remaining energy storage system runtime over one year for the four selected candidate landing sites. The charge to discharge (C/D) ratios are defined to fully recharge the energy storage before the longest continuous shadow duration. The dashed red lines indicate the simulated period for the detailed analysis in the following chapters. Figure from (Kaschubek et al. 2021).129

Figure 6.4-3 Schematic of the ECLSS with mass flows in kg/day if no shadow phase is assumed at all. Values are based on a crew of six with metabolic values from (Anderson et al. 2018: 63). Other values assume ideal stoichiometric conversion. Figure from (Kaschubek et al. 2021).130

Figure 6.4-4 Power and hydrogen/oxygen tank pressures for the Moon base at Mount Kocher (left) and South East Shackleton (right).134

Figure 6.4-5 WPA waste-water tank mass (top) and potable water tank mass (bottom) for the Moon base at Mount Kocher (left) and South East Shackleton (right).135

Figure 6.4-6 Oxygen and carbon dioxide partial pressures in the Moon base for the South East Shackleton site.135

Figure 6.4-7 Average daily mass flow rates for the Mount Kocher site in kg/d.136

Figure 6.4-8 Average daily mass flow rates for the Shackleton South East site in kg/d.137

Figure 6.4-9 Oxygen and Carbon Dioxide Partial Pressures in the Moon base for the Mount Kocher Site with PBR.137

Figure 6.4-10 Average daily mass flow rates for the Mount Kocher site in kg/d with a PBR.138

Figure 6.5-1 LiSTOT analysis of the CELSS life support system.141

Figure 6.5-2 Location of subsystems in mission scenario three and size of the compartments. Greenhouse volume is in m³ per m² plant growth area.141

Figure 6.5-3 Solar power above the atmosphere of Mars over the aerocentric longitude of Mars.143

Figure 6.5-4 Solar power with and without tracking at Martian surface assuming an average atmospheric opacity of $\tau = 0.5$ at the selected landing site of Gusev Crater-Columbia Hills: (14.6°S, 175.4°E)144

Figure 6.5-5 Solar power with and without tracking at Martian surface assuming an average atmospheric opacity of $\tau = 0.5$ at the candidate landing site of Chasma Boreale: (82.6°N, 47.3°W).....144

Figure 6.5-6 Greenhouse temperature and relative humidity for the first day of plant growth with the normal CCAA control logic (old logic) and a newly derived PID control logic (new logic).146

Figure 6.5-7 Total heat flow of the CCAA and angle of the TCCV in the greenhouse for the first day of plant growth with the normal CCAA control logic (old logic) and a newly derived PID control logic (new logic).146

Figure 6.5-8 Averaged daily flowrates over a seven-day period for the base CELSS case with 118 days of prior plant growth.147

Figure 6.5-9 Available food masses in the base CELSS.148

Figure 6.5-10 Atmosphere values for the cabin and greenhouse in the base CELSS.148

Figure 6.5-11 Energy system parameters for the base CELSS.149

Figure 6.5-12 Adsorbed water masses in CDRA for the base CELSS case.150

Figure 6.5-13 Atmosphere values for the cabin and greenhouse in the single cultures CELSS.151

Figure 6.5-14 Averaged daily flowrates for the single culture case with 118 days of prior plant growth.151

Figure 6.5-15 Atmosphere values for the cabin and greenhouse in the full ELS CELSS.152

Figure 6.5-16 Atmosphere values for the cabin and greenhouse in the part ELS CELSS.153

Figure 6.5-17 TCCV Angle for the CCAAs in the part ELS CELSS.153

Figure 6.5-18 Adsorbed water masses in CDRA for the Part ELS case.154

Figure 6.5-19 Adsorbed CO₂ masses in CDRA for the Part ELS case.155

Figure 6.5-20 Averaged daily flowrates for the Part ELS case with 118 days of prior plant growth.155

Figure 6.5-21 Atmosphere values for the cabin and greenhouse in the base CELSS during the startup phase.156

Figure 6.5-22 Energy system parameters for the base CELSS during the startup phase.156

Figure 6.5-23 Averaged daily flowrates over a seven-day period for the base CELSS case during the startup phase.157



A.2 List of Tables

Table 2.1-1: Carbon dioxide removal candidate technologies.	7
Table 2.1-2: Oxygen generation candidate technologies.....	7
Table 2.1-3: Carbon dioxide reprocessing candidate technologies. A human equivalent corresponds to the metabolic outputs of a human as defined by (Anderson et al. 2018: 63).	7
Table 2.1-4: Overview of PC waste management technologies based on (Anthony and Hintze 2014; Anderson et al. 2017b).	8
Table 2.2-1: Plant growth chamber candidate technologies.....	9
Table 2.2-2: Algae reactor candidate technologies.	9
Table 2.2-3: Biological waste recycling candidate technologies.....	10
Table 2.3-1: Closed Ecological Life Support Systems (CELSS) demonstrators.....	11
Table 3.1-1: Available life support simulation tools.	15
Table 3.3-1: Higher plant modelling tools for LSS.	18
Table 3.4-1: Overview of available human models.....	20
Table 4.1-1: Identified research gaps.	25
Table 4.3-1 Research questions for the defined mission scenarios.	27
Table 4.3-2 Additional requirements for the tool.	27
Table 5.1-1: Plant growth chamber ESM values based on (Zabel 2020; Anderson et al. 2018: 163).	33
Table 5.1-2: Target values <i>beq</i> (=) and boundary conditions <i>b</i> , <i>lupper</i> (\geq / \leq) of the optimization algorithm for the different cases.	35
Table 5.1-3: Plant parameters used for the optimization, edible growth rate is fresh basis from (Anderson et al. 2018: 179) page 179 for all crops except chufa and cucumber which are taken from (Fu et al. 2019: 697). Dry base carbon content (C) is from (Anderson et al. 2018: 180) page 180, except for chufa and cucumber where it was estimated based on similar crops. Nutritional data is from (U.S. Department of Agriculture 2021), $C_xH_xO_x$ describes carbohydrates.	36
Table 5.1-4: PGC plant growth areas. Part ELS and Full ELS are based on (Anderson et al. 2018: 181) while the Lunar Palace (LP) case is based on (Fu et al. 2019). The provided information from literature was scaled to 12.7 MJ/d energy demand for better comparability.	37
Table 5.1-5: Nutrient Supply from the different PGC.....	37
Table 5.1-6: Percentage of energy from macro nutrients of the different PGC.....	38
Table 5.1-7: ESM equivalency factors for Mars from (Anderson et al. 2018: 23).	40
Table 5.1-8: Assumed ECLSS parameters.	40
Table 5.1-9: ESM values used for ISS ECLSS.	41
Table 5.1-10: MCA and ESM values of CO ₂ reduction options.	44
Table 5.1-11: Resupply masses of the different ECLSS options.....	48
Table 5.2-1 Percentage errors in the comparison of V-HAB and ANSYS from (Busch 2019).	57
Table 5.3-1: SCRA validation results compared to test results from (Knox et al. 2005).	69
Table 5.3-2: Proto-flight test setpoints used for CCAA validation.	70
Table 5.3-3: VRA parameters used in the WPA model	73
Table 5.3-4: Parameters used for the ISRU reactor optimization. (Kaschubek et al. 2021).....	85
Table 5.4-1: β correction factor of CO ₂ drawn down tests for the PGC adjusted from (Blank 2019b: 100).....	97
Table 5.5-1: Validation Case Set Points. – Represents Values for which no Information was available.....	115
Table 5.5-2: Human model validation. The differences are always relative to the NASA (Anderson et al. 2018) values. The balance column indicates whether a value is consumed (+) or produced (-) by the human. Feces are not available as parameter in HumMod.....	116
Table 6.3-1 Qualitative crew timeline. Exercise is always assumed for one hour, sleep for eight hours. (Pütz 2017).....	118
Table 6.4-1 Moon Base subsystem power demand.	131
Table 6.4-2 Mass estimation literature parameters.....	133
Table 6.5-1: Assumed crop conditions for the Closed Environmental Life Support System.	142
Table 6.5-2: Assumed crop growth areas for the different cases.	142

Table 6.5-3: Parameters for the PID control logic of the greenhouse CCAA.....145



Appendix B Overview of Carbon Dioxide Reprocessing Reactions

This chapter provides an overview of the stoichiometric chemical reactions of the carbon dioxide reprocessing systems discussed in chapter 2.1.1.3.

B.1 Sabatier Reactor



B.2 Vertical Bosch Reactor



B.3 Solid Oxide Electrolysis



Appendix C Overview of Available System Level ECLSS Models

A detailed discussion of the various system level analysis tools for ECLSS is provided in chapter 3.1.

Table C-1: Overview of the system level analysis tools and the corresponding state of their subsystem models

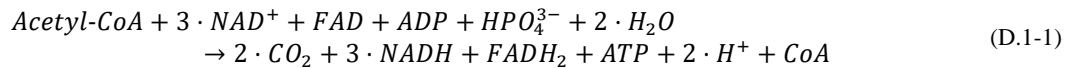
	Human	Plants	Waste Management	PC	Sources
BioSim	Partially Dynamic	MEC	Recovery Percentage	Partially Dynamic	(Goudarzi and Ting 1999; Kortenkamp and Bell 2003; Rodriguez et al. 2007)
HabNet	Partially Dynamic	MEC	Recovery Percentage	Partially Dynamic	(Do et al. 2015)
SICLE	Steady State	-	Recovery Percentage	Performance Percentage	(Moriyama et al. 2015; Eshima et al. 2020)
ELISSA	Steady State	not reported	not reported	Partially Dynamic	(Detrell and Belz 2017; Detrell and Ewald 2019)
EcoSimPro	Steady State	MEC	not reported	Dynamic	(Rodríguez et al. 2005; Rodriguez et al. 2006; EcoSimPro 2018; Ordonez et al. 2004)
V-HAB 1.0	Dynamic	Modified MEC	Recovery Percentage	Dynamic	(Czupalla 2011)



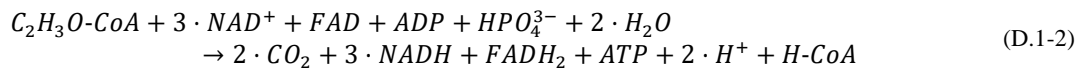
Appendix D Human Model Derivation – Metabolism Layer

D.1 Citric Acid Cycle

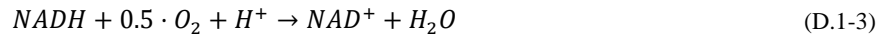
The Citric Acid Cycle is one of the most basic metabolic pathways because most normally used pathways use it in some capacity. Since the human model in this case is not intended as a full model of all metabolic pathways it is not necessary to include all steps of the reaction. Instead, a net-reaction that can easily be implemented into the human model of V-HAB is required. This reaction requires Acetyl-Coenzyme A (Acetyl-CoA) and produces energy from it in the following base reaction of the citric acid cycle from (Berg et al. 2013: 515):



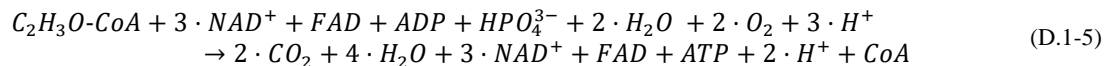
The Acetyl-CoA can be written as $\text{C}_2\text{H}_3\text{O-CoA}$ while the CoA that is produced has one additional H compared to the CoA in Acetyl-CoA. Therefore, we write H-CoA to make the atom balance easier to follow:



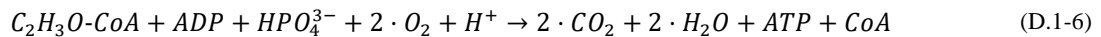
NADH and FADH₂ react with oxygen to produce water (Berg et al. 2013: 535):



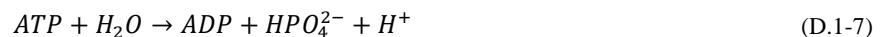
Adding these reactions to the above reaction equation yields:



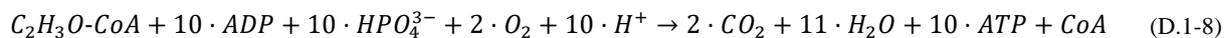
By now removing all substances that are catalytic and not consumed in the process (all substances that exist on both the educt and product side) the following reaction can be derived:



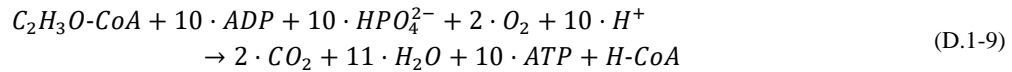
In the reaction in total 3 NADH and 1 FADH₂ were produced. According to (Berg et al. 2013: 655) each NADH yields 2.5 ATP and each FADH₂ yields 1.5 ATP. In total we therefore must add 9 reactions from ADP to ATP. The base reaction for ATP to ADP is described in (Lodish op. 2016: 61) and the reaction of ADP to ATP is the reverse reaction:



Therefore, the net-reaction of the citric acid cycle can be written as:



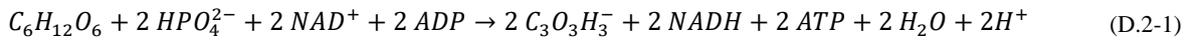
If we now replace the ADP and ATP with the chemical formula for these substances, we have the following reaction over which the atom balance can be checked:



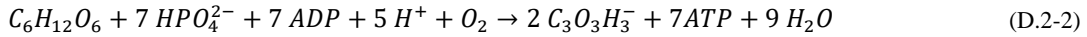
This equation is not used directly in the code but is used to derive the final net reactions in the following chapters.

D.2 Glycolysis

The glycolysis is the process in the human body that oxidizes glucose and generates energy from it. It may seem strange that a detailed derivation of this well-known process is provided here. However, because the original model assumed 36 mol of water to be generated per consumed mol of glucose (Matthias Pfeiffer 2007: 119) while other net reaction models only assumed 6 mol (Volk and Rummel 1987: 141) it became necessary to derive it in detail and understand all aspects to select the correct implementation. Initially, the glucose must be converted to Pyruvate as described in (Berg et al. 2013: 459). The reactions necessary for this step can be summarized to the net reaction:



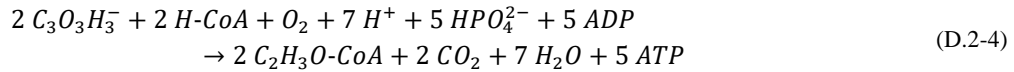
Using the reaction of NADH with oxygen and replacing the NADH with the corresponding amount of ADP to ATP the equation can be converted to:



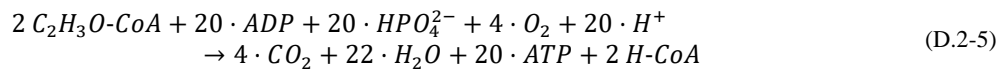
Pyruvate is then converted to Acetyl-CoA which is then used in the citric-acid-cycle (Berg et al. 2013: 503):



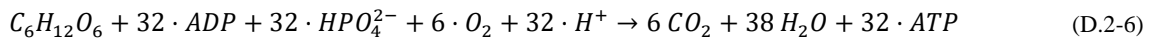
By again replacing the NADH the equation can be transformed to:



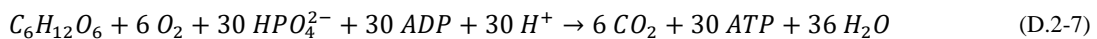
The final step is the net reaction for the Acetyl-CoA equation (D.1-9) for the $2 C_2H_3O-CoA$:



The overall net reaction of the glycolysis can now be obtained by combining the steps (D.2-1) to (D.2-5):



This corresponds to the net reaction for glucose in the case that 32 ATP are generated as mentioned in (Berg et al. 2013: 559). There is also a possible different pathway in which only 32 ATP are generated, which is also mentioned by (Berg et al. 2013) and for which the net reaction is described in (Lodish op. 2016: 515):



However, the current implementation of the human model in V-HAB does not enable to differentiate between the two different pathways that result in the difference of 2 ATP. Therefore, the assumption is made that 32 ATP are generated in all cases of glycolysis. Another important point to mention is, that not 36 mol of H_2O are generated in the body for each mol of glucose that is consumed. The original model made this assumption, as can be seen in Fig.: 8-12 of (Matthias Pfeiffer 2007: 119) which resulted in a metabolic water production of over 1 kg per day. As stated in (Anderson et al. 2018: 50) the metabolic water production should be closer to 0.4 kg per day. The mistake which lead to this discrepancy is also discussed in (Horiike et al. 1996) and can be attribute to the fact that the above equation contains the reaction of ADP to ATP but not the reaction where ADP is regenerated from ATP which is described in equation (D.1-7). Since the implemented original model did not include the back and forth conversion of ADP and ATP this aspect was missed. While the new model also does not include ADP and ATP as modelled substances, the model



uses the net reaction without the ADP to ATP conversion which can be written as and is consistent with (Volk and Rummel 1987: 141):

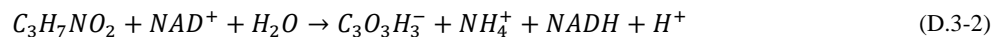
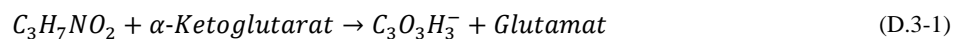


D.3 Protein

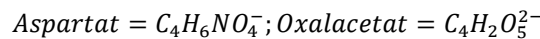
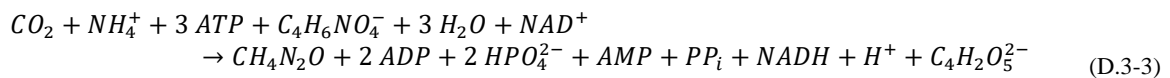
The protein metabolism was not modelled in the previous human model. Instead it simply converted proteins energy wise into fatty acids using the assumption that proteins have an energy content of 4 kcal/g and fats of 9 kcal/g (Matthias Pfeiffer 2007: 144). However, that conversion destroys mass and additionally the production of urea cannot be modelled without the protein metabolism. For these reasons, it was added to the model.

Most proteins are present in food in the form of amino acids, which are also represented in the data used for V-HAB from (United States Department of Agriculture 2019). In this chapter, the metabolization of the amino acid alanine ($C_3H_7NO_2$) is discussed. There are many different types of amino acids which have different metabolic pathways. In the current state of the model only the pathways for alanine are implemented.

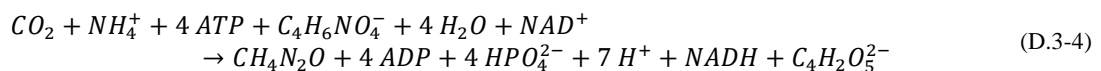
The metabolization of alanine has the following reaction steps (Berg et al. 2013: 700–1):



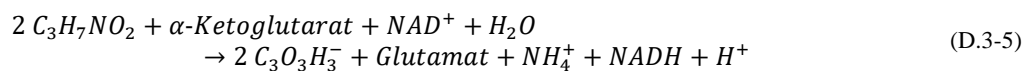
The NH_4 is converted into urea (CH_4N_2O) according to (Berg et al. 2013: 1104):



By checking the atom balance, it becomes obvious that the generated H^+ from the ATP conversion is missing from the equation, and instead of AMP one additional ATP is created which corresponds to the 4 ATP mentioned in (Berg et al. 2013: 697):



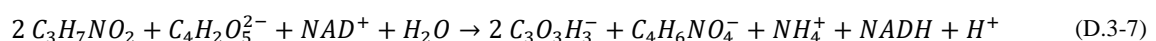
Therefore, alanine must provide one NH_4^+ and one Glutamat for the synthesis of urea, which means equation (D.3-1) and equation (D.3-2) must be combined into:



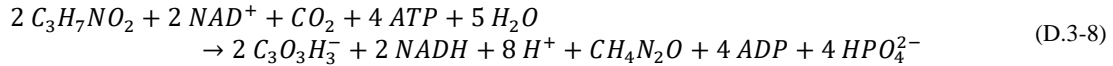
According to (Berg et al. 2013: 240) the following reaction can be used to convert Glutamat and Oxalacetat:



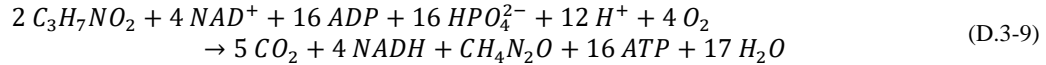
By inserting equation (D.3-6) into (D.3-5) the following reaction can be obtained:



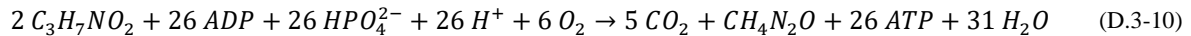
By now also adding the synthesis of urea described in equation (D.3-4) into equation (D.3-7) the following overall reaction can be derived:



Pyruvate ($C_3O_3H_3^-$) can be metabolized the same way as for the glucose metabolism, by first converting it into Acetyl-CoA (equation (D.2-3)) and then using the citric acid cycle (equation (D.1-9)). If these steps are included in the reaction it becomes:



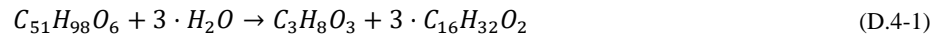
Now the NADH is replaced with the corresponding ATP to get the final net-reaction:



D.4 Fatty Acids

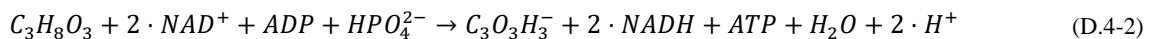
Fatty Acids are generally stored as triacylglycerol compounds for example, the Tripalmitin $C_{51}H_{98}O_6$ with one part glycerol and three parts fatty acids. Since tripalmitin is also the fatty acid up to which fatty acid synthesis occurs, this is the example which will be discussed here. (Berg et al. 2013: 647). While it would be possible to derive a generalized model that can calculate the metabolization of any fatty acid, the current model is limited to the synthesis and metabolization of tripalmitate.

In the initial step, the tripalmitate is broken down into glycerol ($C_3H_8O_3$) and palmitate ($C_{16}H_{32}O_2$) (Berg et al. 2013: 648) which both have different metabolic pathways.

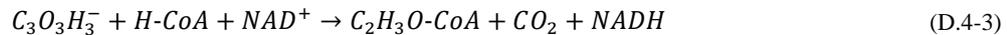


D.4.1 Glycerol:

The initial step in the metabolization of glycerol is the conversion of it to pyruvate which occurs in the following steps (Berg et al. 2013: 483):



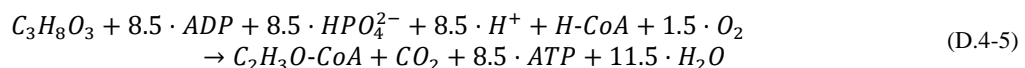
Pyruvate is then converted to Acetyl-CoA which is used in the citric-acid-cycle (Berg et al. 2013: 503).



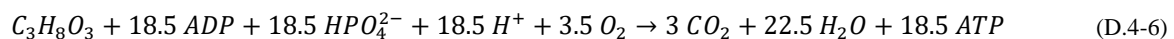
In sum this results in the equation:



By converting the NADH to ATP yields the following equation can be derived:



Overall, after combining the steps into one reaction the net reaction for glycerol can be derived:

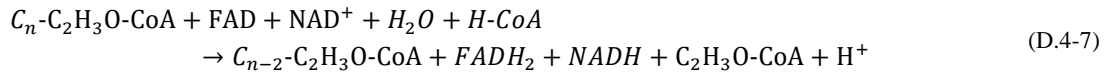


While (McArdle 2015: 154) mentions an ATP yield of 19 for the metabolization of glycerol, this is likely due to rounding.

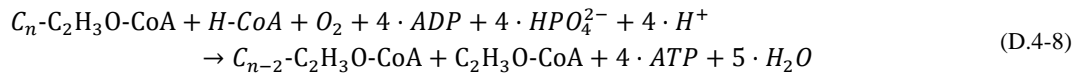


Palmitate:

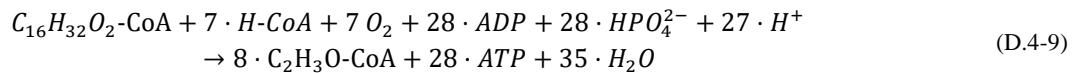
According to (Berg et al. 2013: 654) fatty acids are metabolized in a repetitive cycle using the following base equation:



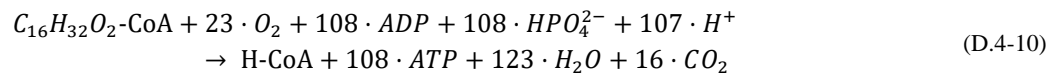
Replacing FAD and NAD with the corresponding reactions and the synthesis of 4 ADP to ATP yields:



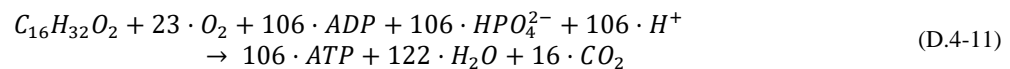
For an even number of C atoms in the fatty acid this process can be repeated $n/2-1$ times (Berg et al. 2013: 654), thus yielding $n/2$ Acetyl-CoA which can be used in the citric acid cycle. For example, for the C16 fatty acid palmitoyl-CoA the process can be repeated 7 times. It is necessary to note that in the last step $C_4H_8O_2$ -CoA is split into 2 C_2H_3O -CoA thus releasing not one H^+ as in the previous steps but 2. Therefore, the overall reaction is:



By now adding 8 times the citrate cycle to the reaction the overall reaction of palmitoyl is:

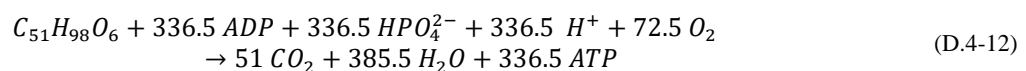


However, 2 ATP are required to activate palmitoyl (Berg et al. 2013: 655), therefore in a net reaction from the base fatty acid only 106 ATP are produced:

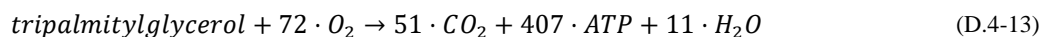


D.4.2 Tripalmitin:

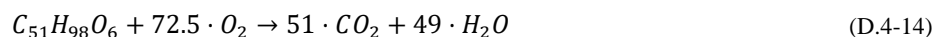
By combining the net reaction for glycerol and three times the net reaction for palmitate the net reaction for the metabolization of Tripalmitin can be derived.



For comparison in the previous model the following equation was used (Matthias Pfeiffer 2007: 117):



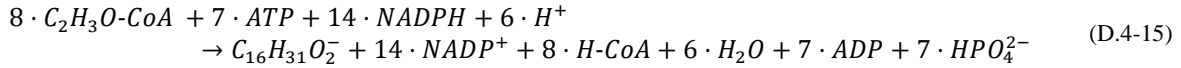
Not only is the ATP yield now significantly lower because of the lower energy yield of the citric acid cycle that was discussed previously. In addition, the consumed oxygen apparently was rounded in the original model and if we derive the net reaction without the ADP to ATP reaction from equation (D.4-12)



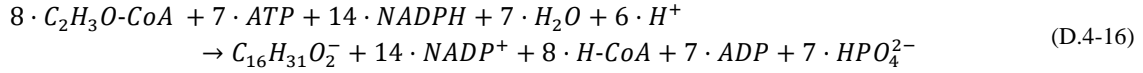
it also becomes obvious that the generated mol of water in the original model was too low, which somewhat counteracted the too high value from the glucose metabolization.

D.4.3 Fatty Acid Synthesis from Glucose

Aside from the metabolization of nutrients to provide energy another core body function is the capability to convert glucose that is not directly needed for energy generation into fatty acids using the fatty acid synthesis metabolic pathways. The base reaction for the synthesis of palmitate is: (Berg et al. 2013: 669)



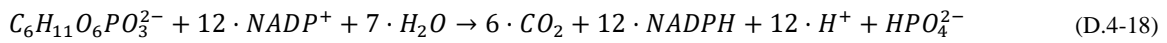
Unfortunately, this equation is not correct. If we check the hydrogen and oxygen atoms on each side we notice that 7 H₂O are missing from the left side, which are required for the ATP to ADP reaction. If we include that water the reaction becomes:



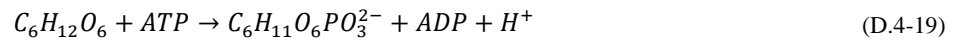
According to (Berg et al. 2013: 671) 8 of the required NADPH are produced when C_2H_3O-CoA is transported into the cytoplasm using the following reaction:



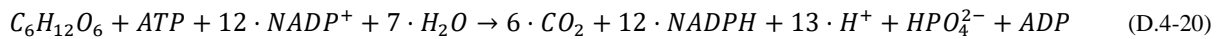
The remaining 6 NADPH are created using the pentosephosphate way according to (Berg et al. 2013: 612):



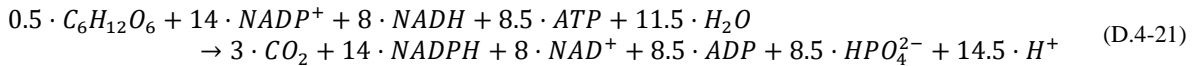
The Glucose-6-phosphat that is required for this process is created through activation by ATP (Berg et al. 2013: 449):



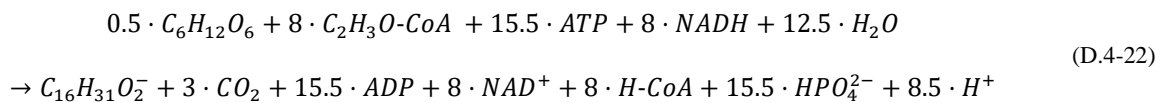
The overall net reaction how NADPH can be created from Glucose is therefore:



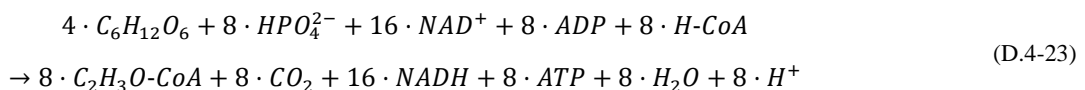
Since only 6 NADPH are needed the reaction can be multiplied with 0.5. In total the 14 NADPH required by the previous reaction can be created in the following net reaction, which combines the two pathways:



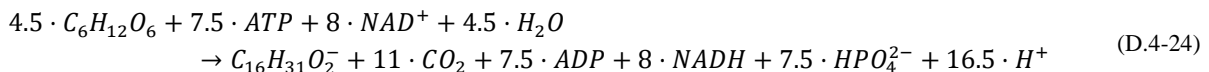
By now inserting equation (D.4-21) into equation (D.4-16) the NADPH can be replaced with substances also used in other metabolic pathways, like ATP and NADH:



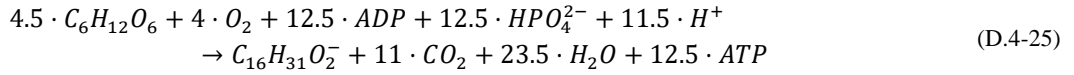
However, this reaction does not yet describe how glucose is stored, as only a small amount of glucose is currently needed for the generation of NADPH. The primary part of the stored energy are the 8 C_2H_3O-CoA which are also created from glucose using a part of the glucose pathway described in chapter D.1, namely equations (D.2-2) and (D.2-3). By combining and multiplying these two reactions with 4 the conversion of glucose to 8 C_2H_3O-CoA is obtained:



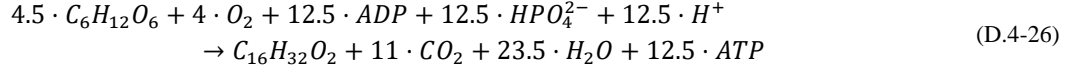
Now the 8 Acetyl-CoA in equation (D.4-22) can be replaced with equation (D.4-23):



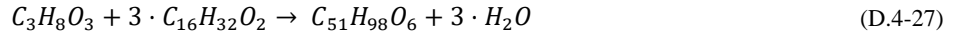
As for the other metabolic pathways, the NADH can be replaced with the corresponding reaction and ATP yield:



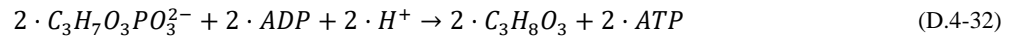
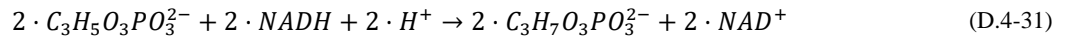
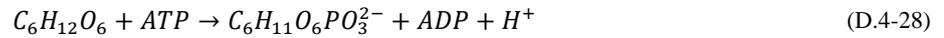
To synthesize the fatty acid without charge, one additional H^+ is required:



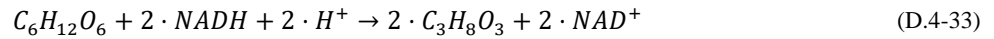
Since fat is stored in the form of triacylglycerol we can reverse the reaction described by equation (D.4-1) to synthesis it from palmitate (Berg et al. 2013: 648):



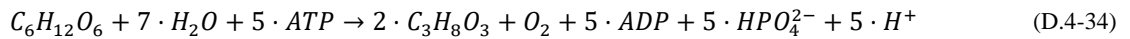
For this reaction glycerol ($C_3H_8O_3$) is required in addition to palmitate, which can be created from glucose according to (Berg et al. 2013: 484) with the following reaction steps:



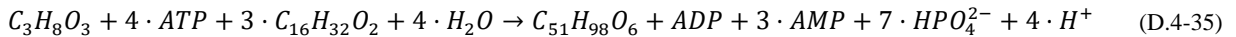
Combining these steps results in the reaction:



Actually, the NADH is taken from other metabolic pathways before it is consumed. However, in the model it is easier to reduce the oxygen consumption by the same amount as the NADH that is not used for energy production, and to also remove the equivalent of 5 ATP. Therefore, the equation is adjusted to consume ATP and produce oxygen:



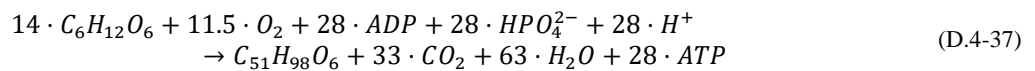
With glycerol and palmitate now available, triacylglycerol can be formed according to (Berg et al. 2013: 1109):



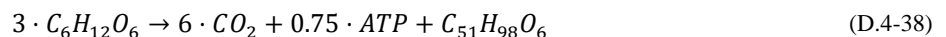
In this reaction the new metabolite Adenosine Mono Phosphate (AMP) occurs. Since the introduction of an additional metabolite just for this reaction would increase the model complexity, the reaction is instead described using ADP:



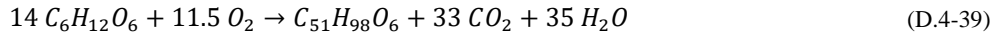
The total net-reaction to synthesize triacylglycerol from glucose therefore is:



This reaction can now also be compared to the reaction used in the original human model (Matthias Pfeiffer 2007: 146):



There is a notable difference between equation (D.4-37) and (D.4-38) which can be attributed to the original model not including all necessary metabolic pathways. For example, the role of glycerol for the generation of triacylglycerol is completely neglected as are other necessary pathways. This becomes obvious if the atoms on the left and right side of the reaction are compared. In addition, no oxygen is required for the synthesis and no water is generated. If the ATP reactions are neglected in equation (D.4-37) the following reaction shows the metabolic water yield:

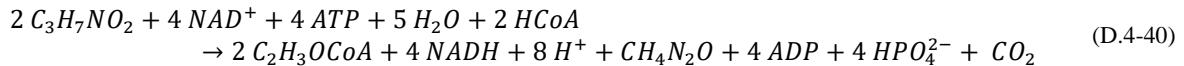


This amounts to a significant contribution of metabolic water (c.a. 780 g H₂O per kg of C₅₁H₉₈O₆) and also a significantly different glucose consumption.

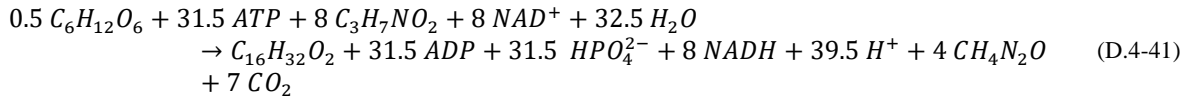
D.4.4 Fatty Acid Synthesis from Protein

As derived in chapter D.3 proteins can create pyruvate using equation (D.3-7) and thus can also create Acetyl-CoA using equation (D.2-3). Therefore, it is possible to use excess proteins in the generation of fatty acids. In this chapter the required net-reaction for this synthesis is derived.

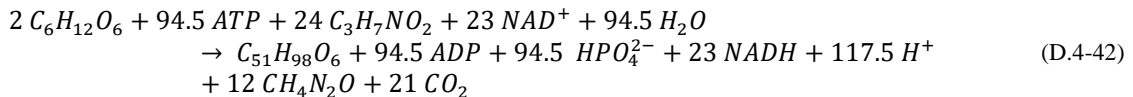
By combining the equations (D.3-7) and (D.2-3) the net-reaction to create Acetyl-CoA from proteins is:



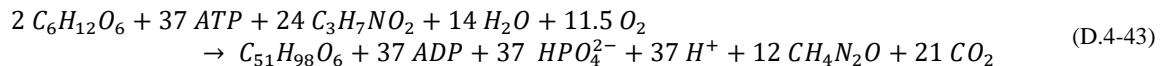
In order to create fatty acids Acetyl-CoA can be converted using equation (D.4-21) and by replacing the Acetyl-CoA in this equation with equation (D.4-40) the following equation is derived:



However, to create tripalmitin glycerol is also required, which can be produced from glucose using equation (D.4-33). By combining equation (D.4-33) and equation (D.4-41) the equation to create tripalmitin from proteins is:



The final net-reaction is derived by converting the NADH reactions using equations (D.1-3) and (D.1-7) with the corresponding ATP yield:



Since the fatty acid synthesis from proteins requires glucose and ATP it is necessary to implement a logic which controls the consumption of these metabolites based on their availability. Figure D.4-1 provides an overview over the decision tree necessary for this and the calculation steps to derive the current impact on the metabolism.

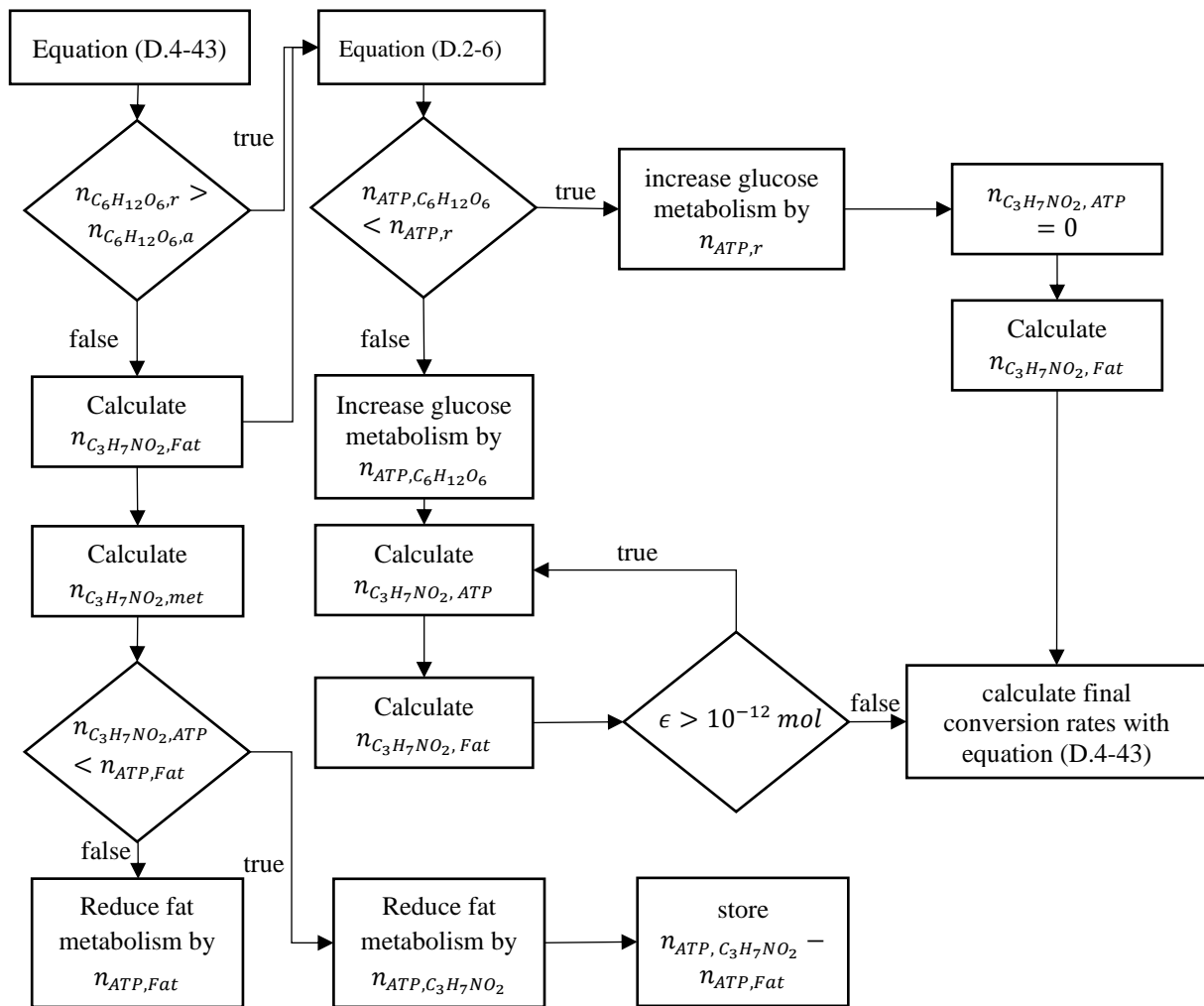


Figure D.4-1 Flow chart for fatty acid synthesis from proteins.

With the following variables:

- $n_{C_6H_{12}O_6,r}$: Required mol of glucose for the fatty acid synthesis
- $n_{C_6H_{12}O_6,a}$: Available mol of glucose after other metabolic reactions
- $n_{ATP,r}$: Required mol of ATP for the fatty acid synthesis
- $n_{ATP,C_6H_{12}O_6}$: Mol of ATP that can be produced from remaining glucose
- $n_{ATP,Fat}$: Mol of ATP that are currently consumed in fat metabolism
- $n_{ATP,C_3H_7NO_2}$: Mol of ATP that is produced by additional metabolization of proteins
- $n_{C_3H_7NO_2,Fat}$: Mol of protein that can be converted to fat based on $n_{C_6H_{12}O_6,a}$
- $n_{C_3H_7NO_2,met}$: Mol of protein that additionally must be metabolized to ATP because of insufficient glucose
- $n_{C_3H_7NO_2,ATP}$: Mol of protein that must be metabolized to generate ATP for fat synthesis
- ϵ : Error in iteration, calculated for iteration i $\epsilon = |n_{C_3H_7NO_2,Fat,i-1} - n_{C_3H_7NO_2,Fat,i}|$